UNIVERSITY OF CALIFORNIA

Los Angeles

How the immune system learns from infections

A dissertation submitted in partial satisfaction

of the requirements for the degree

Doctor of Philosophy in Physics

by

Hongda Jiang

2022

ABSTRACT OF THE DISSERTATION

How the immune system learns from infections

by

Hongda Jiang
Doctor of Philosophy in Physics
University of California, Los Angeles, 2022
Professor Shenshen Wang, Chair

The immune system is a complex system of cells and molecules that work cooperatively to protect us against pathogenic organisms. It can perform complicated tasks such as pattern recognition, learning, and memory, all of which require dynamical coordination among a large number of components across multiple scales. Nevertheless, the multitude of different components makes it challenging to unveil the mechanistic principles that give rise to these remarkable functions.

My thesis focuses on how our immune system learns from infections and improves specificity of pathogens recognition on the fly. This process is known as affinity maturation, where the affinity of B cell receptor improves through Darwinian evolution. Although recent progresses in experiments revealed many details, what remains is a first-principle and quantitative understanding of how different elements come together to achieve the goal. Using statistical physics tools and computational modeling, I study various aspects of the maturation process, including molecular interactions, information extraction, and evolutionary dynamics.

To understand how B cells with different affinities are discriminated during affinity matu-

ration, we investigate the process of antigen extraction, where B cells use cytoskeleton forces to extract antigen molecules from other presenting cell surface. We show this process allows a B cell to infer its receptor affinity by measuring the number of extracted antigens. Our model highlights the regulatory role of mechanical force: Application of a constant force with proper magnitude can enhance discrimination fidelity, and usage of a dynamical force that introduces negative feedback can improve discrimination robustness with respect to fluctuations in antigen concentration.

To illustrate how molecular interactions influence cellular evolution, we couple the physical theory of antigen extraction to a minimal model of affinity maturation and simulate ensembles of cell populations under different conditions. The multiscale model predicts that the affinity ceiling stems from the physical limit of antigen tether strength and identifies strategies to alleviate the constraint.

Lastly, we present a study on the long-term coevolution between evolving pathogen and adaptive immune response. Our work reveals that the asymmetric reaction range between immunogenicity (the ability of pathogens to induce an immune response) and antigenicity (the ability of pathogens to interact with antibodies) is critical in determining the dynamics of coevolution.

The dissertation of Hongda Jiang is approved.

Giovanni Zocchi

Tom Chou

Robijn F. Bruinsma

Shenshen Wang, Committee Chair

University of California, Los Angeles

2022

To Nelly, Mom and Dad

TABLE OF CONTENTS

LIST OF FIGURES

ACKNOWLEDGMENTS

First and foremost, I would like to thank my advisor Dr. Shenshen Wang. Thank you very much for introducing me to the world of biophysics, which fascinated me at my first glance through your Physics 243M lectures. You provided me with various interesting research projects and granted me extraordinary flexibility. I feel sincerely grateful for the countless meetings, discussions and email exchanges with you, which not only lowered the barriers, guided me towards discoveries, but also taught me how to ask scientific questions, how to think deeply and to justify meticulously. The success, failure, excitement, and frustration along the journey have been my invaluable wealth of life, which I will benefit from continuously regardless of what I'm going to pursue in the future.

My sincere gratitude is expressed to Dr. Robijn Bruinsma, Dr. Tom Chou, and Dr. Giovanni Zocchi, for kindly lending the helping hands to serve on my committee and give constructive comments and support. Dr. Robijn Bruinsma was extremely helpful during my writing of this dissertation. I appreciate the valuable feedback and inspirations he provided during our weekly meetings. Dr. Tom Chou has provided various enlightening ideas and financial support for my research projects. I have benefited a lot from the excellent statistical mechanics class taught by Dr. Giovanni Zocchi five years ago. I hope my thesis writing worth your time reading and I look forward to your kind suggestions.

To my colleagues, I was fortunate to work with you and learn from you. Jiming Sheng and I shared the same office, where we discussed from day to day about research, physics, math, life, food and everything else. I really enjoyed and inspired by the numerous presentations given by Jiming on our weekly group meeting. Steven Schulz, being gracious, modest and intelligent, gave me a lot of insightful comments about my project and my writing of the manuscript. Milos Knezevic has been very generous in sharing the source code of his project with me, from which I learned a lot. Thank you, Steven Durr and Casey Barkan, for your interests and all the insightful questions you asked every time I presented my work.

To my classmates, Ji Zou, Ziqi Pi, Andy Chan, Kevin Chen, Yujian Zhao, Teresa Le and many others, I feel very lucky to spend my journey with you at UCLA. I miss the time when we prepared for exams, played boardgames, ate pizza at the P&A social, and had delicious Taco together.

To my dear Mom, thank you for giving me unconditional love and firm support all the time. To my dear Dad, thank you for holding me on your shoulders, from where I can see further and achieve higher. To my beloved financee, thank you for by my side, sharing my stress as well as happiness, and enhancing me to a large extent in many aspects. Your warm company has raised my tempoerature so that I can cross potential barriers and overcome chalenges easily.

Finally, I appreciate the financial support from Dr. Tom Chou's NIH grant (R01HL146552) and NSF grant (DMS-1814364). I want to acknowledge the support from the Rudnick-Ablemann Fellowship. I am grateful for the fellowship from Mani L. Bhaumik Institute for Theoretical Physics at UCLA.

Chapter 6, in full, is a reprint of Jiang and Wang (2019). We thank Sidney Redner and Paul Bressloff for enlightening discussions. I am gratefully acknowledge funding from the Dean of Physical Sciences at University of California, Los Angeles. The dissertation author was the primary investigator and author of this paper.

VITA

2012–2016 B.S. (Applied Physics)
University of Science and Technology of China, P.R.C.

2016–2018 M.S. (Physics)
University of California, Los Angeles, U.S.A.

2019 Ph.D. candidate in Physics
University of California, Los Angeles, U.S.A.

PUBLICATIONS

Hongda Jiang and Shenshen Wang, Physical constraints reveal adaptive potential of immune learning, *Phys. Rev. X, under review*

Hongda Jiang and Shenshen Wang, Immune cells use active tugging forces to distinguish affinity and accelerate evolution, *PNAS, under review*

Hongda Jiang and Shenshen Wang, Trait-space patterning and the role of feedback in antigen-immunity coevolution, *Phys. Rev. Research* **1**, 033164 (2019)

Miloš Knežević, Hongda Jiang, and Shenshen Wang, Active Tuning of Synaptic Patterns Enhances Immune Discrimination, *Phys. Rev. Lett.* **121**, 238101 (2018)

CHAPTER 1

Introduction

"Physics was a point of view that the world around us is, with effort ingenuity, and adequate resources, understanable in a predictive and reasonably quantitative fashion."

John J. Hopfield

The immune system protects ourselves against pathogenic organisms and cells that are diverse and constantly evolving in nature. The past few decades have witnessed an explosion in detailed experimental findings about the cells, molecules, and genes that constitute the intricate yet reliable immune system. What still remains is the task of understanding in a quantitative way how elements of the immune system behave and how they interact with each other to generate the organized activity observed during an immune response.

While the goal of the immune system is well-defined in principle — preventing pathogenic cells from the programmed division — it is not easy to recognize and clear foes from friends. To a large extent, the main challenge is to recognize the unknown: Pathogens are extremely diverse in nature and constantly evolving to escape recognition by the immune system. This can be seen in our everyday experience by the evolving influenza virus, which requires a new vaccination every year. Besides, SARS-CoV-2, the virus that causes the ongoing COVID-19 pandemic, has developed into many thousands of variants in the past two years and continues threatening the global population with novel mutants. Therefore, it is futile and

impossible to code all pathogen information into genetic materials. Instead, organisms must be adaptive and learn from exposures. For this reason, the strategies developed by the immune system require evolution on the fly to generate novel binders in order to recognize the unseen pathogens.

One of the main players in this adaptive immune response is B cell, which is capable of generating highly specific receptors to deal with invading pathogens through a unique process called *affinity maturation* [3]. During an antigen encounter, the B cells that barely recognize the antigen are activated and go through cycles of somatic hypermutations that introduce further diversity, followed by a selection process to eliminate low-affinity and self-reactive specificities. At the same time, a fraction of evolving B cells may differentiate into antibody-secreting B cells (plasma cells) which can create antibody molecules to neutralize antigens, or memory cells in preparation for future encounter of the same antigen.

Since the discovery of affinity maturation in the last century [4], it becomes increasingly clear that this process requires coordination at many scales from the molecular of receptor-antigen bindings, gene recombination, regulation of biochemical pathways, to the cellular of cell-to-cell communication and clonal population dynamics. Despite this complexity, affinity maturation works remarkably robust and reliably. How do these collective interactions on different scales dynamically come together to build a complex evolving system against a high dimensional moving target? This high level question can be broken into smaller problems emerging from the key steps at different levels or scales of affinity maturation, viewed from different perspectives.

First, at the molecular level, the evolution of B cells is mainly driven by the interaction between B cell receptors and antigens. It was recently discovered that, unlike other lymphocytes including T cells, B cells actively used tugging forces to extract and internalize antigens presented on antigen presenting cells [2, 5]. From the biological point of view, this raises the question of how and why evolving B cells expend mechanical energy to physically extract antigens. Besides, from the information perspective, the noisy antigen-receptor in-

teraction allows an immune system to fetch readable signals in order to discriminate B cells with different affinities. Is there any fundamental physical constrain for affinity discrimination? More importantly, how can we approach the limit? What signal a B cell should look at to optimize decision-making? In addition, recent experiments suggested that B cells might be able to actively manipulate the ligand receptor interaction through highly dynamic and adaptive forces [6], which implies a feedback mechanism that allows B cells to control the thermodynamic process. From the perspective of control theory, what types of control can potentially benefit the task of affinity discrimination? How to identify the feedback mechanism in experiments?

Second, at the population level, it is unclear what factors facilitate affinity maturation and what halt it. The information collected from the antigen extraction process is utilized to determine the cell fate (proliferate or die). Collectively, B cell clones with different affinities are iteratively generated, discriminated and selected, which not only increases the affinity and neutralization potency of receptors, but also changes their binding breadth as well as flexibility [7, 8]. However, this evolutionary learning process appears surprisingly ineffective: First, it retains B cells with a wide variety of binding affinities. What's more, it hits a modest ceiling of evolvable affinity [9]. The maximum antibody affinities evolved *in vivo* ($K_a \sim 10^{10}$-$10^{12}\mathrm{M}^{-1}$) tend to be orders of magnitude lower than those achieved by directed evolution *in vitro* ($K_a \sim 10^{13}\mathrm{M}^{-1}$) [10]. Due to the multiscale complexity, what exactly controls affinity maturation dynamics and sets the evolution outcome remains an unresolved puzzle in this field, which limits our ability to alter the constraints and improve response efficacy.

Finally, at a longer timescale, highly variable pathogens may manage to continuously evade immune recognition, leading to a coevolutionary arm races between antigen and immunity. Rapidly mutating viruses, such as human immunodeficiency virus (HIV) or hepatitis C virus (HCV), go through fast intra-host diversification and constantly escape from immune recognition [11, 12]. On the reciprocal side, affinity maturation allows the host immune sys-

tem to adjusts on the fly to recognize the altered versions of the antigen. In this Red Queen [13] scenario, antigen and immune system constitute each other's responsive environment and are mutually driven out of equilibrium. Then the question is, how do antigen and immunity mutually organize when the ecological and evolutionary dynamics occur on comparable timescales? What governs the persistence and outcome of mutual adaptation?

To answer these questions, statistical physics and quantitative modeling provide great instruments to decode the underlying principles. The ultimate goal is similar to the purposes of statistical mechanics. On the one hand, the macroscopic behavior of the immune system, as probed in imaging or other quantitative measurement experiment, can be well characterized. On the other hand, we are lacking of the complete representation for the elementary interactions that would give rise to the coordinate behavior seen in the immune system. The adventure of statistical physics is full of equivalent endeavors, starting from the macroscopic description of thermal properties of gases and solids, on the assumption of independent particles composing a perfect gas and the coupling of harmonic oscillators, respectively, to the three-dimension structure of folding proteins and the description of neural networks. This approach is especially useful to theoretical immunology because of our ignorance about the hierarchy of fundamental physical laws in different scales that are responsible for the observed macroscopic behaviors. Moreover, *in-silico* experiments based on quantitative models not only allow one to identify the core mechanisms, but also help to inform experiments with a view to reducing costs and increasing efficiency. To provide an example, the quantitative model of affinity maturation developed by Wang et al. [14] suggests that sequential immunization with antigen variants is preferred over a cocktail for induction of cross-reactive antibodies, which was preceding experimental verifications.

My thesis aims to address the above problems utilizing the tools from statistical physics and computational quantitative modeling. It presents a comprehensive multiscale study of the B cell affinity maturation process from different perspectives that helps to uncover the underlying principles governing the adaptive immune response.

Chapter 2 focuses on the molecular scale and investigates the dynamics of antigen extraction by B cells. The existing bond disassociation theory mainly focused on the ligand-receptor system with a single binding interface [15, 16, 17]. However, the antigen extraction process involves multiple binding interfaces, and it is the competition between different bond breaking pathways that determines the extraction efficiency. In this dissertation, I extend the bond dissociation theory to a "tug-of-war" system, where multiple binding interfaces present, using a two-dimensional Langevin model. This framework allows one to estimate the probability of successful antigen extraction and study how different components (i.e., force strength) influence the efficiency of antigen uptaking. I show that the tugging force can regulate physical extraction of antigen via deforming the interacting free energy surface, which couples internal dynamics of cells to the mechanical environment. This process allows comparative measurements of the receptor affinity for affinity discrimination.

Chapter 3 integrates the tug-of-war antigen extraction model with an *in silico* model of B cell evolution to show how regulation at the molecular level propagates to and influences the evolution at the population level. Prior models of affinity maturation often assume that the equilibrium binding affinity between B cell receptor and antigen determines the reproductive success of a B cell clone [14, 18, 19, 20]. However, it is evident in experiments that interactions between antigens and receptors are far beyond equilibrium binding and involve contractile cytoskeleton forces [5]. Based on our understanding from the Langevin model in chapter 2, I developed a model of B cell maturation using agent-based simulations where the clonal reproductive fitness is governed by the results of antigen extraction. I find that active force usage can both constrain and enable effective selections, but with regard to different functional objectives. On the one hand, tugging force is able to regulate the relative tether strength, which sets the limit of evolvable B cell affinities. On the other hand, heritable heterogeneity in cytoskeleton forces, combined with evolvable receptor flexibility, can generate a wide spectrum of output binding affinities with similar clonal fitness. This unifies multiple experiments results otherwise hard to reconcile, including the persistence of

low-affinity clones and diverging rates of diversity loss among B cell populations.

Chapter 4 revisits the antigen extraction process and investigates affinity discrimination from the perspective of information theory, focusing on the fundamental physical limit of discrimination accuracy. Existing models [21, 22] mainly studied the task of ligand detection by cells, which is distinct from affinity discrimination in various aspects, including the underlying physical process as well as the output state space. I compare two debating hypotheses of readout signal of BCR affinity, the binding lifetime (known as signal-1 in immunology) and the number of acquired antigens (corresponding to signal-2 in immunology), by looking at the amount of affinity information encoded in each signal. I show that both readouts can be informative, but with regard to different affinity regimes. When B cell affinity is lower than the antigen tether affinity, the binding lifetime carries most of the affinity information. As B cell affinity increases, the information in binding lifetime diminishes due to the breaking of the weak tether bonds and is outperformed by the information in the extracted antigen number when receptors are stronger than antigen tethers. I also discuss how the coupling between different receptors can potentially benefit the task of affinity discrimination.

Chapter 5 presents a study of antigen extraction from the perspective of the control theory. Motivated by recent experimental observations [6, 23, 24], I develop a model where B cells are able to actively manipulate the ligand-receptor clusters using dynamical and adaptive forces. Different forms of feedback are compared in different aspects including discrimination fidelity, speed and robustness. The model suggests that an adaptive force can benefit affinity discrimination either through increasing the sensitivity of cluster formation to affinity change, or by enhancing the sensitivity of extraction efficiency to affinity change. I show that the negative feedback provided by a force that responds nonlinearly to ligand clustering can reduce the dependence of antigen acquisition on antigen ligand concentration, resulting in absolute discrimination for receptor affinity. In addition, I analyze antagonistic effects under different controls when mixtures of different kinds of antigens are presented. Specifically, our model predicts that a strong antagonism can be an indicator of adaptive

forces that sense the cluster size instead of the binding lifetime.

Chapter 6 focuses on the long-time coevolution scenario — the mutual adaptation between B cell receptor repertoires and antigens. I develop a reaction-diffusion model in trait space, based on predator-prey interactions between coevolving immune receptors and antigens, that combines evolutionary diversification and population dynamics. My study reveals that the asymmetric reaction range between immunogenicity (the ability of antigens to induce an immune response) and antigenicity (the ability of antigens to interact with antibodies) is critical in determining the dynamics of coevolution. As such asymmetry varies, transitions between qualitatively distinct regimes seen in nature would follow, including persistent coexistence, antigen elimination and unrestrained growth.

CHAPTER 2

Dynamics of single antigen extraction

2.1 Introduction

Biology background One of the key steps in germinal center (GC) evolution is antigen extraction [25, 3, 7, 26, 27, 28]. It has been known for a long time that B cells use B cell receptors (BCRs) to retrieve antigens (Ags) deposited on the membranes of antigen presenting cells (APCs) in an affinity-dependent manner [29, 30]. Shortly after the contact between a B cell and an APC, an immune synapse forms connecting the cells, that contains clusters of BCR-antigen bonds [29, 31, 32, 24]. Those antigens are acquired by B cells if the connection between antigen and APC breaks [30, 2, 33, 24]. In contrast, if the bond between antigen and BCR breaks, the antigen remains on the surface of APC [2, 33]. Antigens retrieved by B cell can then be presented to helper T cells [34]. Competition between GC B cells displaying different surface densities of processed antigens to a limited number of helper T cells then drives GC selection [9, 34, 35, 36].

Recent experiments suggest that the above antigen extraction process is subject to active regulation [5]. For example, Natkanski et al. [2] observed that B cells acquired antigens by dynamic myosin IIa-mediated contraction. Thus, B cell contractility influences the affinity discrimination. Furthermore, Nowosad et al. [32] showed that, compared to naive B cells, GC B cells used a larger tugging force. This form of active force application is puzzling, because it is not only energy consuming, but also dependent on complicated signaling networks that regulate active bundle formation. It has been suggested that the application of

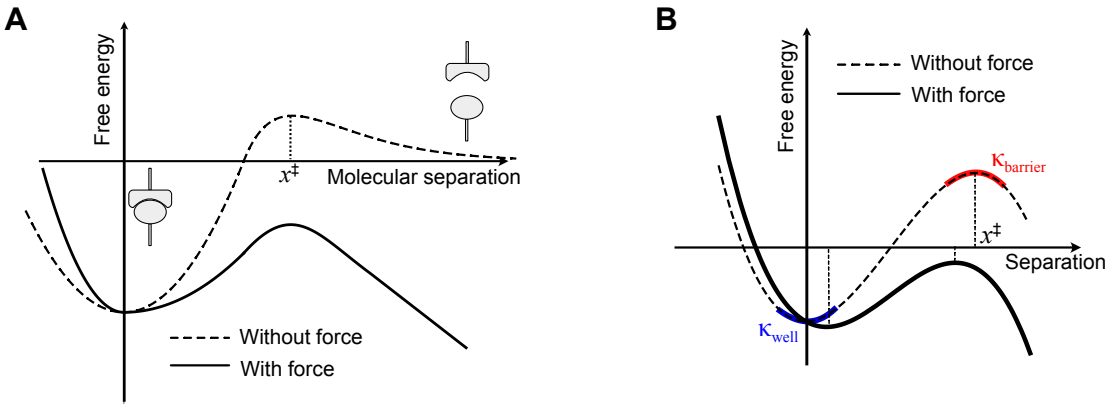

Figure 2.1: Free energy plotted against receptor-ligand separation along direction of pulling. Zero separation corresponds to the bound state. A force that stretches the bond will decrease the free energy linearly with distance. $x^{\ddagger}$ denotes the location of the force-free potential barrier. (A) Bell's phenomenological model. (B) A linear-cubic potential that is tilted by the force. Note that the equilibrium state and the location of the barrier are changed by force. The curvature at the barrier κ_b and curvature at the attractor κ_a are highlighted by colors.

mechanical force may serve to regulate the extraction threshold and improve the discrimination stringency [2, 32, 37], yet the detailed physical principle is still missing.

Bond dissociation theory The physics of bond disassociation under external mechanical force has been investigated extensively since last century. An increase of the disassociation rate under external force was examined by Bell [15] using a simple phenomenological model that becomes the law of "mechanical chemistry". It is an extension of the classical reaction rate theory for noise-assisted bond breaking (see the outstanding review by Hanggi et al. [38]). In the Bell model, force lowers the barrier height (see Fig. 2.1A), leading to an exponential reduction of bond lifetime:

$$\tau = \tilde{\tau} \exp\left(-\frac{F x^{\ddagger}}{k_B T}\right). \tag{2.1}$$

The applied force, F, is assumed to be directed along the reaction coordinate (usually a molecular separation). $\tilde{\tau}$ is the bond lifetime without force. While Bell's insights successfully demonstrated the significant role of mechanical force in biological chemistry, all features of the underlying energy landscape were lumped into a single parameter – the bond length $x^{\ddagger}$. To overcome this limitation, detailed free energy landscapes were introduced by Evans and Ritchie [16] by extending the Brownian dynamics theory of Kramers [39, 38] to the force-driven dissociation of bonds. According to the Kramers theory [39], for a sufficiently high barrier and in the over-damped limit, the average time to escape from a local attractor (metastable minimum) can be approximated by

$$\tau = \frac{2\pi k_B T}{D\sqrt{\kappa_{\text{barrier}}\kappa_{\text{well}}}} \exp\left[\frac{1}{k_B T}(U_{\text{barrier}} - U_{\text{well}})\right]. \tag{2.2}$$

Here, the Arrhenius (exponential) factor contains the potential difference between the attractor and the barrier, scaled by the thermal energy $k_B T$. κ_{well} and κ_{barrier} are the *curvatures* at the attractor and at the barrier, respectively (see Fig. 2.1B). Following Kramers' picture, Evans and Ritchie [16] show that the bond lifetime follows a general form given by

$$\tau = \tilde{\tau} g(F) \exp\Big[-\frac{\Delta G(F)}{k_B T}\Big], \tag{2.3}$$

where the barrier height reduction $\Delta G(F)$ depends on the deformation of the energy landscape by the external force. It does not necessarily change linearly with F. This is because force not only lowers the free energy at $x^{\ddagger}$, but also tilts the potential and changes the minimum-barrier distance (see Fig. 2.1B). The prefactor $g(F)$ characterizes the change in relaxation timescale due to potential tilting.

To connect with laboratory experiments, Evans and Ritchie [16] and Izrailev et al. [40] examined the disassociation dynamics under a ramping force, which is easier to realize in experiments using dynamic force spectroscopy [41] such as atomic force microscope (AFM) [42], optical tweezers [43], or high-speed force spectroscopy (HS-FS) [44], as compared to a constant force. The theory predicts that the average force grows linearly with the logarithm of the force-loading rate. It was later tested in experiments using AFM to pull against

various bonds, including a ligand-receptor complex [45] and bonds connecting two strands of a DNA duplex[46].

More sophisticated but still analytically tractable models were developed by Hummer et al. [47] using a cusp-harmonic potential and Dudko et al. [17] using a linear-cubic potential, which can be summarized into an explicit and unified form [17]:

$$\tau = \tilde{\tau}\Big(1 - \frac{vFx^{\ddagger}}{\Delta G^{\ddagger}}\Big)^{1-\frac{1}{v}} \exp\Big\{\frac{\Delta G^{\ddagger}}{k_B T}[(1 - \frac{vFx^{\ddagger}}{\Delta G^{\ddagger}})^{\frac{1}{v}} - 1]\Big\}. \tag{2.4}$$

Here $\Delta G^{\ddagger}$ is the force-free potential barrier height, and $0 < v \leq 1$ characterizes the shape of potential landscape ($v = 2/3$ and $v = 1/2$ correspond to the linear-cubic and cusp-harmonic free energy surfaces, respectively). For $v = 1$, and for $\Delta G^{\ddagger} \to \infty$, the expression reduces to the Bell's phenomenological result, Eq. 2.1. These models not only provide a detailed understanding of the effect of mechanical forces on the lifetime of chemical bonds ("mechanical chemistry"), but also allow one to extract free energy surfaces to distinguish between different *mechanisms* by repeated pulling experiments [47, 17, 48, 49, 50].

The tug-of-war system Nevertheless, the classical bond disassociation theory cannot address the antigen extraction process. As we show in Fig. 2.2, before the extraction, a BCR-antigen-APC complex has multiple binding interfaces [51]. Where it breaks is crucial in determining whether the B cell can obtain the antigen or not [33]. Therefore, the process involves the competition between different types of bond breaking and can lead to different rupture outcomes (a type of "tug-of-war" problem). The distribution of the rupture outcome is important for B cells to probe their receptor affinities [9, 29, 52], discriminate between different ligands [2, 32] or substrates [33], and determine the cellular fate (die or survive) [35]. Moreover, the difference in the rupture outcome distribution between distinct B cells drives the natural selection and influences the adaptation of a polyclonal population during the GC evolution [25, 35]. However, the classical bond disassociation theory does not distinguish between different binding interfaces and does not care much about the rupture outcome.

Here, we extend the bond disassociation theory to the "tug-of-war" system, where multiple binding interfaces present. In section 2.2, we introduce our Langevin model and investigate how the tugging force influences the efficiency of antigen extraction. In section 2.3, we discuss how the force regulates the discrimination power. Our results show that force can enhance or inhibit antigen extraction, depending on tether (APC-Ag) stiffness and force magnitude. Specifically, if the tether is soft and force is not too large, B cells can get more antigens by applying a tugging force. In contrast, if the tether is stiff or force is too large, antigen extraction will be inhibited by force. Moreover, our model predicts that force usage not only regulates the discrimination stringency but also expands the sensitive window of affinity discrimination.

2.2 Antigen extraction as a first passage problem

To describe the kinetics of antigen extraction, we consider a Langevin model where the motion of molecules is governed by molecular interactions and stochastic random forces from the environment, in a viscous extracellular solvent. The key quantity of interest is the chance of successful antigen extraction, η, which determines on average how many antigens can be acquired by a B cell. In what follows, we first introduce a general framework to describe the kinetics and formulate the antigen extraction chance (section 2.2.1). Then we apply the framework to calculate η in the limit of a static weak-force (section 2.2.2), in the limit of a static strong-force (section 2.2.4), and under a dynamical force (section 2.2.5).

2.2.1 A two-dimensional Langevin dynamics model

Let us first formulate the problem using a Langevin model. We start from the system state space and construct the equation of motion based on the Rayleigh dissipation function and general potential landscapes. The Langevin equation can be converted into a Fokker-Planck equation, which describes the ensemble dynamics. Then the timescale and the success rate

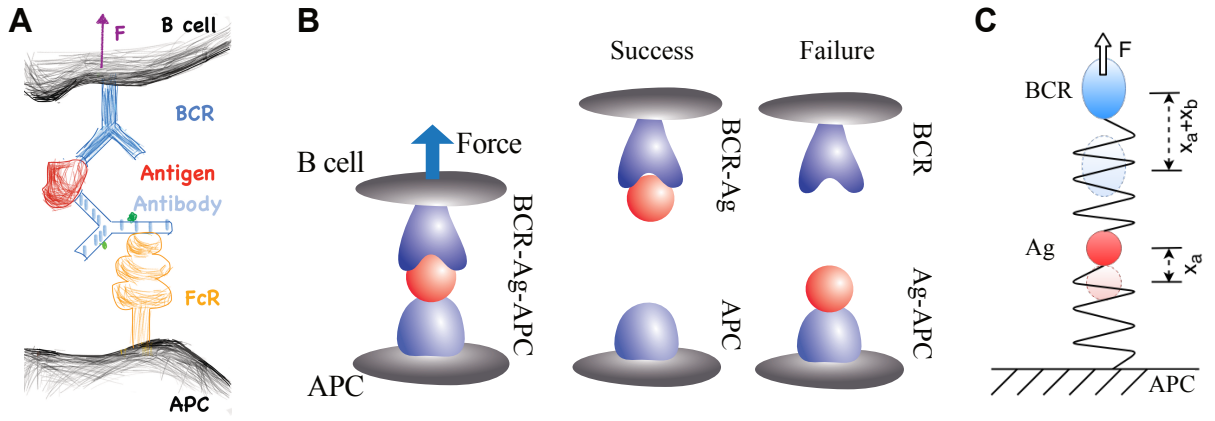

Figure 2.2: Antigen extraction process. (A)Antigens are displayed on APCs as a chain of molecules that include tethering proteins (antibodies and FC receptor (FcR)). B cells bind antigens through their BCRs and apply forces to the bond. (B)Before extraction, the multi-bond structure is modeled by a three-body complex, BCR-Ag-APC. Rupture can happen at either of the two binding interfaces in the complex. One corresponds to successful Ag acquisition by the B cell and the other to failure. (C) Applied pulling forces and random forces affect the bond extension x_a, x_b thereby transferring external forces to the two binding interfaces.

of antigen extraction can be formulated based on the ensemble description.

System states We use a three-body complex to model different binding configurations of APC, Ag, and BCR groups. Before extraction, the complex is in a bound state, BCR-Ag-APC, with two binding interfaces (BCR-Ag and Ag-APC). During extraction, either binding interface may break. After extraction, the B cell will obtain the antigen if the Ag-APC interface breaks or lose the antigen if the BCR-Ag interface breaks (see Fig. 2.2B). We use bond extensions to further characterize the system state. Let x_a and x_b be respectively the extension of the APC-Ag bond and the BCR-Ag bond, as compared to their unstressed equilibrium states (see Fig. 2.2C). The advantage of using bond extension is that it is convenient to describe the dynamics and tell if the bond is broken or not.

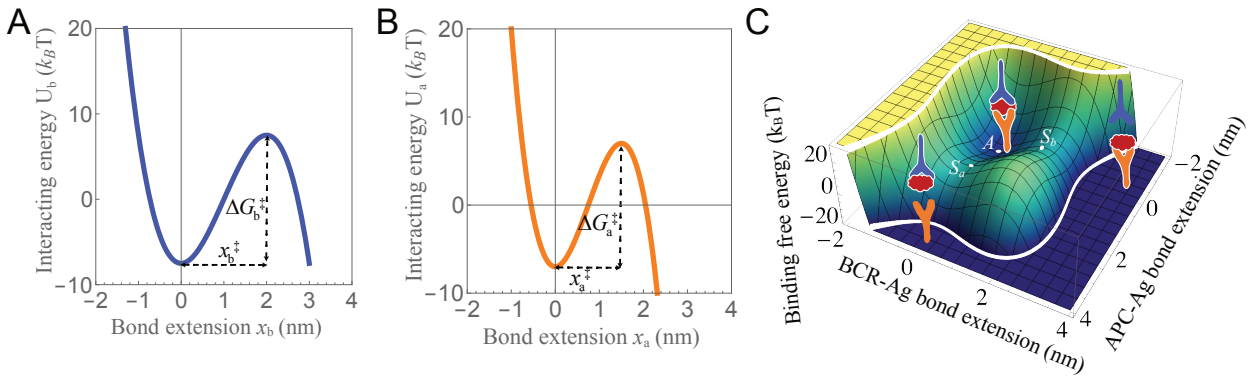

Figure 2.3: (A) The intrinsic free-energy for BCR-Ag bond $U_b(x_b)$ has a minimum at $x_b = 0$ and a barrier at $x_b = x_b^{\ddagger}$ with height $\Delta G_a^{\ddagger}$. (B) The free-energy for APC-Ag bond $U_a(x_a)$ has a barrier is at $x_a = x_a^{\ddagger}$ with a height of $\Delta G_a^{\ddagger}$. (C) The assumed potential of mean force, $U(x_a, x_b)$ used for Brownian motion consists of an attracting well (bound state) and two barriers (successful or failed extraction). The chance of antigen extraction is the probability for the Brownian particle to cross the barrier, corresponding to successful extraction.

Dissipation function We consider the following Rayleigh dissipation function

$$R = \underbrace{\frac{1}{2}\gamma_a \dot{x}_a^2 + \frac{1}{2}\gamma_b(\dot{x}_a + \dot{x}_b)^2}_{\text{hydrodynamic dissipation}} + \underbrace{\frac{1}{2}\gamma_{a0}\dot{x}_a^2 + \frac{1}{2}\gamma_{b0}\dot{x}_b^2}_{\text{internal dissipation}}. \tag{2.5}$$

The first term is hydrodynamic dissipation of the antigen molecule, associated with translation of its center of mass dx_a/dt, with respect to APC. The second term describes hydrodynamic dissipation associated with translation of the center of mass of BCR ($d(x_a + x_b)/dt$). Note that we assume the APC is static. The last two terms capture the internal dissipation within the APC-Ag bond and the internal dissipation within the BCR-Ag bond, respectively, depending on the relative motion of molecules forming a bond. γ_a, γ_b, γ_{a0}, and γ_{b0} are corresponding damping constants. It should be noted that the detailed form of the internal dissipation is complicated and might depend on other degrees of freedom (i.e., configurational changes inside the receptor and the ligand, surrounding buffer ions, etc.) [53, 54, 55]. Nevertheless, our formula gives the simplest way to capture the core behavior: the faster the

relative motion, the stronger the dissipation [45].

To keep the picture simple, in what follows we focus on the strong hydrodynamic damping limit ($\gamma_a, \gamma_b \gg \gamma_{a0}, \gamma_{b0}$), and drop the internal dissipation terms:

$$R \approx \frac{1}{2}\gamma_a \dot{x}_a^2 + \frac{1}{2}\gamma_b(\dot{x}_a + \dot{x}_b)^2. \tag{2.6}$$

Our analysis shows that this simplification does not change the results much in the physically plausible regime (see our discussion in section 2.4).

Interacting potential We consider the following surface as the potential of mean forces

$$U(x_a, x_b) = U_a(x_a) + U_b(x_b) - F \cdot (x_a + x_b). \tag{2.7}$$

Here F is the external tugging force from the B cell. $U_a(x_a)$, respectively $U_b(x_b)$, is the free-energy profile of the APC-Ag bond, respectively the BCR-Ag bond, in the absence of an applied force. These free-energies include the elastic energy due to protein stretching and the binding energy within the chemical bond. In addition, the potential of mean force, $U_a(x_a)$ (or $U_b(x_b)$) are assumed to have a single well at the natural state $x_a = 0$ (or $x_b = 0$), and a barrier at $x_a = x_a^\ddagger$ (or $x_b = x_b^\ddagger$). The barrier heights of $U_a(x_a)$ and $U_b(x_b)$ are denoted by $\Delta G_a^\ddagger$ and $\Delta G_b^\ddagger$ respectively (see Fig. 2.3A-B). Hence, the APC-Ag bond breaks if $x_a > x_a^\ddagger$, and the BCR-Ag bond breaks when $x_b > x_b^\ddagger$.

Equation of motion For an over-damped system, the equation of motion is given by

$$\frac{\partial U}{\partial x_a} = -\frac{\partial R}{\partial \dot{x}_a} + \xi_a, \tag{2.8a}$$

$$\frac{\partial U}{\partial x_b} = -\frac{\partial R}{\partial \dot{x}_b} + \xi_b. \tag{2.8b}$$

ξ_a and ξ_b are stochastic forces from the environment, respectively acting on the Ag-APC bond and BCR-Ag bond, which will be determined using the detailed-balance condition and the fluctuation-dissipation theorem later (see Eq. 2.13). With some rearrangement, the

equation becomes

$$\gamma_a \dot{x}_a = -U_a'(x_a) + U_b'(x_b) + \xi_a - \xi_b, \tag{2.9a}$$

$$\gamma_b(\dot{x}_a + \dot{x}_b) = -U_b'(x_b) + F + \xi_b. \tag{2.9b}$$

Here $-U_a'(z) = -\frac{\mathrm{d}U_a(z)}{\mathrm{d}z}$ and $-U_b'(z) = -\frac{\mathrm{d}U_b(z)}{\mathrm{d}z}$ are interacting forces within APC-Ag and BCR-Ag, respectively. Eq. 2.9 is essentially the Langevin equation that has been widely used to model the dynamics of bond dissociation under force [16]. The first part is the equation of motion of the antigen molecule, determined by the force from the APC side ($-U_a'(x_a)$), the force from the BCR side ($U_b'(x_b)$), and random forces from the environment $\xi_a - \xi_b$ influencing the Ag molecule (recall that ξ_a and ξ_b are random forces acting on the *bonds*). The second part is about the motion of BCR center of mass, determined by the force from the Ag side ($-U_b'(x_b)$), the force from B cell (F), and a random force ξ_b. Note that two degrees of freedom are coupled together. Thus, we convert the problem into a two-dimensional Brownian motion problem.

Two absorbing boundaries are placed in the state space (x_a, x_b) to represent the bond breaking, one along the line $x_a = x_a^\ddagger$ and the other along the line $x_b = x_b^\ddagger$ (see dashed lines in Fig. 2.4A). Therefore, successful antigen extraction corresponds to a barrier-crossing event over the boundary at $x_a = x_a^\ddagger$. In contrast, an antigen is lost when the Brownian particle exits the potential well via the boundary at $x_b = x_b^\ddagger$.

Noise correlation To determine the noise, we follow the Ito type Langevin equation, and rewrite Eq. 2.9 into the standard form,

$$\frac{\mathrm{d}x_i}{\mathrm{d}t} = -\sum_{j=a,b} L_{ij}\frac{\partial U}{\partial x_j} + \sqrt{2k_BT}\tilde{\xi}_i, \tag{2.10}$$

where $i = a, b$ are coordinate indexes. Explicitly,

$$L = \begin{pmatrix} 1/\gamma_a & -1/\gamma_a \\ -1/\gamma_a & 1/\gamma_a + 1/\gamma_b \end{pmatrix}, \qquad \begin{pmatrix} \tilde{\xi}_a \\ \tilde{\xi}_b \end{pmatrix} = \frac{1}{\sqrt{2k_\mathrm{B}T}} \begin{pmatrix} \xi_a - \xi_b \\ (1 + \frac{\gamma_a}{\gamma_b})\xi_b - \xi_a \end{pmatrix}. \tag{2.11}$$

Assume the noise is a linear combination of white noises, $\tilde{\xi}_i = \sum_j B_{ij} w_j$, where w_j is zero mean $\langle w_j \rangle = 0$, delta-correlated $\langle w_i(t) w_j(t') \rangle = \delta_{ij}\delta(t-t')$, and Gaussian distributed. Then the detailed balance condition requires

$$\sum_k B_{ik} B_{jk} = L_{ij} \Longleftrightarrow \langle \tilde{\xi}_i(t) \tilde{\xi}_j(t') \rangle = L_{ij}\delta(t-t'). \tag{2.12}$$

Solving this, we get

$$\begin{pmatrix} \langle \xi_a(t)\xi_a(t') \rangle & \langle \xi_a(t)\xi_b(t') \rangle \\ \langle \xi_a(t)\xi_b(t') \rangle & \langle \xi_b(t)\xi_b(t') \rangle \end{pmatrix} = 2k_B T\delta(t-t') \begin{pmatrix} \gamma_a + \gamma_b & \gamma_b \\ \gamma_b & \gamma_b \end{pmatrix}. \tag{2.13}$$

To clearly see the origin of noise, we define the following independent noises: ξ_1, the white noise associated with the hydrodynamic dissipation of antigen, $\langle \xi_1(t)\xi_1(t') \rangle = 2k_B T\gamma_a \delta(t-t')$; ξ_2, the white noise associated with the hydrodynamic dissipation of BCR, $\langle \xi_2(t)\xi_2(t') \rangle = 2k_B T\gamma_b \delta(t-t')$. Then

$$\xi_a = \xi_1 + \xi_2, \qquad \xi_b = \xi_2. \tag{2.14}$$

Thus, the equation of motion can be written as

$$\gamma_a \dot{x}_a = -U_a'(x_a) + U_b'(x_b) + \xi_1, \tag{2.15a}$$

$$\gamma_b(\dot{x}_a + \dot{x}_b) = -U_b'(x_b) + F + \xi_2. \tag{2.15b}$$

Comparing Eq. 2.15 with Eq. 2.9, we find that ξ_1 and ξ_2 are *independent* random forces acting on the *molecules*, whereas ξ_a and ξ_b are *coupled* random forces acting on the *bonds*.

Ensemble description To provide an ensemble description, we look at the time-evolution of $P(x_a, x_b, t)$, that is, the probability density function finding the system in state (x_a, x_b) at time t. It follows the Fokker-Planck equation

$$\frac{\partial P(x_a, x_b, t)}{\partial t} = \hat{L} P(x_a, x_b, t), \tag{2.16}$$

where

$$\hat{L} \equiv \sum_{i\in\{a,b\}} -\frac{\partial}{\partial x_i} K_i + \sum_{i\in\{a,b\}} \sum_{j\in\{a,b\}} \frac{\partial^2}{\partial x_i \partial x_j} D_{ij}.$$

This is constructed from Eq. 2.15 using the Kramers–Moyal expansion up to the second order [56]. The drift vector $\mathbf{K} = (K_a, K_b)$ and diffusion matrix D read as

$$\mathbf{K} = -\Big[\tfrac{1}{\gamma_a}\partial_{x_a} U(x_a, x_b) - \tfrac{1}{\gamma_a}\partial_{x_b} U(x_a, x_b), \quad (\tfrac{1}{\gamma_a} + \tfrac{1}{\gamma_b})\partial_{x_b} U(x_a, x_b) - \tfrac{1}{\gamma_a}\partial_{x_a} U(x_a, x_b)\Big],$$
$$D = k_{\mathrm{B}}T \begin{pmatrix} 1/\gamma_a & -1/\gamma_a \\ -1/\gamma_a & 1/\gamma_a + 1/\gamma_b \end{pmatrix}. \tag{2.17}$$

The diffusion matrix contains off-diagonal elements, because the random force on the antigen molecule influences both bonds. We can see the detailed balance is ensured in this system since the drift vector $\mathbf{K}$ relates with diffusion matrix through $K_i = \sum_j D_{ij}\partial_{x_j}(U(x_a, x_b)/k_{\mathrm{B}}T)$ for all $i, j \in \{a, b\}$ [57]. The probability flux is given by

$$\mathbf{J} = \mathbf{K}P - \nabla \cdot (DP). \tag{2.18}$$

This allows us to write the Fokker-Planck equation as

$$\partial_t P = -\nabla \cdot \mathbf{J}. \tag{2.19}$$

As such, we constructed a general framework to describe the antigen extraction process. On the one hand, for a given free-energy profile $U(x_a, x_b)$, one can use the Brownian motion simulation to simulate the molecular kinetics until bond breaking based on Eq. 2.15. Statistical distributions of rupture outcomes can be obtained by repeating the simulation for multiple times. On the other hand, starting from the Fokker-Planck equation, one can derive the first passage time distribution and calculate the probability to obtain an antigen, as we detailed below.

Antigen extraction probability As the key quantity of interest, the antigen extraction chance determines B cell's ability to capture antigens. In our model, it is the integrated

probability flux exiting through the boundary corresponding to APC-Ag bond breaking. Explicitly,

$$\eta \equiv \int_0^\infty j_a(t)dt. \tag{2.20}$$

Here $j_a(t) = \int_{x_a=x_a^\ddagger} \mathbf{J}(x_a^\ddagger, x_b, t) \cdot \mathbf{e}_{x_a} dx_b$ is the integrated probability flux along the boundary $x_a = x_a^\ddagger$. $\mathbf{e}_{x_a} = (1, 0)$ is the unit vector pointing to positive x_a direction. One can imagine any change in the underlying potential landscape will be reflected in the antigen extraction chance. For examples, as the potential barrier near the boundary $x_b = x_b^\ddagger$ rises, more flux will exit through the other boundary $x_a = x_a^\ddagger$, which increases the extraction probability.

To elucidate the impact of different factors more explicitly, we consider several cases where analytical understanding of η is feasible. We will first study a general case where potential barriers are high compared to thermal fluctuations so that separation of timescales is available (section 2.2.2). The results allow us to investigate extraction under a small static force (section 2.2.3). Then we consider a large static force under which potential barriers vanish (section 2.2.4). Finally, we will present the results under a slowly changing dynamical force (section 2.2.5).

Timescale for antigen extraction To provide a more complete understanding about the effect of force, we will also present the analysis of antigen extraction timescale. In the framework of Langevin model, the distribution of complex lifetime is represented by the first passage time (FPT) distribution, which is

$$p(t) = -\frac{\mathrm{d}}{\mathrm{d}t} \int_{x_a<x_a^\ddagger, x_b<x_b^\ddagger} P(x_a, x_b, t) dx_a dx_b \tag{2.21}$$

According to the divergence theorem, we have

$$p(t) = j_a(t) + j_b(t). \tag{2.22}$$

Here $j_a(t) = \int_{x_a=x_a^\ddagger} \mathbf{J}(x_a^\ddagger, x_b, t) \cdot \mathbf{e}_{x_a} dx_b$ and $j_b(t) = \int_{x_b=x_b^\ddagger} \mathbf{J}(x_a, x_b^\ddagger, t) \cdot \mathbf{e}_{x_b} dx_a$ is the integrated probability flux along the boundary $x_a = x_a^\ddagger$ and boundary $x_b = x_b^\ddagger$, respectively. The mean

first passage time (MFPT) depicts the timescale of antigen extraction (average complex lifetime). By definition, it is given by

$$\tau \equiv \int_0^\infty tp(t)dt \tag{2.23}$$

The timescale will be calculated explicitly in certain limit, as we present below.

2.2.2 Antigen extraction in the limit of high-barrier

First, we consider a simple circumstance where the potential barrier is high, $U_{\text{barrier}} - U_{\text{well}} \gg k_B T$. In this case, it takes a very long time for the Brownian particle to leave the potential well. This allows us to separate the timescale of bond breaking from the correlation timescale and the timescale of relaxation [38], which makes the system simpler to analyze. In what follows, we will show that, in this limit, the antigen extraction probability can be calculated from the FPT distribution associated with each individual boundary, assuming that the other one is reflective. To simplify the description, we will call the boundary along $x_a = x_a^\ddagger$ by $\partial\Omega_a$, and the boundary along $x_b = x_b^\ddagger$ is named to $\partial\Omega_b$ (see Fig. 2.4A).

The original system is difficult to solve directly because it involves two absorbing boundaries (see Fig. 2.4A). Thus, we consider simpler systems in which one of the boundaries is reflective. First, we can set boundary $\partial\Omega_a$ absorbing and boundary $\partial\Omega_b$ reflective (see Fig. 2.4B). The corresponding solution to the Fokker-Planck equation (Eq. 2.16) is $P_a(x_a, x_b, t)$. Let $\mathbf{J}_a$ be the probability flux. $j_{aa}(t) = \int_{\partial\Omega_a} \mathbf{J}_a \cdot \mathbf{e}_{x_a} dx_b$ is the integrated probability along the absorbing boundary $\partial\Omega_a$ (see Fig. 2.4B). The FPT distribution is given by

$$p_a(t) = -\frac{\mathrm{d}}{\mathrm{d}t} \int_{x_a < x_a^\ddagger} P_a(x_a, x_b, t) dx_a dx_b. \tag{2.24}$$

Note that $j_{aa}(t) = p_a(t)$ according to the divergence theorem. Second, we can set boundary $\partial\Omega_b$ absorbing and assume the other boundary $\partial\Omega_a$ is reflective (see Fig. 2.4C). The solution to Eq. 2.16 is $P_b(x_a, x_b, t)$. Let $\mathbf{J}_b$ be the probability flux. $j_{bb}(t) = \int_{\partial\Omega_b} \mathbf{J}_b \cdot \mathbf{e}_{x_b} dx_a$ is the

integrated probability flux along boundary $\partial\Omega_b$. The FPT distribution is defined by

$$p_b(t) = -\frac{\mathrm{d}}{\mathrm{d}t}\int_{x_b<x_b^\ddagger} P_b(x_a, x_b, t)dx_a dx_b. \tag{2.25}$$

Note that $j_{bb}(t) = p_b(t)$. Those FPTs can be obtained using standard methods [38].

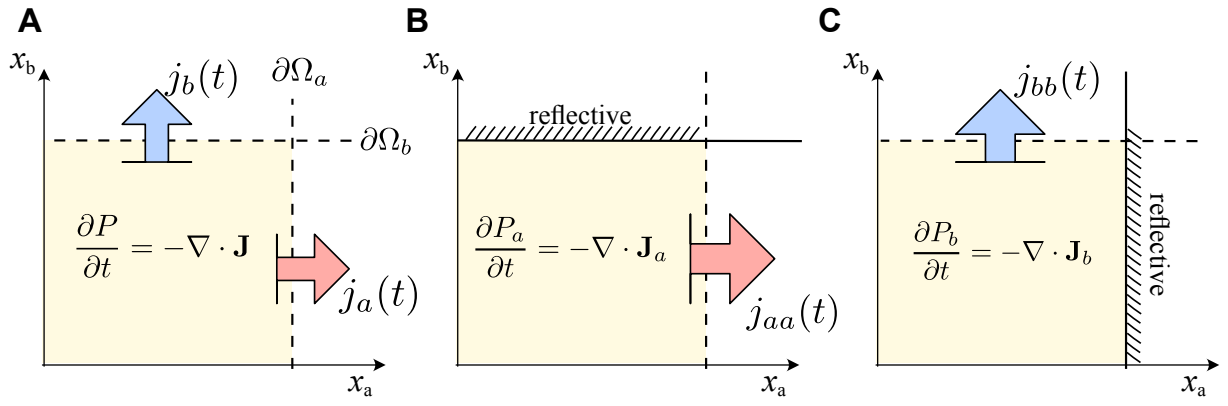

Figure 2.4: Escaping problems with different boundary conditions. (A) Two boundaries are both absorbing, as appeared in the tug-of-war problem. (B) Boundary $\partial\Omega_a$ is absorbing yet boundary $\partial\Omega_b$ is reflective. So the net flux at $\partial\Omega_b$ is zero. (C) Boundary $\partial\Omega_b$ is absorbing and boundary $\partial\Omega_a$ is reflective. The integrated fluxes are labelled in each case.

The main idea is to establish a relationship between the flux in different systems so that we can find $j_a(t)$ based on our knowledge of $j_{aa}(t)$ and $j_{bb}(t)$. In fact, we can decompose $j_{aa}(t)$ into two parts: $j_a(t)$ and the remaining part:

$$j_{aa}(t) = j_a(t) + j'_{aa}(t). \tag{2.26}$$

Here $j_a(t)$ corresponds to trajectories that directly run to boundary $\partial\Omega_a$ without touching the reflective boundary $\partial\Omega_b$. In contrast, $j'_{aa}(t)$ corresponds to trajectories that were reflected by the boundary $\partial\Omega_b$ at least once before running into boundary $\partial\Omega_a$. From this perspective,

$$j'_{aa}(t) = \int p_a(t|t')j_b(t')dt'. \tag{2.27}$$

Here $j_b(t')dt'$ is the probability that a trajectory touches boundary $\partial\Omega_b$ for the first time during $[t', t'+dt')$. Besides, $p_a(t|t')$ is the probability distribution that the system will touch

boundary $\partial\Omega_a$ at time t *conditioned* on that it visited boundary $\partial\Omega_b$ at time t'. The above two equations yield

$$p_a(t) = j_a(t) + \int p_a(t|t')j_b(t')dt'. \tag{2.28}$$

Similarly, we can show

$$p_b(t) = j_b(t) + \int p_b(t|t')j_a(t')dt'. \tag{2.29}$$

Here $p_2(t|t')$ is the probability distribution that the system will reach boundary $\partial\Omega_b$ at time t *conditioned* on that it visited boundary $\partial\Omega_a$ at time t'.

An explicit expression of $p_a(t|t')$ or $p_b(t|t')$ can be obtained in the limit of high-barrier. We consider a trajectory that runs towards the absorbing boundary $\partial\Omega_a$ after visiting the reflective boundary $\partial\Omega_b$. Because the relaxation happens much faster than escaping, the trajectory will quickly approach the attractive well after visiting boundary $\partial\Omega_b$. In addition, the position information at time t' quickly get lost because the correlation timescale is much shorter than the timescale of escaping. Thus, the event at t' only tells us that the trajectory has not reached the absorbing boundary till time t'. This allows us to assume that $p_a(t|t')$ is zero if $t < t'$ and follows the same distribution as $p_a(t)$ (with a different normalization constant) after t'. Explicitly,

$$p_a(t|t') = Ap_a(t)\Theta(t - t'). \tag{2.30}$$

Here $\Theta(t)$ is the Heaviside step function. The normalization constant is given by

$$A = \frac{1}{\int_0^\infty p_a(t'')\Theta(t'' - t')dt''} = \frac{1}{\int_{t'}^\infty p_a(t'')dt''}. \tag{2.31}$$

Similarly, the conditional distribution $p_b(t|t')$ can be approximated by

$$p_b(t|t') = \frac{1}{\int_{t'}^\infty p_b(t'')dt''}p_b(t)\Theta(t - t'). \tag{2.32}$$

Once $p_a(t)$ and $p_b(t)$ are known, the conditional distribution $p_a(t|t')$ and $p_b(t|t')$ can be constructed immediately using the above formulas.

Hence, in the high-barrier limit, Eq. 2.28 and Eq. 2.29 become

$$p_a(t) = j_a(t) + \int_0^t \frac{1}{\int_{t'}^{\infty} p_a(t'')dt''} p_a(t) j_b(t')dt', \tag{2.33a}$$

$$p_b(t) = j_b(t) + \int_0^t \frac{1}{\int_{t'}^{\infty} p_b(t'')dt''} p_b(t) j_a(t')dt'. \tag{2.33b}$$

This yields

$$j_a(t) = p_a(t) \int_t^{\infty} p_b(t')dt', \tag{2.34a}$$

$$j_b(t) = p_b(t) \int_t^{\infty} p_a(t')dt', \tag{2.34b}$$

which can be confirmed by plugging back into Eq. 2.33.

Therefore, the extraction probability can be written as

$$\eta \equiv \int_0^{\infty} j_a(t)dt = \int_0^{\infty} dt p_a(t) \int_t^{\infty} dt' p_b(t'). \tag{2.35}$$

Here, the term $dtp_a(t)$ is the probability for that the APC-Ag bond breaks at the time interval $[t, t+dt)$. The inner integral $\int_t^{\infty} dt' p_b(t') = 1 - \int_0^t dt' p_b(t')$ is the probability for that the BCR-Ag bond has not broken until time t. As such, by Eq. 2.35 we express the antigen extraction chance as the probability that the APC-Ag bond breaks while the BCR-Ag bond remains bound. This probability reflects the *relative* strength, measured by lifetime, of the BCR-Ag bond, as compared to the Ag-APC bond under pulling stress.

Similarly, the distribution of complex lifetime, is also associated with $p_a(t)$ and $p_b(t)$ through

$$p(t) = j_a(t) + j_b(t) = p_a(t) \int_t^{\infty} p_b(t')dt' + p_b(t) \int_t^{\infty} p_a(t')dt'. \tag{2.36}$$

The first part is the first passage time conditioned on that APC-Ag bond breaks first. The second part represents the first passage time conditioned on that BCR-Ag bond breaks first.

It is important to emphasize that Eq. 2.35 works as long as the potential barrier is high so that the escaping happens at a much longer timescale compared to relaxation and

correlation, even if the potential landscape is changing adiabatically. However, when the potential barrier is close to thermal noise or even vanishes, Eq. 2.35 is no-longer applicable. Instead, one need to use simulations or the original definition of η in Eq. 2.20 to find the extraction probability.

2.2.3 Antigen extraction under a small static force

In this section, we consider antigen extraction under a static force. We focus on the small force regime where the high-barrier assumption is valid, so that our results in the previous section still apply.

When the potential barrier under static force is high compared to thermal fluctuations, escaping from the potential well becomes a rare event that happens typically after numerous independent noisy steps, resembling the Poisson process. Because of this, the FPT obeys an exponential distribution [58],

$$p_i(t) = \frac{1}{\tau_i} \exp\Big(-\frac{t}{\tau_i}\Big), \tag{2.37}$$

where τ_i is the MFPT, $i = a, b$, given by $\hat{L}^\dagger \tau_i = 0$. Here $\hat{L}^\dagger$ is the adjoint operator of the Fokker-Planck equation Eq. 2.16. To calculate τ_a and τ_b, we need to set the boundary $x_b = x_b^\ddagger$ and the boundary at $x_a = x_a^\ddagger$ reflective, respectively. Note that $\hat{L}^\dagger$ contains both degrees of freedom, hence τ_a may depend on the property of BCR-Ag bond and τ_b may rely on the APC-Ag bond. Then the extraction chance η in Eq. 2.35 can be simplified into

$$\eta = \int_0^\infty \Big(\int_t^\infty \frac{1}{\tau_b} e^{-\frac{t'}{\tau_b}} dt' \Big) \frac{1}{\tau_a} e^{-\frac{t}{\tau_a}} dt = \frac{1}{1 + \tau_a/\tau_b}. \tag{2.38}$$

We can see it depends on the *relative* bond lifetime of BCR-Ag (τ_b/τ_a): a B cell will almost lose all antigens if $\tau_b \ll \tau_a$ and get all antigens if $\tau_b \gg \tau_a$, as one intuitively expects. The transition from low antigen extraction to high antigen extraction happens when $\tau_b = \tau_a$. Similar results have been obtained by Garg et al. [18], yet our approach is first-principle and more systematic. Furthermore, by Eq. 2.23 and Eq. 2.36, the timescale of antigen extraction

is

$$\tau = \int_0^\infty t\Big[p_a(t)\int_t^\infty p_b(t')dt' + p_b(t)\int_t^\infty p_a(t')dt'\Big]dt = \frac{\tau_a\tau_b}{\tau_a+\tau_b}. \tag{2.39}$$

This is the average lifetime of two binding interfaces. Essentially, it represents the inverse of the total off-rate $k_{\text{off}} = k_{a,\text{off}} + k_{b,\text{off}} = \tau_a^{-1} + \tau_b^{-1}$. In what follows, we dive deeper and calculate the MFPTs.

Mean first passage time With the high-barrier assumption, the MFPT can be calculated explicitly. Since we have a two-dimensional FPT problem, we utilize the Langer's multidimensional generalization of Kramers formula [59] and get

$$\tau = 2\pi\tau^+\Big(\frac{|\det \mathrm{H}_S|}{\det \mathrm{H}_A}\Big)^{1/2} e^{(U_S-U_A)/k_BT}. \tag{2.40}$$

Here U_S and U_A are the potential at the saddle point at the barrier ($\partial_{x_a}U = \partial_{x_b}U = 0, \det \mathrm{H}_S < 0$) and the potential minimum ($\partial_{x_a}U = \partial_{x_b}U = 0, \det \mathrm{H}_A > 0$), respectively. H_A and H_S are Hessian matrixes of potential $U(x_a, x_b)$ at the potential minimum and the saddle point. τ^+ is the unique positive root of $\det(\beta D\mathrm{H}_S + I/\tau^+) = 0$, characterizing the deterministic timescale leaving the saddle point after a small perturbation. $D = k_BT\begin{pmatrix} 1/\gamma_a & -1/\gamma_a \\ -1/\gamma_a & 1/\gamma_a + 1/\gamma_b \end{pmatrix}$ is the diffusion matrix. Essentially, Langer's formula states that the MFPT is given by the time scale τ^+ on which the deterministic dynamical goes away from the saddle, yet stretched by the relative frequency $p_A/p_S = \Big(\frac{|\det \mathrm{H}_S|}{\det \mathrm{H}_A}\Big)^{1/2} e^{\beta(U_S-U_A)}$ of finding the system at the bottom of the potential well instead of the saddle [58].

Therefore, for a smooth mean-force potential $U(x_a, x_b)$ on which the Hessian matrix exists, the MFPT τ_a and τ_b are

$$\tau_a = 2\pi\tau_a^+\Big(\frac{|\det \mathrm{H}_{S_a}|}{\det \mathrm{H}_A}\Big)^{1/2} e^{(U_{S_a}-U_A)/k_BT}, \tag{2.41a}$$

$$\tau_b = 2\pi\tau_b^+\Big(\frac{|\det \mathrm{H}_{S_b}|}{\det \mathrm{H}_A}\Big)^{1/2} e^{(U_{S_b}-U_A)/k_BT}. \tag{2.41b}$$

Here we call the saddle point near the boundary $x_a = x_a^\ddagger$ as S_a and the saddle point near the boundary at $x_b = x_b^\ddagger$ as S_b (see Fig. 2.3). Then the antigen extraction chance is given by

$$\eta = \left[1 + \frac{\tau_a^+}{\tau_b^+}\sqrt{\frac{|\det H_{S_a}|}{|\det H_{S_b}|}}e^{(U_{S_a}-U_{S_b})/k_BT}\right]^{-1}. \tag{2.42}$$

Interestingly, the formula states that, in the high barrier limit, η is sorely determined by the diffusion matrix D, and the geometrical features of the saddles including (1) the gap between apparent activation energies $U_{S_a} - U_{S_b}$; (2) the curvatures of the free energy surface near the saddle points. The energy gap appears in the Arrhenius (exponential) factor scaled by the thermal energy k_BT.

An explicit example In order to show explicitly how η relies on the underlying potential and the external force, we consider the following linear-cubic functions, respectively for the APC-Ag bond and BCR-Ag bond,

$$\begin{aligned} U_a(x_a) &= \tfrac{3}{2}\Delta G_a^\ddagger\left(\tfrac{x_a}{x_a^\ddagger} - \tfrac{1}{2}\right) - 2\Delta G_a^\ddagger\left(\tfrac{x_a}{x_a^\ddagger} - \tfrac{1}{2}\right)^3, \\ U_b(x_b) &= \tfrac{3}{2}\Delta G_b^\ddagger\left(\tfrac{x_b}{x_b^\ddagger} - \tfrac{1}{2}\right) - 2\Delta G_b^\ddagger\left(\tfrac{x_b}{x_b^\ddagger} - \tfrac{1}{2}\right)^3. \end{aligned} \tag{2.43a}$$

Each potential has a minimum at the natural bond extension ($x_a = 0$ or $x_b = 0$) and a barrier at bond length ($x_a = x_a^\ddagger$ or $x_b = x_b^\ddagger$). The barrier heights are $\Delta G_a^\ddagger$ and $\Delta G_b^\ddagger$, respectively. Example potentials depicted in Fig. 2.3 are based on this linear-cubic form. The combined free-energy surface $U(x_a, x_b, F)$ has a minimum (denoted as 'A') at ($x_a = x_a^\ddagger(1 - \sqrt{1 - F/f_a})/2, x_b = x_b^\ddagger(1 - \sqrt{1 - F/f_b})/2$) and two saddle points, one at ($x_a = x_a^\ddagger(1 + \sqrt{1 - F/f_a})/2, x_b = x_b^\ddagger(1 - \sqrt{1 - F/f_b})/2$) (denoted as '$S_a$') and the other at ($x_a = x_a^\ddagger(1 - \sqrt{1 - F/f_a})/2, x_b = x_b^\ddagger(1 + \sqrt{1 - F/f_b})/2$) (denoted as '$S_b$) (see Fig. 2.3). Here we let $f_a = 3\Delta G_a^\ddagger/(2x_a^\ddagger)$, $f_b = 3\Delta G_b^\ddagger/(2x_b^\ddagger)$. It should be noted that conclusion is not limited to this particular choice of energy surface because all smooth combined free-energy surfaces can be well approximated by a cubic polynomial [49, 17].

After direct calculation, we have

$$U_{S_a} - U_A = \Delta G_a^\ddagger(1 - \frac{F}{f_a})^{3/2}, \quad U_{S_b} - U_A = \Delta G_b^\ddagger(1 - \frac{F}{f_b})^{3/2}, \tag{2.44}$$

Besides,

$$\mathrm{H}_{S_a} = \begin{pmatrix} -\kappa_a & 0 \\ 0 & \kappa_b \end{pmatrix}, \quad \mathrm{H}_{S_b} = \begin{pmatrix} \kappa_a & 0 \\ 0 & -\kappa_b \end{pmatrix}, \quad \mathrm{H}_A = \begin{pmatrix} \kappa_a & 0 \\ 0 & \kappa_b \end{pmatrix}, \tag{2.45}$$

where $\kappa_a = \partial^2_{x_a} U|_A = \frac{4f_a}{x_a^\ddagger}\sqrt{1-\frac{F}{f_a}}$, $\kappa_b = \partial^2_{x_b} U|_A = \frac{4f_b}{x_b^\ddagger}\sqrt{1-\frac{F}{f_b}}$ are local curvatures at the potential minimum along coordinates x_a and x_b respectively. This yields $|\det H_{S_a}| = |\det H_{S_b}| = \det H_A = \kappa_a\kappa_b$. By solving $\det(\beta D H_S + 1/\tau^+) = 0$, we get

$$\tau_a^+ = \frac{\gamma_a}{2\kappa_a}\left(\frac{\gamma_b}{\gamma_a}(1-\frac{\kappa_a}{\kappa_b})+1+\sqrt{(\frac{\gamma_b}{\gamma_a}(1-\frac{\kappa_a}{\kappa_b})+1)^2+4\frac{\gamma_b}{\gamma_a}\frac{\kappa_a}{\kappa_b}}\right), \tag{2.46a}$$

$$\tau_b^+ = \frac{\gamma_b}{2\kappa_b}\left(1-\frac{\kappa_b}{\kappa_a}(1+\frac{\gamma_a}{\gamma_b})+\sqrt{(1-\frac{\kappa_b}{\kappa_a}-\frac{\kappa_b}{\kappa_a}\frac{\gamma_a}{\gamma_b})^2+4\frac{\kappa_b}{\kappa_a}\frac{\gamma_a}{\gamma_b}}\right). \tag{2.46b}$$

Therefore,

$$\tau_a = 2\pi\tau_a^+ e^{\Delta G_a^\ddagger(1-\frac{F}{f_a})^{\frac{3}{2}}/k_BT}, \tag{2.47a}$$

$$\tau_b = 2\pi\tau_b^+ e^{\Delta G_b^\ddagger(1-\frac{F}{f_b})^{\frac{3}{2}}/k_BT}. \tag{2.47b}$$

Although these MFPTs still take the form of Kramers' formula (Eq. 2.2 and Eq. 2.4), it is different from the single bond lifetime predicted by the one-dimensional Kramers theory, as τ_b relies on the APC-Ag stiffness κ_a and τ_a depends on BCR-Ag stiffness κ_b. This is because two degrees of freedom are coupled together via the noise (the diffusion matrix has off-diagonal elements), so that the timescale leaving the saddle point (S_a or S_b) depends on both curvatures (κ_a and κ_b).

Now it is clear how the tugging force plays a role. First, as shown in Fig. 2.5, the force application lowers potential barriers for both binding interfaces. The change depends on the ratio between the external force, F, and the bare strength of the bond, $f_a = \Delta G_a^\ddagger/(vx_a^\ddagger)$ (for APC-Ag) or $f_b = \Delta G_b^\ddagger/(vx_b^\ddagger)$ (for BCR-Ag). Hence, the disassociation rates of both binding interfaces are amplified. Second, the applied force modifies the local curvatures (κ_a, κ_b) near the saddle points, and thereby changes relaxation timescales τ_a^+, τ_b^+. The effect is also characterized by F/f_a and F/f_b.

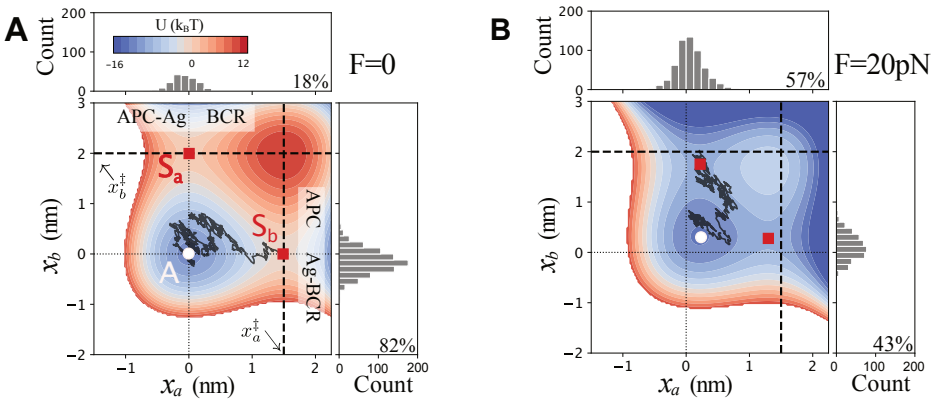

Figure 2.5: We use 2D Brownian simulations to simulate the extraction process. Coordinates represent the extensions in APC-Ag bond and BCR-Ag bond. Interacting potential energy is shown by color. Two thick dashed lines represent boundaries for the breaking of two bonds, respectively. Typical rupture trajectories are shown in black, which cross one of the rupture boundaries at the end. Histograms show the distribution of exit position along each boundary. The percentage shows the fraction of antigen extraction. Attractors and saddle points are labeled by 'A' and 'S_a' or 'S_b' respectively. (A) No force was used, $F = 0$. (B) Force ($F = 20$pN) lowers the barrier, and shifts the location of attractor and saddle points, resulting in changes in the extraction probability.

Then, based on Eq. 2.38, we find

$$\eta = \left[1 + \frac{\tau_a^+}{\tau_b^+} e^{(\Delta G_a^\ddagger (1-\frac{F}{f_a})^{\frac{3}{2}} - \Delta G_b^\ddagger (1-\frac{F}{f_b})^{\frac{3}{2}})/(k_B T)}\right]^{-1}. \tag{2.48}$$

We see the extraction probability depends on not only the BCR property $(\Delta G_b^\ddagger, x_b^\ddagger, \gamma_b)$, but also the tether property $(\Delta G_a^\ddagger, x_a^\ddagger, \gamma_a)$ and the force magnitude F. To understand the results in Eq. 2.48 better, in what follows we discuss the effect of force in two regimes.

The weak force limit First, we take the weak-force limit and show that our results recover the Bell's phenomenological model. For simplicity, we assume the prefacor τ_a^+ and τ_b^+ are independent of force, and focus on the Arrhenius factor, where the main effect of the force stems out. When $F \ll f_a$ and $F \ll f_b$, by Taylor expansion to the leading order, we

have

$$\tau_a \approx \tilde{\tau}_a \exp\big(-Fx_a^\ddagger/k_BT\big), \tag{2.49a}$$

$$\tau_b \approx \tilde{\tau}_b \exp\Big(-Fx_b^\ddagger/k_BT\Big), \tag{2.49b}$$

where $\tilde{\tau}_a = 2\pi\tau_a^+ \exp\big(\Delta G_a^\ddagger/k_BT\big)$ and $\tilde{\tau}_b = 2\pi\tau_b^+ \exp\Big(\Delta G_b^\ddagger/k_BT\Big)$ are the bond lifetimes of APC-Ag bond and BCR-Ag bond without force, respectively. This is exactly the phenomenological expression given by Bell [15]. Then we have

$$\eta = \frac{1}{1 + \frac{\tilde{\tau}_a}{\tilde{\tau}_b} e^{F(x_b^\ddagger - x_a^\ddagger)/k_BT}}. \tag{2.50}$$

This suggests that the effect of force depends on the difference between APC-Ag bond length and BCR-Ag bond length. Specifically, if $x_a^\ddagger > x_b^\ddagger$, then force promotes antigen extraction. In contrast, when $x_a^\ddagger < x_b^\ddagger$, force inhibits antigen extraction. This has been confirmed by Brownian motion simulations (see Fig. 2.6). Additionally, if $x_a^\ddagger = x_b^\ddagger$, force has no effect at all.

An intermediate force Now let us turn to the intermediate force regime ($F < f_a, F < f_b$) but still with high enough barriers ($\Delta G_a^\ddagger(1 - F/f_a)^{3/2} \gg k_BT, \Delta G_b^\ddagger(1 - F/f_b)^{3/2} \gg k_BT$). In this case, the nonlinear terms in the Arrhenius factor, which come from the potential tilting that shortens the barrier-attractor distance, start to play a role. As expected, the value of η predicted by the Bell's model deviates from that based on the landscape model (see Fig. 2.6). More specifically, η is less sensitive to force than what Bell's model predicts. This is because the potential tilting compensates the potential reduction at the boundary, as shown by the Taylor expansion to the second order,

$$\Delta G_i^\ddagger(1 - \frac{F}{f_i})^{\frac{3}{2}} \approx \Delta G_i^\ddagger - Fx_i^\ddagger + \frac{2F^2x_i^2}{3\Delta G_i^\ddagger}. \tag{2.51}$$

Note that $f_i = 3\Delta G_i^\ddagger/(2x_i^\ddagger)$. Notice that the tugging force may still play a role even when $x_a^\ddagger = x_b^\ddagger$, which is different from what Bell's model predicts.

General potentials Our analysis above is not specific to the linear-cubic potential. In Appendix 8.1 we considered a cusp-harmonic potential which gives similar results. Following Dudko et al. [17], we can write the MFPTs in a general formula,

$$\tau_a = \tau_{as}(F) e^{\beta \Delta G_a^{\ddagger} (1 - \frac{v F x_a^{\ddagger}}{\Delta G_a^{\ddagger}})^{\frac{1}{v}}}, \tag{2.52a}$$

$$\tau_b = \tau_{bs}(F) e^{\beta \Delta G_b^{\ddagger} (1 - \frac{v F x_b^{\ddagger}}{\Delta G_b^{\ddagger}})^{\frac{1}{v}}}. \tag{2.52b}$$

τ_{as} and τ_{bs} are relaxation times, depending on the force and bond properties. v counts the shape of the potential. For the linear cubic potential, $v = 2/3$, and for a cusp-harmonic potential, $v = 1/2$. This allows us to express η using a unified form

$$\eta = \frac{1}{1 + \tau_a/\tau_b} = \frac{1}{1 + \frac{\tau_{as}}{\tau_{bs}} \exp\left[\beta \Delta G_a^{\ddagger} (1 - \frac{v F x_a^{\ddagger}}{\Delta G_a^{\ddagger}})^{\frac{1}{v}} - \beta \Delta G_b^{\ddagger} (1 - \frac{v F x_b^{\ddagger}}{\Delta G_b^{\ddagger}})^{\frac{1}{v}}\right]}, \tag{2.53}$$

Furthermore, if we set $v = 1$, the formula is reduced to the phenomenological result given by Bell's model (now τ_{as} and τ_{bs} are independent of force).

It should be noted that if the high-barrier approximation fails, the formula in Eq. 2.53 is not applicable anymore. This happens when the external force F is too large such that the energy barrier becomes comparable to thermal noise or even vanishes. We discuss the case of large force in the next subsection.

2.2.4 Antigen extraction in the limit of strong force

While Eq. 2.53 established analytical understanding of antigen extraction in the weak-force regime, it remains unclear how the system behaves when the tugging force is so large that the potential barrier vanishes. In this section, we proceed to discuss the chance of antigen extraction when $F > \min(f_a, f_b)$. We show that, as opposed to the behavior in the weak-force regime, a strong force always inhibits the antigen extraction regardless of the tether property.

We first note that the dynamics of x_a and x_b follows the deterministic trajectory independent of the thermal noise when the force is large. In the weak force regime, we assumed

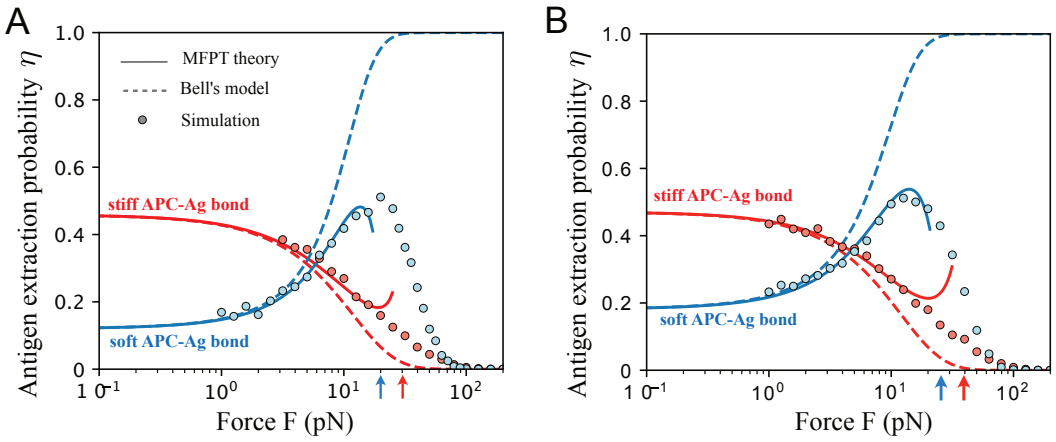

Figure 2.6: The relationship between the extraction chance η and the pulling force F. (A)Results based on the linear-cubic potential. (B) Results for the cusp-harmonic potential. Symbols are based on Brownian motion simulations. Curves are analytical results. Dashed curves represent the Bell's phenomenological expression. Red: stiff APC-Ag bond, $x_a^\ddagger = 1.5$nm. Blue: soft APC-Ag bond, $x_a^\ddagger = 3$nm. Other parameters: $x_b^\ddagger = 2$nm. $\Delta G_a^\ddagger = \Delta G_b^\ddagger = 10 k_{\mathrm{B}}T$, $\gamma_a = \gamma_b$. Arrows mark the bare bond strength $\min(f_a, f_b)$.

that the barrier height was much larger than the thermal noise so that bond disassociation was governed by rare events. When forces are strong, in contrast, BCR molecule and Ag molecule undergo a drift motion governed by deterministic terms in Eq. 2.15, since the noise force ξ_1 and ξ_2 are negligible compared to the applied force. In this drift-dominating regime, the unbinding trajectory mostly follows the deterministic one [40]. Therefore, we can understand the extraction results by working out the deterministic motion explicitly.

To examine the deterministic motion, we start from Eq. 2.15 and turn the noise off. With $\xi_1 = \xi_2 = 0$, Eq. 2.15 becomes

$$\gamma_a \dot{x}_a = -U_a'(x_a) + U_b'(x_b), \tag{2.54a}$$

$$\gamma_b(\dot{x}_a + \dot{x}_b) = -U_b'(x_b) + F. \tag{2.54b}$$

This ordinary differential equation can be solved numerically given the potential function

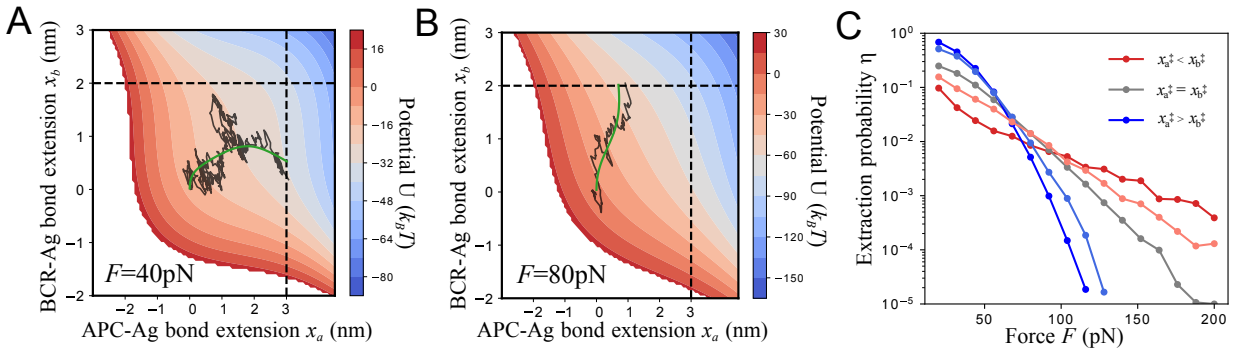

Figure 2.7: Large pulling force inhibits antigen extraction, and the inhibition depends on APC-Ag bond stiffness. (A)Under large force, simulated stochastic trajectories wiggle around the deterministic one. Contour maps show the potential landscape $U(x_a, x_b)$. The solid line in green represents the deterministic trajectory, and the solid black line is a simulated rupture trajectory. $F = 40$pN (B) Same as (A) but for a larger force $F = 80$pN. (C)Large force reduces extraction efficiency. Symbols were obtained from Brownian motion simulations ($\geq$1000 runs) for different APC-Ag bond stiffness (from red to blue: $x_a^\ddagger = 0.5, 1.0, 1.5, 2.0, 3.0$nm), The reduction is more effective for soft APC-Ag bond (blue) than for stiff APC-Ag bond (red). Parameters: $\Delta G_a^\ddagger = \Delta G_b^\ddagger = 10 k_B T, x_b^\ddagger = 1.5$nm. A linear cubic potential was used.

$U_a(x)$ and $U_b(x)$.

As shown by Fig. 2.7, in the deterministic picture, BCR-Ag bond is always stretched by force first before APC-Ag bond is stretched. To show this, we look at the initial 'speed' of extension. Starting from the equilibrium position ($x_a = x_b = 0$), we have $\dot{x}_a(t = 0) \approx 0$ and $\dot{x}_b(t = 0) \approx F/\gamma_b$. This suggests that BCR molecule moves without influencing the Ag location much in the beginning. Intuitively, this is because the mechanical force coming from the B cell side always perturbs the BCR-Ag bond first before propagating to the APC-Ag bond through the extension of BCR-Ag bond. The larger the force, the less APC-Ag deforms before BCR-Ag bond breaks (Fig. 2.7A-B). When there is noise, the unbinding

trajectory wiggles around the deterministic one (Fig. 2.7A-B). Therefore, as the deterministic trajectory deviates from the absorbing boundary $x_a = x_a^\ddagger$, antigen extraction becomes less likely (Fig. 2.7A-B). This implies that a larger force always leads to less antigen extraction in this regime, regardless of tether property (Fig. 2.7C).

In addition, the dependence of η on force is more sensitive for a soft APC-Ag bond (i.e. large $x_a^\ddagger$). This is consistent with the barrier reduction picture (i.e. lifetime of a softer bond is more sensitive to force) when the potential barrier is high, but it is from a kinetic point of view. Under a larger force, the APC-Ag bond is less stretched deterministically due to the shorter response time. Such reduction of deformation is more significant for soft APC-Ag bond than for stiff APC-Ag bond (Fig. 2.7C).

2.2.5 Antigen extraction under a dynamical force

Previously, we assume the tugging force is constant once applied. However, in reality, the pulling force might be dynamic [32, 6]. To appreciate how a dynamical force influences the antigen extraction, in this section we assume the force is time-dependent, $F(t)$. Therefore, the potential landscape becomes,

$$U(x_a, x_b, t) = U_a(x_a) + U_b(x_b) - F(t) \cdot (x_a + x_b). \tag{2.55}$$

Now the first passage time is no-longer exponential even the barrier is high [16]. For example, under a linearly ramping force, the first passage time distribution peaks at some most likely value that is determined by the balance of increasing off-rate and decreasing bond survival likelihood [16]. We assume the potential barrier is high so that Eq. 2.35 is still applicable.

To find the extraction chance, we follow the method developed by Hummer and Szabo [47] and introduce the survival probability of the bond chain $s(t)$ at time t. It is a multiplier of the survival probability of the BCR-Ag bond, $s_a(t)$ and that of the APC-Ag bond, $s_b(t)$.

$$s(t) = s_a(t) s_b(t). \tag{2.56}$$

Note $s(0) = 1$. Then the first passage time can be simply derived by $p(t) = -\dot{s}(t)$. Under the adiabatic approximation, the survival probability satisfies a first-order rate equation [40, 17].

$$\dot{s}_a(t) = -\frac{1}{\tau_a(F(t))} s_a(t), \quad \dot{s}_b(t) = -\frac{1}{\tau_b(F(t))} s_b(t), \tag{2.57}$$

where $\tau_a(F)$ and $\tau_b(F)$ are mean bond lifetimes at constant force F. Integrating both sides, we get

$$s_a(t) = e^{-\int_0^t \frac{1}{\tau_a(F(t'))}\, dt'}, \quad s_b(t) = e^{-\int_0^t \frac{1}{\tau_b(F(t'))}\, dt'}. \tag{2.58}$$

Therefore,

$$p_a(t) = -\dot{s}_a(t) = \frac{1}{\tau_a(F(t))} e^{-\int_0^t \frac{1}{\tau_a(F(t'))}\, dt'}, \tag{2.59a}$$

$$p_b(t) = -\dot{s}_b(t) = \frac{1}{\tau_b(F(t))} e^{-\int_0^t \frac{1}{\tau_b(F(t'))}\, dt'}. \tag{2.59b}$$

With this, we find,

$$\tilde{\eta} = \int_0^\infty p_a(t) \int_t^\infty p_b(t) dt = \int_0^\infty \frac{1}{\tau_a(F(t))} e^{-\int_0^t (\frac{1}{\tau_a(F(t'))} + \frac{1}{\tau_b(F(t'))}) dt'} dt. \tag{2.60}$$

We use $\tilde{\eta}$ to denote the extraction chance under a dynamical force, distinguished from the extraction chance under a constant force, η. The above formula can be evaluated numerically utilizing the relationship between τ_a, τ_b and F as we obtained in earlier sections. In addition, the combined suirvival probability is

$$s(t) = \exp\{-\int_0^t (\frac{1}{\tau_a(F(t'))} + \frac{1}{\tau_b(F(t'))}) dt'\}, \tag{2.61}$$

which gives us the FPT distribution

$$p(t) \equiv -\dot{s}(t) = (\frac{1}{\tau_a(F(t))} + \frac{1}{\tau_b(F(t))}) \exp\{-\int_0^t (\frac{1}{\tau_a(F(t'))} + \frac{1}{\tau_b(F(t'))}) dt'\}. \tag{2.62}$$

Consequently, we can rewrite Eq. 2.60 into

$$\tilde{\eta} = \int_0^\infty \eta(F(t)) p(t) dt. \tag{2.63}$$

This implies that the extraction probability is the integrated probability flux that exits through the boundary for successful antigen extraction, $\eta(F(t))p(t)$, which is rooted in our adiabatic assumption behind Eq. 2.57: force changes slowly so that the system is always in a quasi-equilibrium state with extraction chance $\eta(F(t))$ at time t.

If we are allowed to change variable from t to F (e.g., a linear ramping force, $F(t) = rt$), we get

$$\tilde{\eta} = \int_0^\infty \eta(F(t))p(t)dt = \int_0^\infty \eta(F)p(F)dF. \tag{2.64}$$

Here $\eta(F) = 1/(1 + \frac{\tau_a(F)}{\tau_b(F)})$ is the antigen extraction probability under constant force F. Therefore, with the knowledge of extraction under a static force $\eta(F)$, we are able to estimate the extraction chance as soon as we know the rupture force distribution $p(F)$.

Furthermore, Fig. 2.8 suggests that the mean rupture force alone is predictive of extraction results. As shown in Fig. 2.8, different dynamical forces result in a similar relationship between $\tilde{\eta}$ and mean rupture force $F_r \equiv \int Fp(F)dF$. In the following, we show that this happens when the difference between bond lengths $\Delta x^\ddagger \equiv |x_b^\ddagger - x_a^\ddagger|$ is small compared to the bond length per se. By Eq. 2.64, $\tilde{\eta}$ relies on the rupture force distribution $p(F)$. If η does not change much across the bulk region of $p(F)$ (we will justify this assumption below), we can Taylor expand $\eta(F)$ near F_r,

$$\eta(F) = \eta(F_r) + \frac{\mathrm{d}\eta}{\mathrm{d}F}\bigg|_{F_r}(F - F_r) + \frac{1}{2}\frac{\mathrm{d}^2\eta}{\mathrm{d}F^2}\bigg|_{F_r}(F - F_r)^2 + \mathcal{O}\big((F - F_r)^3\big). \tag{2.65}$$

Thus,

$$\tilde{\eta} = \int \eta(F)p(F)dF \approx \eta(F_r) + \frac{1}{2}\frac{\mathrm{d}^2\eta}{\mathrm{d}F^2}\bigg|_{F_r}\sigma_F^2, \tag{2.66}$$

where $\sigma_F^2 = \int (F - F_r)^2 p(F)dF$ is the variance of rupture force distribution. Thus, the extraction chance can be estimated by

$$\tilde{\eta} = \eta(F_r), \tag{2.67}$$

as long as the rupture force distribution is "narrow".

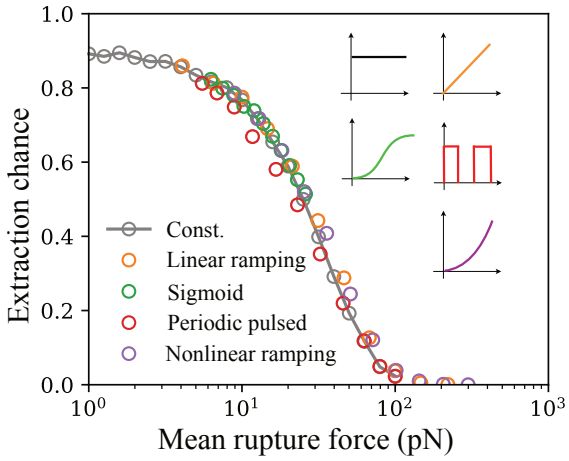

Figure 2.8: The relationship between the extraction chance η and the mean rupture force F_r, under different dynamical forces. The insets show the force dynamics $F(t)$, including a constant force $F(t) = F_0$ (black), a linear ramping force $F(t) = rt$ (orange), a sigmoid force $F(t) = F_{\max}t/(t_F + t)$(green), a periodic pulsed force (red), and a nonlinear ramping force $F(t) = rt^2$ (purple). Symbols in each color are obtained from Brownian simulation by varying force parameters. For instance, we vary the loading rate r for the linear ramping force. Parameters: $x_b^\ddagger = 2\text{nm}$, $x_a^\ddagger = 1.5\text{nm}$, $\Delta G_a^\ddagger = 10k_\text{B}T, \Delta G_b^\ddagger = 14k_\text{B}T$, $\gamma_a = \gamma_b$. Now $(\Delta x^\ddagger/x_b^\ddagger)^2 = 0.0625 \ll 1$.

When can the distribution $p(F)$ be treated as narrow enough? We observed that roughly, $\frac{\mathrm{d}^2\eta}{\mathrm{d}F^2}\big|_{F_r} \sim (\Delta x^\ddagger)^2, \sigma_F^2 \sim \left(\frac{1}{x^\ddagger}\right)^2$, where $\Delta x^\ddagger = |x_b^\ddagger - x_a^\ddagger|$, and $x^\ddagger = x_a^\ddagger$ or $x_b^\ddagger$, depending on which bond is weaker. This is because, to the leading order, η varies with force according to $\exp(F\Delta x/k_BT)$, whereas the width of $p(F)$ falls inversely with the bond length itself [17]. Therefore,

$$\frac{1}{2}\frac{\mathrm{d}^2\eta}{\mathrm{d}F^2}\bigg|_{F_r}\sigma_F^2 \sim \left(\frac{\Delta x^\ddagger}{x^\ddagger}\right)^2, \tag{2.68}$$

This suggests that when the difference between bond lengths, Δx, is small compared to the bond length per se, the rupture force distribution is narrowly peaked relative to the variation of extraction probability with force. So the antigen extraction chance is mostly determined

by the mean rupture force.

Summary So far we constructed the Langevin model for the antigen extraction process and calculated the antigen extraction chance to show how the tugging force played a role. In the weak force regime ($F \ll f_a, F \ll f_b$), the Bell's phenemonological expression is pridictive of extraction chance. The force can promote or inhibit antigen extraction, depending on the relative bond length Δx. When the force gets strong ($F < f_a, F < f_b$), deviations from Bell's model show up because the force not only lowers the potential at the barrier but also tilts the potential and changes the mininum-barrier distance. When force is large enough to destroy the potential barrier ($F > f_a, F > f_b$), it always inhibits antigen extraction because it ruptures the BCR-Ag bond before its effect reaches the APC-Ag bond. If the force is dynamical, in the adiabatic limit, its influence on antigen extraction is characterized by the rupture force distribution.

2.3 Affinity discrimination based on antigen extraction

In addition to the intriguing dynamics, it is interesting to discuss the biological importance of antigen extraction, in terms of B cell affinity discrimination. In this section, we look at how the mechanical force regulates affinity discrimination through the antigen extraction process. For simplicity, we assume different B cells form clusters with the same size and BCR-Ag-APC complexes in a cluster are independent of each other. Then, the number of captured antigens is sorely determined by the extraction probability η. Thus, in what follows, we focus on the dependence of η on affinity $\Delta G_b^\ddagger$ under different tugging forces and different APC properties ($x_a^\ddagger$, $\Delta G_a^\ddagger$). Our analysis suggests that the force regulates the stringency of affinity discrimination and expands the discrimination range.

To see how the antigen extraction changes as BCR affinity improves, we sketch the relationship between η and $\Delta G_b^\ddagger$ (the response curve) in Fig. 2.9, which is supported by

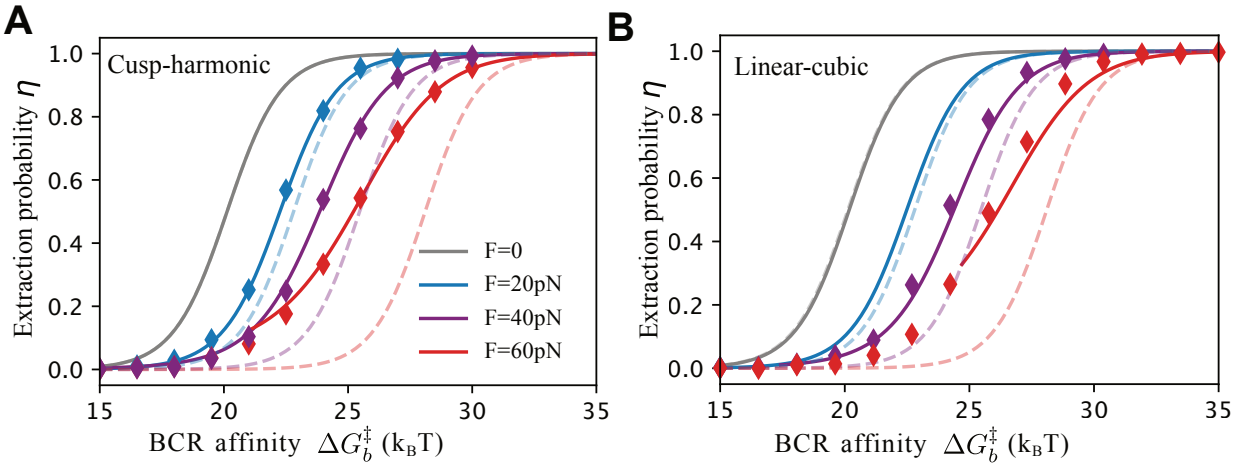

Figure 2.9: Applied force shifts the response curve and enhances the ceiling affinity. We plot the extraction probability as a function of BCR affinity, under different forces. Solid curves are analytical predictions given by Eq 2.53. Symbols are obtained from 200 independent Brownian simulations. Dashed lines are given by Bell's model, Eq. 2.50. (A) Cusp-harmonic potential was used. (B) We use the linear-cubic potential. Parameters: $\Delta G_a^{\ddagger} = 20k_BT, x_a^{\ddagger} = 1.5\text{nm}, x_b^{\ddagger} = 2\text{nm}$.

Brownian dynamics simulations. The curve displays a sigmoid shape: starting from 0, η increases with affinity and saturates when affinity is sufficiently high. Therefore, a small difference in affinity is distinguishable only when B cell affinities fall into the transition region where η changes sensitively as $\Delta G_b^{\ddagger}$ varies. We call this transition region the "sensitive window".

Fig. 2.9 shows that, as we raise the force magnitude, the sensitive window shifts (see solid lines). When pulling against a stiff APC ($x_a^{\ddagger} < x_b^{\ddagger}$), force inhibits antigen extraction (Fig. 2.6) and thereby the response curve shifts toward higher affinities, as predicted by Bell's model. Consequently, by applying a large force, B cells with high affinities become distinguishable. If the APC is soft ($x_a^{\ddagger} > x_b^{\ddagger}$), a small force improves η and a large force decreases η (Fig. 2.6). Therefore, as we increase force, the response curve first shifts toward the low-affinity end

and then shifts to the high-affinity end. This suggests that the mechanical force can be an active regulator of the sensitive window for discrimination.

In addition to the shift, Fig. 2.9 demonstrates that the response curve is stretched so that the sensitive window expands. This is because landscape deformation compensates the force-induced barrier reduction, which is more significant for low-affinity B cells, as seen by

$$\Delta G^{\ddagger}(1-\frac{vFx^{\ddagger}}{\Delta G^{\ddagger}})^{\frac{1}{v}} \approx \Delta G^{\ddagger} - Fx^{\ddagger} + \frac{1-v}{2}\frac{(Fx^{\ddagger})^2}{\Delta G^{\ddagger}} + o(F^3). \tag{2.69}$$

Note that the nonlinear offset (third term on the right-hand side) is positive and depends inversely on the intrinsic affinity, $\Delta G^{\ddagger}$. In other words, as pulling applies, lower affinity B cells can maintain the extraction level by making a smaller improvement in affinity. Therefore, the "shifting" is affinity-dependent, suggesting that force application substantially broadens the discrimination range.

To provide a quantitative understanding, we define the discrimination range as the affinity span between almost vanishing $\eta_{\min}$ and nearly full ($\eta_{\max}$) antigen extraction, where η is sensitive to affinity changes. Explicitly,

$$\Delta\Delta G_b^{\ddagger}(F) \equiv \Delta G_b^{\ddagger}(\eta_{\max}; F) - \Delta G_b^{\ddagger}(\eta_{\min}; F), \tag{2.70}$$

depending on force F. As we show in Fig. 2.10, the discrimination range (orange region) expands as the pulling force increases. This intriguing behavior is beyond the Bell's model.

We can appreciate the effect analytically. To do so, we solve for $\Delta G_b^{\ddagger}(\eta; F)$, namely, the BCR affinity that corresponds to η antigen extraction under force F. It is defined by the implicit equation below,

$$\Big[1 + \frac{\tau_{as}}{\tau_{bs}} e^{\beta\Delta G_a^{\ddagger}(1-\frac{vFx_a^{\ddagger}}{\Delta G_a^{\ddagger}})^{\frac{1}{v}} - \beta\Delta G_b^{\ddagger}(1-\frac{vFx_b^{\ddagger}}{\Delta G_b^{\ddagger}})^{\frac{1}{v}}}\Big]^{-1} - \eta = 0. \tag{2.71}$$

We assume the major dependence on force and affinity goes into the exponential factor. In other words, τ_{as} and τ_{bs} are assumed to be constant. Then, in the limit of a weak force, by Taylor expansion, we have

$$\Delta G_b^{\ddagger}(\eta; F) = \Delta G_b^{\ddagger}(\eta; 0) + \frac{\partial \Delta G_b^{\ddagger}}{\partial F}\Big|_{F=0} F + \frac{1}{2}\frac{\partial^2 \Delta G_b^{\ddagger}}{\partial F^2}\Big|_{F=0} F^2 + \mathcal{O}\big(F^3\big). \tag{2.72}$$

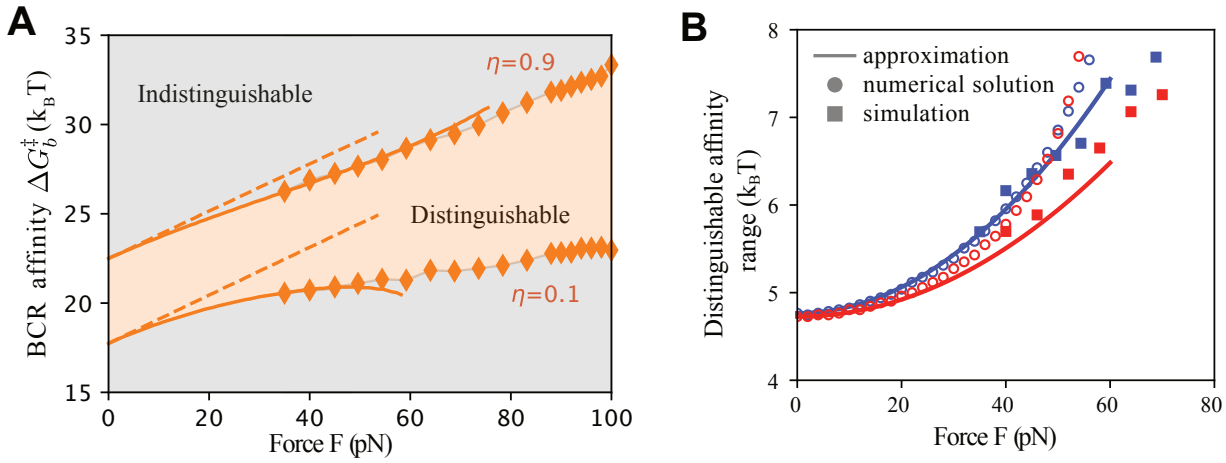

Figure 2.10: Applied force enhances ceiling affinity and extends the distinguishable affinity range. (A) Phase diagram for distinguishable affinity under different forces. Distinguishable affinity $\Delta G_b^{\ddagger}$ is defined as $\eta_{\min} < \eta(\Delta G_b^{\ddagger}; F) < \eta_{\max}$, as shown in the colored region. The boundaries ($\eta = \eta_{\min}$ and $\eta = \eta_{\max}$) are represented by solid curves (obtained from Eq. 2.73) and symbols (obtained from Brownian simulations). The dashed lines are analytical prediction by Bell's model. The cusp-harmonic potential was used. (B) Discrimination range increases with force. Filled squares are from Brownian simulations. Blue for cusp-harmonic potential and red for linear-cubic potential. Solid curves are based on Eq. 2.74. Open circles are numerical results to Eq. 2.70. Both results suggest the discrimination range increases with force. And in the limit of small force, the relation is quadratic. Parameters: $\Delta G_a^{\ddagger} = 20 k_B T, x_a^{\ddagger} = 1.5\text{nm}, x_b^{\ddagger} = 2\text{nm}$.

The derivative can be obtained utilizing the implicit differentiation and the chain rule, $\frac{\partial \Delta G_b^\ddagger}{\partial F} = -\frac{\partial z/\partial F}{\partial z/\partial \Delta G_b^\ddagger}$, where $z \equiv 1/(1+\tau_a/\tau_b) - \eta$. After calculation, we get,

$$\Delta G_b^\ddagger(\eta; F) \approx \Delta G_b^\ddagger(\eta; 0) + (x_b^\ddagger - x_a^\ddagger)F + \frac{1-v}{2}\Big[\frac{(Fx_a^\ddagger)^2}{\Delta G_a^\ddagger} - \frac{(Fx_b^\ddagger)^2}{\Delta G_b^\ddagger(\eta; 0)}\Big] + \mathcal{O}\big(F^3\big), \quad (2.73)$$

where $\Delta G_b^\ddagger(\eta; 0)$ is the required affinity without force. All terms behind $\Delta G_b^\ddagger(\eta; 0)$ describe the "shifting" of discrimination curve by force, that is, how much affinity should be improved to maintain the extraction level as pulling force applies. If $v = 1$ when the model reduces to the phenomenological theory, the shifting depends linearly on F and is affinity-independent. In contrast, for a landscape model with $v < 1$, higher order terms play a role and the shifting depends on BCR affinity. By Eq. 2.70, we have

$$\Delta\Delta G_b^\ddagger(F) \approx \Delta\Delta G_b^\ddagger(0)\Big[1 + \frac{1-v}{2}\Big(\frac{Fx_b^\ddagger}{\Delta G_a^\ddagger}\Big)^2\Big]. \quad (2.74)$$

This agrees with numerical simulations when F is small (see Fig. 2.10B). As expected, only the force-induced stretching that starts at the quadratic order contributes to range expansion.

Furthermore, under a dynamical force, this expansion of discrimination range is even more significant. This can be seen from Eq. 2.67, the extraction chance $\tilde{\eta}$ depends on the mean rupture force, which increases with BCR affinity (because the complex gets stronger). This further flattens the response curve because the higher the affinity, the force-induced inhibition of antigen extraction is more significant. Therefore, this affinity-dependent force application further broadens distinguishable affinities.

2.4 Discussion

In this section, we performed detailed analysis regarding the antigen extraction process using a Langevin model, investigated how the force regulates antigen extraction chance, and explored its beneficial effect in affinity discrimination. We found that force application is able to lower the potential barrier and deform the potential landscape. Consequently, it

can improve or inhibit antigen extraction, depending on the relative bond length and force magnitude. This regulates the discrimination stringency and expands the sensitive window.

Timescale of antigen extraction We have shown in the limit of high potential barrier, the average complex lifetime is given by $\tau = \tau_a\tau_b/(\tau_a + \tau_b)$. It is straightforward to show a larger force leads to shorter timescale of extraction. Nevertheless, the overall contact duration between a B cell and an APC also depends on the binding process and cytoskeleton reorganization. Roughly, $\tau_{\text{contact}} \approx \tau_{\text{binding}} + \tau_{\text{force-trigger}} + \tau_{\text{extraction}}$. Here $\tau_{\text{extraction}} = \tau$. Therefore, increasing the force magnitude can speed up the process significantly only when the affinity is sufficiently high so that a complex never almost breaks within the contact duration.

Supporting evidence from experiments Our results agree well with experimental observations. First, it has been discovered that naive B cells rapidly internalized the antigen from the flexible plasma membrane sheets (PMSs) but not stiff planar lipid bilayers (PLBs), even though B cell spreading and antigen clustering were induced on both substrates [31, 33, 2]. This suggests that naive B cells are able to extract antigens from a flexible membrane but not a stiff membrane. Consistent with the observation, our results predict that under a high-enough pulling force, a softer tether (larger $x_a^\ddagger$) results in a higher chance of antigen extraction (see Fig. 2.6). This is because, when pulling against a flexible substrate, force significantly weakens the tether strength by lowering the potential barrier. Second, compared to naive B cells, GC B cells are usually more diverse, with higher average affinity, and thereby more difficult to distinguish. Therefore, GC B cells display distinct properties compared to naive B cells. For example, they usually interact with stiffer APCs such as follicular dendritic cells (FDCs) and deploy a larger force [32, 33]. Our model indicates that this regulation is beneficial for discrimination of high-affinity B cells. Indeed, Nowosad et al. investigated the extraction of two similar specific antigens (the low-affinity 4-hydroxy-3-nitrophenylacetyl (NP) and the high-affinity 4-hydroxy-3-iodo-5-nitrophenylacetyl (NIP)

haptens) by naive B cells and GC B cells, and demonstrated that GC B cells achieved better affinity discrimination than naive B cells [32].

Potential experimental tests In addition, predictions of our theory can be tested using dynamic force spectroscopy combined with live-cell imaging. The extraction curve $\tilde{\eta} \approx \eta(F_r)$, if able to collapse the dynamic-force data onto the constant-force theory, will assist in understanding rupture dynamics and predicting extraction propensity based on mean rupture force;a smaller difference in stiffness between the tugging and tethering complexes is expected to improve the match. In these cases, η can be estimated by counting successful events out of many ex-traction attempts; success is determined by tracking anti-gen fluorescence during rupture. Importantly, by fitting data to the analytical theory, one can extract intrinsic parameters characteristic of the multidimensional binding landscape, especially the strength of antigen tether in the absence of force that would otherwise be hard to measure.

Strong internal dissipation limit Our model focused on the strong hydrodynamic dissipation limit, whereas it is possible that the internal dissipation dominates the energy dissipation during bond rupture [54]. To see how the internal dissipation plays a role, we consider the following Rayleigh dissipation function

$$R = \frac{1}{2}\gamma_{a0}\dot{x}_a^2 + \frac{1}{2}\gamma_{b0}\dot{x}_b^2, \tag{2.75}$$

where we dropped the hydrodynamic dissipation by assuming $\gamma_{a0}, \gamma_{b0} \gg \gamma_a, \gamma_b$. Then the equation of motion becomes

$$\gamma_{a0}\dot{x}_a = -U_a'(x_a) + F + \xi_a, \tag{2.76a}$$

$$\gamma_{b0}\dot{x}_b = -U_b'(x_b) + F + \xi_b. \tag{2.76b}$$

As opposed to Eq. 2.15, now the force influences two bonds simultaneously and the two degrees of freedom are decoupled. Therefore, the model becomes effectively one-dimensional. In the limit of high potential barrier, the MFPT is given by the Kramers theory (see Eq. 2.4).

Compared to Eq. 2.52, the exponential term takes exactly the same form and the only difference lies in the pre-factor. Hence, our unified formula of η in Eq. 2.53 is still applicable. Therefore, most of our results (section 2.2.3, 2.2.5, and 2.3) are qualitatively unchanged. Nevertheless, under the limit of a large force, results will be different due to the different kinetics. More specifically, a large force may enhance antigen extraction if $\gamma_{a0} < \gamma_{b0}$, because it stretches the APC-Ag bond faster ($\dot{x}_a(t=0) \approx F/\gamma_{a0}$) than it extends the BCR-Ag bond ($\dot{x}_b(t=0) \approx F/\gamma_{b0}$).

Clustering Our treatment of antigen extraction is mean-field in nature and neglecting rebinding. However, in reality, complexes form clusters [32], which introduces coupling between different complexes. For example, force may be shared by all closed complexes within a cluster. Therefore, different complexes break under a different force magnitude. In addition, there are chances of rebinding before the entire cluster is fully detached. How this hierarchy of complexity modulates the extraction results and the discrimination function is not captured by our mean field model. We will investigate the coupling between bonds in chapter 4.

CHAPTER 3

Evolutionary significance of antigen extraction

"Nothing in biology makes sense except in the light of evolution."

Theodosius Dobzhansky

3.1 Introduction

In the previous chapter, we have shown that the physical extraction of antigen using tugging forces relates the receptor affinity to rupture outcomes and allows a gradual dependence of antigen acquisition on BCR affinity over a wide dynamic range. But whether, and how, does active sensing by cells influence the adaptation of a polyclonal population? An ultimate test of plausible physical behaviors is to subject the resulting phenotype to natural selection. Therefore, in this chapter, we will combine the antigen extraction model with an *in silico* evolution model of GC to show how the regulation at the molecular level propagates to and influences the evolution at the population level.

Biology background It is known for a long time that the average affinity of specific antibodies increases dramatically over the course of an immune response. Back in 1964, Eisen and Siskind [4] found that the association constant (K_a) between antigens and serum antibodies yielded from immunized rabbits increased progressively with time from 10^5-$10^6\mathrm{M}^{-1}$ to 10^7-$10^8\mathrm{M}^{-1}$ after a few months. The difference can be as large as 10^4-fold in K_a [4].

Repeated experiments with different antigens invariably confirmed the same results [60, 61]. This phenomenon is known as *affinity maturation*. Besides, the sequence analysis of antibody genes provides correlated results: sequences of early antibodies were identical to that of the germline, whereas antibodies derived later in the response had somatically acquired point mutations [62]. Crystal structure analysis suggests that those point mutations are important in improving the chemical complementarity of the antibody-antigen interface [63].

To uncover the mechanism that drives affinity maturation, a lot of effort has been devoted to understanding the structure of germinal center (GC), the place where the affinity maturation takes place (see the review given by Victora et al. [3] Mesin et al. , [26] and Cyster and Allen [27]). Shortly after an infection, GCs form in the center of B cell follicles of secondary lymphoid organs, interspersed within a network of follicular dendritic cells (FDCs). Each GC has two compartments, or "zones" (see Fig. 3.1). The zone rich in FDCs is called the light zone (LZ). LZ contains B cells and a crucially important population of T follicular helper (Tfh) cells. The other one is known as the dark zone (DZ), which is less diverse and consists primarily of highly proliferative B cells.

In the past two decades, the understanding of GC dynamics has been tremendously advanced due to the development in the sequencing and imaging technique. At the initial stage of the GC reaction, naïve B cells are recruited. The population expands and diversifies through hypermutation. In the LZ, B cells contact with FDCs to form synapses and extract antigens that are displayed on the surface of FDCs [30]. Then those extracted antigens are internalized, processed into peptide, and displayed on the surface of each B cell. These B cells then compete for a limiting number of Tfh cells for survival signals [34, 64]. After the competition, some B cells die due to lack of sufficient surviving signal [65], and a few B cells differentiate into antibody-producing plasma cells or memory cells. The majority of B cells migrate to the DZ [34, 64]. In the DZ, B cells proliferate with a rate proportional to the amount of proliferation signal received from Tfh cells [35], during which random mutations in the gene coding for the BCR happens at a high rate. After proliferating and mutating in

the DZ, B cells migrate back to the LZ [34, 64]. Iterative cycles of such hypermutation and selection result in an increase in B cell affinity over time.

Existing models *In-silico* models of GC reaction have proven to be a powerful tool to appreciate and predict how the elegant structure of GC could facilitate the affinity maturation process. The seminal work of Perelson et al. [66] showed that cyclic re-entry of B cells between the DZ and the LZ is optimal for the affinity improvement. Meyer-Hermann et al. [67] conducted very detailed simulations to reproduce the cellular dynamics within a GC. Recent computational studies focused on the effect of different immunization strategies with multiple variant antigens on the development of broadly neutralized antibodies (bnAbs) [68, 14, 69, 70, 19, 20, 71]. For instance, Wang et al. [14] developed a stochastic rule–based model to show that sequential immunization with variant antigens may elicit bnAbs more efficiently than a mixture of the same antigens. Another focus is that how different regulatory factors influence the speed of affinity maturation in a GC reaction. Such factors include antigen availability [72], antibody feedback (antibody injection or passive immunization) [73, 74, 18], and antigen spike density [75]. Besides, several studies have investigated the mechanism behind the wide spectrum of clonal diversity observed across different GCs [76, 77, 78].

However, most existing studies neglected or oversimplified the physical process of BCR-Ag interaction, the key step that drives affinity maturation. For example, one of the widely used formulas is (see [14, 69, 18, 19, 20], we changed notations for consistency)

$$P_{\text{extraction}} = \frac{C_{ag} e^{(\Delta G_b^{\ddagger} - \Delta G_{\text{ref}}^{\ddagger})/k_{\text{B}}T}}{1 + C_{ag} e^{(\Delta G_b^{\ddagger} - \Delta G_{\text{ref}}^{\ddagger})/k_{\text{B}}T}}. \tag{3.1}$$

Here C_{ag} is the antigen concentration and $\Delta G_{\text{ref}}^{\ddagger}$ is the reference affinity that sets the threshold for extraction. This phenomenological formula lumps all details during antigen extraction into a single parameter $\Delta G_{\text{ref}}^{\ddagger}$. Thus, it is hard to see how different individual factors influence evolution. Furthermore, the formula did not include the effect of force. Some researchers

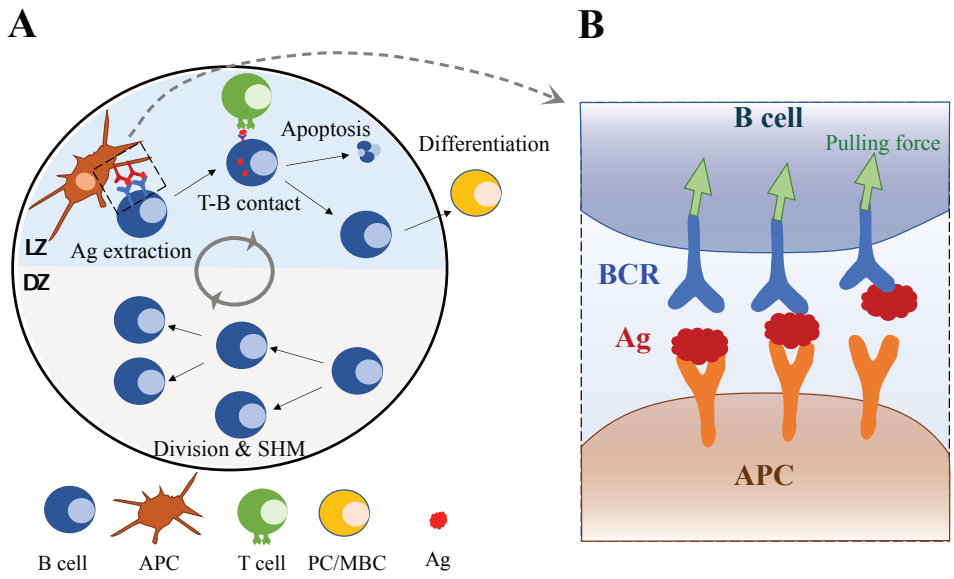

Figure 3.1: (A) Overview of cellular processes within GC during affinity maturation. An established GC consists of a light zone (LZ) and a dark zone (DZ). In the LZ, B cells contact with APC to form synapse and extract antigens. Then they interact with Tfh cells to get a survival signal, after which they recycle to the DZ, differentiate into plasma cells or undergo apoptosis. In the DZ, B cells proliferate according to the survival signal delivered by T cell: B cells that extract more antigens will proliferate more times. Random mutations that modify the binding may take place during each replication. (B)The tug-of-war antigen extraction process. During the interaction between APC and B cell, BCRs bind to antigens that are tethered on the surface of APC. Then the B cell uses the tugging force to extract antigens. We use a Brownian motion model to describe the molecular dynamics and obtain the chance of antigen extraction (see Chapter 2). APC: Ag presenting cell. PC: plasma cell. MBC: memory B cell. Ag: antigen.

introduced the dependence of $P_{\text{extraction}}$ on force [75], but only the phenomenological expression from Bell's model was used. Last but not least, as we show in the previous chapter, the extraction probability may depend on affinity in complicated ways. Whether and how the affinity maturation process would deviate if we use the full expression is yet unknown.

Tug-of-war + GC evolution Here we present a multiscale computational model that integrates the molecular Ag extraction process and population dynamics, operating at different time scales yet both being crucial to the evolution process, to investigate how the immune microenvironment influences affinity maturation. Specifically, we implemented a birth-death-mutation model of GC reaction using agent-based simulations, which incorporates the cyclic action of antigen extraction, competition, proliferation and mutation on cells that drives stochastic clonal expansion and an overall affinity increase. The key ingredient is an affinity-dependent proliferation rate, where our model of the molecular tug of war provides a bridge between BCR affinity and Ag extraction efficiency which, in turn, determines clonal fitness.

Our model shows how the tug-of-war antigen extraction could influence affinity maturation. First, the force application can improve the evolved affinity at the risk of GC death. This is done by adjusting the relative tether strength under force (effectively $\Delta G^{\ddagger}_{\text{ref}}$ in Eq. 3.1). A stronger tether decreases B cell fitness and requires higher BCR affinity for B cells to obtain all antigens presented. Besides, the nonlinear effect of force on potential tilting, as stated in chapter 2, can play an important role in extending the ceiling affinity without increasing the risk of GC death. Second, using feedback mechanisms, cells might be able to alleviate the constraint on response potency against current antigen. We show that a balance between mutation and selection establishes when the tether strength improves at the same pace as BCRs, which can be provided by the antibody feedback.

The results become even more interesting and surprising if the BCR bond length is evolvable. Our model predicts that as active force changes, the evolution direction varies:

High quality BCRs with large bond lengths develop under a small force, whereas a large force results in low-quality stiff BCRs with small bond lengths. Besides, heritable heterogeneity in pulling strength, combined with evolvable receptor flexibility, can generate a wide variety of binding affinities with similar clonal fitness. This discrepancy between antibody quality and B cell fitness reflects an optimization goal other than strong binding. Rather, force-enabled phenotypic plasticity may represent an adaptive strategy for balancing depth and breadth of collective responses aimed at evolving targets. Interestingly, tug-of-war antigen extraction confers an intrinsic geometry to the fitness landscape of B cell selection, which unifies multiple experimental results otherwise hard to reconcile, including the persistence of low-affinity clones [79] and diverging rates of diversity loss among B cell populations [80].

3.2 Germinal center evolution model and results

To investigate the cellular and molecular mechanisms involved in GC reaction, we integrate the antigen extraction model in chapter 2 with an agent-based GC evolution model. At the molecular level, the tug-of-war model outputs the number of Ags extracted by each B cell, which further determines the B cell's fitness. At the cellular level, B cell individuals undergo proliferation, mutation, and death according to their fitness. Fig. 3.1 shows a schematic plot of the model.

This chapter is structured as the following. We first introduce a minimal model and discuss the key quantities that determine the evolved affinity (section 3.2.1). After that, in order to better appreciate the components that might benefit the evolution, we make several modifications: evolution with antibody feedback (section 3.2.2), evolution with mutable bond length (section 3.2.3), and evolution of B cells with heterogeneous forces (section 3.2.4). Those modifications are motivated by recent experimental observations.

3.2.1 The minimal model

It has been reported in experiments that the GC evolution depends on diverse environmental factors such as the physical property of presenting cells [81, 82], and the mechanical feature of immune cells [83, 23]. To appreciate the underlying mechanism, we utilize a baseline model to explore how different environmental factors play a role. Our results suggest that the relative tether strength, characterized by tether affinity, tether stiffness and tugging force, is crucial in regulating the evolution outcome.

3.2.1.1 Model details

We combine our antigen extraction model introduced in Chapter 2 with a minimal GC reaction model. The GC model mostly inherits the model used by Amitai et al. [76] with essential modifications to fit our antigen extraction part. We will use this model as the baseline model and make modifications in later sections.

We initiate a GC with $N_0 = 1000$ founder B cells with initial affinity $\Delta G^{\ddagger}_{b0} = 14 k_B T$ and bond length $x^{\ddagger}_b = 2\text{nm}$. During the evolution, individual cells undergo many GC cycles. A GC cycle consists of the following steps: antigen extraction, death, differentiation, and birth/mutation, as we detailed below.

Antigen extraction For each B cell i, we calculate the antigen extraction chance η_i based on Eq. 2.48 and sample $n_{\text{ag,i}}$ from a Binomial distribution $B(C_{\text{ag}}A, \eta_i)$ as the number of obtained antigens, assuming different antigens are extracted independently. Here C_{ag} is the 3-body complex (BCR-Ag-APC) concentration on APC and A is the synapse area. We set $C_{\text{ag}}A = 100$ [84].

Death In the death step, all B cells die with a uniform probability $p_a = 0.3$. In addition, if a B cell failed to get any antigen $n_{\text{ag,i}} = 0$, it also underwent apoptosis. With this setting, the death step is weakly dependent on affinity unless receptors of the B cell are damaged, which agrees with recent experimental findings [35, 85, 86].

Differentiation If a B cell survived from the death step, it might differentiate into a plasma cell by a chance of $p_d = 0.05$ [14]. The newly generated plasma cell inherits the affinity.

Birth and mutation The remaining B cells proliferate afterwards. To mimic the stochastic birth step of B cell i, we sample the number of offsprings, n_i, from a Poisson distribution,

$$n_i \sim \text{Poisson}(r_i), \tag{3.2}$$

where r_i is the proliferation rate depending on fitness λ_i,

$$r_i = \lambda_i(1 - \frac{N}{N_c}) = \lambda_{\max}\frac{n_{ag,i}}{n_0 + n_{ag,i}}(1 - \frac{N}{N_c}). \tag{3.3}$$

Here, $1 - N/N_c$ describes the homogeneous pressure from finite resources and space ($N_c = 2000$). $\lambda_{\max} = 8$/cycle is the maximal proliferation rate, corresponding to 3 divisions per cycle. $n_0 = 0.5C_{\text{ag}}A$ is the number of extracted antigens for half maximum proliferation. Mutations that change binding potential may happen when a newborn B cell is generated. In the baseline model, we assume the mutation modifies $\Delta G_b^\ddagger$ only. In each division event, $\Delta G_b^\ddagger$ mutates at a chance of $p_{m,G_b} = 0.5$.

$$\Delta G^\ddagger_{b,\text{daughter}} = \Delta G^\ddagger_{b,\text{parent}} + N(0, \sigma_{G_b}). \tag{3.4}$$

We repeat the GC cycles until either all B cells die out or a maximum duration t_f is reached.

3.2.1.2 Results

Evolution dynamics Fig. 3.2 shows the simulated GC evolutionary dynamics. Starting from the initial affinity ($\Delta G^\ddagger_{b0} = 14k_BT$), the population-averaged affinity increases over time, mimicking the affinity maturation process (see Fig. 3.2A). Moreover, the maturation slows down over time. This is due to the fading discrimination sensitivity as antigen extraction saturates ($\frac{d\eta}{d\Delta G_b^\ddagger} \to 0$ as $\eta \to 1$). Concomitantly, as displayed in Fig. 3.2B, an initial

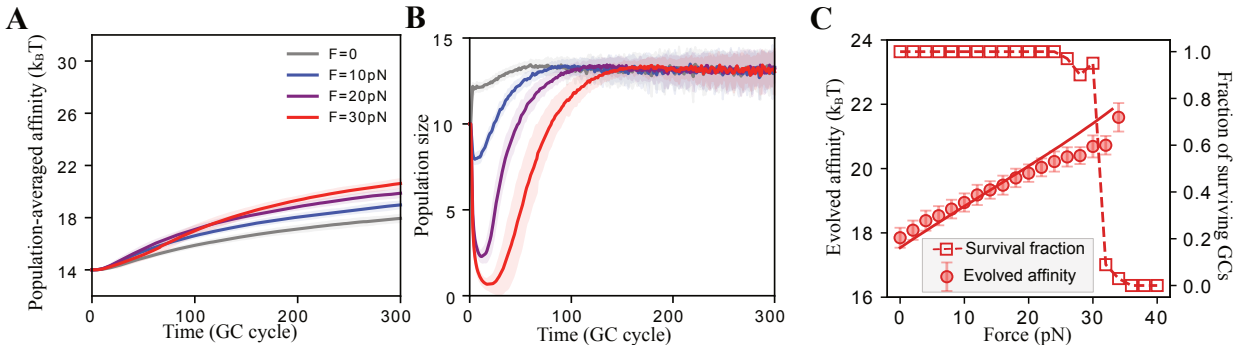

Figure 3.2: Evolution dynamics of the minimal GC evolution model. (A) The evolution of the mean affinity of cells in one GC. Solid curves represent the average trend among 100 GCs. The shade shows the variation among GCs. Different color correspond to different forces. Because $x_b^\ddagger > x_a^\ddagger$, the relative tether strength s increases as we increase force. (B) The evolution of GC population size. Solid lines are average trends, and shades show the variation among different GCs. (C)The relationship between the output affinity and the applied mechanical force. Circles were the mean B cell affinity at t_f, averaged from 100 independent GC simulations under different F. Error bars show stdev across different GCs. Squires were the fraction of surviving GCs at t_f among 100 simulations.

B cell population rapidly falls to a low abundance and subsequently recovers, forming a population bottleneck. This is an effect of evolution: the fitness initially is too low to keep the population size, but improves overtime, which rescues the population from extinction. If the population size drops to zero, the GC dies.

Output affinity and surviving GC fraction Because the GC reaction aims to output high-affinity B cells, we look at the evolved B cell affinity at $t_f = 300$ GC cycles when our simulation terminates. In Fig. 3.2C, we show that as the pulling strengthens, the evolved affinity increases whereas the fraction of surviving GCs drops to zero, consistent with curves in Fig. 3.2A-B. The improvement in evolved affinity is simply because pulling-induced shift of the extraction curve (see Fig. 2.9 in CH.2) promotes the discrimination of strong affini-

ties. Given a long-enough evolution time, the output affinity corresponds to a vanishing discrimination sensitivity. The surviving GC fraction drops because the initial B cell fitness decreases with the pulling strength, which places B cells population under higher risk of extinction during the bottleneck period.

To provide a quantitative understanding, we use the condition of vanishing fitness gradient to estimate the output affinity. Explicitly,

$$\Delta G^{\ddagger}_{b,t=t_f} \approx \Delta G^{\ddagger}_{b,\text{ceiling}}, \tag{3.5}$$

where the ceiling affinity $\Delta G^{\ddagger}_{b,\text{ceiling}}$ is the solution to

$$\frac{\mathrm{d}\eta}{\mathrm{d}\Delta G^{\ddagger}_{b}} = \alpha_{\text{threshold}}. \tag{3.6}$$

$\alpha_{\text{threshold}}$ is a threshold value of η gradient. For a given α, the above condition can be solved numerically. We choose the value of α that gives us the best fit (minimal mean square distance) to the simulation results. The solid curve in Fig. 3.2C demonstrates beautiful agreement.

Compared with Bell's model How does the stretch of discrimination curve (see Fig. 2.9 in chapter 2) influence affinity maturation? To show this, we compare our results based on the microscopic landscape model (Eq. 2.42) to the GC evolution based on the Bell's model (no stretch of discrimination curve). Note that by Bell's model we mean using the following phenomenological expression for antigen extraction probability,

$$\eta = \frac{1}{1 + \frac{\tau_{a0}}{\tau_{b0}} e^{F(x^{\ddagger}_{b} - x^{\ddagger}_{a})/k_B T}}, \tag{3.7}$$

where τ_{a0} and τ_{b0} are force-free APC-Ag bond lifetime and BCR-Ag bond lifetime respectively. As we show in chapter 2, this excludes the effect of potential tilting by force and provides good approximation when the force is weak. Fig. 3.3A shows that two models converge at the weak force limit, but behave differently when force is large, as expected.

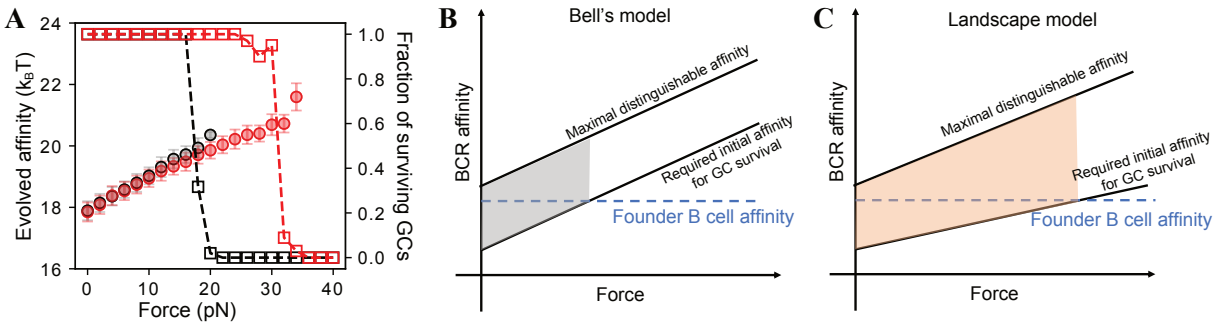

Figure 3.3: The effect of expansion of distinguishable affinity range. (A) Compare the evolution outcome between Bell's model and the microscopic landscape model. Red symbols are the same as Fig. 3.2C. The black symbols were based on the phenomenological Bell's model. (B) Schematic plots that explain the difference in (A). The shade labels the "reachable" affinity range, starting from the minimal B cell affinity that could avoid GC death to the maximal affinity that is "distinguishable" through antigen extraction, resembling Fig. 2.10 in CH2. The blue dotted lines are the founder B cell affinity used in simulations. GC dies if the founder B cell lies below the shaded region. We can see the expansion of distinguishable affinity range improves the maximal achievable output affinity.

Specifically, in the microscopic landscape model, the evolved affinity extends to higher affinity values and the GC extinction begins at higher force magnitude. This is explained in Fig. 3.3B. The nonlinear stretching effect expands the distinguishable affinity range and facilitates survival of lower affinity clones. Therefore, even under a large force, the low-affinity founder B cells are able to survive initially and evolve into high affinity ones. These effects thus sustain adaptation and potentially support clonal diversity at once.

The importance of relative tether strength How do other parameters influence the evolution? To provide a simple and generic picture, we define the relative tether strength as,

$$s \equiv \frac{\tau_a}{\tau_{b0}}, \tag{3.8}$$

which is the APC-Ag lifetime τ_a under force F, scaled by the founder BCR-Ag lifetime τ_{b0} under force. Note that s depends on force F. The extraction chance becomes $\eta = \tau_b/(\tau_b + s\tau_{b0})$, where τ_b is the BCR-Ag lifetime under force. Thus, the tether strength essentially characterizes the reference affinity $\Delta G^{\ddagger}_{\text{ref}}$ in Eq. 3.1. For founder B cells, $\eta_0 = 1/(1+s)$. Therefore, B cells get fewer Ags when interacting with stronger tethers. This has been vividly shown in recent experiments done by Spillane and Tolar [33].

To further show the influence of tether strength on evolution, we systematically varied the tether bond length $x^{\ddagger}_a$ and the tugging force F, and measured the evolved BCR-Ag affinity (barrier height $\Delta G^{\ddagger}_b(t = t_f)$). Fig. 3.4 suggested a strong correlation between the relative tether strength and the evolution output, as well as the GC survival chance. Specifically, a stronger tether corresponds to higher output affinity yet a higher GC death risk. On the one hand, the output affinity increases with tether strength because high-affinity B cells can be distinguished when interacting with a strong tether. On the other hand, if the tether strength is too strong, all B cells fail to acquire enough antigens for surviving, leading to GC apoptosis.

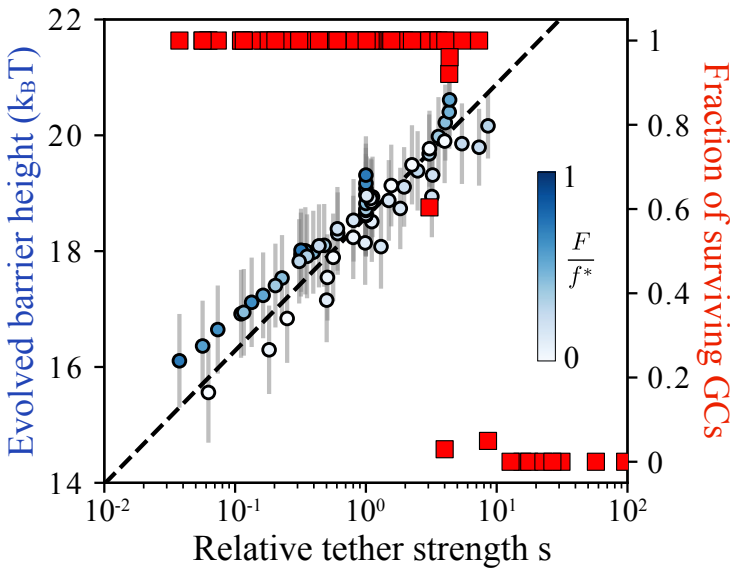

Figure 3.4: The relationship between the output affinity and relative tether strength. Symbols (blue circles) were obtained from GC simulations at different $x_a^\ddagger$ (from 0.5nm to 4nm) and under different F (from 0 to 30pN). Error bars were obtained from 100 GCs. Meanwhile, the GC survival percentage (red squares) quickly declines at high tether strength. The dashed line shows the prediction by Eq. 3.9

To make this intuition more qualitative, we estimate the output affinity $\Delta G_b^\ddagger$ by inverting the relation $\eta(\Delta G_b^\ddagger) = \eta_{\text{th}}$ to find the affinity that provides sufficient antigen extraction η_{th}. When activation barriers are high and forces are modest, we can approximate the relationship $\eta(\Delta G_b^\ddagger)$ using Bell's phenomenological expression $\eta(\Delta G_b^\ddagger) \approx \Big(1 + s\exp\Big(-(\Delta G_b^\ddagger - \Delta G_{b0}^\ddagger)/k_BT\Big)\Big)^{-1}$, then the output affinity can be solved analytically, which follows a logarithmic dependence on tether strength,

$$\Delta G_b^\ddagger \approx \Delta G_{b0}^\ddagger + k_BT\Big[\ln s + \ln\Big(\frac{\eta_{\text{th}}}{1-\eta_{\text{th}}}\Big)\Big]. \tag{3.9}$$

Recall that $\Delta G_{b0}^\ddagger$ is the founder affinity. As shown in Fig. 3.4, evolved affinities of simulated ensembles match the prediction (dashed line) over a wide range of tether strengths. Mild deviation raises when force is strong, which is due to a neglected effect in our estimation —

the considerable landscape deformation that causes a nonlinear reduction in the potential barrier by force, as we discussed in chapter 2.

3.2.2 The minimal model combined with antibody feedback

In the baseline model, we assumed that the tether remains unchanged during the evolution. This happens when antigens are directly loaded on receptors such as Fc receptors (FcRs) or complement receptors (CRs) [87]. Nevertheless, antibodies secreted by newly differentiated plasma cells, thus having improved affinities, may preferentially present antigens on the APC in the form of immune complexes [87, 73]. This is known as antibody feedback, that is, the secreted antibodies re-enter the GC in the form of immune complexes and act as tethers connecting antigens with APC [88, 73, 37]. Our tug-of-war configuration naturally supports the inter-generation feedback via antibodies. In this section, we demonstrate its influence on affinity maturation.

3.2.2.1 Model details

To simulate the antibody feedback effect, we draw the top-K high-affinity plasma cells (K=100) to form the feedback antibody pool. This captures the competition between secreted antibodies when binding to antigens. Then, at the antigen extraction step, each B cell will encounter a random tether sampled from the feedback antibody pool instead of a fixed tether. In other words, $\Delta G_a^\ddagger$ is sampled from the antibody feedback pool that is updated on the fly,

$$\Delta G_a^\ddagger \in \{\Delta G_{b1,\text{plasma}}^\ddagger, \Delta G_{b2,\text{plasma}}^\ddagger, \ldots, \Delta G_{bK,\text{plasma}}^\ddagger\}_t, \tag{3.10}$$

$\{\Delta G_{bj,\text{plasma}}^\ddagger\}$ is the list of top-K high affinity of plasma B cells. Note that the plasma B cell was generated in previous cycles and $\Delta G_{bj,\text{plasma}}^\ddagger$ is expected to improve over GC cycles. Consequently, as affinity maturation proceeds, the tether affinity improves at a similar pace.

It should be noted that we only updated the value of $\Delta G_a^\ddagger$ according to the feedback

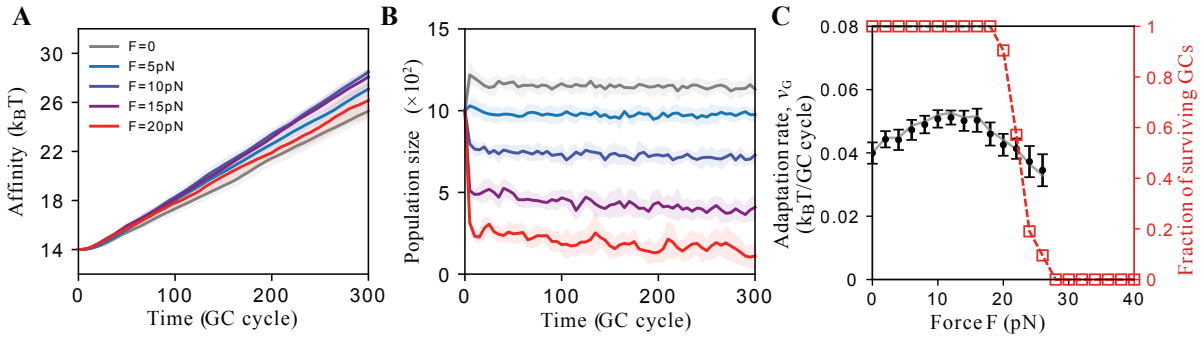

Figure 3.5: GC evolution with Ab feedback. (A-B) are similar to Fig. 3.2. (A) we plot the evolution of average affinity, under different forces. Note that an intermediate force gives the highest evolution rate. (B) The evolution of population size. (C) The adpatation rate as a function of the applied force, obtained by tracking the mean affinity improvement per cycle averaged from the last 200 GC cycles. Error bars are obtained from 100 GCs. The solid curve is the prediction given by Eq. 3.13. The red curve shows the surviving GC fraction at t=300 GC cycle.

antibody, while keeping $x_a^\ddagger$ fixed during the evolution. This is because the bond stiffness may be controlled by other components within the APC-Ag bond, such as the APC membrane. All other steps remain the same as the baseline model.

3.2.2.2 Results

Stabilized evolution As suggested by Fig. 3.5, antibody feedback introduces significant changes in the evolution dynamics. First, the affinity maturation did not slow down but achieved a steady rate (Fig. 3.5A), as opposed to the evolution against a fixed tether. This is because, as tether strength improves, it becomes harder for B cells to obtain Ags. Therefore, the saturation of Ag extraction is avoided so that the discrimination stringency maintains. Second, the population size stabilizes to a force-dependent level (Fig. 3.5B), reflecting that the population-averaged fitness $\overline{\eta}$ decreases with increasing pulling strength.

These observations are consistent with the recent work from Garg et al. [18]. They showed in an *in-silico* model that the evolved B cell affinity is improved after introducing high-affinity exogenous antibodies as presenting tethers, while the output B cell population is decreased, unraveling a quality-quantity trade-off that constrains the GC response. Here, we further show that if the quality of feedback antibodies improves continuously, a steady affinity maturation might emerge.

Adaptation rate To better appreciate the steady evolution, we seek for a quantitative understanding of the adaptation rate. As the updated tether antibodies provide negative feedback by continuously improving the Ag-APC affinity and impeding extraction, a steady selection pressure can be established; once η becomes steady, so does the fitness and the population size. The steady selection pressure and a steady population size constitutes the basis of mutation-selection balance [89]: random mutations broaden the fitness distribution while selection narrows it, creating a steady-state variance around an increasing mean fitness. Hence, the average affinity advances at a steady speed,

$$v_G \equiv \frac{\mathrm{d}\overline{\Delta G_b^\ddagger}}{\mathrm{d}t} \propto\!\!\!\approx \alpha \ln N. \tag{3.11}$$

Here $\overline{\Delta G_b^\ddagger}$ is the population-averaged affinity. The logarithm dependence on population size N comes from the interference between different clones: only the population at the "nose" of fitness distribution are essential to produce novel clones with higher fitness. α characterizes how sensitively fitness responds to affinity changes and thus governs selection strength, defined by

$$\alpha \equiv \frac{\mathrm{d}\lambda}{\mathrm{d}\Delta G_b^\ddagger} = \frac{\eta_0}{\eta(\eta_0+\eta)}\frac{\mathrm{d}\eta}{\mathrm{d}\Delta G_b^\ddagger} \approx \frac{1}{k_B T}\frac{\eta_0(1-\eta)}{\eta_0+\eta}. \tag{3.12}$$

Where $\eta_0 \equiv n_0/(C_a g A)$. In the second step, we assumed the affinity is high such that the dependence of MFPT on affinity is purely exponential $\tau_b \sim e^{\Delta G_b^\ddagger/k_B T}$ (note that $\eta = 1/(1+\tau_a/\tau_b)$ and τ_a is assumed to be independent of $\Delta G_b^\ddagger$ for simplicity). We can see α decreases with the extraction probability. Note that the proportional relationship is not

exact, since the adaptation rate may depend on other factors, such as multi-mutation effect [89].

A consistent understanding can be made based on the Price equation [90]. According to Price, the evolution rate is related to the covariance of fitness and the trait of interest. In our model, it states that

$$\langle v_G \rangle = \frac{\mathrm{d}\langle \overline{\Delta G_b^{\ddagger}} \rangle}{\mathrm{d}t} = \langle \frac{1}{\bar{\lambda}} \mathrm{Cov}(\Delta G_b^{\ddagger}, \lambda) \rangle \approx \langle \alpha(\overline{\Delta G_b^{\ddagger}}) \mathrm{Var}(\Delta G_b^{\ddagger}) \rangle, \tag{3.13}$$

where overbars denote population mean and angular brackets stand for ensemble average. Covariance and variance are taken with respect to one population. The second relation holds since fitness varies mildly over the affinity distribution across a population. Consistently, we can see the adaptation rate is controlled by the discrimination stringency α and the population diversity $\mathrm{Var}(\Delta G_b^{\ddagger})$.

Notably, the adaptation rate v_G exhibits a non-monotonic dependence on force magnitude, peaked around F = 10-20pN (Fig. 3.5). This can be understood from the mutation-selection balance picture or the Price equation. As force increases, η decreases (we assumed $x_b^{\ddagger} > x_a^{\ddagger}$) hence the population size N or the affinity variance $\mathrm{Var}(\Delta G_b^{\ddagger})$ falls, while the selection strength α rises (see Eq. 3.12). In other words, stronger pulling first accelerates adaptation by enhancing the selection pressure, before it slows adaptation as affinity variance falls with shrinking population size. Different from the potential role of antibodies in ending GC reaction by masking antigen [73], our work suggests their alternative role as renewable tethers in maintaining the adaptation rate.

3.2.3 The minimal model combined with mutable bond length

In addition to the potential barrier height $\Delta G_b^{\ddagger}$, other physical properties of BCR may also evolve. For example, sequence coding for the framework region (FWR) of BCR may mutate to change the stiffness or rigidity of BCR, which has been shown to be beneficial in the development of broadly neutralizing antibodies [91, 92]. Meanwhile, in short-term evolution,

the mutation in the FWR seems to be inhibited since the distribution of mutations across the sequence coding for BCR is shown to be strongly nonuniform, with mutations more likely to occur in the complementarity-determining regions (CDRs) outside FWR[93]. Nevertheless, very few existing GC evolution models have looked at the evolution of molecular properties other than the binding affinity.

3.2.3.1 Model details

In this section, we allow mutations that change the entire binding potential, including $\Delta G_b^\ddagger$ and $x_b^\ddagger$. We assume the mutation that modifies $\Delta G_b^\ddagger$ and the mutation that changes $x_b^\ddagger$ take place independently. Specifically, in each division event, $\Delta G_b^\ddagger$ mutates at a chance of $p_{m,G_b} = 0.5$. And $x_b^\ddagger$ mutates at a chance of $p_{m,x_b} = 0.5$.

3.2.3.2 Results

Diverse evolving directions Fig. 3.6A demonstrates the evolution in the $x_b^\ddagger$-$\Delta G_b^\ddagger$ plane under different circumstances, which displays diverse evolving directions as the tether or force changes. Specifically, under vanishing tugging force, evolution soften BCRs by selecting B cells with large $x_b^\ddagger$. This is because soft BCRs have relatively long intrinsic lifetime without force [38]. However, under a large force, the evolution drives the population towards the region with stiff BCRs, which experience smaller lifetime reduction by force and thereby are more favored, compared with soft BCRs. Besides, it should be noted that GCs at the opposite corners (large $x_a^\ddagger$ small F and small $x_a^\ddagger$ large F) experience high risk of collapse (survival percentage $< 20\%$), due to strong tethers.

Binding quality To compare output B cells directly, we define the binding quality Q as

$$Q \equiv \log_{10} \frac{\tilde{\tau}_b}{\tilde{\tau}_{b0}},$$

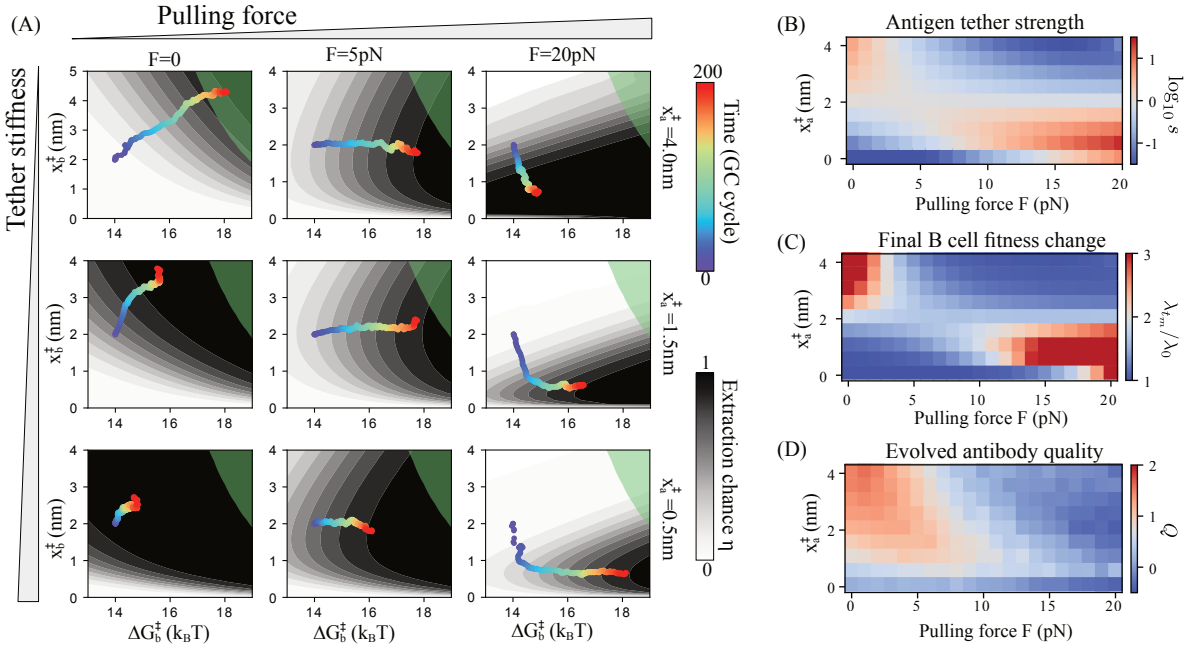

Figure 3.6: Evolution with mutable $x_b^\ddagger$. (A)Evolution trajectories in the $x_b^\ddagger$-$\Delta G_b^\ddagger$ plane under different forces and against different tethers. The contour map in gray indicates the Ag extraction chance η, which characterizes the fitness landscape. High-quality (high intrinsic bond lifetime, $Q > \log_{10} 50$) parameter region is colored in green. Simulated evolution trajectories are shown by the colorful lines. We can see force application modifies the fitness landscape and changes the evolution direction to favor stiff BCR bonds. (B) Tether strength as a function of force F and tether bond length $x_a^\ddagger$, obtained from MFPT calculation. When $x_a^\ddagger < x_b^\ddagger$, tether strength increases with force. In contrast, when $x_a^\ddagger > x_b^\ddagger$, force reduces the tether strength. (C) The dependence of evolved B cell fitness (at $t_f = 100$cycle) on pulling force and tether property. Each symbol is an average of 20 independent GC simulations. We can see the evolved B cell fitness follows the same trend as tether strength. (D) The binding quality of output BCRs(at $t_f = 100$cycle), Q. In the low-force regime, both the binding quality and B cell fitness are improved after evolution. In contrast, in the high-force regime, optimizing the B cell fitness conflicts with improving BCR binding quality. Parameters: $\Delta G_a^\ddagger = 14 k_B T$, $p_{m,Gb} = 0.5$, $p_{m,x_b} = 0.5$, initial condition: $\Delta G_{b0}^\ddagger = 14 k_B T$, $x_{b0}^\ddagger = 2$nm.

where $\tilde{\tau}_{b0}$ and $\tilde{\tau}_b$ are the intrinsic BCR lifetime at time 0 and output time t_f (we use the tilde notation $\tilde{\tau}$ to denote force-independent intrinsic lifetime), measured without force. This captures the lifetime of binding between the secreted antibody and the Ag, which happens in the absence of tugging force.

As shown in Fig. 3.6B-D, while a strong tether indeed leads to large enhancement of B cell fitness through GC reaction, the binding quality of BCRs is not necessarily optimized. In contrast to what have been observed in experiment, our simulation shows that a system with vanishing forces is favored to produce high binding quality BCRs (Fig. 3.6D), compared to cases with large forces. The reason behind is intuitive: the learning is effective only when the training environment (GC) is similar to the testing environment (plasma). Under a large tugging force, the fitness landscape becomes different from what underlies the binding quality (Fig. 3.6). Consequently, the learning is "misled". This implies an intriguing paradox that may be overlooked before, that is, when $x_b^\ddagger$ is allowed to mutate, the force application by B cells in the GC may conflict with the target of optimizing the intrinsic BCR lifetime.

There are several possibilities to reconcile the above paradox. First, this paradox highlights the importance of integrating different readout signals to make a decision. For example, it has been shown that BCR signaling and synapse formation are vital for B cell selection [31, 94, 95], which may depend strongly on the intrinsic BCR-Ag lifetime. In this way, clones with low quality BCRs are constantly removed from the population due to the low intrinsic signaling lifetime. Second, B cells might intentionally inhibit the evolution of BCR-Ag bond length. This is supported by the observation of mutation hot spots which mainly appear in the CDR but not the FWR [93]. In addition, the fitted value of $x_b^\ddagger$ obtained from different stages of evolution were shown to be similar [96]. This implies that GC evolution may focus on the mutations that are beneficial for both selection in GC and recognition of Ag outside the GC through modulating the mutation hot-spot. Third, the GC structure may be optimized for multiple tasks, such as enhancing the range of discrimination or enlarging the output binding breadth. These hypotheses can be tested by inducing the mutations that

change the BCR-Ag stiffness during a course of GC evolution.

3.2.4 The minimal model combined with heterogeneous forces

The diverse evolving direction motivates us to examine the change in B cell clone diversity when noise presents. What is the evolution dynamics if different B cell clones apply distinct forces? How does the evolved B cell diversity correlate with the randomness in force application?

Experimentally, people have observed that the diversity in affinity can persist for at least over a period of a few weeks during GC evolution, with B cells of widely disparate affinities co-existing within the same GC [80] or across the output B cells [97, 79]. In other words, GCs are capable of supporting the maturation of a diversity of clones in parallel without being taken by a high-affinity "winner". Such concurrence of selection and diversification is puzzling. It was believed to related to stochasticity in the probabilistic selection of B cells("intrinsic noise") [76] or the inheritable non-genetic heterogeneity across founder B cells ("extrinsic noise") [98].

To explore how the randomness in force plays a role, we simulated GC evolutions starting from B cells with diverse affinity, bond length and force magnitude. In particular, the force of each founder B cell is sampled from a uniform distribution between $(F_{\rm ave} - \sigma_{F0},\, F_{\rm ave} + \sigma_{F0})$. Here, σ_{F0} quantifies the initial force heterogeneity. We assume the force is inheritable, meaning daughter B cells use the same force as parent cells. Our model suggests that an intermediate heterogeneity in force application enhances the binding quality diversity. The diversification origins from the disparate evolution directions of B cells applying different forces. They can coexist because of the presence of a saddle point in the fitness landscape where selection pressure on $(F, x_b^\ddagger)$ pairs vanishes.

3.2.4.1 Model details

To model the heterogeneity, we assume the founder B cells are diverse in affinity, bond length and force. The initial affinity follows a Gaussian distribution, $N(\Delta G^{\ddagger}_{b0}, \sigma_{0,G_b})$ with $\Delta G^{\ddagger}_{b0} = 14k_BT$, and $\sigma_{0,G_b} = 0.2k_BT$. The bond length also follows a Gaussian distribution $N(x^{\ddagger}_{b0}, \sigma_{0,x_b})$. We used $x^{\ddagger}_{b0} = 2$nm, and $\sigma_{0,x_b} = 0.5$nm. The distribution of force is assumed to be uniform between $(F_{\text{ave}} - \sigma_{F0}, F_{\text{ave}} + \sigma_{F0})$. Using a truncated Gaussian distribution produces similar results (data not shown). We further assume the force is inheritable and immutable, meaning the daughter cells always apply the same force as the parent cell. Other settings are the same as the baseline model.

3.2.4.2 Results

Evolution dynamics We first examine the evolution dynamics under different force heterogeneity, σ_{F0}. As shown in Fig. 3.7, the fitness landscape in the $x^{\ddagger}_b$-F plane has multiple peaks: lineages with small force evolve towards large $x^{\ddagger}_b$ whereas lineages with large force evolve towards small $x^{\ddagger}_b$. At low σ_{F0}, the evolution follows the dynamics presented in Fig. 3.7A: the population evolves according to the fitness gradient and ends up with an unimodal distribution of bond length $x^{\ddagger}_b$ (Fig. 3.7B) around the optimal value, illustrated by the red line in Fig. 3.7A. In contrast, an intermediate force heterogeneity resulted in a bimodal distribution: B cells applying small forces develop large $x^{\ddagger}_b$, whereas B cells that use large forces are popularized at small $x^{\ddagger}_b$ (Fig. 3.7B). This is because different combination of parameters could result in similar Ag extraction chance and thereby B cell fitness, as indicated by the saddle point in the fitness landscape on $x^{\ddagger}_b$-F space (Fig. 3.7A). Therefore, B cells with distinct properties could co-exist, yet using different strategies to extract sufficient number of Ags and survive. In consequence, the evolved B cells display a broad range of binding quality but share similar fitness values (Fig. 3.7 C-D). Interestingly, at large σ_{F0}, the distribution becomes unimodal again, which is dominated by clones that apply vanishing

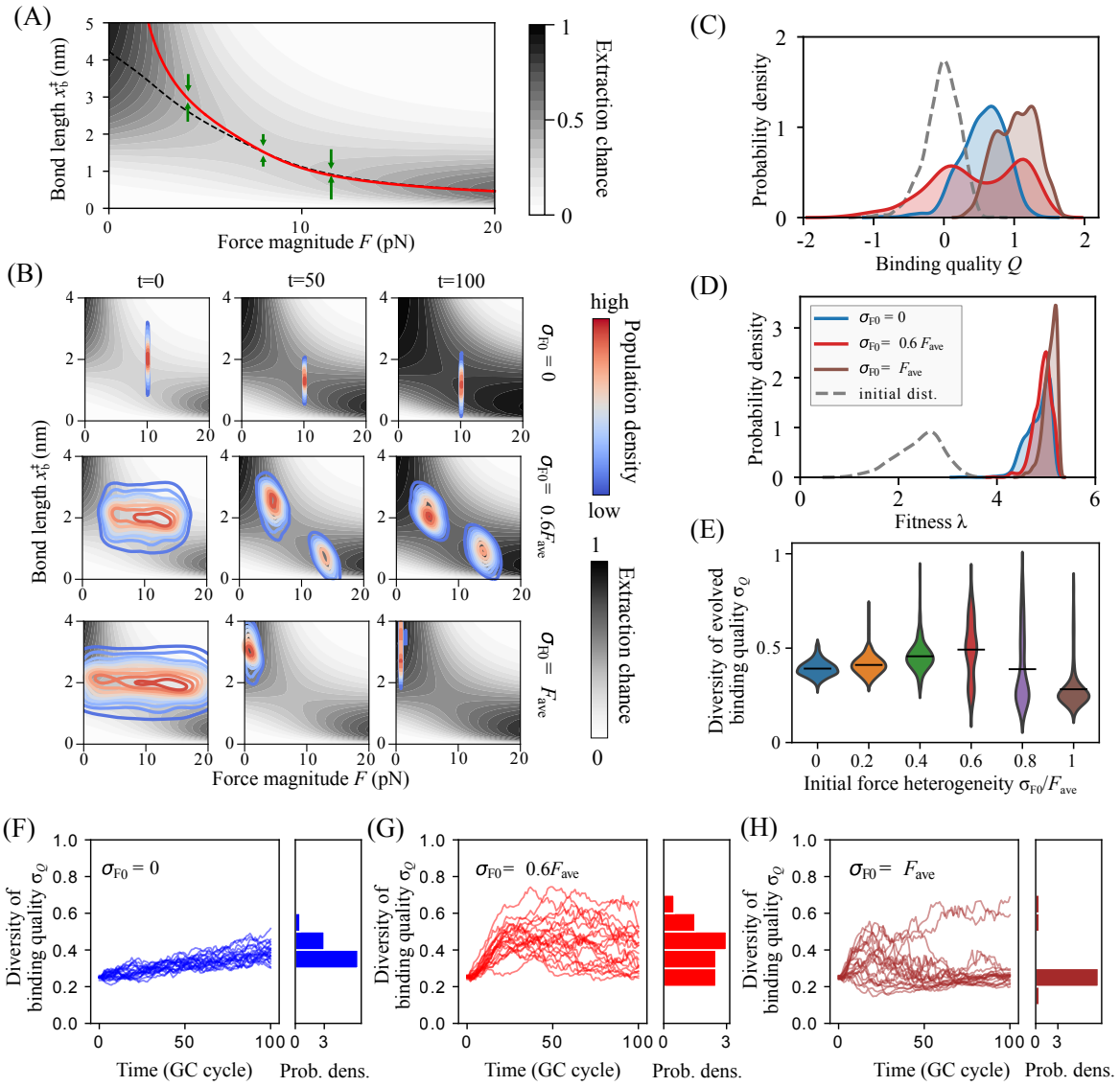
(A)
Bond length $x_b^\ddagger$ (nm)
Force magnitude F (pN)
Extraction chance
(B)
t=0
t=50
t=100
$\sigma_{F0} = 0$
$\sigma_{F0} = 0.6F_{ave}$
$\sigma_{F0} = F_{ave}$
Bond length $x_b^\ddagger$ (nm)
Force magnitude F (pN)
high
Population density
low
Extraction chance
(C)
Probability density
Binding quality Q
(D)
$\sigma_{F0} = 0$
$\sigma_{F0} = 0.6\,F_{ave}$
$\sigma_{F0} = F_{ave}$
initial dist.
Probability density
Fitness λ
(E)
Diversity of evolved binding quality σ_Q
Initial force heterogeneity σ_{F0}/F_{ave}
(F)
$\sigma_{F0} = 0$
Diversity of binding quality σ_Q
Time (GC cycle)
Prob. dens.
(G)
$\sigma_{F0} = 0.6F_{ave}$
Diversity of binding quality σ_Q
Time (GC cycle)
Prob. dens.
(H)
$\sigma_{F0} = F_{ave}$
Diversity of binding quality σ_Q
Time (GC cycle)
Prob. dens.

Figure 3.7: Intermediate heterogeneity in force maximizes diversity of binding quality. (A)Fitness landscape on F-$x_b^\ddagger$ space. The contour lines show the antigen extraction chance η (or effectively fitness) landscape. Green arrows show the gradient along the $x_b^\ddagger$ axis, indicating the evolution direction within lineages of the same force. The red dashed line represents the steady state of $x_b^\ddagger$ at different forces, where the gradient along $x_b^\ddagger$ vanishes. Note that it differs from the "ridgeline" (dashed black line) of local maxima along the principal direction corresponding to the negative curvature (see "height definition" by Eberly et al. [1]). (B) Examples of evolution on the F-$x_b^\ddagger$ space. Different rows represent individual realization of GC reactions starting from different initial force heterogeneity. Each column shows snapshots of fitness landscape (in gray) and population density (in colors) at a certain time point. Population-averaged $\Delta G_b^\ddagger$ was used to evaluate the η landscape at each time point. (C) Distribution of binding quality. Each colorful curve corresponds to one simulation result in (B) at $t = t_f$. The dashed line shows the initial distribution that was shared by all simulations. We can see, with intermediate force heterogeneity, the high-binding quality B cells and low-binding quality B cells coexist after evolution. (D) Distribution of B cell fitness λ. The black dashed line shows the initial fitness distribution for $\sigma_{F0} = 0$(the other two cases have similar initial distributions). Colorful lines are the evolved fitness distribution at $t = t_f$. (E) Violin plot of evolved binding quality diversity, characterized by the stdev of the binding quality distribution σ_Q. The black bars show the average value among 50 realizations. (F)Temporal trajectories of B cell binding quality diversity σ_Q at low force heterogeneity $\sigma_{F0} = 0$. Each trajectory represents one realization. The histogram on the right shows the distribution of diversity of evolved binding quality σ_Q at $t = t_f$. (G)Similar to (F) but at an intermediate force heterogeneity $\sigma_{F0} = 0.6F_{\text{ave}}$. (H)Similar to (F) but at a large force heterogeneity $\sigma_{F0} = F_{\text{ave}}$. Parameters: $x_a^\ddagger = 1.5$nm, $\Delta G_a^\ddagger = 14k_BT$, $F_{\text{ave}} = 10$pN, $p_{m,x_b} = 0.5$, $t_f = 100$ cycle. Initial condition: $x_{b0}^\ddagger = 2nm$, $\Delta G_{b0}^\ddagger = 14k_BT$. Initial diversity $\sigma_{0,G_b} = 0.2k_BT$, $\sigma_{0,x_b} = 0.5$nm. No antibody feedback.

forces or clones with large forces. This is due to a simple mechanism: with a large initial diversity, some founder B cells can be much fitter than others. Those better-fitted clones out compete other clones so that the system quickly loses force heterogeneity.

Saddle point The saddle point underlying the enhanced diversity is a general feature of the tug-of-war configuration of antigen extraction. To provide a simple and intuitive picture, we focus on the small force limit when the effect of force on MFPT mainly comes from the exponent factor. The extraction chance is

$$\eta \approx \frac{1}{1+\frac{\tilde{\tau}_a}{\tilde{\tau}_b}e^{-F(x_a^\ddagger - x_b^\ddagger)/k_BT}} = \frac{1}{1+e^{-F(x_a^\ddagger - x_b^\ddagger)/k_BT - \ln\frac{\tilde{\tau}_b}{\tilde{\tau}_a}}}.$$

Here $\tilde{\tau_a}$ and $\tilde{\tau}_b$ are intrinsic APC-Ag lifetime and BCR-Ag lifetime, independent of force F. The above equation suggests there are two factors influencing the extraction chance: the intrinsic bond lifetime ratio and the external force, which have the opposite dependence on $x_b^\ddagger$. Specifically, the intrinsic lifetime part $\left(\ln\frac{\tilde{\tau}_b}{\tilde{\tau}_a}\right)$ increases with $x_b^\ddagger$ due to an increased relaxation timescale τ_{bs} for flatter potential according to the Kramers theory [39, 38] (see chapter 2), while the external force part $F(x_a^\ddagger - x_b^\ddagger)$ decreases with $x_b^\ddagger$ because of greater barrier reduction. Such opposite effects underlie the saddle point that appears when the sign of dependence flips. To show the condition for saddle point explicitly, we conduct detailed calculations below. Since there is only one extremum point on the landscape, the saddle point is simply given by the following two conditions,

$$\frac{\partial \eta}{\partial F} = 0, \tag{3.14a}$$

$$\frac{\partial \eta}{\partial x_b^\ddagger} = 0. \tag{3.14b}$$

Plugging in Eq. 3.2.4.2, we get

$$x_{b,\text{saddle}}^\ddagger = x_a^\ddagger, \tag{3.15a}$$

$$F_{\text{saddle}} = k_BT\frac{\partial \ln \tilde{\tau}_b/\tilde{\tau_a}}{\partial x_b^\ddagger} = \frac{2k_BT}{x_a^\ddagger}(-\kappa_b)\frac{\partial \ln(\tilde{\tau}_b/\tilde{\tau_a})}{\partial \kappa_b}. \tag{3.15b}$$

To confirm that the above solution represents a saddle point, we calculated the product of principle curvatures near the solution. Explicitly, it is equal to $\det(H_{\text{saddle}}) = -\frac{1}{(k_BT)^2}\frac{(\tilde{\tau}_a\tilde{\tau}_b)^2}{(\tilde{\tau}_a+\tilde{\tau}_b)^4} < 0$, suggesting that the principle curvatures have opposite sign and thereby the above solution is indeed a saddle point. Here H_{saddle} is the Hessian matrix at the saddle point.

Therefore, the saddle point appears when tether bond length and BCR-Ag bond length are comparable. In addition, it requires an intermediate force such that when $x_b^\ddagger$ varies, the change in force effect compensates the change in intrinsic lifetime. To provide more quantitative understanding, we assume $\Delta G_b^\ddagger = \Delta G_a^\ddagger$ so that $\kappa_b = \kappa_a$ at the saddle point. This gives $F_{\text{saddle}} \approx 2k_BT/x_a^\ddagger$. Plugging in parameters used, $x_{b,\text{saddle}}^\ddagger = 1.5\text{nm}$, $F_{\text{saddle}} \approx 5.3\text{pN}$, which roughly agree with Fig. 3.7 ($x_{b,\text{saddle}}^\ddagger = 1.5\text{nm}$, $F_{\text{saddle}} \approx 8.1\text{pN}$). In addition, F_{saddle} is small enough compared to $f_a = f_b = 56.3\text{pN}$ to allow us to use the small-force approximation.

Binding quality diversity To better appreciate the enhanced diversity in binding quality at intermediate σ_{F0}, we quantified the diversity using σ_Q, the standard deviation of binding quality distribution. Consistent with Fig. 3.7B, σ_Q on average shows a non-monotonic dependence on the initial force heterogeneity σ_{F0} (Fig. 3.7E). It should be noted that the qualitative results do not rely on a particular choice of the diversity measure. For example, using the Shannon entropy gives the same trend of dependence.

In addition, at a given force heterogeneity, there are large variations between different realizations (see Fig. 3.7E). In some cases, the system quickly loses clone diversity (Fig. 3.7F-H) and the population is narrowly distributed on $x_b^\ddagger - \Delta G_b^\ddagger$ plane. In other cases, the bimodal distribution can persist for a long time. This is due to the intrinsic stochasticity of the probabilistic mutation and selection in GC evolution. The population converges to an unimodal distribution when some B cells in one of the branch become much fitter than others. Consistent with this prediction, experiments have shown that GCs lose clonal diversity at widely disparate rates: some become heavily dominated by few clones in days, while others

maintain high diversity for several weeks [80].

3.3 Discussion

Over the past decades, fundamental breakthroughs in experiments make it promising to appreciate the fundamental principle governing GC evolutions. On the one hand, high-resolution imaging technology helps to reveal the microenvironment and cellular dynamics of GC reactions. On the other hand, the advance of sequencing technology allows us to directly read the evolution of BCR during the course of GC reaction. What remains unclear is how those two ends of observations are connected. Specifically, how does the specialized GC structure benefit the affinity maturation process? What are the key components that we should look at? What are feasible mechanisms that one can utilize to further optimize the GC evolution during vaccination or infection?

To tackle the above intriguing and critical questions, we developed a multiscale model that integrated the start-of-art knowledge of GC, including the molecular Ag extraction process and the cellular dynamics. Our model allowed us to investigate how the regulations at the molecular level propagate to the evolutionary dynamics and determine the learning outcome. Specifically, we looked at the regulation through the property of presenting tethers and the tugging forces from B cells, which can be constant or dynamical or even heterogeneous. Our results demonstrated how those key components influenced the fitness, binding quality and diversity of output B cells.

Population dynamics Our model predicts different population dynamics given different assumptions. If the relative tether strength is fixed, the population will either collapse or evolve towards its maximal capacity (Fig. 3.2), depending on the relative tether strength compared with the initial B cell affinity. If the tether affinity changes at the same rate as BCR affinity due to antibody feedback, the population size may reach a force-dependent steady

state (Fig. 3.5) due to the mutation-selection balance. In contrast, if the changing speed in tether strength and BCR-Ag bond strength are not synchronized, we expect a gradual shift of the population size. For instance, if the pulling force is dynamic, stronger binding to antigen results in larger rupture force (see chapter 2). As BCR affinity improves during the evolution, the rupture force changes and so does the tether strength. Consequently, the population size changes accordingly during a GC reaction.

Our predictions are consistent with experimental observations. For example, Yewdell et al. found that GC B cell population declined after initial expansion and stabilized and persisted for a long time (22 weeks) [99], which agrees with our model prediction in Fig. 3.5. It should be pointed out that, in an acute infection, however, GC volume gradually declines during the infection [99]. This is potentially due to clearance of pathogens and thereby a decrease in antigen access — a factor that has been excluded in our model. Furthermore, the GC collapse, an important feature that underlies the condition of optimal GC structure in our model, has been observed in experiments. Mayer et al. have shown that B cells are programmed to die unless they are rescued when receiving enough surviving signal from follicular-helper T cells [86]. Vinuesa et al. showed that GCs induced by non-processable antigens only last for 3 days before all GC B cells undergo apoptosis [100]. Consistent with this, measurement of GC volume distribution implies frequent and sudden collapses of GCs [101].

However, to the best of our knowledge, there is no direct observation of population bottleneck. One reason might be that existing studies measured the *ensemble* GC dynamics by sampling from different mice sacrificed at different time points, which might differ from individual GC kinetics. Indeed, the quantification of GC volume distribution from Wittenbrink et al. suggested that GC growth was nonsynchronized [101].

Critical role of tether strength An important insight from our model is the critical function of tether strength, which has been underestimated in most existing studies. Indeed,

a lot of experiments have shown that the tether strength or the mechanical property of presenting cells plays an important role in B cell activation, Ag extraction as well as affinity maturation. By modeling the tug-of-war process explicitly, we demonstrate that the tether property governs when the discrimination stringency disappears and determines the ceiling affinity. This is consistent with recent study of passive immunization with external antibodies [18]. More importantly, we show that the tether strength is tunable from the B cell end, which appreciates the application of tugging force in a simple picture. Finally, the antibody feedback mechanism naturally imposes a time-dependent tether strength, which helps the system to avoid the issue of vanishing discrimination stringency.

Beneficial impact of mechanical force In addition, the mechanical force applied from B cells seems to be important in tuning the tether strength, influencing the evolution direction and generating B cell diversity. All those effects are done by regulating the Ag extraction process. Specifically, forces enhance Ag extraction when $x_a^\ddagger > x_b^\ddagger$ while inhibit Ag extraction if $x_a^\ddagger < x_b^\ddagger$. Consequently, the interplay between force and the environment determines the fitness landscape that underlies the B cell selection (Fig. 3.6). This suggests that our immune system needs to coordinate different components to facilitate the affinity maturation and satisfy the functional needs. Furthermore, our study suggested that a heterogeneous force can be beneficial in terms of producing B cells with diverse binding qualities. In fact, low-affinity output B cells have been frequently observed in experiments in healthy GCs. Our model provides one possibility to appreciate such unexpected results.

CHAPTER 4

Information acquisition in immune sensing through antigen extraction

"Focusing on information flow will help us to understand better how cells and organisms work."

Paul Nurse

4.1 Introduction

Biology background In the previous chapters, we focused on the chance of antigen extraction. This essentially ignores the demographic noise and assumes the number of antigens available is infinity. However, the process of antigen extraction is noisy in nature, due to the finite number of ligands, heterogeneity in molecular concentration, or random contact between ligands and receptors. How is it possible for a B cell to read the receptor affinity accurately from the noisy thermodynamic process? What is the fundamental physical limit of discrimination accuracy? How do B cells approach this optimal bound using biochemical solutions? These questions relate to a central question in physics: Given a system described by a set of parameters, how much information about the physical system can be obtained by observing some measurable quantities? This motivates us to apply the information theory to study B cell affinity discrimination.

It has been discovered that a single cell can sense and process external chemical signals with extremely high accuracy. For example, *Escherichia coli* can detect attractant aspartate as low as 3 particles in the volume of the cell [102]. In immunology, T cell detection of agonists (foreign antigens) on APCs is remarkably sensitive and selective: 1 to 10 agonists with binding half-lives only three times longer than thousands of weakly binding ligands can lead to activation but not the latter ones [103, 104, 105]. For B cells, affinity maturation is effective despite all uncertainty of B cell mutation, antigen presentation, and antigen acquisition [80]. These observations raise the question of how close cells operate to the fundamental physical limit of sensing or discrimination accuracy set by the underlying thermodynamic process?

Information theory of ligand detection Information theory has been a powerful tool to address such questions. Early studies focused on the task of ligand detection. In their pioneering work, Berg and Purcell derived the fundamental bound on the accuracy of ligand concentration sensing [106]. They considered that the time correlations of particles bound to receptors and found the minimal estimation error (variance) $\langle(\delta c)^2\rangle$ can be given by the Berg-Purcell limit,

$$\frac{\langle(\delta c)^2\rangle}{c_0^2} = \frac{1}{2Dac_0(1-\bar{p})T}, \tag{4.1}$$

where D is the diffusion coefficient, a is the effective receptor size, $\bar{p}$ is the equilibrium probability for receptor to be bound. Later, Endres and Wingreen re-investigated the problem using maximum likelihood estimation and discovered that the Berg-Purcell limit is closely related to the inverse of the Fisher information (Cramér-Rao bound) [21],

$$\frac{\langle(\delta c)^2\rangle}{c_0^2} = \frac{2}{c_0^2\mathcal{I}_c}. \tag{4.2}$$

Here, $\mathcal{I}_c = -\langle\frac{\mathrm{d}^2 \ln P(\{t_+,t_-\};c)}{\mathrm{d}c^2}\rangle_{c_0}$ is the Fisher information, where $P(\{t_+,t_-\};c)$ is the probability for a time series of binding and unbinding events (with timestamps $\{t_+,t_-\}$) to occur given the ligand concentration c, and the average is over the probability distribution of all binding events. Fisher information quantifies the effect of smooth parameter variations and

encodes the maximum amount of information that can be gained by measuring readouts. Therefore, the larger the information a thermodynamic process can generate, the smaller the sensing error.

This has fueled the interest in noise and its implications for information processing by cells. General or refined bounds on sensing accuracy have been extended to spatial or temporal gradient sensing[107, 108], amid spurious ligand sensing [22], while the trade-offs between metabolic cost, speed and sensing accuracy have been explored [109, 110]. Recently, there is a growing interest in understanding how the immune system works from the perspective of information theory [111, 112, 71, 113]. For instance, Ganti et al. quantified T cell discrimination capacity using channel capacity to show how affinity information was decoded by the topology and rates of kinetic proofreading signaling steps inside T cells [71].

The task of affinity discrimination Nevertheless, the task of B cell affinity discrimination is distinct from what have been studied about ligand detection. First, the quantity of interest is the binding quality of receptors instead of the concentration of antigen ligands. Second, it is not a simple binary discrimination as T cells'. Rather, mutations and selections continuously modify the B cell affinity distribution during affinity maturation. Therefore, the system has to work on a dynamic and wide spectrum of B cell affinities. Lastly, the cellular behavior of B cells is different from T cells'. In addition to ligand-receptor binding, B cells use mechanical force to extract and internalize the antigens. All these features make B cell affinity discrimination a unique task with many properties to be explored.

More specifically, recent progress in experiments has revealed many unexpected behaviors related to B cell affinity discrimination. A prevailing model for naïve B cell activation argues that B cells integrate antigen-dependent BCR signals and T cell-derived signals to make cell-fate decisions [25, 114, 115, 116]. The former one uses the binding lifetime of BCR and Ag clusters as readout of affinity [116, 23], whereas the latter one depends on the number of Ags captured by B cells [65, 36]. Interestingly, as opposed to this canonical affinity

discrimination picture, much experimental evidence suggests that the selection of GC B cells strongly depends on the Ag number but not the BCR signaling [117, 32, 6, 94, 95, 118]. For example, in contrast to naïve B cells who have significant downstream signaling after BCR Ag binding, most highly proliferative GC B cells undergoing Ag-driven selection cannot execute BCR signaling [117]. Besides, BCR antigen binding is shown to be insufficient to promote GC B cell selection, whereas T cell help is able to rescue B cells lacking BCR Ag binding and promote the selection [65, 118]. Those observations indicate that the affinity discrimination process in GC might be optimized by preferring one type of signal over the other.

It is puzzling that why these transitions are necessary and important. It has been postulated that the transition may serve to shift the dynamic range such that competing clones of relatively high affinity can more easily be distinguished [119]. Yet, the underlying physical mechanism remains illusive.

Information theory of B cell affinity discrimination Here we use the information theory to study how the affinity discrimination is made possible from the stochastic, non-equilibrium and collective antigen acquisition process, and understand what underlies the unexpected behavior of GC B cells. Our model incorporates the vital components of antigen extraction process, such as the tug-of-war structure and mechanical pulling force. We compare two readouts of BCR affinity, the cluster lifetime τ (τ-discriminator) and the acquired antigen number n_{ag} (n-discriminator), by quantifying their sensitivity to affinity change using the Fisher information (FI). Our results show both readouts can be used for affinity discrimination, but fit to different affinity regimes. As BCR affinity increases, the affinity information in cluster lifetime diminishes due to the breaking of the weak tether bonds and is outperformed by the affinity information in n_{ag} when BCR-Ag lifetime exceeds the APC-Ag bond lifetime. In addition, our model suggests that mechanical forces are able to couple bonds within a cluster and improve information extraction in both readouts.

Our results provide a profound understanding of a series of observations of GC B cell behavior in recent experiments. All the changes happening in GC B cells seem to serve a unified purpose: making the competing B cells of high affinity more distinguishable. As BCR affinity improves, readouts inevitably saturate when BCR affinity is much higher than the tether affinity. Additionally, the thermal noise in ligand receptor reactions corrupts discrimination. To distinguish high-affinity B cells, the switch of focus and the application of large forces help to suppress the noise effect and enhance discrimination fidelity.

The chapter is structured as follows. In section 4.2 we define the antigen extraction model, introduce different affinity readouts, and quantify the discrimination performance. In section 4.3.1 we present our calculation of readout distributions. In section 4.3.2 calculate Fisher information and compare different readouts in several scenarios, including independent extraction (no force-sharing, no rebinding, section 4.3.2.1), extraction of coupled ligands (with force-sharing, no rebinding, section 4.3.2.2), and extraction under rebinding (with rebinding, section 4.3.2.3). We conclude with a discussion in section 4.4.

4.2 Model

Antigen extraction by force We consider the extraction of multiple antigens. In chapter 2 we studied the extraction of a single antigen. Now let us consider a cluster of m_0 APC-Ag-BCR complexes, all of which are initially closed and undergo rupture or rebinding according to appropriate rates after force application (Fig. 4.1). For each complex, the rupture can happen in either the APC-Ag or Ag-BCR bond, respectively, with off rate k_a and k_b [18]. Meanwhile, the broken bonds can rebind and form a complex again with a diffusion-limited rate k_{on}. Thus, four types of reactions can happen including the breaking of APC-Ag bond, the breaking of BCR-Ag bond, the binding of BCR and Ag, and the rebinding between APC and Ag.

The state of the system at time t is described by the probability $P_{m,n}(t)$ to have a cluster

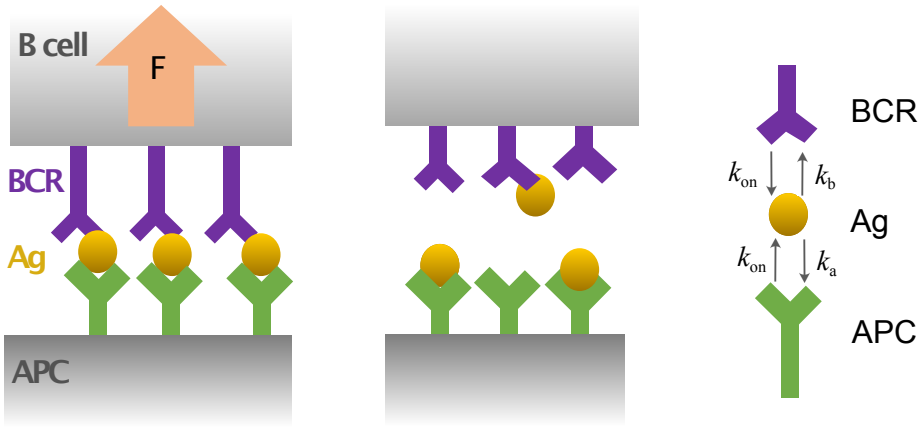

Figure 4.1: Schematic plot of the antigen extraction process. B cell uses force to extract antigens (Ags) that are tethered on the surface of antigen presenting cell (APC). Pulling forces are uniformly shared by all closed bonds. Each bond may break at either binding interface, leading to failed or successful antigen extraction. There are four kinds of reactions involved in this process: BCR-Ag unbinding, APC-Ag unbinding, BCR Ag binding, and APC Ag binding, respectively with rate k_b, k_a, k_{on} and k_{on}.

of size m (the number of APC-Ag-BCR complexes) and n antigen extraction (the number of Ag-BCR bonds). Assuming each reaction is a discrete Markov jump process, we can describe the ensemble dynamics of the system via a master equation [120]

$$\frac{\mathrm{d}P_{m,n}(t)}{\mathrm{d}t} = W_{m,n}P_{m,n}(t), \tag{4.3}$$

where

$$W_{m,n} = (\xi^{1,-1}-1)mk_a(m) + (\xi^{1,0}-1)mk_b(m) + (\xi^{-1,0}-1)(m_0-m-n)k_{\mathrm{on}} + (\xi^{-1,1}-1)nk_{\mathrm{on}} \tag{4.4}$$

is an operator matrix. Here $\xi^{i,j}$ is the step operator, $\xi^{i,j}G(x,y) = G(x+i,y+j)$ for an arbitrary function $G(x,y)$. Each term on the right-hand side describes one of the four reactions considered. The off-rates may depend on the cluster size m. When all complexes break ($m=0$), the antigen extraction process finishes and the B cell detaches from the APC.

To connect the off-rates with bonds affinity and pulling force, we use Bell's phenomenological expression [15]

$$k_a(m) = k_0 e^{-(\Delta G_a^{\ddagger} - f(m)x_a^{\ddagger})/k_{\mathrm{B}}T}, \quad k_b(m) = k_0 e^{-(\Delta G_b^{\ddagger} - f(m)x_b^{\ddagger})/k_{\mathrm{B}}T}, \tag{4.5}$$

where $\Delta G_a^{\ddagger}$ and $\Delta G_b^{\ddagger}$ are respectively the binding affinity of APC-Ag bond and BCR-Ag bond. k_{B} is the Boltzmann constant and T is the temperature. We assume the applied force is shared by all complexes in the cluster. Thus, the force per individual bond $f(m) = F/m$, depending on the total force F and the cluster size m. If $F=0$, then different complexes break independently with constant off-rates. In contrast, if $F>0$, then complexes within the cluster are coupled together through force-sharing. We will discuss the effect of force-sharing in detail in section 4.3.2.2. k_0 characterizes other factors influencing both bonds. $x_a^{\ddagger}$ and $x_b^{\ddagger}$ are respectively the minimal-to-barrier distances within the interacting potential of APC-Ag bond and BCR-Ag bond, effectively characterizing the bond stiffness (see chapter 2). In this section, we assume APC-Ag bond to be softer than BCR-Ag bond ($x_a^{\ddagger} < x_b^{\ddagger}$). Examples of simulated trajectories of (m,n) are shown in Fig. 4.2.

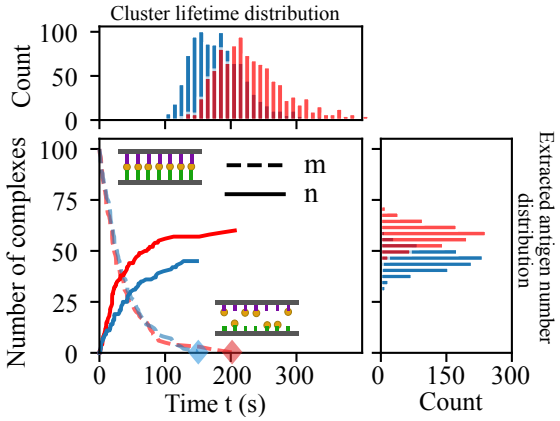

Figure 4.2: The extraction trajectory and readouts differ as BCR affinity changes and thereby are informative about BCR affinity. We plot the cluster size $m(t)$ (dashed lines) and the number of antigen extracted $n(t)$ (solid lines) trajectories obtained from simulations. Red for the high affinity B cell ($\Delta G_b^\ddagger = 9.5 k_\mathrm{B}T$) and blue for the low affinity B cell ($\Delta G_b^\ddagger = 9 k_\mathrm{B}T$). The diamond symbols mark the time points when the clusters break. The histograms show distribution of cluster lifetime (top) and extracted antigen number (right) from 1000 independent runs. Parameter used: $m_0 = 100, f = 10\mathrm{pN}$, $\Delta G_a^\ddagger = 8 k_\mathrm{B}T$, $x_a^\ddagger = 1.5\mathrm{nm}$, $x_b^\ddagger = 2.0\mathrm{nm}$, $k_\mathrm{on} = 0$. Independent extraction.

In principle, one should use Kramers theory to describe the relationship between off-rates and applied force. However, as we discussed in chapter 2, the Bell's formula gives the simplest description and captures the leading order effect of force on off-rates when force is weak. Besides, our main conclusion stems from the tug-of-war nature of antigen extraction process and thereby still holds if one uses more realistic description of reaction rates.

Readouts of binding affinity To achieve affinity discrimination, B cells need to infer the underlying BCR affinity by measuring some "readouts" generated by the above thermodynamic process that are measurable using internal signaling circuits.

Motivated by experimental observations, we consider two particular affinity readouts, the cluster lifetime τ (τ-discriminator) and the number of extracted antigens n_ag in the end

(n-discriminator) (see Fig. 4.2). The former one is supported by recent experiments showing B cells actively generated traction force to test the bond strength [2, 23]. The invagination lifetime is measurable through force-induced receptor conformation change and downstream signaling [121]. The latter readout determines how much help a B cell can gain from T-helper cells and displays direct correlation with B cell survival and proliferation [36]. Those two readouts correspond to the conventional 2-signal model for B cell activation [122, 116]. The distribution of affinity readouts can be solved analytically in some special cases or obtained numerically by propagating the master equation starting from the initial condition $P_{m,n}(0) = \delta_{m,m_0}\delta_{n,0}$.

Quantification of discrimination performance To quantify how well B cells with different affinities are discriminated based on certain readout, we introduce Fisher information (FI). The classical way of measuring the discrimination performance used the ratio of the mean readouts of different cells [123]. As suggested by a diverse literature, a more reasonable way is to look at how sensitive the *entire* readout distribution to the change in affinity [124, 113]. In this sense, one can consider FI to describe such sensitivity. For readout type Y, the FI in its distribution $P_Y(\mathbf{y}; \Delta G_b^\ddagger)$ with respect to B cell affinity $\Delta G_b^\ddagger$ is defined mathematically as follows [125]:

$$\mathcal{I}_Y = \int \Big(\frac{\mathrm{d} \ln P_Y(\mathbf{y}; \Delta G_b^\ddagger)}{\mathrm{d}\Delta G_b^\ddagger}\Big)^2 P(\mathbf{y}; \Delta G_b^\ddagger) d\mathbf{y}. \tag{4.6}$$

FI measures how much information the readout contains about the underlying B cell affinity. If the readout distribution does not depend on the affinity, the associated FI is zero and no information about BCR affinity can be gained from a measurement of Y. On the other hand, if a small variation of the affinity leads to a large change in the readout distribution, then the FI is large and a B cell can make precise estimate of the BCR affinity. This is because, according to the Cramer-Rao inequality [126], the inverse of the Fisher information is a lower bound on the variance of any unbiased estimator of the underlying

parameter $\Delta G_b^\ddagger$. Specifically,

$$\sigma^2_{\Delta G_b^\ddagger} \geq \frac{1}{\mathcal{I}_Y}, \tag{4.7}$$

where $\sigma_{\Delta G_b^\ddagger}$ is the inference error of any unbiased estimator.

The choice of FI is further motivated by the fact that it is closely related to the discrimination power. To show this, we define the selection fidelity ξ_Y, namely the probability to rank an advantageously mutated B cell (with affinity $\Delta G_b^\ddagger + \epsilon$) higher than its low-affinity competitor (with affinity $\Delta G_b^\ddagger$) by observing the readout Y. Explicitly,

$$\xi_Y \equiv \int dy P_Y(y; \Delta G_b^\ddagger + \epsilon) \int_{y'<y} dy' P_Y(y'; \Delta G_b^\ddagger). \tag{4.8}$$

We demonstrate that in the hard-discrimination regime $\epsilon \ll 1$, there is a universal upper bound of ξ for any readout distribution (see Appendix)

$$\xi_Y \leq \mu_{\rm CDF} + \sigma_{\rm CDF}\sqrt{I_Y}\epsilon + o(\epsilon^2), \tag{4.9}$$

where $\mu_{\rm cdf}$ and $\sigma^2_{\rm cdf}$ are respectively the mean and variance of the cumulative distribution function of readout Y, respectively. For a continuous distribution, $\mu_{\rm cdf} = 1/2$, $\sigma^2_{\rm cdf} = 1/12$. For a discrete distribution, $\mu_{\rm cdf} \to 1/2$, $\sigma^2_{\rm cdf} \to 1/12$ as the number of possible states increases. This relationship is reminiscent of the universal connection between information and the fundamental physical limit of decision accuracy based on thermodynamic processes [21].

We are aware of other evaluation metrics such as Kullback–Leibler (KL) divergence may be alternative choices to quantify the sensitivity of a distribution, but we prefer to stay on FI because it is easy to evaluate and can provide analytical understandings. Besides, our calculations suggest that using other metrics (such as KL divergence) does not change our main conclusion.

4.3 Results

4.3.1 Readout distributions

Before discussing the Fisher information associated with any readout Y, we need to obtain its distribution for a given BCR affinity, $P_Y(y;\Delta G_b^\ddagger)$. In this section, we present our calculation for the distribution of cluster lifetime and extracted antigen number. In addition, since the cluster dissociation trajectory encodes the full information generated by the antigen extraction process, we will calculate the distribution of dissociation trajectory in some simple cases.

Cluster lifetime distribution To access the distribution of cluster lifetime, we look at the dynamics of cluster size m. At any time t, the probability distribution of cluster size is

$$P_m(t) \equiv \sum_{m=0}^{m_0-m} P_{m,n}(t). \tag{4.10}$$

Then for a fixed m, summing over all n-states in Eq. 4.3 gives the master equation for m, which reads as the following one-step birth-death process,

$$\dot{P}_m(t) = \mathcal{A}_m^{(f)} P_m(t) = [(\xi^1 - 1)r_m + (\xi^{-1} - 1)g_m]P_m(t), \tag{4.11}$$

where $\mathcal{A}_m^{(f)}$ is the operator. The superscript $^{(f)}$ indicates that it is a forward master equation. The reverse and forward rates are

$$r_m = (k_a(m) + k_b(m))m, \quad g_m = k_{\text{on}}(m_0 - m). \tag{4.12}$$

Note at the absorbing boundary $g_0 = 0$. Then our cluster lifetime can be expressed in the form of first passage time distribution

$$P_\tau(t) \equiv -\frac{\mathrm{d}}{\mathrm{d}t}\sum_{m=1}^{m_0} P_m(t). \tag{4.13}$$

Here $\sum_{m=1}^{m_0} P_m(t)$ is the survival probability. In principle, one can solve the master equation Eq. 4.11 and use the definition to calculate the cluster lifetime distribution. However, the

analytical solution becomes infeasible when m_0 is large, since the computation complexity of solving differential equations explodes with m_0

Alternatively, the first passage time distribution can be calculated using the backward formalism of Eq. 4.11. The backward master equation describes the first step out of the initial state $m = m_i$ at time t_i, rather than the last step of the trajectory leading to the current state m at time t [127]. This feature makes it especially useful in the context of first passage problems where the ending state is fixed. It can be shown the first passage time follows the backward master equation [127],

$$\frac{\mathrm{d}P_\tau(t|m_i)}{\mathrm{d}t} = \mathcal{A}^{(b)}_{m_i} P_\tau(t|m_i) = \left[r_{m_i}(\xi^{-1} - 1) + g_{m_i}(\xi^1 - 1)\right] P_\tau(t|m_i). \tag{4.14}$$

where $P_\tau(t|m_i)$ is the first passage time distribution starting from the state $m = m_i$ at $t = 0$. $\mathcal{A}^{(b)}_{m_i}$ is the backward operator acting on m_i (i.e., $\xi^{\pm 1} P_\tau(t|m_i) = P_\tau(t|m_i \pm 1)$). Note $P_\tau(t|0) = \delta(t)$. We are interested in $P_\tau(t|m_0)$, the first passage time distribution starting from all bound state $m_i = m_0$. Although solving the backward equation is not necessarily easier than solving the forward master equation of Eq. 4.11, it provides an easy way of calculating the moments of first passage time, as we show below.

To get more insights about the cluster lifetime, we calculate the mean cluster lifetime $\overline{\tau}$ and its variance σ^2_τ analytically from Eq. 4.14. Define the q-th moment of first passage time starting from the state m_i as

$$\tau^{(q)}_{m_i} \equiv \int_0^\infty t^q P_\tau(t|m_i) dt. \tag{4.15}$$

Then applying the backward operator on both sides gives

$$\mathcal{A}^{(b)}_{m_i} \tau^{(q)}_{m_i} = -q\tau^{(q-1)}_{m_i}, \tag{4.16}$$

where we used the boundary condition $P_\tau(t = \infty|m_i) = 0$. Here m_i ranges from 1 to m_0. Explicitly, the first moment $\tau^{(1)}_{m_i}$ satisfies

$$r_{m_i}\tau^{(1)}_{m_i-1} + g_{m_i}\tau^{(1)}_{m_i+1} - (r_{m_i} + g_{m_i})\tau^{(1)}_{m_i} = -1. \tag{4.17}$$

Note we set $g_{m_0} = g_0 = 0$. Solving this using iterative method with condition $\tau_0^{(1)} = 0$ and $\tau_{m_0}^{(1)} - \tau_{m_0-1}^{(1)} = 1/r_{m_0}$, one gets [120, 128]

$$\tau_m^{(1)} = \sum_{i=1}^{m} \frac{1}{r_i} + \sum_{i=1}^{m} \sum_{j=i+1}^{m_0} \frac{1}{r_j} \frac{\prod_{k=i}^{j-1} g_k}{\prod_{k=i}^{j-1} r_k}. \tag{4.18}$$

Hence the mean cluster lifetime reads as

$$\overline{\tau} = \tau_{m_0}^{(1)} = \sum_{i=1}^{m_0} \frac{1}{r_i} + \sum_{i=1}^{m_0-1} \sum_{j=i+1}^{m_0} \frac{1}{r_j} \frac{\prod_{k=i}^{j-1} g_k}{\prod_{k=i}^{j-1} r_k}. \tag{4.19}$$

The first term in Eq. 4.19 is the result of vanishing rebinding $k_{on} = 0$, and the second term increases the lifetime as a polynomial of order $m_0 - 1$ in k_{on}. In addition, by Eq. 4.16 the second moment follows

$$r_{m_i} \tau_{m_i-1}^{(2)} + g_{m_i} \tau_{m_i+1}^{(2)} - (r_{m_i} + g_{m_i}) \tau_{m_i}^{(2)} = -2\tau_{m_i}^{(1)}. \tag{4.20}$$

Again, one can solve this with boundary condition $\tau_0^{(2)} = 0$ and $\tau_{m_0}^{(2)} - \tau_{m_0-1}^{(2)} = -2\tau_{m_0}^{(1)}/r_{m_0}$ to get

$$\tau_{m_0}^{(2)} = \sum_{i=1}^{m_0} \frac{2\tau_i^{(1)}}{r_i} + \sum_{i=1}^{m_0-1} \sum_{j=i+1}^{m_0} 2\tau_j^{(1)} \frac{\prod_{k=i}^{j-1} g_k}{\prod_{k=i}^{j} r_k}. \tag{4.21}$$

Then the variance is simply given by

$$\sigma_\tau^2 = \tau_{m_0}^{(2)} - (\tau_{m_0}^{(1)})^2. \tag{4.22}$$

Eq. 4.19 and Eq. 4.22 certainly provide a closed formula to calculate the mean cluster lifetime and its variance. We will use Eq. 4.19 and Eq. 4.22 to estimate Fisher information in the following sections.

In order to understand the cluster lifetime in a more transparent way, we look at how the rebinding plays a role. If the rebinding is negligible ($k_{\text{on}} = 0$), then

$$\overline{\tau} = \sum_{i=1}^{m_0} 1/r_i. \tag{4.23}$$

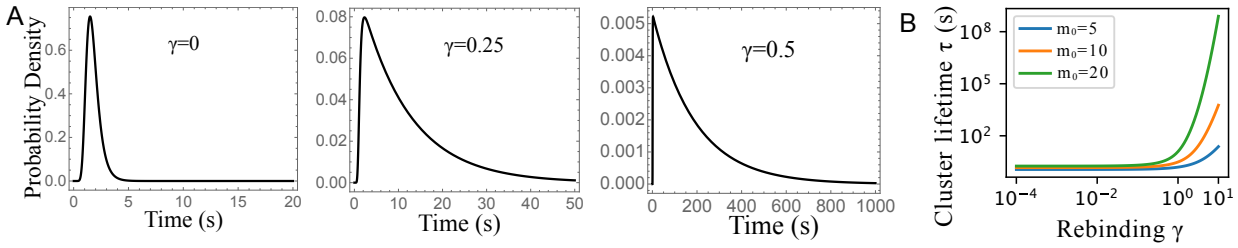

Figure 4.3: Rebinding increases mean cluster lifetime and changes the lifetime distribution to exponential-like. In A, we plot the lifetime distribution at different on-rates. Curves are obtained by solving the forward master equation numerically. In B we plot the average lifetime based on Eq. 4.19. Parameters: $m_0 = 20, k_b = k_a = 1s^{-1}, F = 0$.

Note that $1/r_i$ is the expected waiting time for $(m_0 - i)$-th reaction to take place after $(m_0 - i + 1)$-th reaction. So $\overline{\tau}$ is the sum of m_0 expected waiting times. This is because the m_0 complexes break sequentially. In contrast, the rebinding opens diverse pathways for cluster dissociation: Some broken bonds can close again and break later. Those additional pathways increase the expected cluster lifetime, as captured by the second term in Eq. 4.19. For simplicity, we assume the complexes are independent (no force application $F = 0$) so that the off-rates k_a and k_b are independent of cluster size. Then the product in Eq. 4.19 simply becomes Binomial coefficients. Combining two terms on the right-hand side of Eq. 4.19 together, we have

$$\overline{\tau} = \frac{1}{k_a + k_b} \sum_{i=1}^{m_0} \frac{\sum_{j=i}^{m_0} \binom{m_0}{j} \gamma^{j-i}}{\binom{m_0}{i} i} = \frac{1}{k_a + k_b} \sum_{i=1}^{m_0} \frac{(1+\gamma)^{i-1}}{i}. \tag{4.24}$$

Here $\gamma = k_{\text{on}}/(k_a + k_b)$ is the relative on rate. The second step can be proven by expanding the right-hand side and collecting terms according to the order of γ. We can see $\overline{\tau}$ is a polynomial of order $m_0 - 1$ in γ. When $\gamma < 1$, the cluster lifetime grows only weakly (logarithmic) with m_0. When $\gamma > 1$, the higher order term in γ takes over and the increase in τ with m_0 becomes exponential. This is demonstrated in Fig. 4.3: For a large cluster, increasing γ to values larger than unity leads to strong increase in lifetime. Besides, from Fig. 4.3, we can see at high rebinding rate, the lifetime distribution becomes exponential-like. In fact, one can

show the standard deviation σ_τ also has a polynomial order $m_0 - 1$ in γ. Thus, when $\gamma \gg 1$, we have $\sigma_\tau \approx \overline{\tau}$, which is a feature of the exponential distribution. Therefore, rebinding not only increases the mean cluster lifetime, but also makes the distribution exponential-like.

Extracted antigen number distribution Now let us turn to the extracted antigen number n_{ag}. The distribution of n_{ag} is the steady distribution of Eq. 4.3 at the absorbing boundary,

$$P_{n_{\text{ag}}}(n) \equiv P_{0,n}(t = \infty).$$

For a general reaction matrix $W_{m,n}$, we will show that instead of solving the differential equations in Eq. 4.3 directly, we can construct a set of linear equations to compute the steady distribution.

To obtain the steady distribution at the boundary, we integrate the master equation Eq. 4.3 over time, which gives

$$P_{m,n}(\infty) - P_{m,n}(0) = \int_0^\infty \dot{P}_{m,n}(t)dt = W_{m,n} \int_0^\infty P_{m,n}(t)dt. \tag{4.25}$$

Recall $W_{m,n}$ is the time-independent operator in the original master equation Eq. 4.3 and may change the indexes of quantities after it. The physical meaning of Eq. 4.25 is that the probability change in a state is given by the integrated net probability current into that state, which is determined by the time-integrated probability at adjacent states and the transition matrix, due to the Markovian property of our system. As a special example, at the absorbing boundary,

$$P_{0,n}(\infty) = k_{a1} \int_0^\infty P_{1,n-1}(t)dt + k_{b1} \int_0^\infty P_{1,n}(t)dt. \tag{4.26}$$

Hence, the stationary probability at boundary state $(0, n)$ is determined by the integrated probability at two adjacent states $(1, n-1)$ and $(1, n)$ that are directly connected to $(0, n)$. This motivates us to define the integrated probability at each transition state (m, n) over time, $Q_{m,n} \equiv \int_0^\infty P_{m,n}(t)dt$. For a given initial condition $P_{m,n}(0) = \delta_{m,m_0}\delta_{n,0}$ and known

stationary distribution at non-absorbing ($m > 0$) states $P_{m,n}(\infty) = 0$, Eq. 4.25 provides coupled linear equations about the integrated probability $Q_{m,n}$ at different non-absorbing states. Explicitly, at the bulk ($1 < m < m_0, 0 \leq n \leq m_0 - m$)

$$0 = (m+1)k_a(m+1)Q_{m+1,n-1} + (m+1)k_b(m+1)Q_{m+1,n} + k_{\text{on}}(n+1)Q_{m-1,n+1} + k_{\text{on}}(m_0 - m - n + 1)Q_{m-1,n} - (mk_a(m) + mk_b(m) + k_{\text{on}}(m_0 - m))Q_{m,n}, \quad (4.27a)$$

and at the edge cases

$$-1 = k_{\text{on}}Q_{m_0-1,1} + k_{\text{on}}Q_{m_0-1,0} - m_0(k_a(m_0) + k_b(m_0))Q_{m_0,0}, \quad (4.28a)$$

$$0 = 2k_a(2)Q_{2,n-1} + 2k_b(2)Q_{2,n} - (k_a(1) + k_b(1) + k_{\text{on}}(m_0 - 1))Q_{1,n}. \quad (4.28b)$$

The non-physical terms of $Q_{m,n}$ (i.e., $n < 0$, $m < 0$ or $n + m > m_0$) are set to be 0. There are totally $m_0(m_0 + 1)/2$ unknown variables of $Q_{m,n}$ ($m = 1, 2, ..., m_0$, $n = 0, 1, ..., m_0 - m$). Correspondingly, there are $m_0(m_0 + 1)/2$ coupled linear equations in Eq. 4.27 and Eq. 4.28. Therefore, for any general off rates $k_a(m)$ and $k_b(m)$, in principle one can obtain the distribution $P_{n_{\text{ag}}}(n)$ by solving the linear equations about $Q_{m,n}$ and get the stationary distribution at the absorbing boundary through

$$P_{n_{\text{ag}}}(n) = k_a(1)Q_{1,n-1} + k_b(1)Q_{1,n}, \quad n > 0 \quad (4.29a)$$

$$P_{n_{\text{ag}}}(0) = k_b(1)Q_{1,0}. \quad (4.29b)$$

By doing so, we convert the $m_0^2/2$ *ordinary differential equation* in Eq. 4.3 into $m_0^2/2$ *linear equations* in Eq. 4.27 that can be solved with much lower time complexity.

To get more intuition, we consider a simple scenario where the off-rates k_a and k_b are constant ($F = 0$). If k_{on}=0, then Eq. 4.27, Eq. 4.28 and Eq. 4.29 essentially become the recurrent formula for Binomial coefficients: $\binom{m_0-m}{n} = \binom{m_0-m-1}{n} + \binom{m_0-m-1}{n-1}$. We can easily get

$$P_{n_{\text{ag}}}(n) = \frac{k_a^n k_b^{m_0-n}}{(k_a + k_b)^{m_0}} \binom{m_0}{n}, \quad (4.30)$$

which is the Binomial distribution. This agrees with the intuition that antigen extraction is the Bernoulli process if the probability to get the antigen is the same at each rupture event. For non-zero $k_{\rm on}$, intuitively the rebinding should not change the distribution given that two binding interfaces have the same on-rate. In other words, closing and re-opening the complex do not change the chance to get that antigen. So $n_{\rm ag}$ still follows the Binomial distribution. This can be confirmed by plugging Eq. 4.30 back into Eq. 4.27-4.29 with non-vanishing $k_{\rm on}$.

The average antigen extraction $\langle n_{\rm ag}\rangle$ and its variance σ_n^2 can be obtained implicitly from $3m_0$ linear equations. We first define,

$$R_m^{(k)} \equiv \sum_{n=0}^{m_0} n^k Q_{m,n}. \tag{4.31}$$

Then

$$\begin{aligned}\langle n_{\rm ag}\rangle &\equiv \textstyle\sum_{n=1}^{m_0} nP_{n_{\rm ag}}(n) = k_{a,1}\sum_{n=1}^{m_0} nQ_{1,n-1} + k_{b,1}\sum_{n=1}^{m_0} nQ_{1,n}\\ &= k_{a,1}(R_1^{(1)} + R_1^{(0)}) + k_{b,1}R_1^{(1)}.\end{aligned} \tag{4.32}$$

We used $\sum_{n=0}^{m_0} nQ_{1,n-1} = \sum_{n=0}^{m_0-1}(n+1)Q_{1,n} = \sum_{n=0}^{m_0}(n+1)Q_{1,n}$. Similarly,

$$\begin{aligned}\langle n_{\rm ag}^2\rangle &\equiv \textstyle\sum_{n=1}^{m_0} n^2P_{n_{\rm ag}}(n) = k_{a,1}\sum_{n=1}^{m_0} n^2Q_{1,n-1} + k_{b,1}\sum_{n=1}^{m_0} n^2Q_{1,n}\\ &= k_{a,1}(R_1^{(2)} + 2R_1^{(1)} + R_1^{(0)}) + k_{b,1}R_1^{(2)}.\end{aligned} \tag{4.33}$$

Thus, $\langle n_{\rm ag}\rangle$ and σ_n^2 can be calculated once we know $R_1^{(0)}, R_1^{(1)}$ and $R_1^{(2)}$. The remaining work is to establish linear equations about $R_m^{(k)}$ based on Eq. 4.27. For $k=0$, we can simply sum over all n-states on both sides of Eq. 4.27. This yields,

$$\begin{aligned}-\delta_{mm_0} = \;& (m+1)(k_{a,m+1}+k_{b,m+1})R_{m+1}^{(0)} + (m_0-m+1)k_{\rm on}R_{m-1}^{(0)}\\ &-(mk_{a,m}+mk_{b,m}+(m_0-m)k_{\rm on})R_m^{(0)},\end{aligned} \tag{4.34}$$

$m = 1, 2, ..., m_0$. Besides, we know $R_0^{(0)} = 0$, $R_1^{(0)} = 1/(k_{a,1}+k_{b,1})$ (obtained from Eq. 4.29 based on $\sum_n P_{n_{\rm ag}}(n) = 1$). Thus, $R_m^{(0)}$ can be calculated iteratively using Eq. 4.34. For $k=1$, we can multiply Eq. 4.27 by n on both sides and sum over all n-states. This gives,

$$\begin{aligned}0 = (m+1)k_{a,m+1}(R_{m+1}^{(1)} + R_{m+1}^{(0)}) + (m+1)k_{b,m+1}R_{m+1}^{(1)}\\ +(m_0-m)k_{\rm on}R_{m-1}^{(1)} - (mk_{a,m}+mk_{b,m}+(m_0-m)k_{\rm on})R_m^{(1)},\end{aligned} \tag{4.35}$$

$m = 1, 2, ..., m_0$. Given $R_0^{(1)} = 0, R_{m_0+1}^{(1)} = 0$ and calculated $R_m^{(0)}$, one can find $R_m^{(1)}$ by solving the m_0 linear equations above. Similarly, we multiply Eq. 4.27 by n^2 on both sides and sum over all n-states, which yields,

$$\begin{aligned} 0 = (m+1)k_{a,m+1}(R_{m+1}^{(2)} + 2R_{m+1}^{(1)} + R_{m+1}^{(0)}) + (m+1)k_{b,m+1}R_{m+1}^{(2)} \\ +k_{\text{on}}[(m_0 - m - 1)R_{m-1}^{(2)} + R_{m-1}^{(1)}] - (mk_{a,m} + mk_{b,m} + (m_0 - m)k_{\text{on}})R_m^{(2)}, \end{aligned} \tag{4.36}$$

$m = 1, 2, ..., m_0$. Hence, $R_m^{(2)}$ can be obtained by solving m_0 linear equations once we know $R_m^{(0)}$ and $R_m^{(1)}$. Therefore, the first two moments of antigen number distribution can be calculated from $3m_0$ linear equations.

Cluster disassociation trajectory In a particular realization of cluster disassociation process defined by Eq. 4.3, all stochastic reaction events constitute a disassociation trajectory, characterized by $(\mathbf{t}, \mathbf{s}) = \{(t_i, s_i); i = 1, \ldots, N_R\}$ where $t_i \in (0, \infty)$ is the waiting time between $(i-1)$-th reaction and i-th reaction, and s_i labels the type of i-th reaction. N_R is the total number of reactions till complete disassociation. We will calculate the distribution of such trajectories $P(\mathbf{t}, \mathbf{s})$. For simplicity, we only focus on the case with negligible rebinding ($k_{\text{on}} = 0$). Then only two types of reactions are allowed, APC-Ag breaking ($s = s_a$) or BCR-Ag breaking ($s = s_b$). Besides, the total number of reactions is fixed at $N_R = m_0$. The probability density function of observing a trajectory $(\mathbf{t}, \mathbf{s})$ is given by

$$P(\mathbf{t}, \mathbf{s}) = P(\mathbf{t}) \cdot P(\mathbf{s}), \tag{4.37a}$$

$$P(\mathbf{t}) = \textstyle\prod_{i=1}^{m_0}(m_0 - i + 1)(k_a + k_b)e^{-(m_0-i+1)(k_a+k_b)t_i}, \tag{4.37b}$$

$$P(\mathbf{s}) = \textstyle\prod_{i=1}^{m_0}(\eta\delta_{s_i,s_a} + (1-\eta)\delta_{s_i,s_b}). \tag{4.37c}$$

The first part is because the waiting time $\mathbf{t}$ and reaction type $\mathbf{s}$ are independent random variables. In other words, knowing the value of $\mathbf{t}$ does not help to predict $\mathbf{s}$. In the second part, we assume that the waiting time follows the exponential distribution with a mean value of $1/((m_0 - i + 1)(k_a + k_b))$. Note there are $m_0 - i + 1$ closed complexes before the

i-th reaction. The last part means s_i follows the Bernoulli distribution. The formulation of Eq. 4.37 is based on the "fundamental premise of stochastic chemical kinetics", which assumes that the probability for reaction s_i to take place after sojourn time t_i is given by $P(t_i, s_i|m, n, t) = a_i(m, n)e^{-t_i \sum_j a_j(m,n)}$. Here, each of the a terms are propensity functions of an elementary reaction.

Now we are ready to calculate FI in the readout distributions. If the analytical form of readout distribution is available, one can evaluate Eq. 4.6 to get the FI. If the distribution cannot be determined explicitly, FI can still be calculated numerically with acceptable accuracy for a small cluster ($m_0 \sim 10$). For a large cluster ($m_0 \gg 1$), however, direct evaluation of FI is unfeasible due to the amplified numerical error in the tail part of a distribution after taking logarithm ($|\ln P_Y(\mathbf{y})|$ is large when $P_Y(\mathbf{y}) \to 0$). Instead, one can use the first two moments of the distribution to obtain a general lower bound of FI, which is predictive of FI when the distribution is close to Gaussian. In the following sections, we will compare FI between readouts in different cases. We will start from a simple case: vanishing force ($F = 0$) and vanishing rebinding ($k_{\text{on}} = 0$). Then we will investigate how force-sharing plays a role. Lastly, we will discuss the effect of rebinding.

4.3.2 Fisher information in affinity readout

4.3.2.1 Vanishing force ($F = 0$) and negligible rebinding ($k_{\text{on}} = 0$)

To provide some intuition about the antigen extraction process, we look at readout distributions in a simple case where complexes are decoupled ($F = 0$) and rebinding is negligible ($k_{\text{on}} = 0$). Complexities such as cooperativity and rebinding will be discussed in later sections. Solving Eq. 4.14 iteratively gives

$$P_\tau(t) = m_0 \lambda e^{-\lambda t}(1 - e^{-\lambda t})^{m_0 - 1}, \tag{4.38}$$

which depends on the off-rate of a complex $\lambda = k_a + k_b$. The cumulative distribution function (CDF) reads as $\int_0^t P_\tau(t')dt' = (1 - e^{-\lambda t})^{m_0}$, which is the probability for no complex surviving

till time t. Therefore, Eq. 4.38 suggests that the cluster lifetime is governed by the complex that survives for the longest period, as expected. Besides, based on Eq. 4.30, the antigen extraction follows

$$P_{n_{\mathrm{ag}}}(n) = \eta^n (1-\eta)^{m_0-n} \binom{m_0}{n}. \tag{4.39}$$

Here $\eta = k_a/(k_a + k_b)$ is the probability to get the antigen in every breaking event. Because antigens are extracted independently and with fixed probability η, antigen extraction is simply the Binomial process. In Fig. 4.4A we show as affinity increases, the mean value of both readouts increases, which agrees with the observation *in vivo* that a high-affinity B cell forms longer contact with APC and acquires more antigens from APC than a low-affinity B cell [52]. Besides, both readouts saturate at the high-affinity end. The saturation is simply because at high $\Delta G_b^\ddagger$, APC-Ag bond becomes the weaker bond in each complex and the BCR-Ag bond almost never breaks ($\lambda \approx k_a, \eta \approx 1$). Thus, further improving BCR affinity did not improve cluster lifetime or antigen extraction much. Indeed, an affinity ceiling of affinity maturation has been observed *in vivo* which turned out to be far below the inherent potential of antibodies for ligand binding [30, 129].

In a particular extraction event, however, both cluster lifetime and extracted antigen number are inherently stochastic due to the random binding and unbinding of ligand-receptor pairs. Thus, a higher affinity B cell may have a lower affinity readout, which leads to discrimination mistakes.

To compare the discrimination performance of two discriminators, we compute the FI by direct evaluation of Eq. 4.6 using Eq. 4.38 and Eq. 4.39. This gives

$$\mathcal{I}_\tau \approx \frac{(\ln m_0)^2}{(1+e^{(\Delta G_b^\ddagger - \Delta G_a^\ddagger)/k_{\mathrm{B}}T})^2}, \quad \mathcal{I}_n = \frac{m_0 e^{(\Delta G_b^\ddagger - \Delta G_a^\ddagger)/k_{\mathrm{B}}T}}{(1+e^{(\Delta G_b^\ddagger - \Delta G_a^\ddagger)/k_{\mathrm{B}}T})^2}. \tag{4.40}$$

The approximation in $\mathcal{I}_\tau$ holds when $m_0 \gg 1$. Interestingly, $\mathcal{I}_\tau$ and $\mathcal{I}_n$ show distinct dependence on the B cell affinity $\Delta G_b^\ddagger$ and cluster size m_0, as we detailed below.

First, $\mathcal{I}_\tau$ decreases with $\Delta G_b^\ddagger$ whereas $\mathcal{I}_n$ peaks at some intermediate $\Delta G_b^\ddagger$ (Fig. 4.4B). This is because cluster lifetime is informative about $\Delta G_b^\ddagger$ when most breaking events happen

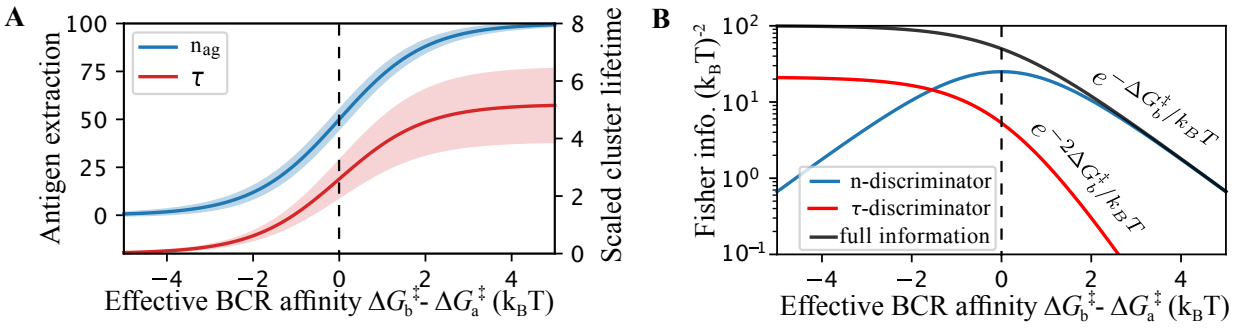

Figure 4.4: n-discriminator and τ-discriminator complement each other for broad affinity discrimination. (A): the readout as a function of effective BCR affinity. Solid lines are the ensemble mean, and the shades mark the standard deviation. The plotted cluster lifetime is relative to $1/k_a$. (B) Fisher information encoded in cluster lifetime (red, $\mathcal{I}_\tau$ from Eq. 4.40), antigen extraction number (blue, $\mathcal{I}_n$ from Eq. 4.40), and the entire unbinding trajectory (greym I_{full} from Eq. 4.41). As affinity increases, the information encoded in the waiting time measure decays much faster than the information from antigen number data. The vertical dashed line marks the condition $\Delta G_b^\ddagger = \Delta G_a^\ddagger$. We considered independent antigen extraction without rebinding. Parameters: $x_a^\ddagger = 1.5\text{nm}, x_b^\ddagger = 2.0\text{nm}, m_0 = 100, \Delta G_a^\ddagger = 10 k_{\text{B}}T, F = 0\text{pN}$.

at BCR side ($\lambda \approx k_b$) and its information decreases as the number of BCR-Ag breaking events decreases. In contrast, the Binomial process of antigen extraction is most sensitive to $\Delta G_b^\ddagger$ when $\eta = 1/2$, that is, the BCR-Ag off rate matches the APC-Ag off rate ($\Delta G_b^\ddagger = \Delta G_a^\ddagger$).

Second, $\mathcal{I}_n$ exceeds $\mathcal{I}_\tau$ and decays more slowly ($\sim e^{-\Delta G_b^\ddagger/k_\mathrm{B}T}$) than $\mathcal{I}_\tau$ ($\sim e^{-2\Delta G_b^\ddagger/k_\mathrm{B}T}$) as $\Delta G_b^\ddagger$ increases. This is related to the fluctuation in two readouts. At high affinity end, the noise in APC-Ag lifetime keeps fluctuations in cluster lifetime large. In contrast, the noise in antigen extraction diminished as $\Delta G_b^\ddagger \to \infty$ because the influence of APC-Ag lifetime fluctuation on n_ag is factored out by the long BCR-Ag lifetime when taking the ratio between off-rates. These differences imply the two readouts have distinct operation ranges of affinity.

Additionally, $\mathcal{I}_\tau$ has a slower scaling relation with cluster size m_0 than $\mathcal{I}_n$, ($(\ln m_0)^2$ vs m_0). This difference, which implies $\mathcal{I}_n > \mathcal{I}_\tau$ at $m_0 \gg 1$, is rooted in the way different breaking events contribute to the final readout. For the cluster lifetime, most time was spent on the last few breaking events because the disassociation of bonds slowed down during the antigen extraction process due to the decreasing number of closed complexes. In contrast, $\mathcal{I}_n$ is linear in m_0 because all complex contribute to n_ag equally and independently through m_0 Bernoulli processes.

To compare two discriminators with the ideal discriminator, we obtained the full information encoded in the entire extraction trajectory $(\mathbf{t}, \mathbf{s}) = \{t_1, s_1, t_2, s_2, ..., t_{m_0}, s_{m_0}\}$ (recall t_i is the waiting time between $(i-1)$-th reaction and i-th reaction, and s_i is the type of i-th reaction). The full information can be calculated from the probability of observing each trajectory $P(\mathbf{t}, \mathbf{s})$,

$$\mathcal{I}_\mathrm{full} = \frac{m_0}{1 + e^{(\Delta G_b^\ddagger - \Delta G_a^\ddagger)/k_\mathrm{B}T}}. \tag{4.41}$$

We immediately see $\mathcal{I}_n \to \mathcal{I}_\mathrm{full}$ when $\Delta G_b^\ddagger \gg \Delta G_a^\ddagger$ (see Fig. 4.4B). In other words, n_ag contains almost all the affinity information generated by the extraction process at high $\Delta G_b^\ddagger$ end. This suggests that B cells do not need to look at the cluster lifetime at all and should focus on counting the extracted antigen number when BCR affinity is much higher than the

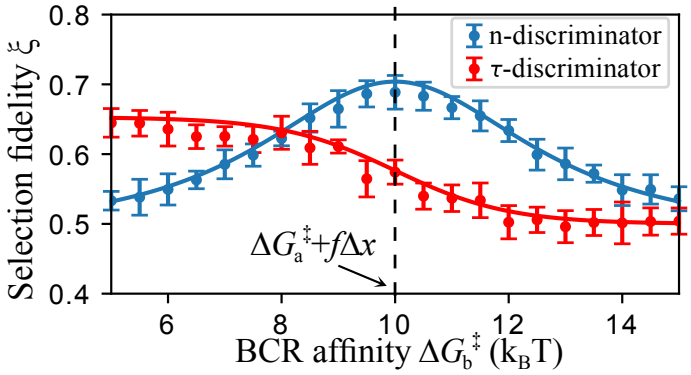

Figure 4.5: Selection fidelity (see definition in Eq. 4.8) between two B cells with a small affinity difference $\epsilon = 0.1k_{\mathrm{B}}T$. Symbols are the ensemble average over 500 Gillespie simulations of the master equation and error bars from 10 independent realizations of the ensemble. Curves depict the upper bound in relation to Fisher information (Eq. 4.9) derived from first principles. Vertical dashed lines mark the condition of vanishing affinity gap under force, $\Delta G_b^{\ddagger} = \Delta G_a^{\ddagger} + f\Delta x$. Independent extraction events without rebinding. Parameters: $x_a = 1.5\mathrm{nm}, x_b = 2\mathrm{nm}, m_0 = 200, \Delta G_a^{\ddagger} = 9k_{\mathrm{B}}T,\ f = k_{\mathrm{B}}T/\Delta x$.

presenting tether affinity.

To see how the above differences in Fisher information between two readouts propagate to the performance of a realistic affinity discrimination task, we calculated the selection fidelity by simulating the antigen extraction processes of different B cells. We consider two B cells with a small affinity difference and calculate the selection fidelity (see Eq. 4.8) by simulating the antigen extraction processes many times. In Fig. 4.5 we show that the simulated selection fidelity follows a similar trend to the Fisher information as the average BCR affinity improves. Since a sensitive response in readout to affinity change means readout distributions of different B cells are well separated, it is not surprising that there exists a strong connection between Fisher information and the practical selection fidelity.

4.3.2.2 Finite force ($F > 0$) and negligible rebinding ($k_{\rm on} = 0$)

In the previous section, we ignored the force application and assume complexes are independent of each other. However, the intrinsic covalent property of BCR allows formation of cross-linking micro-clusters. Indeed, recent experiments suggest GC B cell may actively manipulate receptors into correlated assemblies, which may have functional importance to be explored [32, 6]. How the cooperativity between different complexes modifies the information encoded in readouts?

As one particular example, we consider that different complexes within a local cluster share the tugging force and thereby are coupled together, which is a common feature in ligand-receptor systems [130, 131]. Assuming that cytoskeleton force is uniformly distributed in the cluster, the off-rates depend on cluster size m through

$$k_a(m) = k_0 e^{-(\Delta G_a^\ddagger - \frac{F}{m} x_a^\ddagger)/k_{\rm B}T}, \quad k_b(m) = k_0 e^{-(\Delta G_b^\ddagger - \frac{F}{m} x_b^\ddagger)/k_{\rm B}T}. \tag{4.42}$$

F is the total force. As more and more bonds break, the force on each bond F/m will increase. In this section, we assume the rebinding is negligible for simplicity ($k_{\rm on} = 0$). The coupling between different complexes makes calculation of FI in readouts difficult. We turn instead to a general lower bound on the FI. For readout mean μ_Y and standard deviation σ_Y, we have [132]

$$\mathcal{I}_Y \geq \tilde{\mathcal{I}}_Y \equiv \frac{1}{\sigma_Y^2} \Big(\frac{{\rm d}\mu_Y}{{\rm d}\Delta G_b^\ddagger} \Big)^2. \tag{4.43}$$

This simplification has the advantage that the calculation of two required moments is easier than evaluating the integral in Eq. 4.6. Similar approach has appeared in a diverse literature [133, 113, 134]. Besides, the results of Eq. 4.43 show good agreement with the exact FI of small clusters.

Surprisingly, our model suggests that this simple force-sharing feature can introduce nontrivial effect. Unlike the case with vanishing force where the cluster lifetime mostly depends on few long-lived complexes, force-sharing accelerates rupture at the late stage such

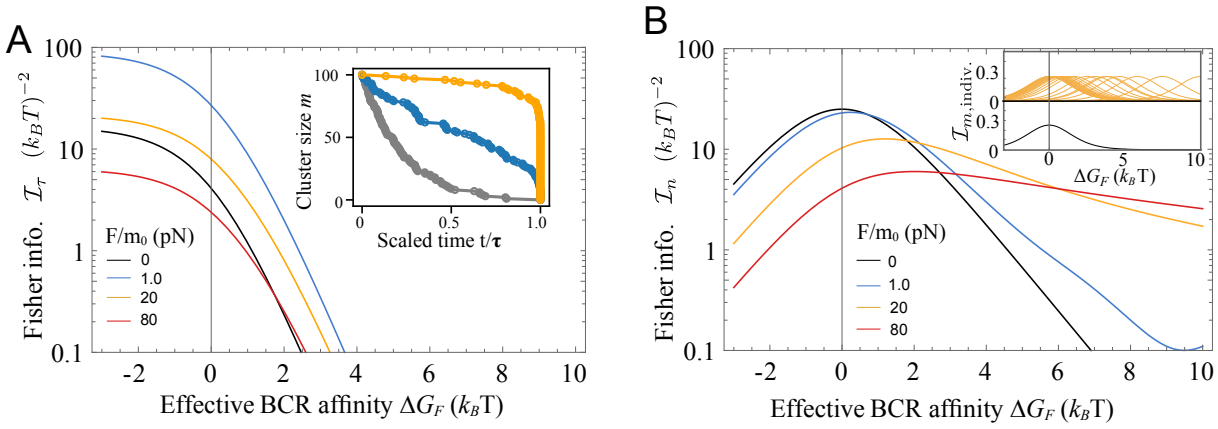

Figure 4.6: Cooperativity arising from force sharing enhances information extraction. We plot Fisher information as a function of effective BCR affinity $\Delta G_F = \Delta G_b^\ddagger - \Delta G_a^\ddagger - F\Delta x/m_0$ under various forces. The curve with $F = 0$ (in black) also represents independent extraction results, which is independent of force when plotting against ΔG_F. (A): Fisher information in cluster lifetime, calculated based on Eq. 4.44. The inset shows examples of cluster disassociation trajectories for independent complexes (black), or under shared force F/m_0 =1pN (blue) and 20pN (orange). (B): Fisher information in extracted antigen number, obtained from Eq. 4.45. In the inset, we plot information encoded in each rupture event for two cases: black for $F/m_0 = 0$pN and orange for $F/m_0 = 20$pN. Parameters: $x_a^\ddagger = 1.5\text{nm}, x_b^\ddagger = 2.0\text{nm}, k_a = 1\text{s}^{-1}, m_0 = 100$.

that most complexes contribute roughly equally to the total cluster lifetime. This reduces the relative variance of τ and enhances its information (Fig. 4.6A). In addition, because different complexes break under different values of force per bond, the n-discriminator can sense a much wider affinity range compared to the case without force (Fig. 4.6B). We explain these effects in details below.

Specifically, the FI of τ can be enhanced by a shared weak force. Direct evaluation of $\tilde{\mathcal{I}}$ (see Eq. 4.43) using the mean $\mu_\tau = \sum_{i=1}^{m_0} 1/(i\lambda_i)$ (See Eq. 4.19) and variance $\sigma_\tau^2 = \sum_{i=1}^{m_0} 1/(i\lambda_i)^2$ (See Eq. 4.22, here $\lambda_i = k_a(i) + k_b(i)$) gives

$$\tilde{\mathcal{I}}_\tau = \frac{1}{\sum_{i=1}^{m_0}(i\lambda_i)^{-2}} \Big(\sum_{i=1}^{m_0} \frac{k_{bi}}{i\lambda_i^2} \Big)^2. \tag{4.44}$$

In Fig. 4.6A, we show under force-sharing, a small force ($F/m_0 \approx 1$pN) greatly increases information in τ at low BCR affinities, compared to the case with $F = 0$.

To understand the intriguing behavior, we look at the cluster disassociation trajectory (Fig. 4.6A inset). Shared force accelerates complex breaking as rupture proceeds due to the increasing force per bond, which changes the distribution of waiting time between adjacent reactions. For some intermediate force ($\max(\Delta G_a^\ddagger/x_a^\ddagger, \Delta G_b^\ddagger/x_b^\ddagger) < F < \min(m_0\Delta G_a^\ddagger/x_a^\ddagger, m_0\Delta G_b^\ddagger/x_b^\ddagger)$, the cluster size decreases roughly at a constant rate (Fig. 4.6A inset, blue trajectory) and thereby waiting times have a uniform distribution. This reduces the relative variance in cluster lifetime [128] and increases FI. In addition, the scaling of FI on the cluster size changes from $(\ln m_0)^2$ to m_0 (fixing F/m_0 while increasing m_0). However, if the force is too large, the improvement due to force-sharing disappears since the distribution of waiting time is highly biased towards the initial few breaking events due to the 'domino' effect [130]: The force per bond dramatically increases after the initial few breaking events and the remaining complexes break almost instantly (see the orange trajectory in Fig. 4.6A inset).

For n-discriminator, cooperativity may serve to expand the distinguishable affinity range. Without rebinding, the antigen extraction process consists of m_0 breaking events. In each

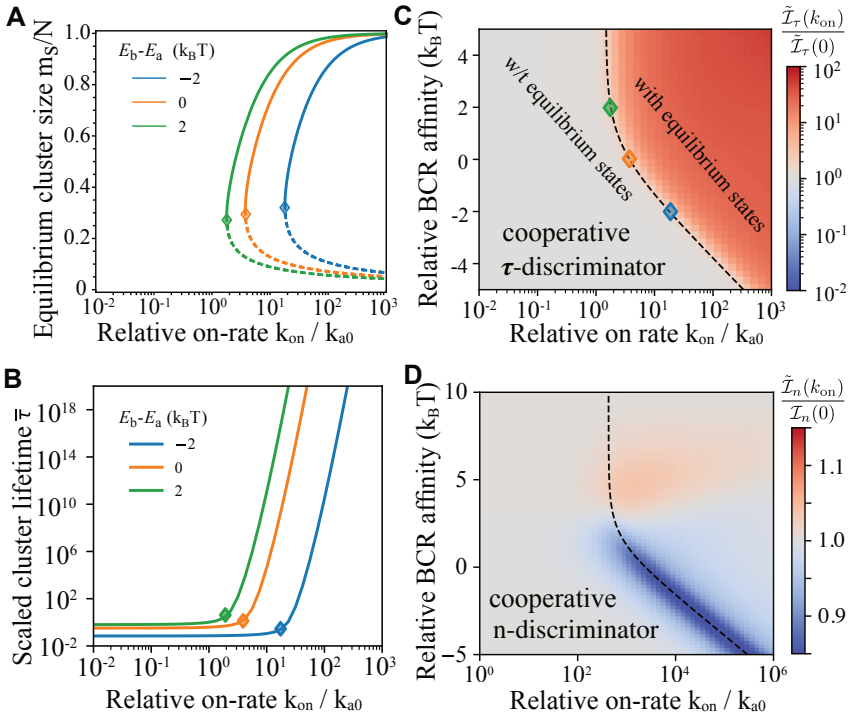

Figure 4.7: **Rebinding enhances Fisher information in cluster lifetime at a cost of speed, but does not alter n-discriminator performance much**. (A)Equilibrium cluster size in the deterministic picture. Curves are steady solutions to Eq. 4.46. The solid branch shows the stable solution and the dashed part shows the unstable solution. The symbols mark the bifurcation points where the equilibrium states disappear when decreasing $k_{\rm on}$. (B)The average cluster lifetime as a function of rebinding rate with symbols corresponding to the bifurcation points in (A). (C) The color-coded ratio between Fisher information in cluster lifetime with rebinding and that without rebinding, $\tilde{\mathcal{I}}_\tau(k_{\rm on})/\tilde{\mathcal{I}}_\tau(0)$, as a function of on rate and relative BCR affinity $\Delta G_b^\ddagger - \Delta G_a^\ddagger$. Symbols correspond to the bifurcation points in (A). The dashed line is a collection of bifurcation points at various $\Delta G_b^\ddagger$. $F/m_0 = 1$pN. (D) Fisher information in $n_{\rm ag}$, compared to $\mathcal{I}_n$ without rebinding, $\tilde{\mathcal{I}}_n(k_{\rm on})/\tilde{\mathcal{I}}_n(0)$. A relatively large shared force ($F/m_0 = 10$pN) was used. The dashed line marks the bifurcation points. Other parameters: $x_a^\ddagger = 1.5$nm, $x_b^\ddagger = 2.0$nm, $k_a = 1\text{s}^{-1}$, $m_0 = 30$.

breaking event, the number of antigen obtained is a random variable $X_i \sim B(1, \eta_i)$. Here $\eta_i = \frac{k_a(i)}{k_a(i)+k_b(i)}$. Using mean $\mu_n = \sum_{i=1}^{m_0} \eta_i$ and variance $\sigma_n^2 = \sum_{i=1}^{m_0} \eta_i(1-\eta_i)$, we get

$$\tilde{\mathcal{I}}_n \approx \sum_{i=1}^{m_0} \mathcal{I}_{i,\text{indiv.}} = \sum_{i=1}^{m_0} \frac{e^{(\Delta G_b^\ddagger - \Delta G_a^\ddagger - F\Delta x/i)/k_\text{B}T}}{(1+e^{(\Delta G_b^\ddagger - \Delta G_a^\ddagger - F\Delta x/i)/k_\text{B}T})^2}, \tag{4.45}$$

as plotted in Fig. 4.6B. Here $\mathcal{I}_{i,\text{indiv.}}$ is the information encoded in the reaction type of $(m_0 - i + 1)$-th breaking event. So $\mathcal{I}_n$ is the sum of information generated by each individual breaking event. More importantly, each bond has its own sensitive window for affinity discrimination where the $\mathcal{I}_{i,\text{indiv}}$ peaks ($(\Delta G_b^\ddagger)^*(i) = \Delta G_a^\ddagger + F\Delta x/i$, see Fig. 4.6B inset), because different complexes break under different force per bond. At small force, all sensitive windows are nearly coincident and the total $\mathcal{I}_n$ peaks at a narrow affinity window. Under shared-force, those windows for individual bonds are placed at different locations on the affinity spectrum and overlap with each other. Consequently, FI is high over a broad range (Fig. 4.6B). Nevertheless, the force can't be too large since otherwise all sensitive windows are well separated and the total information is low.

4.3.2.3 Finite rebinding ($k_\text{on} > 0$)

To understand the effect of rebinding, in this section we relax our assumption and consider $k_\text{on} > 0$. As pointed out by other studies focusing on ligand-receptor interaction, one important effect of crowding is the increased chance of rebinding: Ligands may rebind to the receptors nearby before diffusing away [135]. Here we show rapid rebinding greatly enhances FI in cluster lifetime but has negligible impact on FI in n_ag.

In Fig. 4.7, we show that frequent rebinding enables a non-zero equilibrium state, which greatly amplifies $\hat{\mathcal{I}}_\tau$. The equilibrium state m_s is the steady solution to the deterministic equation about mean cluster size

$$0 = \frac{\mathrm{d}\overline{m}}{\mathrm{d}t} = -\overline{m}k_0(e^{-(\Delta G_a^\ddagger - \frac{Fx_a^\ddagger}{\overline{m}})/k_\text{B}T} + e^{-(\Delta G_b^\ddagger - \frac{Fx_b^\ddagger}{\overline{m}})/k_\text{B}T}) + (m_0 - \overline{m})k_\text{on}. \tag{4.46}$$

At low rebinding rate, the above equation does not have non-zero solution. So the cluster di-

rectly disassociates from the all-closed state without many rebinding events, which is similar to the case where $k_{\text{on}} = 0$. When k_{on} is larger than a critical value (diamonds in Fig. 4.7), a steady state emerges (Fig. 4.7A). Both FI and mean cluster lifetime are greatly amplified (Fig. 4.7B-C). This is consistent with the idea of nonequilibrium sensing, which lowers the inference error by raising the number of measurements per receptor, at a cost of decreased speed [109].

To make the results more transparent, we calculate the FI in the limit of large rebinding rate, $k_{\text{on}} \gg k_a(i) + k_b(i)$ $(i = 1, ..., m_0)$. Now the system persists near the equilibrium state for a long time before the rapid disassociation driven by some rare large fluctuations. Thus, $P_\tau(t)$ can be approximated by an exponential distribution,

$$P_\tau(t) \approx \frac{m_0 \lambda}{\gamma^{m_0 - 1}} e^{-\frac{m_0 \lambda}{\gamma^{m_0-1}} t}, \tag{4.47}$$

obtained by taking $k_{\text{on}} \gg k_a + k_b$. This gives

$$\mathcal{I}_{\tau,\text{large rebinding}} \approx \Big(\sum_{i=1}^{m_0} \frac{1}{1 + e^{(\Delta G_b^\ddagger - \Delta G_a^\ddagger + F\Delta x/i)/k_{\text{B}}T}} \Big)^2, \tag{4.48}$$

independent of k_{on}. At low affinity limit $(\Delta G_b^\ddagger - \Delta G_a^\ddagger + F\Delta x/i \ll k_{\text{B}}T)$, $\mathcal{I}_\tau \approx m_0^2$, which increases with m_0 much faster than extraction without rebinding. However, rebinding does not change the dependence on $\Delta G_b^\ddagger$ because APC-Ag bond still dominates the majority of breaking events at high $\Delta G_b^\ddagger$. This can be seen by taking high affinity limit $(\Delta G_b^\ddagger \gg k_{\text{B}}T)$ in Eq. 4.48, which gives $I_\tau \propto e^{-2\Delta G_b^\ddagger / k_{\text{B}}T}$.

In contrast, the change in $\mathcal{I}_n$ due to rebinding is typically insignificant(Fig. 4.7D). To understand this, we first need to know how rebinding changes antigen extraction. The key insight is that rebinding can alter the expected chance to get the antigen in some complexes by closing the broken bond and 're-extracting' the antigen later under a different force. This is only important for complexes which broke before the system reached the equilibrium state, since the new force per bond at equilibrium (F/m_s) is greater than the force used to break the same bond earlier $(F/i,\ i > m_s)$. Nevertheless, this effect diminishes at large

k_{on}, because the fraction of complexes whose extraction chance can be altered via rebinding ($i = m_0, m_0 - 1, ..., m_s$) decreases as m_s approaches m_0. This is why the change in $\mathcal{I}_n$ due to rebinding is limited to some intermediate value of k_{on}(Fig. 4.7D). More importantly, the scaling dependence of I_τ on m_0 and $\Delta G_b^\ddagger$ remains the same. Thus, one expects that $\mathcal{I}_n$ still exceeds $\mathcal{I}_\tau$ at high $\Delta G_b^\ddagger$ limit even in the presence of rebinding.

4.4 Discussion

One of the key challenges in immunology is to understand how an adaptive immune system generates a robust immune response despite stochasticity at genetic, molecular, and cellular levels. In particular, selection of high affinity B cells relies on the ability to rank B cells based on the noisy affinity readouts. The task is complicated because GC reaction is an evolutionary system with dynamical B cell affinity distributions, which makes the conventional 'thresholding' model inapplicable. With the abundance of data regarding the molecular dynamics, synaptic kinetics and cellular behavior, the time is ripe to tackle the problem from a theoretical modeling perspective.

In this study, we present a detailed analysis of stochastic antigen extraction dynamics and influences of thermal noise on affinity discrimination. Our simplified model takes account of the key factors that determine the efficiency of antigen acquisition, including BCR, the presenting tether, and mechanical pulling force. We quantified discrimination performance using FI, which measures the sensitivity of the readout distribution to affinity change. Our results reveal different readouts complement each other to cover a wide range of affinity spectrum for accurate discrimination. Specifically, rapid disassociation of low affinity BCR-Ag bond enables accurate measurement of BCR-Ag lifetime via BCR signaling, which is overwhelmed at high BCR affinity by APC-Ag bond disassociation that terminates the forceful contact between B cell and APC. Instead, by comparing the BCR-Ag lifetime to APC-Ag lifetime, the extracted antigen number retains some information about BCR affinity even

though most breaking events happen at the APC side.

Our study emphasizes several strategies which are beneficial for affinity information extraction. First, the complementary role of cluster lifetime and extracted antigen number highlights the importance of adaptation. At different stage of affinity maturation, the BCR signal and the T cell derived signal are not equally informative. Thus, as other adaptation strategy utilized by immune system, an active switch of focus allows access of affinity information while minimizing the energy cost. Second, mechanical force plays a key role in regulating the distinguishable affinity window and prompting affinity discrimination. In ligand discrimination by T cell, it has been shown that the force application can be extremely important to select the correct ligand. Here we demonstrate that the cellular force of B cell can adjust the sensitive window of affinity discrimination by regulating the chance of antigen extraction, which enables a dynamical control of affinity discrimination during GC evolution. Therefore, by actively tuning the force strength and switching the discriminator, GC B cells are able to recognize beneficial mutants even in a high-affinity background.

Existing experiments support the above optimal affinity discrimination strategy. Diverse experiments suggest a switch of focus from BCR signaling to T cell help during GC reaction [25, 65, 117]. Other experiments show that naive B cells spend a lot of time engaging with APCs whereas GC B cells only pause on APC for a few minutes [25, 52]. This is consistent with our prediction that prolonged contact does not elevate the BCR affinity information encoded in the number of extracted antigen. Besides, it has been shown that GC B cells applied stronger and more persistent forces on antigen than naive B cells [32, 6], which is necessary for a stringent affinity discrimination at the high-affinity regime in our model. Additionally, in contrast with a low affinity naive B cell or a memory B cell which gathers antigens toward the synapse center to form a large cluster, a GC B cell extracts antigen using peripheral clusters with smaller sizes [32, 6]. This active manipulation not only ensures large force per bond, but also suppresses rebinding and shortens the contact duration.

Our results may provide an understanding of experimental observations regarding B

cell selection. First, there have been contradictory phenomena about BCR signaling in experiments. On the molecular level, while some studies suggested GC B cells did not directly signal through their BCRs [117], others reported that signaling was observed in a subpopulation of GC B cells [136]. Likewise, on the cellular level, Victora et al. demonstrated T cell derived signal limits GC B cell selection [65], but a more recent experiment by Turner et al. showed BCR signaling augmented B cell selection in GC [118]. All those results can be explained by the adaptation picture: BCR signaling may contribute to B cell selection at early stage of GC evolution, but diminished at later stage. Indeed, experiments such as Turner et al. [118] focused on the response in the first few days of GC reaction (i.e., the first week after immunization) whereas Victora et al. [65] analyzed GC B cells after 2-4 weeks since immunization. Second, another long-standing mystery of GC evolution is the retention of GC B cells expressing low- and moderate- affinity BCRs while high-affinity B cells are generated [80, 97], which seems contradictory to the competitive affinity-dependent selection model of affinity maturation. However, if there is an adaptive transition during affinity maturation, different B cell clones may render different "affinity-thresholds" of survival, that is, the antigen-affinity thresholds for a portion of GC B cells may be lower than others [6]. Within this picture, the co-existing of low-affinity and high-affinity B cells is not impossible. Indeed, recent experiment observed a permissive selection of GC B cell which ensures clonal diversity for broad protection [79].

It is straightforward to design experiments and verify our results. First, one can quantify the BCR signaling activity over the entire GC reaction period to see whether there is a dynamic regulation or a sharp transition of BCR signaling strength. Second, the selection fidelity can be measured by injecting a mixture of many wild-type B cells and a few beneficially mutated B cells and mount the chance for the mutated B cell to survive and replicate. Then our results can be verified by varying the background wild-type B cell affinity. Lastly, in experiments, people are able to delivery antigens to B cell in a BCR-independent way. Hence, it is possible to reduce the affinity information in T cell derived signal via delivering

abundant antigens to all the B cells and see whether the affinity maturation is suppressed.

CHAPTER 5

Dynamic control and feedback that optimize affinity discrimination

5.1 Introduction

Motivation In previous chapters, we focused on antigen extraction stage and assumed that B cells applied tugging forces *after* cluster formation. Nevertheless, recent experiments demonstrated that B cells might apply highly dynamic and adaptive forces during the formation of ligand-receptor cluster, implying that the entire process, including cluster formation and dissociation, is actively regulated by the B cell through mechanical stress. More importantly, this suggests a feedback mechanism that couples binding kinetics, cytoskeleton dynamics, and level of mechanical transition together into a sophisticated yet powerful system, since B cells need to sense the binding configuration and apply force accordingly in order to implement a dynamic control. How does this coupled system behave? If a B cell is able to actively manipulate the ligand-receptor interaction, what is the optimal form of feedback? Is it possible to reveal the underlying feedback by looking at some observable? To tackle these intriguing questions, we generalize our model in chapter 4 to incorporate systems with dynamical forces.

Feedback in affinity discrimination of T cells It has been suggested that feedback played an important role in enhancing discrimination sensitivity and specificity of T cells. It is known for a long time that the T cell signal transduction satisfies a tight set of properties,

including *speed*, *sensitivity* and *specificity*. Specifically, discrimination among antigens is achieved within a time window of 1-5 min (*speed*); a three- to five-fold increase in binding lifetime is sufficient to distinguish antigens that activate T cells (agonists) from those that do not (non-agonists) (*sensitivity*); T cells usually do not respond to self-ligands, even if presented in numbers as high as 10^5 or more (*specificity*, aka *absolute discrimination*) [137]. The high sensitivity is explained by the classical kinetic proofreading (KPR) model [123], which introduces a temporal lag between ligand binding and receptor signaling, allowing amplification of the difference between agonists and non-agonists through non-equilibrium reactions. Nevertheless, the KPR model cannot account for specificity as well as the observed phenomenon of antagonism (presence of nonagonists can inhibit response to agonists). To overcome this inconsistency, Germain and colleagues [138] added to the basic KPR process a negative feedback mediated by SHP-1 and a positive feedback mediated by ERK kinase. Given plausible parameters, the elaborate model was able to satisfy the constraints of speed, sensitivity, and specificity [139]. With the insights of feedback, François et al. [105] proposed a simple analytical model that relied on just the SHP-1 negative feedback yet successfully recapitulated experimental observations. These models highlighted the effect of negative feedback in T cell affinity discrimination.

Mechanical control during antigen extraction Nevertheless, B cells display distinct behavior from T cells [140]. For example, growing evidence suggested GC B cells may make decisions based on the efficiency of antigen capture instead of receptor signaling [117, 141, 95, 118]. Besides, the pulling machine in B cell is found to be dissimilar from T cell's, consisting of not only in-plane contraction force but also strong dynamical out-of-plane normal forces [2]. Regardless of those significant differences in cellular behavior, B cells also show surprisingly efficient and absolute affinity discrimination. For example, antigens that differ in affinity by six-fold resulted in a significant difference in antigen extraction [2]. In addition, given that antigens are nonhomogeneously distributed over space and B cells

cannot sample the entire GC structure [52], selection of high affinity B cells is still effective, indicating that it can reduce the influence from antigen concentration fluctuations and focus on antigen binding affinity. Therefore, a new model is demanded to understand how such properties emerge from the non-equilibrium antigen extraction process.

Recent experiments provided insights about the regulatory role of dynamical mechanical force. The reorganization of member cytoskeleton initiates just seconds after B cell receptor binding to antigen [142], which is far before the cluster size begins to shrink. A direct observation was made by Kwak et al. [6]. By utilizing time-lapse live-cell imaging, they showed that B cells applied highly dynamical pulling force during the formation of ligand-receptor clusters when contacting with substrates coated with antigens [6]. Quantification of actin localization indicates that the amount of myosin IIa and F-actin correlates with the size of antigen microclusters [2]. Further studies reported correlations between pulling force and the antigen cluster size [23, 24]. These observations indicate that the cytoskeleton structure may be able to sense and feed back to the ligand receptor interaction. It remains unclear whether and how such feedback influences the affinity discrimination function. It is speculated that B cells might utilize the mechanical force to regulate the antigen extraction process and achieve the desired properties of affinity discrimination [32, 6], resembling the idea of mechanical proofreading [143]. Yet the underlying physical principle is missing.

Additionally, the kinetics of the antigen extraction process under dynamical force itself is an intriguing problem. Existing studies focused on the stability of pre-existing clusters. The dynamics of cluster rupture has been described long ago by Bell [15] and Erdmann et al. [130]. Bell [15] assumed a constant pulling force uniformly distributed on all connected bonds in a pre-existing cluster. The deterministic model predicted a critical force that was just sufficient to rupture the cluster. A stochastic version of the Bell's model has been investigated in very detailed form by Erdmann and Schwarz [130], which suggested distinct cluster stability compared to the deterministic model. However, one common assumption in existing studies is that forces (either constant or dynamical) are deployed long *after* cluster

formation and independent of binding state. How does the system behave under an adaptive force? What is the bridge connecting passive binding with active mechanical transition? Is it possible to reveal the underlying force dynamics by looking at the observable?

To tackle those questions, we build a model that integrates cluster formation, force development, and cluster disassociation to investigate the role of dynamical force in antigen acquisition and affinity discrimination by B cells. The coupled system reproduces the cluster formation-disassociation dynamics observed in experiments. To break the cluster within a reasonable timescale, the force has to respond fast enough or be large enough. Based on the dynamics, we propose that the contact duration can potentially be a good indication of underlying force schemes. Additionally, antigen acquisition depends on both cluster formation and cluster disassociation, both of which are mediated by force. Based on this, we show force can contribute to affinity discrimination either through increasing the sensitivity of cluster formation to affinity change, or by enhancing the sensitivity of extraction efficiency to affinity change. Both methods require a dynamical force that is adaptive to the underlying BCR affinity.

Furthermore, our model predicts that force can benefit affinity discrimination in other aspects. We show that by tuning the force schedule, the system can prioritize speed in one context and discrimination fidelity in another. More interestingly, for low-affinity B cells, speed and fidelity can be improved simultaneously by guiding the liand-receptor system towards the bifurcation point in parameter space, where the cluster formation becomes extremely sensitive to affinity perturbations. Besides, if a B cell could sense the cluster size and apply force accordingly, a natural negative feedback on clustering is created, which consequently reduces the influence of fluctuations in ligand concentration, resulting in absolute discrimination.

Lastly, our model allows us to study the interference between different antigen types under a dynamical force. We show an antagonism effect naturally emerges as antigens are coupled together by collectively triggering and sharing the force, that is, the presence of a

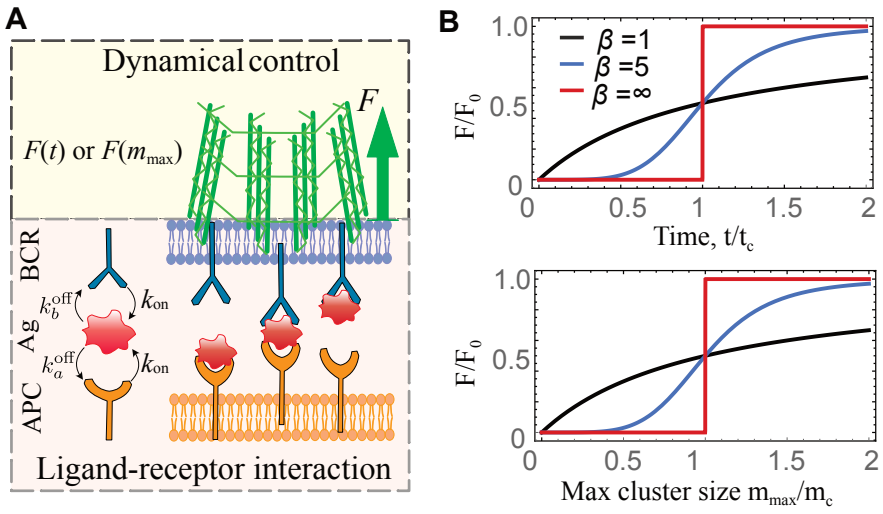

Figure 5.1: B cells extract antigens from the APC using dynamically controlled cytoskeletal forces. (A) Adhesion of B cell to APC relies on clusters with receptors (blue) binding to antigens (red) tethered on the APC receptors (brown), forming three-body complexes. The tight linkage of BCR to the actin cytoskeleton network (green) generates and transmits dynamical out-of-plane forces to binding complexes as instant feedback to cluster formation, which serves to extract antigens from APC. (B) We assume the force is time-dependent or max-cluster-size dependent, which follows the Hill function parameterized by F_0, m_c (or t_c) and β.

secondary self antigen inhibits the extraction of foreign antigens.

5.2 Model

The interaction between B cell and APC involves ligand receptor binding, cluster formation and extraction by force (Fig. 5.1A) [144, 5, 37]. We focus on the dynamics of a local cluster within a synapse. Antigen ligands and receptors are assumed to be uniformly distributed and move freely, so that one can omit the spatial resolution. In the beginning, B cell uses BCRs to bind to antigens that are tethered on the surface of APC, forming three-body

complexes APC-Ag-BCR. This simple coarse grained structure captures the key point of antigen acquisition: B cell obtains antigen only when BCR-Ag bond persists longer than APC-Ag bond. The initial engagement of BCR and antigen triggers the reorganization of cytoskeletons, which exerts force on the bonds and accelerate the unbinding. We assume the interaction terminates when all complexes are broken. Below, we show our mathematical model that describes the above process.

Ligand receptor interaction The stochastic chemical reactions between ligand, receptor and tether are modeled by a master equation. Let m and n be the number of BCR-Ag-APC complexes and BCR-Ag complexes at time t, respectively. We assume there is no antigen in the soluble form. Then, given the total number of antigen ligands available, L_0, the number of antigens in the form of APC-Ag is $(L_0 - m - n)$. Thus, the system state is completely described by (m, n). The probability for the system to be in state (m, n) evolves according to

$$\frac{\mathrm{d}P(m,n;t)}{\mathrm{d}t} = \Big[(\xi^{+1,-1}-1)mk_a + (\xi^{+1,0}-1)mk_b + (\xi^{-1,+1}-1)nk_{\mathrm{on}} + (\xi^{-1,0}-1)(L_0-m-n)k_{\mathrm{on}}\Big]P. \tag{5.1}$$

Here $\xi^{i,j}$ is the step operator: $\xi^{i,j}G(m,n) = G(m+i, n+j)$ for any function $G(m,n)$. We assume that free tethers and free BCRs are abundant, which do not change much during reactions. In addition, we assume two binding interfaces (BCR-Ag and APC-Ag) share the same diffusion-limited on-rate k_{on} but differ in their off-rates. The off-rates of APC-Ag bond (k_a^{off}) and of BCR-Ag bond (k_b^{off}) are given by,

$$k_a(m) = k_0 e^{-(\Delta G_a^{\ddagger} - \frac{F x_a^{\ddagger}}{m})/k_{\mathrm{B}}T}, \tag{5.2a}$$

$$k_b(m) = k_0 e^{-(\Delta G_b^{\ddagger} - \frac{F x_b^{\ddagger}}{m})/k_{\mathrm{B}}T}. \tag{5.2b}$$

Here the off-rates depend on the force per closed bond F/m, where F is the total force on the entire cluster, and m is the instantaneous cluster size. $\Delta G_a^{\ddagger}$ and $\Delta G_b^{\ddagger}$ are respectively the APC-Ag binding affinity and BCR-Ag binding affinity. $x_a^{\ddagger}$ and $x_b^{\ddagger}$ are bond lengths. k_0 accounts for other factors that are not considered in our model, such as the effect of

membrane fluctuations. The above process is the same as the model in chapter 4. The differences lie in the force scheme and the initial condition, as we describe below.

Force schemes To model dynamical forces, we utilize the phenomenological functions with tunable parameters. Experiments show that the force produced by B cell can be dynamic and correlated with the ligand-receptor binding state [32, 23]. Explicitly, we consider time-dependent dynamic force and cluster size-dependent force, which are assumed to take the following forms

$$F(t) = F_0 \frac{t^\beta}{t^\beta + t_c^\beta}, \quad \text{or} \quad F(m_{\max}) = F_0 \frac{m_{\max}^\beta}{m_{\max}^\beta + m_c^\beta}. \tag{5.3}$$

Here, F_0 controls the force magnitude, and t_c or m_c characterizes the on-set threshold. $m_{\max}(t) = \max_{t'<t}[m(t')]$ is the maximal cluster size in the history of a cluster. The non-linearity is determined by β: small β corresponds to early force initiation but slow force development, whereas large β represents step-like force (Fig. 5.1B). By tuning parameters, we are able to cover a wide range of possible force schemes.

Stochastic reaction simulations We use Gillespie algorithm [145] to simulate the stochastic reactions associated with Eq. 5.1. The reactions include: (1)binding between BCR and antigen: BCR + Ag $\rightarrow$ BCR-Ag; (2)unbinding between BCR and antigen: BCR-Ag $\rightarrow$ BCR + Ag; (3)unbinding between APC and antigen: APC-Ag $\rightarrow$ APC + Ag; (4) binding between APC and antigen: APC + Ag $\rightarrow$ APC-Ag. The reaction rates are the same as what appears in the master equation. For the time-dependent force, we use a stochastic reaction to simulate the change in force: $F \rightarrow F + \Delta F$. ΔF is fixed at 1pN and the reaction rate is determined according to the force schedule. To avoid unrealistically short contact, we require the contact to be greater than $t_{\min} = 1$s. Besides, to avoid unrealistically long contact, we also end the simulation when the time reaches an upper limit $t_{\max} = 30$min. Note that in the stochastic reaction simulations, molecules are unlabeled. Thus, we can only keep track of the number of complexes, (m, n).

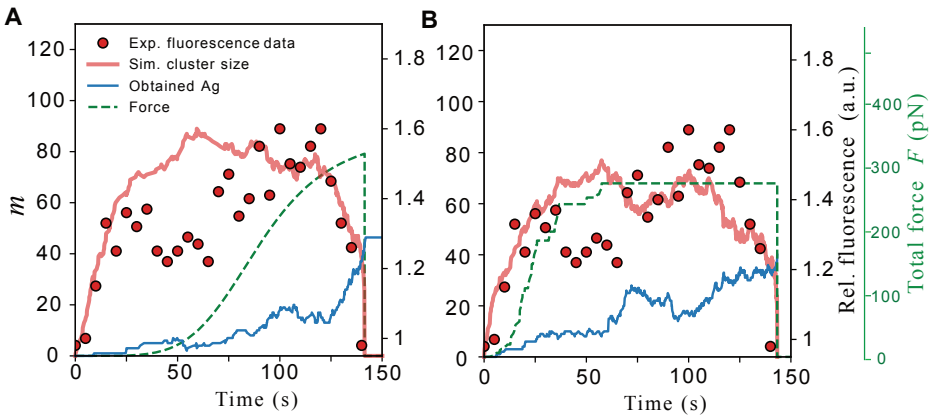

Figure 5.2: Simulated trajectories (solid line) reproduce experimental observations (symbols). Experiment data was extracted from [2]. A time-dependent $F(t)$ was used in the simulation for panel (A). Panel (B) shows a trajectory under cluster-size-dependent force. Parameters: $L_0 = 100, k_{\text{on}} = 0.05\text{s}^{-1}, \Delta G_a^{\ddagger} = 12.6k_{\text{B}}T, \Delta G_b^{\ddagger} = 13.3k_{\text{B}}T$. Force parameter: $F_0 = 350\text{pN}$, $\beta = 5$, $t_c = 1.5\text{min}, m_c = 60$.

Agent-based simulation To better understand the process, we perform explicit agent-based simulation according to the trajectory obtained in the stochastic reaction simulations. The Gillespie algorithm above generates a time series of reaction events. For each reaction event, we randomly draw individual agents (i.e., BCR, Ag, etc.) to perform the reaction explicitly. Because all complexes are labeled and distinguishable in the agent-based simulation, we can keep track of all visited antigens and unvisited antigens. This allows us to get the total number of visited antigens (those who have bound to BCR, m_{tot}, see definition in section 5.3.2 below).

5.3 Results

5.3.1 Cluster formation and dissociation dynamics

Recently, a lot of efforts have been devoted to visualize the interaction between B cells and APCs at different scales using advanced imaging technique [30, 34, 52, 2, 32, 6]. Experiments vividly show that binding of B cell receptor to antigen ligands leads to synapse formation followed by antigen acquisition [30]. Despite the difference in synapse architecture [32], pulling force, affinity selection threshold [6] between germinal center B cells and naive B cells, the cluster formation-disassociation process is shared by all observations [2]. In this section, we show that our model reproduces the observed dynamics. Furthermore, by analyzing a mean filed model in the deterministic picture, we discuss how the criticality emerges and influences dynamics.

In Fig. 5.2, we overlay the simulated trajectories $m(t)$ above the experimental data obtained from real-time fluorescence imaging, which shows beautiful agreement. At the beginning of a contact, the cluster grows because the pulling force is small. When the force is large enough, a cascade of unbinding reactions takes place, leading to rapid cluster dissociation. This is a feature of load sharing: the more bond breaks, the larger force per bond applied to complexes that remain closed. Therefore, the disassociation is accelerated over time during the rupture stage. At the end of the interaction when all complexes are ruptured, some antigens are acquired by the B cell, whereas others remain on APC. It should be noted that though the cluster formation and rupture cascade are ubiquitous in all simulations that successfully break the cluster, the timescale of contact may vary significantly between different parameter settings or even different realizations. In some cases, if the force is too weak, clusters never break before our simulation terminates.

To gain a quantitative understanding, we look at a mean field model. In the deterministic

picture, dynamics of Eq. 5.1 can be described by the following ODE,

$$\frac{\mathrm{d}m}{\mathrm{d}t} = -(k_a(m) + k_b(m))m + k_{\mathrm{on}}(L_0 - m - n) + k_{\mathrm{on}}n, \tag{5.4a}$$

$$\frac{\mathrm{d}n}{\mathrm{d}t} = k_a(m)m - k_{\mathrm{on}}n. \tag{5.4b}$$

Note that this mean field equation applies when $m \geq 1$. $m = 0$ is an absorbing boundary. To find the steady state under a given force F, we solve for $dm/dt = 0, dn/dt = 0$. This provides a condition for steady state cluster size m_s, reading as

$$(L_0 - m_s)k_{\mathrm{on}} = m_s(k_a(m_s) + k_b(m_s)), \tag{5.5}$$

which balances the on- and off-propensity. Steady states of Eq. 5.4 exist if the above equation has solutions. Otherwise, the system will be driven to the absorbing boundary at $m = 0$. Fig. 5.3 shows l.h.s. and r.h.s. of Eq. 5.5. It suggests that, under a small force F, there are two crossing points which correspond to two steady states (denoted as m_s^{low} and m_s^{high}). As force increases, two steady solutions converge and disappear, indicating a bifurcation transition. Perturbation analysis suggests that the larger solution m_s^{high} is stable, whereas the smaller one m_s^{low} is unstable.

To find the critical force at the point of bifurcation, F^*, we solve the following condition in addition to Eq. 5.5,

$$\frac{\mathrm{d}}{\mathrm{d}m_s}k_{\mathrm{on}}(L_0 - m_s) = \frac{\mathrm{d}}{\mathrm{d}m_s}m_s(k_a(m_s) + k_b(m_s)). \tag{5.6}$$

This locates the point along the steady state curve m_s-F where the gradient over m vanishes. For given internal parameters $(k_a, k_b, k_{\mathrm{on}}, L_0, f_a, f_b)$, the solution (F^*, m^*) does not have explicit form. Hence, to get analytical understanding, we consider the limit of strong BCR ($k_a(m_s) \gg k_b(m_s)$) or weak BCR ($k_a(m_s) \ll k_b(m_s)$). In the former case, we let $f \equiv f_a, K \equiv k_{\mathrm{on}}/(k_0 e^{-\Delta G_a^{\ddagger}/k_{\mathrm{B}}T})$. For the later case, we let $f \equiv f_b, K \equiv k_{\mathrm{on}}/(k_0 e^{-\Delta G_b^{\ddagger}/k_{\mathrm{B}}T})$. The condition for bifurcation point becomes

$$m^* e^{\frac{F^*}{m^* f}} \approx K(L_0 - m^*), \tag{5.7a}$$

$$(1 - \frac{F^*}{m^* f})e^{\frac{F^*}{m^* f}} \approx -K. \tag{5.7b}$$

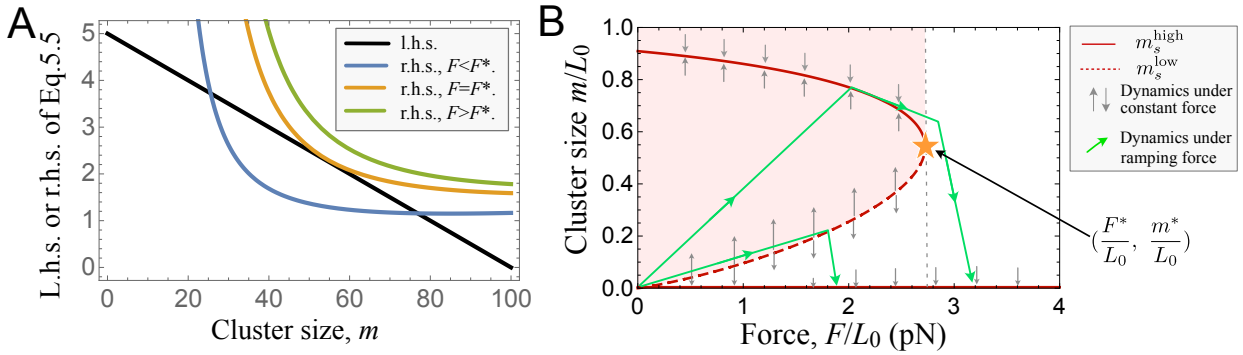

Figure 5.3: Steady state and bifurcation curve in the deterministic picture, under a constant force. (A)We plot the l.h.s. (black line) and r.h.s. (colorful lines) of Eq. 5.5. Under a large force, the system does not have a non-zero steady solution. (B)The system undergoes a bifurcation behavior as force increases. The red lines are numerical solutions to Eq. 5.5. We label the bifurcation tipping point by a star. Gray arrows show the evolution trajectory under constant force, determined by perturbation analysis. The green arrows show two schematic plots of typical trajectories under a ramping force. Thus, deterministically, the cluster is stable when $m > m_s^{\text{low}}$ and $F < F^*$ (the region in red), and it becomes unstable when $m < m_s^{\text{low}}$ or $F > F^*$ (the white region).

This gives

$$F^* \approx L_0 f \mathrm{pln}(\frac{K}{e}), \tag{5.8a}$$

$$m^* \approx L_0 \frac{\mathrm{pln}(\frac{K}{e})}{\mathrm{pln}(\frac{K}{e})+1}. \tag{5.8b}$$

Here $\mathrm{pln}(a)$ is defined as the solution x to $xe^x = a$. e is the Euler's number. The results above resemble what Bell found [15] except that now the critical force is characterized by the weaker bond (the bond that can resist a smaller force) in the bond chain structure. Finally, we combine the strong BCR limit and weak BCR limit, and express the critical point in a general formula:

$$F^* \approx L_0 \min\left(f_a \mathrm{pln}(\frac{k_{\mathrm{on}}}{k_0 e^{1-\Delta G_a^{\ddagger}/k_{\mathrm{B}}T}}),\quad f_b \mathrm{pln}(\frac{k_{\mathrm{on}}}{k_0 e^{1-\Delta G_b^{\ddagger}/k_{\mathrm{B}}T}})\right), \tag{5.9a}$$

$$m^* \approx L_0 \min\left(\frac{\mathrm{pln}(\frac{k_{\mathrm{on}}}{k_0 e^{1-\Delta G_a^{\ddagger}/k_{\mathrm{B}}T}})}{\mathrm{pln}(\frac{k_{\mathrm{on}}}{k_0 e^{1-\Delta G_a^{\ddagger}/k_{\mathrm{B}}T}})+1},\quad \frac{\mathrm{pln}(\frac{k_{\mathrm{on}}}{k_0 e^{1-\Delta G_b^{\ddagger}/k_{\mathrm{B}}T}})}{\mathrm{pln}(\frac{k_{\mathrm{on}}}{k_0 e^{1-\Delta G_b^{\ddagger}/k_{\mathrm{B}}T}})+1}\right). \tag{5.9b}$$

Numerical solution of Eq. 5.5 and Eq. 5.6 agree well with the above approximation. The system is unstable when $F > F^*$. Thus, F^* characterizes the maximal force a cluster can resist in the deterministic picture. From Eq. 5.9, we can see the critical force scales linearly with L_0.

The mean field analysis above tells us when the cluster is likely to break. First, when F is small, if the cluster size is below $m_s^{\mathrm{low}}(F)$, it may disassociate quickly without reaching the stable equilibrium cluster size m_s^{high} due to the large force per bond (see the bottom green trajectory in Fig. 5.3B). Second, when force is beyond the critical value F^*, no non-zero m_s exists and thereby the cluster is unlikely to maintain (see the top green trajectory in Fig. 5.3B). Therefore, one expect a fast force directly rupture the system when m is below m_s^{low}, whereas a large force ($F > F^*$) is needed to break the cluster if force develops slowly.

5.3.2 Contact duration and extracted antigen number

Two measurable quantities about the interaction dynamics are (1) the total contact duration and (2) the number of extracted antigen [25, 33]. In this section, we discuss the influence of

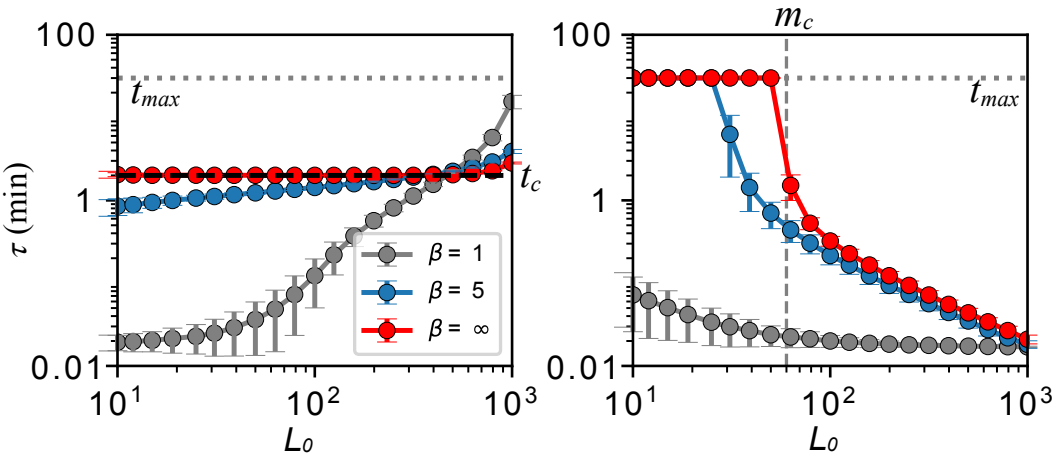

Figure 5.4: Different forcing schemes yield distinct scaling relationships between contact duration and antigen density. Each symbol shows the average contact duration τ of 1000 independent simulations. Error bars show the standard deviation. Under time-dependent force (left panel), the contact duration increases with ligand number. In contrast, under cluster-size-dependent force (right panel), the duration decreases with L_0. Note that we terminated the simulation at $t_{\max} = 30$min when the cluster didn't break before that. Parameters: $\Delta G_a^{\ddagger} = 12.6 k_{\mathrm{B}}T$, $\Delta G_b^{\ddagger} = 15 k_{\mathrm{B}}T$, $F_0 = 4000$pN, t_c=2min, m_c=60.

different force schemes on the timescale of contact and the efficiency of antigen extraction.

Contact duration We first look at the average contact duration τ as a function of ligand number L_0 (Fig. 5.4). Interestingly, the scaling relationship between τ and L_0 varies as the underlying force scheme changes. Under a time-dependent force $F(t)$, more ligands always result in longer expected contact. In contrast, τ decreases with L_0 under $F(m_{\max})$. This qualitative difference arises from a simple principle: The contact duration is mostly determined by the time when the force is large enough to stop cluster growth and break all closed complexes. The time it takes B cell to develop a large enough force depends on how the force is triggered. We show this explicitly below.

For a slowly developing force that is time-dependent $F(t)$, the system collapses when F goes beyond the bifurcation point F^*. When $F_0 \gg F^*$, we have $F(t) \approx F_0(\frac{t}{t_c})^\beta$. Then, the condition $F(\tau) \approx F^* \propto L_0$ indicates that

$$\tau \propto L_0^{1/\beta}. \tag{5.10}$$

In contrast, for a cluster size sensing force, the contact duration is determined by the time it takes to form a large enough cluster, that is $F(m_{\max}(\tau)) \approx F^*$. To get a simple scaling relation, we assume the force is step-like ($\beta = \infty$). Because there is no force before m reaches $m_{\max}$, we can solve the ODE Eq. 5.4 to get $m_{\max}(t) = m(t) = L_0 k_{\text{on}}(1-e^{-(k_{\text{on}}+k_a+k_b)t})/(k_{\text{on}}+k_a+k_b) \approx L_0 k_{\text{on}} t$. The approximation holds when $t \ll 1/(k_{\text{on}}+k_a+k_b)$. The condition $m_{\max}(\tau) \approx m_c$ suggests that

$$\tau \approx \frac{m_c}{L_0 k_{\text{on}}} \propto L_0^{-1}. \tag{5.11}$$

The scaling relationships agree with simulation results well (Fig. 5.4).

Therefore, the distinct scaling relationships imply that one might be able to determine what force scheme is used by a B cell via quantifying the dependence of contact duration on free antigen ligand number. Specifically, if higher ligand density results in longer contact,

then B cells might read the binding time to trigger force. In contrast, force might be cluster-size dependent if contact duration gets shorter when more ligands are available.

Number of extracted antigens While the contact duration is mostly determined by the cluster formation stage, the number of extracted antigen n_{ag} depends on both the cluster formation and disassociation progress. First, a B cell must bind to Ag in order to obtain it. We define m_{tot} as the total number of distinct Ags that have been visited by BCRs. Note that m_{tot} can be larger than m_{max} because unbinding may happen before a BCR visits a new antigen ligand. Second, in the dissociation stage, an Ag is successfully extracted when BCR-Ag bond persists longer than APC-Ag bond. Since BCR-Ag lifetime and APC-Ag lifetime are assumed to be independent, antigen extraction becomes coin-flipping event, meaning the B cell gets a antigen with a chance η. Note that η may change as force per bond changes. Explicitly,

$$\eta(f_r) = \frac{1}{1+\frac{k_b}{k_a}} = \frac{1}{1+e^{(\Delta G_a^\ddagger - \Delta G_b^\ddagger - f_r(x_a^\ddagger - x_b^\ddagger))/k_{\mathrm{B}}T}}, \tag{5.12}$$

where f_r is the force per bond right before the bond rupture. For stiff APCs ($x_a^\ddagger < x_b^\ddagger$), the larger the force, the lower the extraction probability. Besides, η depends on BCR affinity $\Delta G_b^\ddagger$: As $\Delta G_b^\ddagger$ improves, η increases from 0 to 1. Therefore, antigen extraction becomes m_{tot} Bernoulli events (with different η because the values of f_r are different). Explicitly,

$$n_{\mathrm{ag}} = \sum_{i=1}^{m_{\mathrm{tot}}} X_i, \tag{5.13}$$

where $X_i \in \{0,1\}$ is a random variable indicating whether i-th antigen is successfully extracted or not. From this perspective, the distribution of n_{ag} can be written as

$$P(n_{\mathrm{ag}}) = \sum_{m_{\mathrm{tot}}=0}^{L_0} P(m_{\mathrm{tot}}) P(n_{\mathrm{ag}}|m_{\mathrm{tot}}), \tag{5.14}$$

where $P(n_{\mathrm{ag}}|m_{\mathrm{tot}}) = \mathrm{Prob}(\sum_{i=1}^{m_{\mathrm{tot}}} X_i = n_{\mathrm{ag}})$. $P(m_{\mathrm{tot}})$ and $P(n_{\mathrm{ag}}|m_{\mathrm{tot}})$ can be obtained from agent-based simulations. The above formula suggests that the more antigens a B cell encounters, or the larger the extraction chance, the more antigens a B cell can acquire.

To provide more analytical understanding of the distribution $P(n_{\text{ag}})$, we look at the first two moments, the mean μ_n and the variance σ_n^2. From Eq. 5.13, we have

$$\mu_n \equiv \langle n_{ag} \rangle = \langle \sum_{i=1}^{m_{tot}} X_i \rangle = \langle \sum_{i=1}^{m_{tot}} \eta(f_{r,i}) \rangle \approx \langle m_{tot} \int \eta(f_r) P(f_r) df_r \rangle = \langle m_{\text{tot}} \overline{\eta} \rangle. \tag{5.15}$$

Because for each antigen, extraction is a coin-flipping event, $\langle X_i \rangle_{m_{\text{tot}}, f_{r,i}} = \eta(f_{r,i})$, where $\langle \cdot \rangle_{m_{tot}, f_{r,i}}$ is averaging many realizations that have the same m_{tot} and same rupture force for i-th antigen $f_{r,i}$. $P(f_r)$ is the rupture force per bond distribution across all visited m_{tot} antigens. $\langle \cdot \rangle$ is the ensemble average, i.e., averaging many independent realizations (with labeled antigens). $\overline{\eta}$ is the mean extraction chance, averaged over the force per bond distribution $P(f_r)$. We can clearly see it depends on both the cluster formation m_{tot} and the extraction chance $\overline{\eta}$. Meanwhile, the variance can be expressed as

$$\sigma_n^2 \equiv \langle n_{\text{ag}}^2 \rangle - \langle n_{\text{ag}} \rangle^2. \tag{5.16}$$

Although it is difficult to find the explicit expression for μ_n and σ_n^2 in general, we can gain analytical understanding in some special cases. For instance, if a large step force F_0 applies long after the system reaches an equilibrium state $m_s = m_s^{\text{high}}(F = 0)$, we have $m_{\text{tot}} = L_0$ (all antigens will be visited given a long enough time at the equilibrium state). The rupture force per bonds are $\{f_r\} = \{\underbrace{0, ..., 0}_{L_0 - m_s}, \underbrace{\frac{F_0}{m_s}, \frac{F_0}{m_s - 1}, ..., F_0}_{m_s}\}$. Therefore,

$$\mu_n = \underbrace{(L_0 - m_s)\eta(0)}_{\text{extraction at equi.}} + \underbrace{\sum_{i=1}^{m_s} \eta(\frac{F_0}{i})}_{\text{extraction during rupture}}, \tag{5.17a}$$

$$\sigma_n^2 = (L_0 - m_s)\eta(0)[1 - \eta(0)] + \sum_{i=1}^{m_s} \eta(\frac{F_0}{i})[1 - \eta(\frac{F_0}{i})]. \tag{5.17b}$$

Note that we replaced the integral in Eq. 5.15 and Eq. 5.16 with summation because we know the exact values of force per bond. Furthermore, if the fluctuation in m_{tot} is small compared to itself, then $m_{\text{tot}} \approx \langle m_{\text{tot}} \rangle$. We can simplify Eq. 5.15 and Eq. 5.16 into

$$\mu_n = \langle m_{\text{tot}} \rangle \langle \overline{\eta} \rangle, \tag{5.18}$$

$$\sigma_n^2 \approx \langle m_{\text{tot}} \rangle \langle \overline{\eta} - \overline{\eta^2} \rangle. \tag{5.19}$$

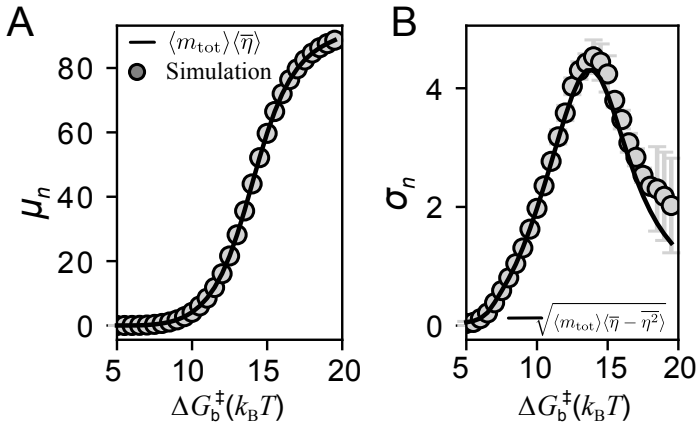

Figure 5.5: Simulation results (symbols) of mean antigen extraction (A) and standard deviations (B) agree with Eq. 5.19 (black lines). We use a time-dependent force ($F_0 = 600$pN, $t_c = 1$min, $\beta = 5$).The fluctuations are larger than expected at high $\Delta G_b^{\ddagger}$, which is because some contact lasts for longer than $t_{\rm max}$.

Here $\overline{\eta^2} \equiv \int_0^\infty \eta^2(f_r)P(f_r)df_r$. When $m_{\rm tot}$ and $P(f_r)$ are available, the above equation can be evaluated from the first principle. Alternatively, $\langle m_{\rm tot}\rangle$ and $\langle\overline{\eta}\rangle$ can be obtained from the agent based simulations. In Fig. 5.5 we show that the above formula agrees with simulation well.

The above analysis clearly suggests that the number of extracted antigens mainly depends on (1) the number of antigen ligands have been visited by BCR during the contact; (2) the average chance to obtain an antigen when the three-body complex breaks. In the next section, we discuss how different force schemes modulate those two factors and influence affinity discrimination.

5.3.3 Optimal force schemes for affinity discrimination

The functional purpose of antigen extraction is affinity discrimination, that is, higher affinity B cells are expected to get larger number of Ags. In this section, we quantify the affinity

discrimination performance and ask what are the optimal force schemes that give the best affinity discrimination. Our results suggest the optimal force scheme may vary as B cell affinity changes.

Selection fidelity To quantify the performance of affinity discrimination, we use the selection fidelity, namely the probability for a high-affinity B cell to get more antigens than its low-affinity peer. We consider the discrimination between two B cells with different affinities ($\Delta G_b^\ddagger$ vs $\Delta G_b^\ddagger + \epsilon$). A 'correct' selection means that the high-affinity B cell gets more antigen than the low-affinity one and thus is selected for further evolution. Nevertheless, due to the stochastic nature of the antigen extraction process, this is not guaranteed. Thus, the probability for our system to make a correct decision is

$$\xi = \text{Prob}[n_{\text{ag}}(\Delta G_b^\ddagger + \epsilon) > n_{\text{ag}}(\Delta G_b^\ddagger)], \tag{5.20}$$

which can be an evaluation matrix for affinity discrimination. The higher the value of ξ, the better the discrimination.

We are aware of other evaluation matrix such as KL divergence that could potentially be useful, but we prefer to focus on the selection fidelity because it is easy to evaluate using stochastic simulations and is more biologically meaningful.

To provide more intuition about selection fidelity, we discuss some special cases. If two B cells are identical ($\epsilon = 0$), then $\xi = 0.5$, meaning two B cells have equal chance to be selected. If the distribution of $n_{\text{ag}}(\Delta G_b^\ddagger + \epsilon)$ is well separated from the distribution of $n_{\text{ag}}(\Delta G_b^\ddagger)$, then $\xi \approx 1$, suggesting high selection accuracy (Fig. 5.6A). Moreover, if n_{ag} follows Gaussian distributions with affinity-dependent mean $\mu_n(\Delta G_b^\ddagger)$ and variance σ_n^2, in the limit of $\epsilon \ll 1$,

$$\xi \approx \frac{1}{2} + \frac{1}{2\sqrt{\pi}\sigma_n} \frac{\mathrm{d}\mu_n}{\mathrm{d}\Delta G_b^\ddagger} \epsilon. \tag{5.21}$$

Therefore, the selection fidelity is high when (1)the mean antigen extraction is sensitive to affinity change (large $\frac{\mathrm{d}\mu_n}{\mathrm{d}\Delta G_b^\ddagger}$) or (2) n_{ag} is narrowly distributed (small σ_n). Based on our

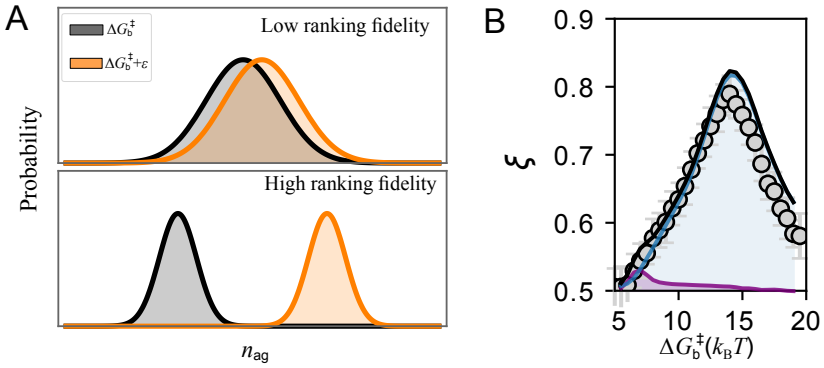

Figure 5.6: (A) Ranking fidelity ξ quantifies how well the extracted antigen distributions of two B cells are separated. (B) The ranking fidelity as a function of BCR-Ag affinity. Symbols were obtained from the simulation. The black curve is the approximation based on Eq. 5.22. We plotted the contribution from cluster size and extraction chance respectively in blue and purple (see Eq. 5.22). We use a time-dependent force($F_0 = 600$pN, $t_c = 1$min, $\beta = 5$). $\epsilon = 0.3k_BT$.

results in Eq. 5.19, we get

$$\frac{\mathrm{d}\mu_n}{\mathrm{d}\Delta G_b^{\ddagger}} \approx \langle\overline{\eta}\rangle \frac{\mathrm{d}\langle m_{\mathrm{tot}}\rangle}{\mathrm{d}\Delta G_b^{\ddagger}} + \langle m_{\mathrm{tot}}\rangle \frac{\mathrm{d}\langle\overline{\eta}\rangle}{\mathrm{d}\Delta G_b^{\ddagger}}, \tag{5.22}$$

which contains two parts: contribution from cluster formation and from cluster disassociation (Fig. 5.6B). Specifically, the first term enters because B cells with different affinities may engage with different number of ligands during a contact, and the second term suggests B cells can be discriminated through extraction chance. Both of the mechanisms have been demonstrated vividly in experiments [31, 2].

Optimal force scheme Then the question is how a dynamical force can help to enhance the fidelity? More specifically, what force scheme can provide the best discrimination?

To find the optimal force scheme, we use the simulated annealing algorithm to optimize ξ for given internal parameters($\Delta G_a^{\ddagger}, \Delta G_b^{\ddagger}, L_0$ etc.) and fixed β. First, we generate random initial parameters (F_0, m_c or t_c), drawn from a uniform distribution within a realistic range

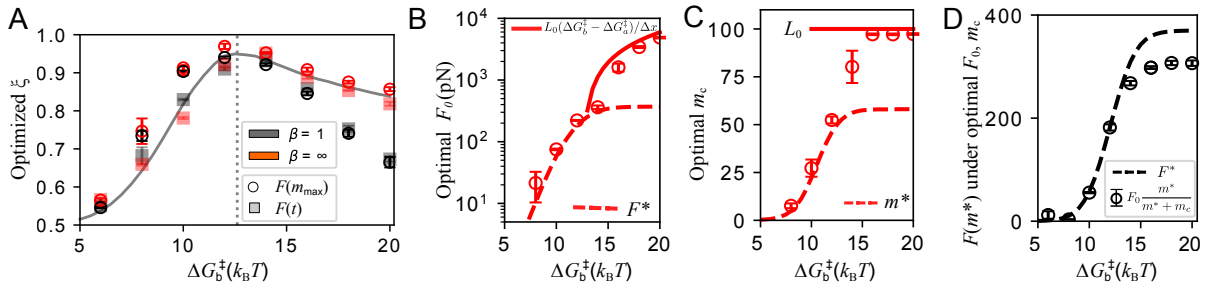

Figure 5.7: (A) To optimize discrimination, dynamical force needs to focus on different stages of antigen acquisition at different BCR affinities. For each β, the simulated annealing algorithm was used to find the optimal fidelity (symbols) at various background BCR affinity $\Delta G_b^\ddagger$. The solid curve, which agrees with the global optimal when $\Delta G_b^\ddagger > \Delta G_a^\ddagger$ but displays significant deviation when $\Delta G_b^\ddagger < \Delta G_a^\ddagger$, shows the optimized fidelity when force applies after the cluster stabilizes and thereby contributes only through the rupture process. The vertical dotted line marks $\Delta G_a^\ddagger$. (B-D) The optimal force parameters that generated the optimized ξ in (A). Panel (A) and (B) (red symbols) are for step force ($F(m_{\max}; \beta = \infty)$). Panel (C) (black symbols), which shows the optimal F_0 and m_c satisfy $F(m^*) = F_0 m^*/(m^* + m_c) = F^*$ at low affinity, is for $F(m_{\max}; \beta = 1)$. Parameters: $L_0 = 100, \Delta G_a^\ddagger = 12.6 k_B T, k_{on} = 0.05 s^{-1}, x_a^\ddagger = 1.5 nm, x_b^\ddagger = 2 nm, \epsilon = 0.5 k_B T$. Error bars were obtained from 5 runs.

($0 < F_0 < 6000$pN, $0 < m_c < L_0$, $t_{\min} < t_c < t_{\max}$). Then we evaluate the fidelity ξ by repeatedly comparing the antigen extraction of two similar B cells for 5000 times. After that, we attempt parameter changes ($F_0' = F_0 + \delta_F, m_c' = m_c + \delta_m, \ln(t_c') = \ln(t_c) + \delta_t$) and evaluate the corresponding fidelity ξ'. Note that t_c is perturbed in a logarithmic scale. The perturbations of δ_F, δ_m and δ_t follow standard normal distributions with standard deviation respectively 200pN, 20, 0.5. Nonphysical perturbations that lead to $m_c < 0$ or too long contact ($t > t_{\max}$) are rejected. We calculate the change in fidelity $\xi' - \xi$ and decide whether to accept the perturbation according to Metropolic-Hastings criterion. Specifically, if the fidelity is improved, we accept the change. Otherwise, we accept it with the probability $P_{\text{accept}} = e^{(\xi'-\xi)/T_0}$. We repeat this perturbation-evaluation-accept procedure for 300 steps. At the same time, we decrease the "temperature" T_0 by $T_0 = 1/i$, where i is the optimization step. This gives us one result of the optimized fidelity and optimal parameters. To make sure that our results are global optimal, we repeat the above process for 5 times starting from different initial parameters. All repeated simulations gave similar results. In addition, we scanned parameters in the realistic range ($0 < F_0 < 2000$pN, $0 < m_c < L_0$, $t_{\min} < t_c < t_{\max}$) with fixed step size, which provided consistent results.

Fig. 5.7 suggests the optimal force schemes depend on the underlying BCR affinity. On the one hand, at high BCR affinity ($\Delta G_b^\ddagger > \Delta G_a^\ddagger$), a step force $\beta = \infty$ (either $F(t)$ or $F(m_{\max})$) gives the optimal ξ. At low $\Delta G_b^\ddagger$, on the other hand, the nonlinearity β is not important, but the force needs to satisfy $F(m^*) = F^*$. We explain these results in detail below.

At high $\Delta G_b^\ddagger$, a step force is needed to produce a large enough rupture force to optimize sensitivity in antigen extraction $d\overline{\eta}/d\Delta G_b^\ddagger$. When $\Delta G_b^\ddagger > \Delta G_a^\ddagger$, cluster formation is limited by $\Delta G_a^\ddagger$ and weakly depends on $\Delta G_b^\ddagger$. Hence, the sensitivity mostly comes from the rupture process. In fact, the optimal ξ can be reached if force only contributes through the rupture stage(Fig. 5.7A). To maximize ξ, one needs a large m_{tot} and a large $d\overline{\eta}/d\Delta G_b^\ddagger$. The former condition can be satisfied by a large on-set condition (m_c or t_c). The later one requires a

proper rupture force to close the affinity gap between BCR and tether, because $d\overline{\eta}/d\Delta G_b^{\ddagger}$ peaks at $k_b^{\text{off}} = k_a^{\text{off}}$, that is

$$F\Delta x/m_r \approx \Delta G_b^{\ddagger} - \Delta G_a^{\ddagger}. \tag{5.23}$$

m_r is the cluster size right before force application. For a step force, this can be achieved by tuning F_0 accordingly (Fig. 5.7B-C). However, if force increases gradually, Eq. 5.23 cannot be met at high $\Delta G_b^{\ddagger}$ because the system will quickly collapse once the force exceeds F^*. That's why a step force is expected to optimize the discrimination.

In contrast, at low $\Delta G_b^{\ddagger}$, a dynamical force that controls cluster formation optimizes discrimination. In Fig. 5.7A we show the fidelity at low $\Delta G_b^{\ddagger}$ can be significantly improved if the force is applied before cluster formation reaches the steady state (symbols above the solid line), implying that the cluster formation can play an important role. More intriguingly, the optimal force schemes at low $\Delta G_b^{\ddagger}$ satisfies a general condition (Fig. 5.7B-D), that is

$$F(m^*) = F_0 \frac{(m^*)^{\beta}}{(m^*)^{\beta} + m_c^{\beta}} = F^*. \tag{5.24}$$

This is due to the high sensitivity of cluster formation near the tipping point in the steady state curve (Fig. 5.3), which corresponds to the bifurcation transition. Near the tipping point, a small increase (say ϵ) in $\Delta G_b^{\ddagger}$ greatly changes the dynamics from force driven disassociation ($F > F^*(\Delta G_b^{\ddagger})$, small m_{tot}) to fluctuation driven disassociation ($F < F^*(\Delta G_b^{\ddagger} + \epsilon)$, large m_{tot}). Therefore, to maximize $dm_{\text{tot}}/d\Delta G_b^{\ddagger}$, the applied force needs to guide the system towards the bifurcation point ($F = F^*, m = m^*$). To achieve this, a cluster-size dependent force satisfying Eq. 5.24 is desired.

In practical, even though it might be impossible for a B cell to know precisely where is the tipping point or what is the force that matches the affinity gap, our results are still meaningful because they imply different strategies should be deployed depending on whether $\Delta G_b^{\ddagger}$ is below or above $\Delta G_a^{\ddagger}$, a critical affinity might be known by B cells. This is because the tether bonds consist of antibodies generated by plasma cells. Thus, in the early stage

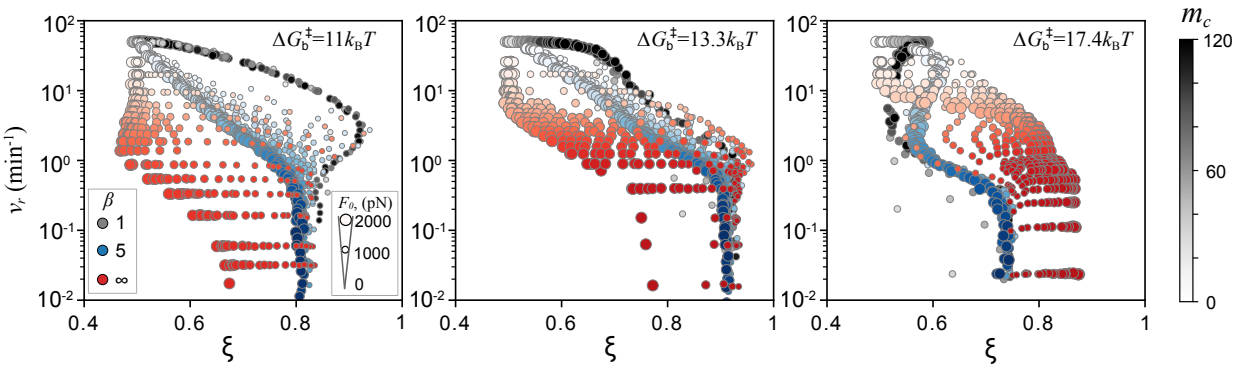

Figure 5.8: Discrimination by antigen extraction exhibits speed-fidelity trade-off. We plot speed against fidelity, evaluated for sampled force schedules (changing F_0, β, and t_c) at different affinity (from left to right, $\Delta G_b^{\ddagger} = 11k_BT$, $13.3k_BT$, $17.4k_BT$). Each symbol represents the average of 10000 independent runs for one parameter set. The value of F_0, β and m_c are coded in the size, color and opacity of each symbol, respectively. The figure shows that, at high $\Delta G_b^{\ddagger}$ (right), a step force sets the Pareto front, whereas a linear sensing force can optimize the trade-off at low $\Delta G_b^{\ddagger}$(left). Parameters: $\Delta G_a^{\ddagger} = 12.6k_{\mathrm{B}}T, L_0 = 100, k_{\mathrm{on}} = 0.05\mathrm{s}^{-1}$. Time-dependent force was used. Cluster size dependent forces generate similar behavior.

of GC reaction, $\Delta G_b^{\ddagger}$ is roughly equal to or lower than $\Delta G_a^{\ddagger}$. As affinity maturates, $\Delta G_b^{\ddagger}$ becomes higher than $\Delta G_a^{\ddagger}$ due to positive selection. Therefore, our model predicts a switch of forcing scheme during the progress of affinity maturation to optimize affinity discrimination, consistent with our results in chapter 4.

5.3.4 Discrimination speed and fidelity trade-off

One common feature in cellular sensing or discrimination task is the trade-off between fidelity and speed [123, 146, 147]. In the traditional proofreading scheme, the fidelity was enhanced at a cost of signaling transmitting speed. In practice, therefore, biological systems may not be able to reach the optimal limit due to time constrains.

Here, the antigen extraction process provides distinct ways to sense and discriminate

BCR affinity. Are there similar constrains in this physical process? Our results suggest that a trade-off between speed and fidelity also emerges in B cell affinity discrimination. To show this, we consider the selection fidelity and speed $v = 1/\tau$.

Speed and discrimination fidelity for various sampled value of F_0 and β are depicted in Fig. 5.8, which shows that adjusting the force scheme can trade off fidelity against speed. Specifically, for a fixed nonlinearity β, the value of F_0 sets the Pareto front in the fidelity-speed diagram, whereas the onset time t_c (or cluster size m_c) moves the system along the Pareto front. This trade-off is intuitive from the perspective of information gathering, as it takes time to accumulate BCR-Ag breaking events to infer the binding affinity.

In addition, depending on the affinity, different nonlinearity β results in different Pareto fronts (Fig. 5.8). At high $\Delta G_b^\ddagger$, a step force sets the optimal front. This is because it allows rapid cluster formation, and can generate higher fidelity for a given m_{tot}, as we note in the last section. In contrast, at low $\Delta G_b^\ddagger$, a linear sensing force $\beta = 1$ can optimize the trade-off. At $\beta = 1$, force applies at the beginning of contact, which prevents low-affinity B cells from forming clusters but allows high-affinity ones to have large clusters before extraction. This ensures fast discrimination.

It is worth noting that the trade-off in Fig. 5.8 displays turning points. At low affinity, both ξ and v_r can be optimized simultaneously. The turning point corresponds to the Eq. 5.24 where ξ is maximized by the sensitivity of the bifurcation tipping point. At high affinity, after the turning point, further delaying force application did not improve fidelity much but greatly slowed down the process. Therefore, the turning points provide an optimal solution to balance speed and discrimination fidelity when BCR affinity is low.

5.3.5 Absolute discrimination by cluster sensing force

Another intriguing feature of affinity discrimination is its insensitivity to variations in ligand concentration. Fluorescent images display inhomogeneous distribution of antigens across

GC. Different B cells show distinct migrating paths in GC [52], which implies that some B cells might see more antigens (larger L_0) than others. Nevertheless, the selection should be only based on B cell's quality (affinity) and independent of seen antigen quantities (L_0). How B cells could overcome the heterogeneity of antigen distribution and make discrimination "absolute"? Is it possible to utilize mechanical control to separate receptor quality from ligand quantity? In this section, we show that the cluster-size-dependent force indeed can reduce the dependence of antigen extraction on ligand number and achieve absolute discrimination.

We show that if a B cell is able to sense the cluster size and apply force accordingly in a non-linear form, it can provide negative feedback. As shown in Fig. 5.9A, for cluster-size-dependent force with $\beta > 1$, the force per bond F/m increases with cluster size before the total force saturates. In other words, the larger the cluster size, the larger the force per bond, and it is harder to form new complexes. This is similar to the negative feedback provided by SHP-1 in TCR signaling cascade[105], but now the feedback is provided by mechanical force, rather than chemical signaling, and can be regulated by changing the force schedule.

The negative feedback provided by the mechanical control can decouple receptor quality from ligand quantity. To show this, we quantify the sensitivity of antigen extraction to affinity change and to ligand number change respectively using

$$\alpha_E = \frac{1}{\sigma_n}\frac{\mathrm{d}\mu_n}{\mathrm{d}\Delta G_b^{\ddagger}}, \qquad \alpha_L = \frac{1}{\sigma_n}\frac{\mathrm{d}\mu_n}{\mathrm{d}L_0}. \tag{5.25}$$

In Fig. 5.9B we show α_L and α_E simultaneously at various force schemes. For time-dependent force, α_L and α_E are strongly correlated. In contrast, non-linear cluster-size-dependent force can achieve high α_E while maintaining low α_L, meaning the antigen extraction is sensitive to affinity improvement but insensitive to perturbation in L_0. This is because the negative feedback reduces the dependence of max cluster size on L_0. Meanwhile, the antigen extraction chance η is still affinity-dependent, which preserves the affinity information in n_{ag}.

To see how the above difference in sensitivity propagates into the selection fidelity, we look

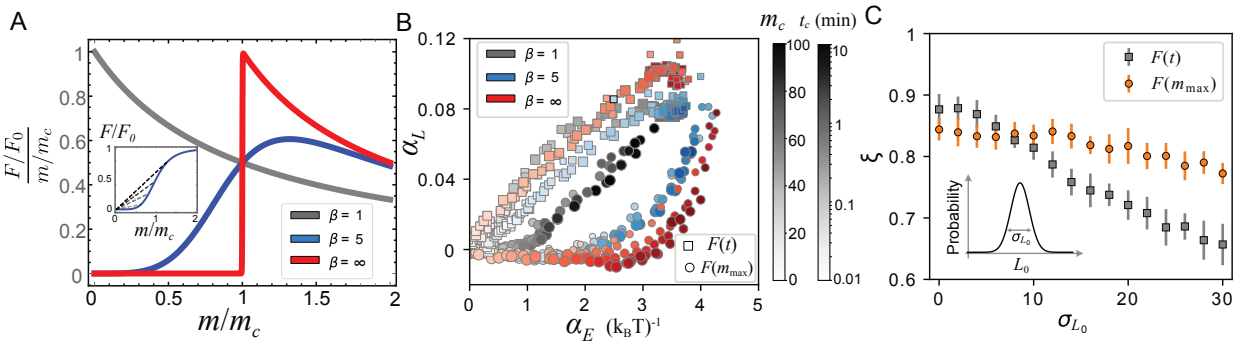

Figure 5.9: Non-linear cluster-sensing force enables absolute affinity discrimination. (A) The force per bond (F/m) of a sensing force increases with cluster size m before F saturates for $\beta > 1$, providing the negative feedback (the larger the cluster, the larger the force per bond). The inset shows $F(m, \beta = 5)$, where the force per bond is represented by the slope of dashed lines. (B) We systematically scan force parameters (F_0, β, m_c (or t_c)) and plot the sensitivity to ligand number change $\sigma_L = \frac{1}{\sigma_n}\frac{\mathrm{d}\bar{n}_{\mathrm{ag}}}{\mathrm{d}L_0}$ against the sensitivity to BCR affinity change $\sigma_E = \frac{1}{\sigma_n}\frac{\mathrm{d}\bar{n}_{\mathrm{ag}}}{\mathrm{d}\Delta G_b^{\ddagger}}$. The parameter F_0, β, and m_c (or t_c) are respectively represented by the size, color and color gradient of symbols. F_0 was chosen from 100pN to 1000pN with a spacing of 100pN. We see the sensing force can provide high α_E with low α_L. α_E and α_L are calculated using Euler method, averaged from 6000 runs. (C) Discrimination performance is robust to ligand number fluctuation under $F(m_{\max})$. In each realization, the antigen number L_0 seen by a B cell is sampled from a Gaussian distribution with variance σ_L. We simulate 6000 pairs of B cells to obtain the ranking fidelity. The inset shows the distribution from which L_0 was sampled. Two forces share the same $F_0 = 800$pN and $\beta = 5$. $t_c = 1$min, $m_c = 60$. Other parameters: (B and C) $L_0 = 100, \Delta G_a^{\ddagger} = 12.6k_{\mathrm{B}}T, \Delta G_b^{\ddagger} = 13.3k_{\mathrm{B}}T, k_{\mathrm{on}} = 0.05\mathrm{s}^{-1}$.

at the discrimination performance under a heterogeneous antigen ligand distribution. Instead of fixing antigen ligand number, for each B cell we sample L_0 from a Gaussian distribution $N(L_0, \sigma_L)$ and then perform simulation to calculate the ranking fidelity. As displayed in Fig. 5.9C, as σ_L increases, the fidelity under time-dependent force significantly decreases, whereas the results of cluster-size dependent force only decreases marginally. This indicates that under $F(m_{\max})$, the discrimination is robust to fluctuations of antigen concentration.

5.3.6 Antagonism effect due to coupling through force

In previous sections, we have considered affinity discrimination when only one type of ligands is presented. However, a more realistic situation is that agonist ligands are presented simultaneously with many low affinity (self) ligands. The interaction between different antigens is inevitable. It is indeed experimentally known that the response to agonists is inhibited (or antagonized) when immune cells are exposed to a mixture of agonists and low affinity ligands (antagonists), named antagonism effect, for both T cells and B cells [148, 149, 150, 151]. It gains increasing attention over the years due to its potential application in autoimmune diseases [152] and cocktail vaccines for protections against HIV [153].

As for the antigen acquisition process, it remains unclear how the co-presentation of weak self ligands influences the extraction of strong foreign ligands. Here, we use our model to explore this question and provide qualitative predictions.

To investigate the interference between different antigen types, we consider a minimal model where two types of antigens (Ag1 and Ag2) with distinct off-rates are presented on APC in a well mixed form. B cells blindly bind to and extract two types of antigens, Nevertheless, in the T cell selection step, only the foreign antigen (Ag1) is effective for B cells to compete for T cell help. Since different antigens within a cluster trigger and share the same loading force, acquisition of two types of antigens are coupled through force application. To quantify the interference between different types of antigens, we define antagonism effect

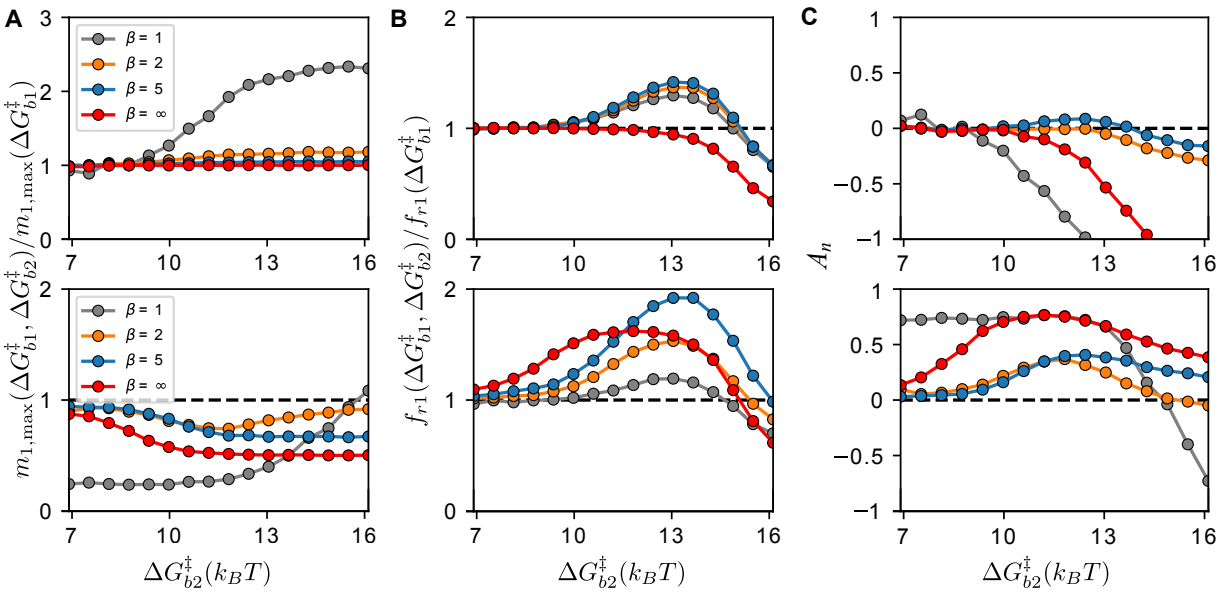

Figure 5.10: **Antagonism due to load sharing in the presence of multiple antigen types**. We compare the max agonist cluster size (A), mean rupture force per bond on agonists (B) between cases with and without antagonists: $m_{1\max}(\Delta G^{\ddagger}_{b1}, \Delta G^{\ddagger}_{b2})/m_{1\max}(\Delta G^{\ddagger}_{b1})$, and $f_{r1}(\Delta G^{\ddagger}_{b1}, \Delta G^{\ddagger}_{b2})/f_{r1}(E_{b1})$. The antagonism effect, quantified by A_n (see Eq. 5.26), is plotted in (C). Top panels are for time-dependent force $F(t)$, and bottom panels are for $F(m_{\max})$. All quantities are an average of 500 runs. Under time-dependent force, the interaction between agonists and antagonists are mostly cooperative $A_n < 0$. In contrast, under $F(m_{\max})$, the interaction is antagonistic $A_n > 0$, because antagonists inhibits agonist cluster formation and agonist extraction. Parameters: $k_{\text{on}} = 0.05\text{s}^{-1}$, $\Delta G^{\ddagger}_a = 12.6k_{\text{B}}T, \Delta G^{\ddagger}_{b1} = 15k_{\text{B}}T$, $L_{10} = L_{20} = 100$. Top panels: $F_0 = 700\text{pN}$, $m_c = 60$. Bottom panels: $F_0 = 500\text{pN}$, $t_c = 1\text{min}$.

by the relative reduction in antigen extraction in the presence of a secondary antigen:

$$A_n \equiv -\frac{\mu_n(\Delta G_{b1}^{\ddagger}, \Delta G_{b2}^{\ddagger}) - \mu_n(\Delta G_{b1}^{\ddagger})}{\mu_n(\Delta G_{b1}^{\ddagger})}, \tag{5.26}$$

where $\mu_n(\Delta G_{b1}^{\ddagger})$ is the mean antigen acquisition when only Ag1 presents and $\mu_n(\Delta G_{b1}^{\ddagger}, \Delta G_{b2}^{\ddagger})$ is the average amount of obtained Ag1 when both Ag1 and Ag2 are available. If two antigens are uncorrelated, we have $A_n = 0$. Our results show the interaction between Ag1 and Ag2 can be cooperative or competitive, depending on the mechanical response provided by B cells. We discuss the interactions in two stages as follows.

First, in the cluster formation stage, if the force is time-dependent, adding Ag2 can promote Ag1 cluster formation by cooperatively sharing the developed forces. In contrast, under cluster sensing force, introducing Ag2 inhibits formation of Ag1 clusters by triggering large pulling forces (Fig. 5.10 A).

Second, in the cluster disassociation stage, those additional Ag2 ligands trigger larger extraction force than Ag1-only case, because the cluster can be larger or persist longer. On the other hand, closed Ag2 bonds can help to share the extraction force so that the average extraction chance for Ag1 gets larger. As we show in Fig. 5.10B, Ag2 with intermediate affinities create the strongest rupture force per bond on Ag1, resulting in the strongest inhibition on extraction chance. This is because the binding of antagonists with intermediate affinity helps to trigger the tugging force which creates large rupture force but does not share the force at the rupture stage.

The overall effect, which depends on affinity, is the combination of interactions in two stages. Our model suggests that under time-dependent force the interaction is mostly cooperative ($A_n < 0$), whereas the cluster sensing force leads to strong antagonism effect ($A_n > 0$) (see Fig. 5.10C). This, together with the observation of antagonism effect in antigen extraction, may imply that B cells use a mechanical sensing force when extracting antigens.

5.4 Discussion

Our model highlighted the interplay between ligand-receptor reaction kinetics and force generation dynamics. Focusing on equilibrium steady states failed to capture the complete picture, as dynamical forces may keep pushing the system away from equilibrium states. Moreover, under rapidly developing force, rupture of the cluster takes place before it reaches the equilibrium. In addition, it is the force-controlled cluster formation-disassociation two-phase process that enables B cells to infer receptor affinity through antigen extraction. Simply counting equilibrium binding may exclude important factors that influence affinity discrimination.

In addition, dynamical force provides a diverse range of degrees of freedom for cells to tune, which enables the system to adapt to a wide range of antigen properties and optimize function needs. For instance, the lifetimes or length-scales of systems with passive ligand-receptor interaction may differ in order of magnitude as on- or off-rates change [128]. In contrast, systems under dynamical force are more adaptable to the changing conditions and needs of the cell. On the one hand, the forcing schedule defines a spatial length- or timescale at which affinity discrimination is performed regardless of antigen affinities or concentrations. This adaptation is especially crucial for B cells due to the wide range of operating parameter space. On the other hand, by simply tuning forcing parameters, the scheme can prioritize speed in one context, and discrimination fidelity in another. Such transition has been observed recently between naive B cells and GC B cells, with GC B cells apply a larger force compared to naive B cells [32, 6]. The activation of naive B cells requires high fidelity since the cost of error can be deadly (autoimmunity), whereas speed is favored in GC B cells for rapid maturation. Another tunable knob provided by dynamical force is the form of feedback. We have shown non-linear cluster sensing forces are able to provide negative feedback on clustering, leading to absolute discrimination.

We analyzed antagonistic effects when mixtures of antigens are presented, which indicated

that the adoption of dynamical force may not be absolutely beneficial. Consistent with recent experiments [154], we assume the triggered forces are shared by all close bonds, which couple different bonds together. This leads to the interference between different antigen types. We show antagonism effect emerges under cluster sensing force, which peaks at intermediate agonists affinities. A similar feature has been observed for T cell receptor antagonists [105]. For B cells, further experiments will be needed to test our predictions.

CHAPTER 6

Coevolution between antigen and immunity

"Now, here, you see, it takes all the running you can do, to keep in the same place. If you want to get somewhere else, you must run at least twice as fast as that!"

Lewis Carroll

6.1 Introduction

While the evolutionary learning process in the germinal center protects living organisms against a vast variety of microscopic invaders, highly variable antigenic challengers, such as fast evolving viruses and cancers, may manage to continuously evade immune recognition through rapid replication and mutation [155, 156]. This leads to a coevolutionary arms races between antigen and immunity that happens on a timescale much longer than GC evolution, and might even endure through an individual's lifetime [11]. How does this coevolution between antigen and immunity takes place? What strategy can be used by the immune system to win the arms race? In this chapter, we will turn to the long-term coevolution between antigen and immunity and explore possible beneficial strategies.

In this coevolution scenario, antigen and receptor populations constitute each other's responsive environment and are mutually driven out of equilibrium: Specific immune receptors

recognize and prey on matching antigens and hence alter both the composition and overall abundance of antigens, which in turn modifies selective pressures on distinct receptors thus causing re-organization of the repertoire, and vice versa. Consequently, neither population has enough time to equilibrate, and yet they mutually engage in a dynamic balance. In this sense, the Red Queen state represents a nonequilibrium steady state [157, 158]. Then the question is whether alternative evolutionary outcomes characteristic of non-steady states occupy a larger volume of the state space of coevolving systems than does the Red Queen state.

Recent progress has been made toward understanding various aspects of coevolutionary dynamics in antigen-immunity systems [68, 159, 160, 161, 162, 163, 164, 165, 166], ranging from antibody evolution against HIV and influenza viruses to evolution of tumors and bacterial phage under host immunity. Yet we are still short of insights into certain fundamental questions: How do receptor repertoire and antigen ensemble mutually organize, when ecological and evolutionary dynamics occur on comparable timescales? What govern the persistence and outcome of mutual adaptation?

In existing generic models where both ecological and evolutionary processes are considered, a separation of timescales is often assumed so that the fast dynamics is slaved to the slow one (reviewed in [167]). In cases where timescales are not treated as separated [168, 169, 170, 171, 172, 173, 174, 175], the feedback between changes in diversity and population dynamics tends to be ignored. The goal of this study is to consider inseparable timescales and at the same time account for feedback effect in order to address the questions raised above.

Specifically, we develop a phenotypic model, based on predator-prey interactions between coevolving immune receptors and antigens, that combines evolutionary diversification and population dynamics. By formulating an ecological model in a trait space, we describe coevolutionary changes in the distribution of trait values and trait-dependent predation in the same framework. Importantly, this allows us to study the stability of speciation (pattern

formation in the trait space) and its impact on the persistence of coevolution. Our model abstracts the key features of adaptive immunity: antigens and receptors move (due to trait-altering mutations) and behave like activators and inhibitors that react through predation; both antigens and receptors are cross-reactive — one receptor recognizes many distinct antigens and one antigen is recognized by multiple receptors — this flexibility in recognition stems from structural conservation of part of the receptor/antigen binding surface [176] and provides an enormous functional degeneracy [177] among distinct immune repertoires; there is no preexisting fitness landscape for either population so that selection pressures are owing purely to predation.

The theory predicts, counterintuitively, that simultaneous patterning in coevolving populations can emerge solely from asymmetric range of activation and inhibition in predator-prey dynamics, without a need for severely large differences in their rate of evolution [178] (aka mobility in their common phenotypic space), thus representing a Turing mechanism distinct from the classic one. This surprising result can be understood from an intuitive picture: colocalized clusters of antigens and receptors form in the trait space when the "inhibition radii" of adjacent receptor clusters overlap so that inhibition of antigen is strongest in between them; whereas alternate clusters emerge if the "activation radii" of neighboring antigen clusters intersect, because then activation of receptor is most intense in the midway. Biologically, receptor activation and antigen inhibition are distinct processes: the assumed asymmetry in reaction range reflects potential distinction between the ability of antigens to induce protective immune responses (immunogenicity) and the ability to interact with the product, such as antibodies, formed by a response (antigenicity). In fact, this discrepancy between antigenicity and immunogenicity has been known for long [179] and demonstrated for both natural and synthetic antigens [180, 181, 182].

We show for the first time that, as asymmetry in cross-reactivity varies, transitions between qualitatively distinct regimes of eco-evolutionary dynamics seen in nature would follow, including persistent coexistence, antigen elimination and unrestrained growth. While

competitive interactions, whether direct or mediated by resource competition, are known to elicit patterns in a population [183, 184, 185, 186], a new interesting outcome of our analysis is, *mutual feedback* between dynamic patterns of antigens and receptors can drive the arms race off balance. Given sufficient asymmetry, spontaneous oscillations in Turing patterns precede antigen extinction, whereas uncontrolled antigen growth follows the formation of alternate quasispecies, as ineffective receptors exhaust the limited immune resources; these measurable features may serve as precusors of the off-balance fates.

Many theoretical studies have considered adaptation to time-varying environments with prescribed environmental statistics [187, 188, 189, 190, 191, 192, 193]. This work makes a step toward a theory of coevolution from the perspective of responsively changing environments (mutual niche construction [194] in ecological terms), highlighting the role of feedback in driving evolution toward novel organization regimes and non-steady states. As new genomic and phenotypic methods are developed to better characterize antigenic [195, 196, 197] and immunological [91, 198, 199, 200] landscapes as well as bidirectional cross-reactivity [201], the predictions for repertoire composition and coevolutionary outcome derived from this study can be compared with high-throughput profiling of coevolving immune repertoire and antigen ensemble in humans [202, 203, 204].

6.2 Model

A finite repertoire of immune receptors that collectively cover the antigenic space while leaving self types intact is conceivable, if the distribution of potential threats is predetermined [205, 206, 207, 70]. Given a fixed distribution of pathogenic challenges, competitive exclusion is shown to drive clustering of cross-reactive receptors [207]. In coevolution, however, antigen distribution is no longer preset but responds to reorganization of receptors. In addition, cross-reactivity is bidirectional: not only can a receptor be activated by a range of distinct antigens, but an antigen can be removed by a variety of receptors. Then, can

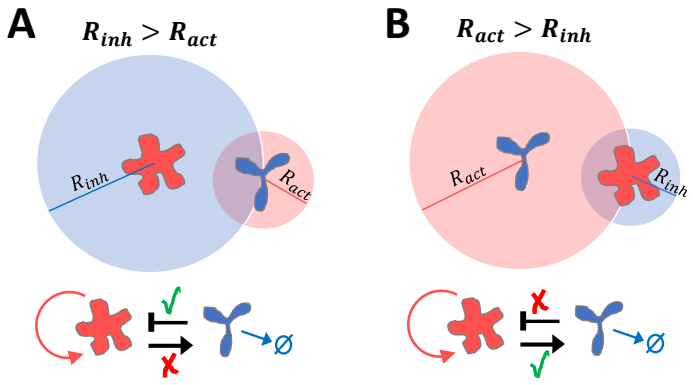

Figure 6.1: Schematic of antigen-receptor interaction with asymmetric range of inhibition and activation in the phenotypic space. (A) $R_{\text{inh}} > R_{\text{act}}$: the receptor (blue Y-shape) is not activated by the antigen (red flower-shape) but nevertheless inhibits it. (B) $R_{\text{act}} > R_{\text{inh}}$: the antigen activates the receptor but is not subject to its inhibition. Lower row: in addition to predation (black arrows; blunt for inhibition, acute for activation), antigens self replicate (red arrow) whereas receptor-expressing cells spontaneously decay (blue arrow pointing to an empty set symbol) in the absence of stimulation. If a finite carrying capacity of receptors, θ_2, is explicitly considered, self-inhibition will also be present (Figs. 6.4C, 6.6B and 6.6C).

predation lead to simultaneous clustering of antigens and receptors in their common trait space? If so, are such patterns stable? Would the concurring patterns interact to affect population dynamics?

To answer these questions, we consider a dynamical system of activators and inhibitors representing antigens and receptors, which diffuse in a shared phenotypic space and react through predator-prey interactions. Population densities of antigens $A(\vec{x},t)$ and receptors $B(\vec{x},t)$ evolve according to

$$\begin{aligned}\partial_t A(\vec{x},t) &= D_1\nabla^2 A(\vec{x},t) + \lambda_1 A(\vec{x},t) - \alpha_1 A(\vec{x},t)\int S_1(|\vec{x}-\vec{y}|;R_{\text{inh}})B(\vec{y},t)\mathrm{d}\vec{y},\\ \partial_t B(\vec{x},t) &= D_2\nabla^2 B(\vec{x},t) - \lambda_2 B(\vec{x},t) + B_{\text{in}} + \alpha_2 B(\vec{x},t)\int S_2(|\vec{x}-\vec{y}|;R_{\text{act}})A(\vec{y},t)\mathrm{d}\vec{y}.\end{aligned} \tag{6.1a}$$

Here, D_1 and D_2 denote isotropic diffusion constants of antigens and receptors, respectively,

that mimic the rates of trait-altering mutations. Other forms of jump kernels do not change qualitative results. Antigens self replicate at rate λ_1 whereas receptors spontaneously decay at rate λ_2. Receptors inhibit antigens with an intrinsic rate α_1 and grow at rate α_2 upon activation; R_{inh} denotes the range of receptors that can inhibit a given antigen, while R_{act} represents the range of antigens by which a receptor can be activated (Fig. 6.1). In real systems, there is likely a distribution of reaction range; we assume a single value to simplify analysis. The term B_{in} corresponds to a small influx of lymphocytes that constantly output from the bone marrow and supply nascent receptors; without stimulation, receptors are uniformly distributed at a resting concentration given by B_{in}/λ_2. We choose the lifetime of receptors, λ_2^{-1}, as the time unit and the linear dimension L of the phenotypic space as the length unit. To account for the discreteness of replicating entities and hence avoid unrealistic revival from vanishingly small population densities, we impose an extinction threshold; antigen or receptor types whose population falls below this threshold are considered extinct and removed from the system.

In the spirit of Perelson and Oster [208], we think of receptors and antigens as points in a high-dimensional phenotypic space, whose coordinates are associated with physical and biochemical properties that affect binding affinity. We assume that the strength of cross-reactive interaction only depends on the relative location, $\vec{r} = \vec{x} - \vec{y}$, of receptor and antigen in this space, as characterized by the non-local interaction kernels $S_1(|\vec{r}|; R_{\text{inh}})$ and $S_2(|\vec{r}|; R_{\text{act}})$. Close proximity indicates good match between the binding pair leading to strong interaction, whereas large separation translates into weak affinity and poor recognition.

Importantly, cross-reactivity is not necessarily symmetric as typically assumed; differences in biophysical conditions among other factors may well render disparate criteria for antigen removal and receptor activation [209, 210], i.e., $R_{\text{inh}} \neq R_{\text{act}}$. For instance, removing an antigen may only require modest on rate (wide reaction range, large R_{inh}) of multiple receptors that together coat its surface, which boils down to multivalent binding and cross-linking at thermal equilibrium. Whereas activating an immune cell expressing a unique type

of receptors can demand lasting antigen stimulation hence small off rate (close match of shape, small R_{act}), so that downstream events leading to a response can finish. How this asymmetry impacts coevolution is our focus.

6.3 Results

6.3.1 Phases under local predator-prey interactions

This reaction-diffusion system (Eq. 6.1) presents a homogeneous fixed point of population densities, $A_s = \lambda_2/(\alpha_2\Omega_2)$ and $B_s = \lambda_1/(\alpha_1\Omega_1)$, where $\Omega_1 = \int \mathrm{d}\vec{r} S_1(|\vec{r}|; R_{\text{inh}})$ and $\Omega_2 = \int \mathrm{d}\vec{r} S_2(|\vec{r}|; R_{\text{act}})$ are respectively the shape-space volume of the "inhibition sphere" centered at an antigen and that of the "activation sphere" surrounding a receptor. When receptor-antigen interactions are local, depending on the ratio of the rates λ_1/λ_2 and diffusivity D_1/D_2, coevolving populations exhibit two main phases within the chosen parameter range (Fig. 6.2A): antigen early extinction (colored region) and persistence (white region); the latter divides into two subphases, steady traveling waves (upper) and uniform coexistence (lower); as seen in typical kymographs of the 1D density fields (insets), starting from localized antigens and uniform receptors.

Extinction is expected when antigens replicate fast (large λ_1/λ_2) but mutate slowly (small D_1/D_2): after a brief delay during which antigen reaches a sufficient prevalence to trigger receptor proliferation, receptors rapidly expand in number and mutate to neighboring types; the pioneer receptors stay ahead of mutating antigens and eliminate them before escape mutants arise. Once antigen is cleared, the receptor population regresses to the resting level (Fig. 6.2B upper panel). With sufficiently high replication rates, faster mutation allows antigen mutants to lead the arms races against receptors resulting in a persistent evolving state — a traveling wave Red Queen state, similar to that shown in a recent model of influenza evolution under cross-immunity [211]. Interestingly, as λ_1/λ_2 increases, while the rate of extinction (color-coded in the phase region) increases, a smaller D_1/D_2 is needed

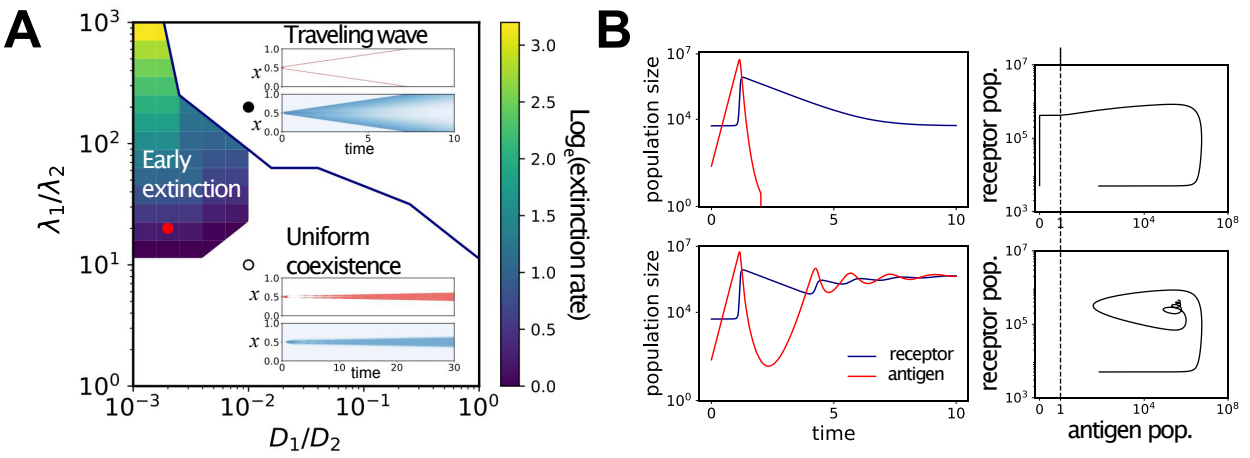

Figure 6.2: Phases in a 1D reaction-diffusion system under local predator-prey interactions. (A) Phase diagram on the plane spanned by the ratio between diffusion constants D_1/D_2 and that between birth and death rates λ_1/λ_2 of antigens (activators) and receptors (inhibitors). Dynamics start from a local dose of antigens and uniform receptors. The early extinction phase is color coded for the logarithm of the inverse time to antigen extinction. The persistence phase (blank) divides into a propagating wave state (upper) and a uniform coexistence state (lower). Insets show typical kymographs in each subphase, red for antigen and blue for receptor; the upper pair corresponds to the filled circle at $\lambda_1/\lambda_2 = 200$, $D_1/D_2 = 10^{-2}$, and the lower one corresponds to the open circle at $\lambda_1/\lambda_2 = 10$, $D_1/D_2 = 10^{-2}$. (B) Representative abundance trajectories. Top: $\lambda_1/\lambda_2 = 20$, $D_1/D_2 = 10^{-3}$ (red dot in panel A); bottom: $\lambda_1/\lambda_2 = 10$, $D_1/D_2 = 10^{-2}$ (white dot in panel A). Corresponding phase plots are shown on the right; vertical dashed lines indicate the extinction threshold. $B_{\mathrm{in}} = 10$, $\alpha_1 = 10^{-3}$, $\alpha_2 = 10^{-4}$.

for transition to the traveling wave state. On the other hand, at modest λ_1/λ_2, a uniform coexistence phase is reached following population cycles dampened by mutation (Fig. 6.2B lower panel). Under local interactions, this homogeneous fixed point is stable to perturbation and does not support spontaneous antigen speciation (i.e., breakup of a continuum into fragments in the shape space). Thus, in what follows, we start from this uniform steady state and introduce the key ingredient — asymmetric nonlocal interaction — to show how it drives spontaneous organization.

6.3.2 Simultaneous patterning under asymmetric cross-reactivity

The analogy between antigen-immunity interaction and predation has been made before [212, 213, 159, 166]; however, spontaneous speciation has not been described yet. On the other hand, for general activator-inhibitor systems — in the physical space — Turing patterns can emerge, either from demographic stochasticity which prevents the system from reaching its homogeneous fixed point [186, 214], or, more classically, from prohibitively large differences in diffusivity between the autocatalytic and the inhibitory reactants [178]. Here, using a simple phenomenological model accounting for cross-reactivity (Eq. 6.1), we show that coevolutionary speciation is possible, without requiring any of the aforementioned patterning mechanisms.

To identify the onset of patterning instability, we perturb the uniform stationary state (A_s, B_s) with non-uniform variations. We define $A(\boldsymbol{x}, t) = A_s + \sum_k \delta A_k \exp(\omega_k t + i\boldsymbol{k}\cdot\boldsymbol{x})$ and $B(\boldsymbol{x}, t) = B_s + \sum_k \delta B_k \exp(\omega_k t + i\boldsymbol{k}\cdot\boldsymbol{x})$. Then we linearize the equation of motion (Eq. 6.1) around the homogeneous fixed point (A_s, B_s) and work in the Fourier space. This gives

$$\omega(k)\begin{pmatrix}\delta A_k\\ \delta B_k\end{pmatrix} = \begin{pmatrix}-D_1k^2 & -\alpha_1 A_s \hat{S}_1(k)\\ \alpha_2 B_s \hat{S}_2(k) & -D_2k^2\end{pmatrix}\begin{pmatrix}\delta A_k\\ \delta B_k\end{pmatrix}, \tag{6.2}$$

where $\hat{S}_1(k)$ and $\hat{S}_2(k)$ are the Fourier transform of interaction kernels $S_1(r)$ and $S_2(r)$, respectively. Solving this characteristic equation gives the dispersion relation, i.e., the linear

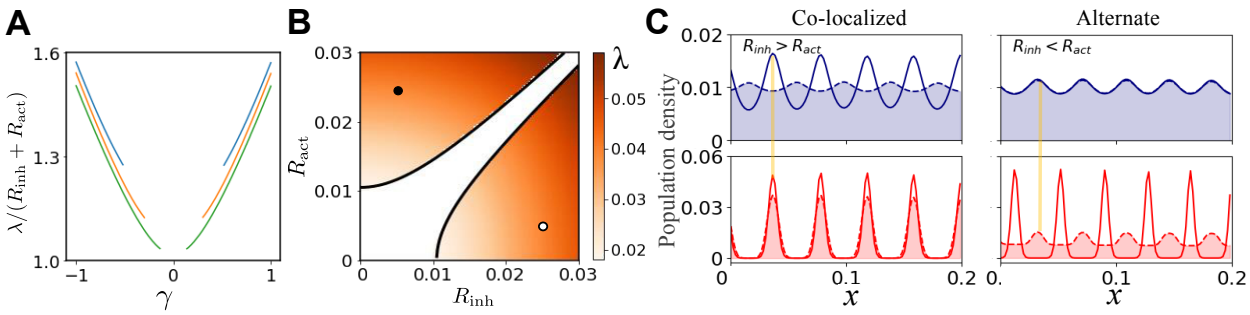

Figure 6.3: Asymmetric cross-reactive interactions simultaneously organize receptor and antigen distributions. (A and B) The pattern wavelength, λ, identical for both populations, is symmetric under the interchange of the interaction ranges $R_{\rm inh}$ and $R_{\rm act}$. (A) The scaled wavelength increases with the extent of asymmetry $\gamma \equiv (R_{\rm inh} - R_{\rm act})/(R_{\rm inh} + R_{\rm act})$; $R_{\rm inh} + R_{\rm act} = 0.015, 0.02, 0.03$ from top to bottom. (B) Pattern diagram in the $(R_{\rm act}, R_{\rm inh})$ plane. The white region corresponds to stable behavior, whereas patterning occurs in the colored areas. Solid lines indicate the instability onset (Eq. 6.8). The color bar shows the values of the wavelength determined from the critical mode. (C) Typical mutual distributions of receptor (blue) and antigen (red) in a 1D trait space with coordinate x. The actual (solid line) and effective (dashed line) population densities (scaled by total abundance) show mismatch for receptors (antigens) when $R_{\rm inh} > R_{\rm act}$ ($R_{\rm inh} < R_{\rm act}$), leading to colocalized (alternate) density peaks between two populations, as indicated by the yellow bars. Shaded are the effective density fields $A_{\rm eff}(x)$ and $B_{\rm eff}(x)$. These two examples correspond to the open circle ($R_{\rm inh} = 0.025$, $R_{\rm act} = 0.005$) and the filled circle ($R_{\rm inh} = 0.005$, $R_{\rm act} = 0.025$) in panel B. $\lambda_1 = 10$, $\lambda_2 = 1$, $\alpha_1 = 10^{-3}$, $\alpha_2 = 10^{-4}$, $D_1 = 10^{-6}$, $D_2 = 10^{-4}$.

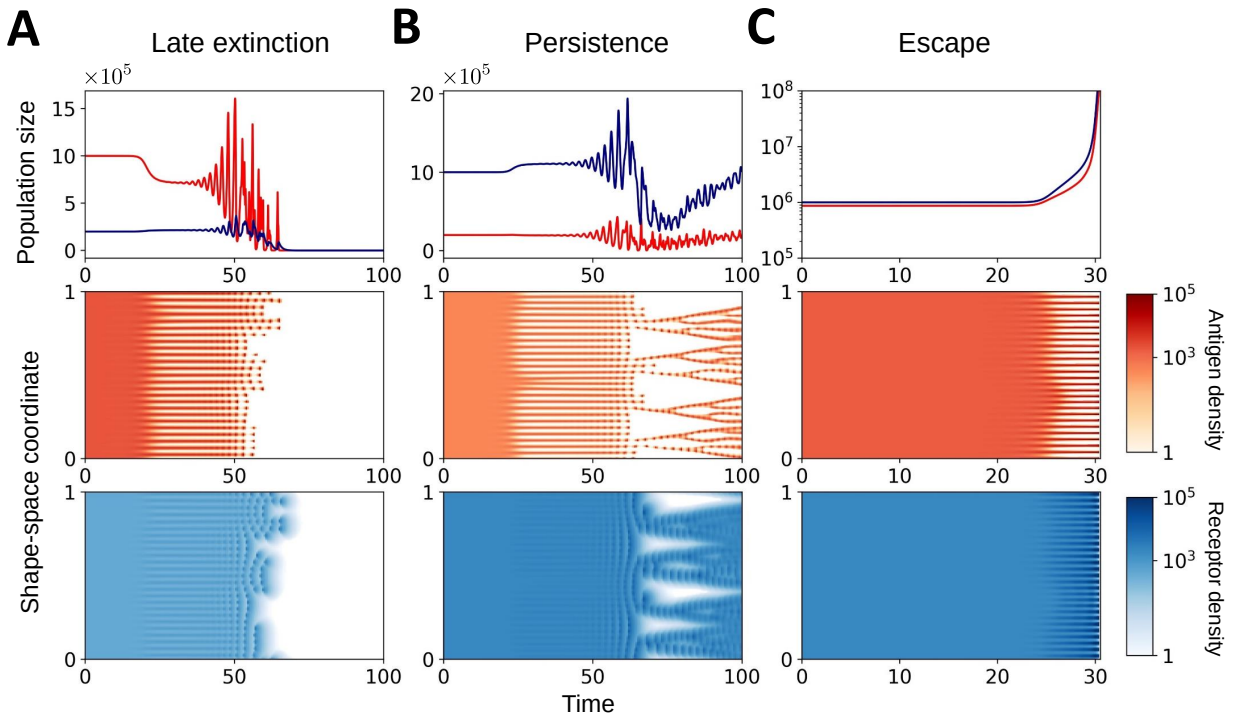

Figure 6.4: Distinct regimes of coevolutionary dynamics. Population trajectories (top row) and concomitant pattern evolution (lower rows) of antigen (red) and receptor (blue) are shown for late antigen extinction (A), persistent coexistence (B) and antigen escape (C), which are realized by varying the range of cross-reactivity and the size of carrying capacity. Concentration changes progress via three distinct stages: uniform steady state, stationary pattern, and oscillatory pattern. An extinction threshold is crucial for the termination of branches (A, B) and the formation of forks (B) shown in the evolutionary kymographs. Color bars code for population densities. (A) $R_{\text{inh}} = 0.025$, $R_{\text{act}} = 0.005$, $\theta_2 = \infty$; (B) $R_{\text{inh}} = 0.005$, $R_{\text{act}} = 0.025$, $\theta_2 = \infty$; (C) $R_{\text{inh}} = 0.005$, $R_{\text{act}} = 0.025$, $\theta_2 = 3.5 \times 10^5$. Other parameters are identical to those in Fig. 6.3.

growth rate of the Fourier modes:

$$\omega(k) = -(D_1 + D_2)k^2 + \sqrt{(D_1 - D_2)^2 k^4 - 4\lambda_1\lambda_2 \frac{\hat{S}_1(k)\hat{S}_2(k)}{\hat{S}_1(0)\hat{S}_2(0)}}. \tag{6.3}$$

Turing instability occurs when the least stable mode (with a wavevector k_c) begins to grow, namely,

$$Re[\omega(k_c)] \geq 0, \tag{6.4}$$

where the wavenumber of the critical mode can be determined by $\partial_k \omega|_{k=k_c} = 0$. This gives the pattern-forming condition:

$$\frac{D_1 D_2}{\lambda_1 \lambda_2} \leq -\frac{1}{k_c^4} \frac{\hat{S}_1(k_c)\hat{S}_2(k_c)}{\hat{S}_1(0)\hat{S}_2(0)}, \tag{6.5}$$

where $\hat{S}_1(k)$ and $\hat{S}_2(k)$ are the Fourier transform of the interaction kernels. It immediately follows that Turing instability in our system is purely driven by *asymmetric nonlocal* interactions and independent of diffusion: if the kernels were symmetric, i.e., $S_1(r; R_{\text{inh}}) = S_2(r; R_{\text{act}})$, the right hand side of Eq. 6.5 can never be positive and hence patterns do not develop; on the other hand, when $D_1 D_2 = 0$, the patterning condition is most readily satisfied, implying that diffusion is not necessary. In fact, the commonly assumed Gaussian kernel represents a marginal case which does not robustly warrant instability [184]. Instead, $\hat{S}(k) < 0$ is guaranteed if the strength of interaction decreases steeply with increasing separation across the edge of the interaction range. For simplicity, we assume step-function kernels, $S_1(r) = \Theta(R_{\text{inh}} - r)$ and $S_2(r) = \Theta(R_{\text{act}} - r)$. Then the Fourier transform are

$$\hat{S}_1^{(n)}(k) = \left(\frac{2\pi}{kR_{\text{inh}}}\right)^{\frac{n}{2}} {R_{\text{inh}}}^n J_{\frac{n}{2}}(kR_{\text{inh}}), \qquad \hat{S}_2^{(n)}(k) = \left(\frac{2\pi}{kR_{\text{act}}}\right)^{\frac{n}{2}} R_{\text{act}}^n J_{\frac{n}{2}}(kR_{\text{act}}). \tag{6.6}$$

where n is the dimension of the shape space. $J_\alpha(x)$ is the Bessel function. The most unstable wavenumber can be determined under a modest extent of asymmetry, i.e., $\gamma \equiv (R_{\text{inh}} - R_{\text{act}})/(R_{\text{inh}} + R_{\text{act}}) \ll 1$. To the lowest order of γ, we find k_c satisfies $J_{\frac{n}{2}}(k_c(R_{\text{inh}} + R_{\text{act}})/2) = 0$. Therefore, pattern-forming condition can be explicitly expressed in terms of

γ:

$$|\gamma| \geq \gamma_c \equiv \frac{C_n}{(R_{\text{inh}} + R_{\text{act}})^2} \sqrt{\frac{D_1 D_2}{\lambda_1 \lambda_2}}, \tag{6.7}$$

or equivalently,

$$|R_{\text{act}}^2 - R_{\text{inh}}^2| \geq C_n \sqrt{\frac{D_1 D_2}{\lambda_1 \lambda_2}}. \tag{6.8}$$

Here C_n is a constant that only depends on the dimension, n, of the shape space,

$$C_n = \frac{x_*^{1+\frac{n}{2}}}{2^{\frac{n}{2}-2}\Gamma(1+\frac{n}{2}) J_{1+\frac{n}{2}}(x_*)}, \tag{6.9}$$

where x_* is the smallest positive root of $J_{\frac{n}{2}}(x) = 0$. This suggests a rapid increase of C_n with n, indicating that stable uniform coexistence extends to stronger asymmetry as the phenotypic space involves higher dimensions. Therefore, under sufficient asymmetry, a continuum of antigen (receptor) types spontaneously segregates into species-rich and species-poor domains with densities on either side of A_s (B_s). The spacing between adjacent antigen or receptor density peaks, i.e., the pattern wavelength $\lambda \simeq 2\pi/k_c$, is modestly larger than the sum of activation and inhibition radii (Fig. 6.3A) due mainly to asymmetry and slightly to diffusion. Note that the minimum level of asymmetry required for patterning decreases with increasing range of cross-reactivity as $\gamma_c \sim (R_{\text{inh}} + R_{\text{act}})^{-2}$ (Eq. 6.7); furthermore, the pattern wavelength is symmetric under the interchange of R_{act} and R_{inh} (Figs. 6.3A and 6.3B).

However, mutual distributions of receptor and antigen break the symmetry (Fig. 6.3C): co-localized patterns form when $R_{\text{act}} < R_{\text{inh}}$ (left panel) while alternate patterns emerge when $R_{\text{act}} > R_{\text{inh}}$ (right panel). This seemingly counterintuitive behavior can be explained by a rather general mechanism. When $2R_{\text{inh}} > \lambda$, the "inhibition sphere" of an antigen may enclose adjacent receptor density peaks. As a result, locations between the peaks, where the actual receptor density $B(x)$ (blue solid line) is in fact the lowest, are instead the worst positions for antigens to be in, because the effective receptor density field acting on antigens at position x, $B_{\text{eff}}(x) = \int_{x-R_{\text{inh}}}^{x+R_{\text{inh}}} B(y)\mathrm{d}y$ (blue dashed line), is maximal when x is right amid receptor peaks. Thus the antigen distribution winds up tracking the receptor distribution

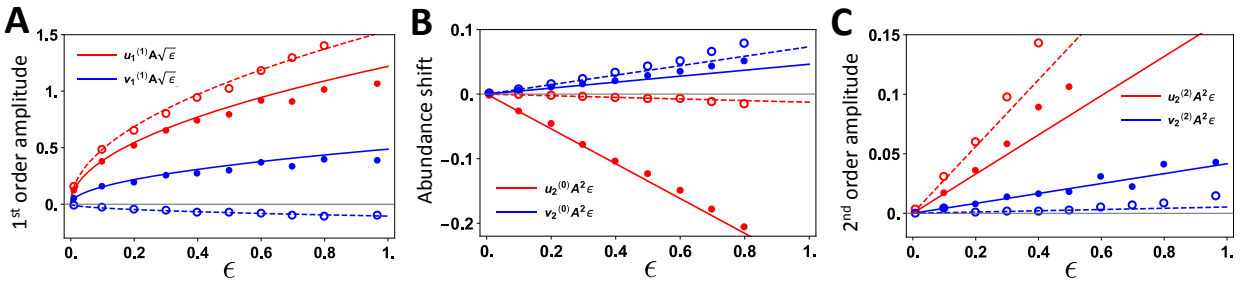

Figure 6.5: Theory predicts pattern amplitudes and abundance shift induced by coupling between Turing modes. Shown are scaled first (A) and second (C) order pattern amplitudes and abundance shift (B) as a function of ϵ, the dimensionless deviation from D_1^*. Lines are analytical predictions; symbols are numerical solutions. Solid line and filled symbol: $R_{\text{inh}} = 0.025$, $R_{\text{act}} = 0.005$; dashed line and open symbol: $R_{\text{inh}} = 0.005$, $R_{\text{act}} = 0.025$. Red (blue) for antigen (receptor). $\theta_2 = \infty$.

(yellow bar, left panel). Conversely, when $2R_{\text{act}} > \lambda$, the "activation sphere" of a receptor may encompass adjacent antigen peaks; the stimulation for receptor replication is strongest in between the peaks, according to the effective antigen densities $A_{\text{eff}}(x) = \int_{x-R_{\text{act}}}^{x+R_{\text{act}}} A(y)\mathrm{d}y$ (red dashed line). Consequently, receptors view antigens as most concentrated in positions where they are actually least prevalent (red solid line). Therefore, depending on whether R_{inh} or R_{act} is larger, colocalized or alternate distributions result, which reflect a mismatch between the actual distribution and the effective one seen by the apposing population. In what follows we show that distinct spatial phase relations between mutual distributions will lead to drastically different pattern dynamics and evolutionary outcomes.

6.3.3 Coevolutionary regimes and ecological feedback

Multi-stage patterning. Shown in Fig. 6.4 are the abundance trajectories (top row) and kymographs of concurring patterns (lower rows) demonstrating their concomitant progression and mutual influence. Depending on the sign of asymmetry and the size of carrying capacity, qualitatively distinct regimes appear, including late antigen extinction, persistence, and

escape (panels A to C).

Intriguingly, concentrations and patterns evolve via three distinct stages: uniform steady state, stationary pattern, and oscillatory pattern. Right after co-patterns spontaneously emerge from the homogeneous steady state, concentration changes in both populations are observed: in the absence of homeostatic constraints (panels A and B), antigen abundance (red) shifts downward whereas receptor prevalence (blue) shifts upward. This is unanticipated because patterning instability in a density field is not expected to alter the overall abundance: growing unstable modes merely redistribute densities in space without changing the average concentration. This appears to break down when patterns develop in two interacting density fields. In fact, the most unstable modes (with wavenumber k_c) from both populations couple and modify the zero modes, resulting in a shift in mean population densities.

Co-localized and alternate quasispecies. A weakly nonlinear analysis close to the critical point quantitatively captures both the phase relation between patterns and the shift in overall abundances (Fig. 6.5). For analytical tractability, we perform the calculation in 1D. Below, we only stress the essential results.

Close to the patterning transition, $D_1 = D_1^\star(1-\epsilon)$, where $D_1^\star$ is the critical diffusion constant of antigen and ϵ is small and positive, we seek stationary solutions of the form $A(x) = A_s(1+u(x))$ and $B(x) = B_s(1+v(x))$, where the deviation $\boldsymbol{w} = (u(x), v(x))^T$ from the homogeneous steady state $(A_s, B_s)^T$ is expanded in powers of $\epsilon^{1/2}$ to the second order:

$$\boldsymbol{w} = \boldsymbol{w}_1^{(1)} \cos(k_c x)\mathcal{A}\epsilon^{1/2} + \left(\boldsymbol{w}_2^{(0)} + \boldsymbol{w}_2^{(2)} \cos(2k_c x)\right)\mathcal{A}^2\epsilon. \tag{6.10}$$

$\boldsymbol{w}_1^{(1)} = (u_1^{(1)}, v_1^{(1)})^T$, $\boldsymbol{w}_2^{(0)} = (u_2^{(0)}, v_2^{(0)})^T$, and $\boldsymbol{w}_2^{(2)} = (u_2^{(2)}, v_2^{(2)})^T$ are coefficients to be determined by linearizing Eq.6.1. The saturated amplitude $\mathcal{A}$ of the perturbation is determined by the amplitude equation at the order of $\epsilon^{3/2}$. The spatial phase difference between the leading pattern modes in antigen and receptor populations, $u_1^{(1)}$ and $v_1^{(1)}$, respectively, can

be found from

$$\xi \equiv \frac{v_1^{(1)}}{u_1^{(1)}} = \frac{\lambda_2}{D_2 k_c^2} \frac{\sin(k_c R_{\text{act}})}{k_c R_{\text{act}}} = -\frac{D_1^\star k_c^2}{\lambda_1} \frac{k_c R_{\text{inh}}}{\sin(k_c R_{\text{inh}})}, \tag{6.11}$$

which implies that $\xi \propto \sin\left(\frac{2\pi}{\lambda}\frac{(R_{\text{act}}+R_{\text{inh}})}{2}(1-\gamma)\right) = \sin\left(\pi \frac{1-\gamma}{\lambda/(R_{\text{act}}+R_{\text{inh}})}\right)$, with λ being the pattern wavelength and $\gamma = (R_{\text{inh}} - R_{\text{act}})/(R_{\text{inh}} + R_{\text{act}})$. It immediately follows that when $\gamma < 0$ (i.e., $R_{\text{act}} > R_{\text{inh}}$), $1-\gamma > \lambda/(R_{\text{act}}+R_{\text{inh}}) > 1$ (see Fig. 6.3A), thus $\xi < 0$; when $\gamma > 0$ (i.e., $R_{\text{inh}} > R_{\text{act}}$), $1-\gamma < 1 < \lambda/(R_{\text{act}}+R_{\text{inh}})$, thus $\xi > 0$. Therefore, the spatial patterns of antigen and receptor distributions are either in phase ($\xi > 0$) or out of phase ($\xi < 0$), purely determined by the sign of asymmetry (Fig. 6.5A). This provides rigor to the intuitive argument we made earlier in relation to Fig. 6.3C.

Furthermore, the changes in the overall abundance of antigens and receptors are proportional to $u_2^{(0)}$ and $v_2^{(0)}$, respectively. At $\mathcal{O}(\epsilon)$, we find $u_2^{(0)} \propto -\xi \sin(k_c R_{\text{act}}) < 0$ and $v_2^{(0)} \propto -\xi \sin(k_c R_{\text{inh}}) > 0$, i.e., the direction of abundance shift is independent of the sign of asymmetry, in line with numerical solutions (Figs. 6.4A and 6.4B, top row; Fig. 6.5B). Importantly, $u_2^{(0)}, v_2^{(0)} \propto u_1^{(1)} v_1^{(1)}$, indicating that shift in abundance indeed results from coupling between simultaneous Turing modes.

Dynamic transients. A further surprise comes at longer times: the stationary co-patterns are only metastable. Soon after abundance shift takes place, instability starts to grow, visible as increasingly strong oscillations that eventually drive the antigen population to pass below the extinction threshold (Fig. 6.4A top panel). By perturbing around the abundance-shifted stationary patterns, we indeed identify a growing oscillatory instability from the dispersion relation of linearized dynamics. The interrupted oscillation amplitudes at later times arise from asynchronous extinction of local antigen clusters (Fig. 6.4A middle panel). Note that this late extinction phase only occurs to colocalized population densities, i.e., when $R_{\text{inh}} > R_{\text{act}}$.

Upon interchange of R_{inh} and R_{act} (Fig. 6.4B), pattern evolution exhibits new features: as some antigen clusters go extinct as a result of oscillatory instability, neighboring clusters

migrate to these just vacated sites, where receptors decay due to a lack of stimulation and delay in response, thus locally and temporarily evading immune inhibition. These surviving clusters then go through successive branching events (i.e., widening then splitting), forming a tree-like structure over time. The coevolving receptor population drives the branching and subsequently traces the newly formed branches. Such coevolutionary speciation, enabled by mutation, persists for extended periods of time so that it effectively overcomes the growing oscillations and maintains antigen at modest prevalence indefinitely. Note that the persistent ramifying pattern only emerges from alternate density peaks, i.e., when $R_{\text{act}} > R_{\text{inh}}$.

Finite repertoire. Is there a chance that antigen population can achieve a global escape from immune control, as is often envisaged as a catastrophic failure? This does happen as soon as we turn on a sufficiently strong homeostatic constraint on receptor abundance (Fig. 6.4C).

Considering global homeostasis, the decay rate of receptors now is given by $\lambda_2 B(x,t)(1+\int_0^1 B(y,t)\mathrm{d}y/\theta_2)$, which includes an additional contribution from the global constraint characterized by carrying capacity θ_2. Interestingly, reducing the immune capacity appears to alter the nature of the instability (Fig. 6.6C): a critical value of θ_2 marks the transition from supercritical bifurcation (yellow region), where nonlinearity acts to saturate the growth of the perturbation, to subcritical bifurcation (red region) where higher order processes have to intervene for stabilization. The latter corresponds to the antigen escape phase (Fig. 6.4C): an unrestrained growth indicates a loss of immune control.

Higher dimension. Similar progression of patterns and population dynamics in distinct regimes is also seen in 2D starting from the uniform steady state. An analogous "branching" scenario in the persistence phase is particularly intriguing: antigen droplets deform and migrate to neighboring vacant loci and resist elimination. Oscillations of dense spots in both populations resemble the "twinkling eyes" pattern proposed for synthetic materials. It has been suggested [215] that oscillatory patterns can arise in a system consisting of two coupled reaction-diffusion layers, one capable of producing Turing patterns while the

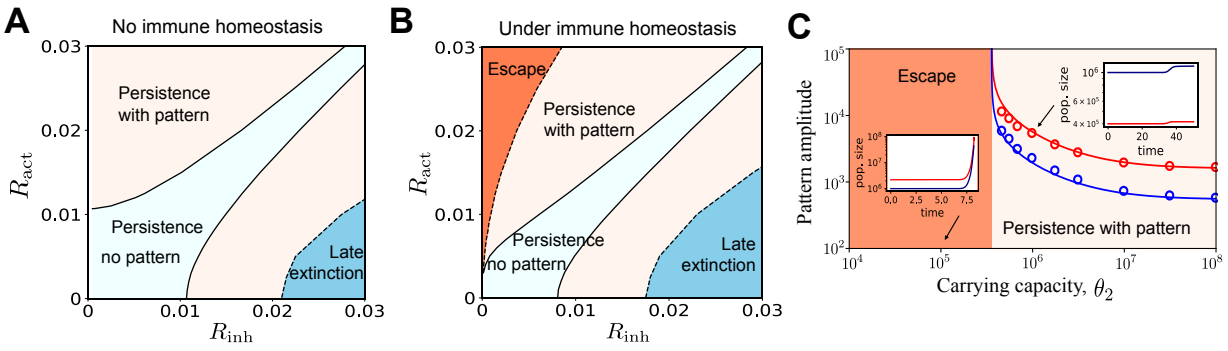

Figure 6.6: Asymmetric cross-reactivity yields diverse phases. (A) Without homeostatic constraints on lymphocyte counts ($\theta_2 = \infty$), above the critical asymmetry (beyond the light blue region), patterns form. The pattern-forming boundaries are symmetric about the diagonal. The boundary between the late antigen extinction phase (blue) and the persistent patterned phase (yellow) is determined by tracking the prevalence trajectories until $t = 100$. (B) Under a finite carrying capacity ($\theta_2 = 3 \times 10^5$), the pattern-forming region is no longer symmetric and an antigen escape phase (red) emerges at the small-R_{inh} large-R_{act} corner, where the phase boundary corresponds to the transition between supercritical and subcritical bifurcations. (C) First order pattern amplitudes as a function of carrying capacity θ_2. Lines are analytical solutions of amplitude equations, and symbols are numerical values extracted from Fourier spectrum of stationary patterns right after abundance shift. Insets show examples of population dynamics in escape (subcritical) and persistence with pattern (supercritical) phases; pattern amplitudes diverge near the transition. Red (blue) for antigen (receptor).

other supporting Hopf instability. Distinct from these built-in mechanisms, instabilities in our system are self-generated: interacting populations spontaneously fragment in the trait space, and the resulting Turing modes resonate in space, leading to abundance shift and subsequent growing oscillations.

Phase diagram. To stress the role of asymmetric cross-reactivity in governing the diverse behaviors, we present phase diagrams on the $(R_{\text{act}}, R_{\text{inh}})$ plane (Fig. 6.6). Without homeostatic constraints ($\theta_2 = \infty$, panel A), patterns form above the critical asymmetry marked by solid lines that are symmetric about the diagonal; the enclosed patternless phase (light blue region) corresponds to stable homogeneous coexistence like for local interactions. On the $R_{\text{inh}} > R_{\text{act}}$ side, the late extinction phase (blue) transitions to the persistent patterned phase (yellow) at a boundary (dashed line) determined by tracking the prevalence trajectories until $t = 100$; longer tracking time would expand the extinction phase.

Under a finite carrying capacity ($\theta_2 = 3 \times 10^5$, panel B), two major changes occur: First, the pattern-forming region is no longer symmetric but expands on the $R_{\text{act}} > R_{\text{inh}}$ side toward the diagonal. Second, the antigen escape phase (red region) emerges at the small-R_{inh} large-R_{act} corner; the phase boundary corresponds to the transition between supercritical and subcritical bifurcations in the amplitude equation. The escape phase enlarges as the carrying capacity diminishes. Thus, our model predicts expansion of the antigen escape phase with age, owing to diminishing counts of renewable lymphocytes [216]. The regime of persistence with pattern (yellow), irrespective of the homeostatic constraint, differs between the flanks; while oscillations occur on both sides off the diagonal, antigen branching (Fig. 6.4B) only appears when $R_{\text{act}} > R_{\text{inh}}$, manifesting the potential for evasion.

6.4 Discussion

Environment becomes a relative concept in light of coevolution. We present a general model of mutual organization between continuous distributions of antigens and receptors that in-

teract cross-reactively. In a shared phenotypic space, the receptor repertoire and antigen population constitute each other's environment and adapt to mutually constructed fitness seascapes. This phenomenological approach allows us to describe the interplay between ecological and evolutionary processes that do not separate in timescales, thus revealing a variety of dynamic transients observed in nature, such as antigen extinction, chronic persistence, and unrestrained growth until saturation.

We propose that the transient nature of host-pathogen coevolution could, at least in part, stem from distinct conditions for receptor activation and antigen inhibition. On the one hand, the ability of antigens to be recognized by the immune system, i.e., antigenicity, can be reduced to the level of chemistry and measured by *in vitro* lymphocyte proliferation and cytokine production. On the other hand, the ability to induce protective immunity, i.e., immunogenicity, depends on complex interactions with various elements in the host immune system, thus demanding immunization studies *in vivo*. Indeed, experiments have demonstrated for diverse pathogens that strong antigenicity does not guarantee protection and vice versa; this lack of correlation has posed significant challenges to vaccine design [180, 181, 182].

Our simple model accounts for this intrinsic asymmetry and predicts its influence on antigen-immunity coevolution. While it might be intuitive that under reciprocal cross-reactivity, antigen and receptor populations simultaneously fragment in the phenotype space (Fig. 6.3), more surprises come after the co-pattern emerges (Fig. 6.4): When two distributions are in phase ($R_{\text{act}} < R_{\text{inh}}$), spatial resonance between the lowest Turing modes precedes growing oscillations in the overall abundance, driving antigens to extinction; when apposing populations are out of phase ($R_{\text{act}} > R_{\text{inh}}$), strong homeostatic constraints on immune cells alter the nature of pattern instability from supercritical to subcritical, leading to uncontrolled growth. The intuitive picture is, when $R_{\text{act}} < R_{\text{inh}}$, antigens are inhibited by receptors that they do not activate and hence fail to evade immune attack; when $R_{\text{act}} > R_{\text{inh}}$, receptors are activated by antigens that they cannot inhibit, thus, under resource limits, an increasingly

weaker defense results. Such multi-stage patterning and its feedback to population dynamics, triggered by asymmetric non-local interactions, is a qualitatively new phenomenon, clearly different from speciation due to competitive exclusion in a single population. Our predictions are supported by experiments: strong oscillations in antigen abundance prior to crash to extinction have been seen in viral evolution within humans and attributed to cross-reactive antibody response [217], whereas strategies of distracting immune attention are indeed used by many viruses that create a vast excess of defective particles than functional ones [218].

These predictions can potentially be tested by tracking both the pathogen load and diversity history via high-throughput longitudinal sequencing of receptors and antigens [11, 202, 203, 204]. In addition, phenotypic assays for binding and neutralization [201] can inform the extent of asymmetry. Combining these two sets of experiments in different individuals would allow to correlate the degree of asymmetry with evolutionary outcomes.

Our results also suggest that, the immune system may have evolved to exploit the asymmetry between activation and inhibition by differentiating these processes physically and biochemically. A remarkable example is affinity maturation of B lymphocytes [3] in which rapid Darwinian evolution acts to select for high affinity clones: Immature B cells are trained in lymphoid tissues where antigens are presented in a membrane form and decline in availability; fierce competition for limited stimuli thus provides a sustained selection pressure that constantly raises the activation threshold, i.e., decreasing $R_{\rm act}$. In contrast, mature B cells then released into circulation encounter soluble antigens at higher abundance, corresponding to $R_{\rm inh} > R_{\rm act}$. As a result, enhanced asymmetry between conditions for immune stimulation and antigen removal facilitates elimination of pathogens. Conversely, pathogens evolve immunodominance [219] and make fitness-restoring mutations [220] that increase $R_{\rm act}$ and decrease $R_{\rm inh}$, both of which aid in evasion.

Another implication of this study is persistent coevolution, often pictured as an asymptotic state, can only be sustained when asymmetry is not too strong. It might be favorable if asymmetry stays near the edge between persistence and imbalance, which adjusts to the

tension between the need for defense against foreign pathogens ($\gamma > \gamma_c$) and that for tolerance toward benign self tissues ($|\gamma| \leq \gamma_c$). Interestingly, critical asymmetry γ_c increases with the number of phenotypic dimensions, suggesting that dynamic balance could be easier to maintain for more complex antigens.

Because the present model of antigen-immunity coevolution is a sufficiently abstract one, having properties which seem quite robust and independent of the details of predation, we expect that the results and predictions are relevant for a wide range of coevolving systems, including cancer cells and T lymphocytes, embryonic tissues and self-reactive immune cells, as well as bacteria and bacteriophage. This model can be adapted to be more biologically faithful, e.g., by incorporating preexisting antigenic landscapes, taking rates to be age-dependent, and treating cross-reactivity as an evolvable character.

Stochasticity arising from demographic noise does not change qualitative model behaviors in all regimes. Albeit not required for pattern formation, stochastic fluctuations appear to speed up instability growth, thus accelerating antigen extinction; this observation and other effects of demographic noise will receive a careful analysis in future work.

We hope that this work proves useful in providing a framework for understanding and testing how cross-reactive interactions — ubiquitous and crucial for biological sensory systems — can lead, in part, to the generation, maintenance and turnover of diversity in coevolving systems. More broadly, our work provides the basis for a theory of evolution in responsively changing environments, highlighting that ecological feedback in pattern-forming systems can yield dynamic transients and drive evolution toward non-steady states that differ from the Red Queen persistent cycles.

6.5 Acknowledgements

Chapter 6 is a reprint of the material as it appears in *Phy. Rev. Research* **1**, 033164 (2019). We thank Sidney Redner and Paul Bressloff for enlightening discussions. We are gratefully

acknowledges funding from the Dean of Physical Sciences at University of California, Los Angeles.

CHAPTER 7

Conclusions and Discussions

"A complex system can be characterized by the fact that it must be attacked via many models. No single model will ever suffice. Moreover, the more models required, the more complex the system must be."

Lee A. Segel

The immune system is a good instant of a highly complex system, characterized by the need to employ a large number of models for a comprehensive system description. Beginning with Bell [221], Perelson [66] and other pioneer scholars, for several decades modelers have been dedicated to understanding the immune system by developing a variety of models ranging from the molecular interactions to the evolution of immune system in the lifespan of a single organism [222]. Recent discoveries made by cell and molecular biologists have raised various novel questions that could not be addressed by existing models. Here, we are attempting to understand one of the vital components of adaptive immune response — affinity maturation — from different perspectives. Specifically, chapter 2, 4 and 5 look at the same antigen extraction process but have different levels of details (single antigen vs clusters), focus on different stages (extraction only vs cluster formation and extraction) and emphasize different aspects (dynamics, information or control). Chapter 3 combines the insights of antigen extraction together with models of B cell evolution by mapping the

molecular binding quality to clonal fitness via tug-of-war antigen extraction. This theoretical framework allows us to explore how physical constrains shape selection pressure. Chapter 6 takes further coarse graining and focus on the long-term coevolution between antigen and B cells.

One of the main questions discussed in my dissertation is how and why B cells expend mechanical energy to physically extract antigens. In chapter 2, we have demonstrated that a tugging force is able to regulate the extraction chance by lowering the potential barriers (if barriers are high) that separates bound state and broken state, or influencing the bond rupture kinetics (if barriers are low or do not exist). We show that this regulation at the molecular level may serve to shift and expand the discrimination sensitive window. By utilizing a large force pulling against a stiff APC, high affinity B cells become distinguishable even with low-affinity tethers. Furthermore, chapter 3 shows that this effect helps to increase the evolved affinity (without antibody feedback), enhance the adaptation rate (with antibody feedback) or change the evolution direction (if bond stiffness is mutable) of B cells during a GC reaction but sacrifices the GC survival chance. Therefore, a favorable level of mechanical energy expense acting on single receptors is selected on the population level, which balances the needs to adapt both rapidly and sustainably. Nevertheless, this treatment of antigen extraction is mean-filed only. To incorporate the many-body effect, we have introduced a stochastic model to describe the extraction of antigen clusters in chapter 4. Our model suggested that the affinity information encoded in the measuable readouts, which is closely related to the discrimination ability (quantified by the selection fidelity), depends on the applied force. For instance, the coupling between different receptors due to force-sharing is able to further expand the sensitive window. In chapter 5, by assuming B cells were able to adjust the force magnitude on the fly according to the binding configuration between receptors and ligands, we investigated the role of mechanical feedback during antigen extraction. We have demonstrated that the negative feedback provided by a sensing force was able to decouple ligand quality from ligand quantity, resulting in absolute affinity

discrimination. Another interesting insight is that a sensing force allows B cells to optimize both the discrimination ability and speed via utilizing the criticality near the bifurcation point of the antigen extraction system.

In addition, my dissertation has discussed in many aspects how different strategies could benefit the affinity maturation. First, in chapter 3 we highlighted the importance of tether strength s. It determines not only the minimum affinity for B cells to extract enough antigen to survive but also the affinity value above which all B cells can extract most antigens and thereby become indistinguishable. Moreover, a dynamical tether, either achieved by antibody feedback or passive immunization, can help to maintain the selection pressure while avoiding GC extinction. Second, chapter 3 suggests that the evolvability of receptor stiffness may play an important role in determining the evolution direction and the output antibody flexibility and binding quality. The mismatch between the conditions under which training and testing of B cells for antigen recognition are conducted may result in a discrepancy between antibody quality as well as B cell fitness. Therefore, one potential strategy is to restrict the stiffness evolvability so that the selection is acting on the binding affinity only. Lastly, our analysis in chapter 4 implies that it is important to switch focus during affinity maturation. This is because the relative amount of affinity information encoded in measurable readouts varies as affinity improves.

In what follows, I provide an outlook and some future directions.

Experimental tests Predictions of our theory can be tested using various experimental techniques. At the molecular level, different unbinding pathways can be distinguished by labeling tethers, antigens and receptors with different fluorophore [33]. This allows one to quantify the extracted antigen percentage using relative fluorescence intensity [33]. Then, the dependence on tugging force can be seen via inhibition of cytoskeleton motors such as myosin IIa [2]. Additionally, dynamic force spectroscopy [41] can be used to measure the extraction dynamics under different linear ramping forces to test our prediction of $\tilde{\eta} = \eta(\langle F \rangle)$.

At the cellular level, the effect of antibody feedback can be tested using mice models that are deficient in secreting antibodies. In fact, Zhang et al. [73] observed a significantly reduced affinity of GC B cells in mice deficient in the secreted form of IgM (without antibody feedback), compared to the control group (with antibody feedback). However, it was unclear whether this phenomenon was due to masked antigens or improved tethers. To test our hypothesis of antibody feedback, the comparison between single epitope antigen and multi-epitope antigen might be necessary.

T cell/B cell interaction One omitted component in our theory is the T cell/B cell interaction. It is well established in experiments that the germinal center reaction relies on tightly regulated bidirectional interactions between follicular helper T cells (Tfh) and B cells. On the one hand, B cells with different affinities are discriminated and selected by Tfh cells. On the other hand, the maintenance and expansion of Tfh cells require sustained antigenic stimulation presented by B cells. Recently, it was recently discovered that the interaction between Tfh cells and GC B cells also favor affinity-based selection of Tfh cells in the GC [223].

In our theory, this intricate interaction is represented by a phenomenological expression that links the number of extracted antigen with B cell replication rate (see Eq. 3.3), which resembles the logistic growth model. This simplification has been adopted in many studies of GC evolution [76, 75]. An alternative selection rule assumed that a fixed fraction of B cells having the highest antigen extraction would receive Tfh help and survive [69, 20]. Whether such high-level simplicity is indeed an emergent property of the strongly interacting parts is yet unclear. It requires a quantitative study of the T cell/B cell interaction to elucidate how T cells control the proliferation or apoptosis of B cells.

Moreover, the affinity-based selection of Tfh cells suggests that the selection is bidirectional. Therefore, it is possible that the affinity difference between similar B cells (desired signal) becomes amplified through some positive feedback mechansims during T cell/B cell

interaction, and so do the fluctuations. Then, it is important to understand how the information collected in the antigen extraction step influences the coupled T cell/B cell population dynamics.

Spatial degree of freedom Another interesting aspect for future study is to include the spatial degree of freedom in the model of antigen extraction. Our theory assumed receptors and ligands are homogeneous and free to move. Nevertheless, it was suggested that the synaptic architecture regulated selection of high-affinity B cells in GCs [32]. B cells with different affinities may form different patterns of complexes [31].

The pattern formation during interaction between B cell and APC may introduce nontrivial effect on antigen extraction. First, the membrane introduces cooperative effects between bonds [224, 225], which changes the nucleation and dissociation dynamics of ligand-receptor clusters [226], especially when an out-of-plane tugging force presents [227]. Second, as we noted in chapter 4, the cluster size m_0 is critical for the initial force per bond (F/m_0), which is one of the key factors that determine the overall extraction chance. These may characterize a preferred cluster size that optimizes the discrimination function. It will be very interesting to explore whether a favored cluster size requires active regulation or could naturally emerge from the membrane-mediated ligand receptor interactions.

In summary, the research in my thesis examines several key steps in the affinity maturation process, illustrates its dynamics and identifies the key components that give rise to the observed behavior. I hope my study will inspire and motivate further work on principles that govern the immune response.

CHAPTER 8

Appendices

8.1 Derive the MFPT of a two-dimensional cusp-harmonic potential surface

In chapter 2 we considered a linear-cubic potential as an example to calculate the MFPT explicitly. Another widely used potential is the so called cusp-harmonic potential [16, 17, 47]. Explicitly,

$$U(x_a, x_b) = \begin{cases} \Delta G_a^{\ddagger}\left(\frac{x_a}{x_a^{\ddagger}}\right)^2 + \Delta G_b^{\ddagger}\left(\frac{x_b}{x_b^{\ddagger}}\right)^2 - F(x_a + x_b), & x_a \leq x_a^{\ddagger} \text{ and } x_b \leq x_b^{\ddagger}, \\ -\infty, & \text{otherwise.} \end{cases} \tag{8.1}$$

For short, we let $f_a = 2\Delta G_a^{\ddagger}/x_a^{\ddagger}, f_b = 2\Delta G_b^{\ddagger}/x_b^{\ddagger}$. The potential has a minimum at ($x_a = F/f_a, x_b = F/f_b$) and a cusp-like barrier at the boundary ($x_a = x_a^{\ddagger}$ or $x_b = x_b^{\ddagger}$).

To find the MFPT for the cusp-harmonic potential at each boundary, we introduce Talkner's method [58]. According to Talkner [58], the MFPT in the $n-$dimensional space Ω with boundary $\partial\Omega$ can be expressed in terms of a stationary state probability distribution $w(\vec{\mathbf{x}})$ of the Fokker Planck equation ($\hat{L}w = 0$) and the probability flux passing through the boundary. Define the relative MFPT $f(\vec{\mathbf{x}}) = \tau(\vec{\mathbf{x}})/\tau$ along the escaping pathway, where $\tau(\vec{\mathbf{x}})$ is the MFPT starting from the position at $\vec{\mathbf{x}}$, satisfying the Kolmogorov backward equation given by

$$\hat{L}^{\dagger}\tau(\vec{\mathbf{x}}) = 0. \tag{8.2}$$

Here $\hat{L}^{\dagger}$ is the adjoint operator of the Fokker-Planck equation. τ is the MFPT starting from

the potential minimum. By Gauss' theorem [58],

$$\int_\Omega w d\Omega = -\int_{\partial\Omega} \sum_i ds_i \cdot w \sum_j D_{ij} \frac{\partial \tau(\vec{\mathbf{x}})}{\partial x_j} = -\tau \int_{\partial\Omega} \sum_i ds_i \cdot w \sum_j D_{ij} \frac{\partial f(\vec{\mathbf{x}})}{\partial x_j}, \tag{8.3}$$

where $\vec{\mathbf{ds}}$ is the oriented surface element at the boundary $\partial\Omega$. D is the diffusion matrix. Index j loops through all degrees of freedom. The right-hand side describes the probability flux through the boundary $\partial\Omega$. This gives

$$\tau = \frac{\int_\Omega w d\Omega}{-\int_{\partial\Omega} \sum_i ds_i \cdot w \sum_j D_{ij} \frac{\partial f(\vec{\mathbf{x}})}{\partial x_j}}. \tag{8.4}$$

To evaluate the right-hand side, one can estimate $w(\vec{\mathbf{x}})$ and $f(\vec{\mathbf{x}})$ using WKB approximations [58]. This is because, given a potential with a high barrier separating the attractor and boundary, a trajectory starting within Ω will typically first approach the attractor and stay within its neighborhood for a long time until an occasional fluctuation drives it to the boundary (see Fig. 8.1). Thus, we can assume $f(\vec{\mathbf{x}}) = 1$ for all $\vec{\mathbf{x}} \in \Omega$, except for a thin layer $\Delta\Omega$ along the boundary $\partial\Omega$. Therefore, $f(\vec{\mathbf{x}})$ follows

$$\begin{aligned} \hat{L}^\dagger f(\vec{\mathbf{x}}) &= 0, \quad \vec{\mathbf{x}} \in \Delta\Omega_i \\ f(\vec{\mathbf{x}}) &= 0, \quad \vec{\mathbf{x}} \in \partial\Omega_i \\ f(\vec{\mathbf{x}}) &= 1, \quad \vec{\mathbf{x}} \in \Omega - \Delta\Omega_i \end{aligned} \tag{8.5}$$

This can be solved by making ansatz about the form of $f(\vec{\mathbf{x}})$ and Taylor expanding the coefficient near the boundary.

We first write down the Fokker-Planck operator and its adjoint explicitly.

$$\begin{aligned} \hat{L} = &\frac{\partial}{\partial x_a} \frac{\kappa_a x_a - \kappa_b x_b}{\gamma_a} + \frac{\partial}{\partial x_b} \Big(\frac{\kappa_b x_b - \kappa_a x_a}{\gamma_a} + \frac{\kappa_b x_b - F}{\gamma_b} \Big) + \\ &k_B T \Big(\frac{1}{\gamma_a} \frac{\partial^2}{\partial x_a^2} + \frac{\gamma_a + \gamma_b}{\gamma_a \gamma_b} \frac{\partial^2}{\partial x_b^2} - \frac{2}{\gamma_a} \frac{\partial^2}{\partial x_a \partial x_b} \Big), \\ \hat{L}^\dagger = &-\frac{\kappa_a x_a - \kappa_b x_b}{\gamma_a} \frac{\partial}{\partial x_a} - \Big(\frac{\kappa_b x_b - \kappa_a x_a}{\gamma_a} + \frac{\kappa_b x_b - F}{\gamma_b} \Big) \frac{\partial}{\partial x_b} + \\ &k_B T \Big(\frac{1}{\gamma_a} \frac{\partial^2}{\partial x_a^2} + \frac{\gamma_a + \gamma_b}{\gamma_a \gamma_b} \frac{\partial^2}{\partial x_b^2} - \frac{2}{\gamma_a} \frac{\partial^2}{\partial x_a \partial x_b} \Big). \end{aligned} \tag{8.6}$$

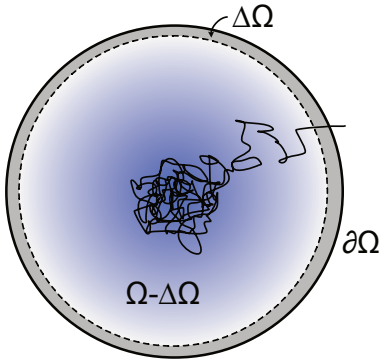

Figure 8.1: The WKB approximation used in Talkner's method. A typical trajectory will stay within the neighborhood of the attractor for a long time until it suddenly escapes from the domain. Thus, we divide the domain Ω into three parts, the bulk region $(\Omega - \Delta\Omega)$, a thin layer $(\Delta\Omega)$, and the boundary $\partial\Omega$.

Here $\kappa_a = 2\Delta G_a^\ddagger/(x_a^\ddagger)^2$ and $\kappa_b = 2\Delta G_b^\ddagger/(x_b^\ddagger)^2$ are curvatures. We can see this corresponds to the multivariate Ornstein-Uhlenbeck process, characterizing the noisy relaxation process.

Then we find the stationary probability distribution $\omega(\vec{\mathbf{x}})$ by solving the stationary Fokker-Planck equation. This gives,

$$\omega(x_a, x_b) = c \exp[-U(x_a, x_b)/k_\mathrm{B}T], \tag{8.7}$$

which takes the form of Boltzmann distribution with c being a normalization constant that will be canceled later. This can be verified by plugging into $\hat{L}\omega(\vec{\mathbf{x}}) = 0$. The stationary distribution takes the Gaussian form, so we can easily evaluate the numerator of Eq. 8.4, given by,

$$\int_\Omega w d\Omega \approx \int_{-\infty}^{\infty}\int_{-\infty}^{\infty} w(x_a, x_b) dx_a dx_b = c\frac{2\pi k_\mathrm{B}T}{\sqrt{\kappa_a \kappa_b}} \exp\left[(\frac{F^2}{2\kappa_a} + \frac{F^2}{2\kappa_b})/k_\mathrm{B}T\right]. \tag{8.8}$$

Note that we assumed the probability distribution is localized at the attractor so that we can replace the integrating limit by infinities.

Then we calculate the dependence of MFPT on initial position, $f(\vec{\mathbf{x}})$. Eq. 8.2 now

becomes

$$\hat{L}^{\dagger} f = 0 \Rightarrow -\frac{\kappa_a x_a - \kappa_b x_b}{\gamma_a}\frac{\partial f}{\partial x_a} - \Big(\frac{\kappa_b x_b - \kappa_a x_a}{\gamma_a} + \frac{\kappa_b x_b - F}{\gamma_b}\Big)\frac{\partial f}{\partial x_b} + k_B T\Big(\frac{1}{\gamma_a}\frac{\partial^2 f}{\partial x_a^2} + \frac{\gamma_a + \gamma_b}{\gamma_a \gamma_b}\frac{\partial^2 f}{\partial x_b^2} - \frac{2}{\gamma_a}\frac{\partial^2}{\partial x_a \partial x_b}\Big) = 0 \tag{8.9}$$

Note that we have to consider two boundaries separately. Each boundary corresponds to a distribution function $f(\vec{\mathbf{x}})$. For the boundary at $x_a = x_a^{\ddagger}$, we can utilize the WKB approximation (Eq. 8.5) and focus on the thin layer $x_a^{\ddagger} - \delta < x_a < x_a^{\ddagger}$. Since $f(x_a^{\ddagger}, x_b) = 0$ for all x_b, we have approximately $\partial_{x_b} f = 0$. Evaluating the coefficient in Eq. 8.9 at the 'saddle' point S_a at $(x_a = x_a^{\ddagger}, x_b = F/\kappa_b)$ gives

$$\frac{\partial^2 f}{\partial x_a^2} = \frac{1}{k_{\mathrm{B}} T}(f_a - F)\frac{\partial f}{\partial x_a}. \tag{8.10}$$

This can be solved based on the boundary condition $f\big|_{x_a \ll x_a^{\ddagger}} = 1$ and $f\big|_{x_a = x_a^{\ddagger}} = 0$. After calculation, we get

$$f(x_a, x_b) = 1 - \exp\big[-(f_a - F)(x_a^{\ddagger} - x_a)/k_{\mathrm{B}} T\big]. \tag{8.11}$$

Similarly, for the boundary at $x_b = x_b^{\ddagger}$, we focus on the thin layer $x_b^{\ddagger} - \delta < x_b < x_b^{\ddagger}$ and evaluate the coefficient in Eq. 8.9 at the 'saddle' point S_b at $(x_a = F/\kappa_a, x_b = x_b^{\ddagger})$. This yields

$$\frac{\partial^2 f}{\partial x_b^2} = \frac{1}{k_{\mathrm{B}} T}(f_b - F)\frac{\partial f}{\partial x_b}. \tag{8.12}$$

With boundary condition $f\big|_{x_b^{\ddagger}} = 0, f\big|_{x_b \ll x_b^{\ddagger}} = 1$, this gives,

$$f(x_a, x_b) = 1 - \exp\Big[-(f_b - F)(x_b^{\ddagger} - x_b)/k_{\mathrm{B}} T\Big]. \tag{8.13}$$

With the stationary probability distribution $\omega(\vec{\mathbf{x}})$ (Eq. 8.7), the MFPT distribution $f(\vec{\mathbf{x}})$ (Eq. 8.11 or Eq. 8.13), and the diffusion matrix (Eq. 2.17) in hand, we are ready to calculate MFPT using Eq. 8.4. For the boundary at $x_a = x_a^{\ddagger}$, the denominator of the right-hand-side

in Eq. 8.4 is given by

$$-\int_{-\infty}^{\infty} w(x_a^\ddagger, x_b)\frac{k_BT}{\gamma_a}\frac{\partial f}{\partial x_a}\bigg|_{x_a=x_a^\ddagger} dx_b = \int_{-\infty}^{\infty} ce^{-U(x_a^\ddagger,x_b)/k_\mathrm{B}T}\frac{k_BT}{\gamma_a}\frac{1}{k_\mathrm{B}T}(f_a - F)dx_b$$
$$= c\frac{f_a - F}{\gamma_a}\sqrt{\frac{2\pi k_\mathrm{B}T}{\kappa_b}}\exp\left[-(\Delta G_a^\ddagger - Fx_a^\ddagger - \frac{F^2}{2\kappa_b})/k_\mathrm{B}T\right].$$

For the boundary at $x_b = x_b^\ddagger$, we have

$$-\int_{-\infty}^{\infty} w(x_a, x_b^\ddagger)(\frac{k_BT}{\gamma_a} + \frac{k_BT}{\gamma_b})\frac{\partial f}{\partial x_b}\bigg|_{x_b=x_b^\ddagger} dx_a = \int_{-\infty}^{\infty} ce^{-U(x_a,x_b^\ddagger)/k_\mathrm{B}T}(\frac{k_BT}{\gamma_a} + \frac{k_BT}{\gamma_b})\frac{1}{k_\mathrm{B}T}(f_b - F)dx_a$$
$$= c\frac{f_b - F}{\gamma_a\gamma_b/(\gamma_a+\gamma_b)}\sqrt{\frac{2\pi k_\mathrm{B}T}{\kappa_a}}\exp\left[-(\Delta G_b^\ddagger - Fx_b^\ddagger - \frac{F^2}{2\kappa_a})/k_\mathrm{B}T\right].$$

Therefore, we have

$$\tau_a = \frac{\sqrt{\pi k_\mathrm{B}T}\gamma_a}{\sqrt{\kappa_a}(\kappa_a x_a^\ddagger - F)}e^{\Delta G_a^\ddagger(1-\frac{F}{f_a})^2/k_\mathrm{B}T},$$
$$\tau_b = \frac{\sqrt{\pi k_\mathrm{B}T}\frac{\gamma_a\gamma_b}{\gamma_a+\gamma_b}}{\sqrt{\kappa_b}(\kappa_b x_b^\ddagger - F)}e^{\Delta G_b^\ddagger(1-\frac{F}{f_b})^2/k_\mathrm{B}T}. \tag{8.14}$$

Recall that $f_a = 2\Delta G_a^\ddagger/x_a^\ddagger$, $f_b = 2\Delta G_b^\ddagger/x_b^\ddagger$, $\kappa_a = 2\Delta G_a^\ddagger/(x_a^\ddagger)^2$, $\kappa_b = 2\Delta G_b^\ddagger/(x_b^\ddagger)^2$.

8.2 Fisher information provides an upper bound of selection fidelity

In chapter 4, I used the Fisher information and selection fidelity to quantify the discrimination performance. Here, I show a connection between Fisher information and the selection fidelity: The Fisher information provides an upper bound on the selection fidelity. This implies that the Fisher information can tell us when the discrimination performance is expected to be poor.

Consider n_B B cells with affinity $E_1, E_2, ..., E_{n_B}$ (we use E to denote the affinity in this section). Without losing generality, we assume E_1 is the highest affinity, $E_1 > E_2, E_3, ...$ Let $P_i(y)$ be the readout distribution associated with affinity E_i ($i = 1, ..., n_B$, here we assume y

is continuous and $P_i(y)$ is differentiable). Then the probability to rank the best B cell (the first B cell with affinity E_1) highest is given by

$$\xi_Y = \int_{-\infty}^{\infty} dy_1 P_1(y_1) \prod_{i=2}^{n_B} \int_{-\infty}^{y_1} dy_i P_i(y_i). \tag{8.15}$$

The fidelity is equivalent to the top-K precision which is a widely used evaluation measure of ranking algorithms. Here we focus on the case of $K = 1$. The generalization of ξ_Y to selection of top-K B cells (the probability to rank the top-K B cells higher than the rest of B cells) is straightforward.

In the hard discrimination regime, we can Taylor expand the readout distributions near $P_1(y)$,

$$P_i(y) = P_1(y) - P_1(y)s(y)\epsilon_i + o(\epsilon_i^2), \tag{8.16}$$

where $\epsilon_i = E_1 - E_i > 0$, $i = 2, ..., n_B$. $s(y) = \frac{\partial \ln(P_1(y))}{\partial E}\big|_{E_1}$ is the score function. Then to the linear order of ϵ_i, Eq. 8.15 can be written as

$$\xi_Y \approx \int_{-\infty}^{\infty} dy_1 P_1(y_1) \Big[\Big(\prod_{i=2}^{n_B} \int_{-\infty}^{y_1} dy_i P_1(y_i) \Big) - \sum_{j=2}^{n_B} \Big(\prod_{i=2, i\neq j}^{n_B} \int_{-\infty}^{y_1} dy_i P_1(y_i) \Big) \int_{-\infty}^{y_1} dy_j P_1(y_j) s(y_j) \epsilon_j \Big].$$

We consider each term on the right hand side separately. First,

$$\int_{-\infty}^{\infty} dy_1 P_1(y_1) \Big(\prod_{i=2}^{n_B} \int_{-\infty}^{y_1} dy_i P_1(y_i) \Big) = \int_{-\infty}^{\infty} dy_1 P_1(y_1) (F(y_1))^{n_B - 1} = \langle (F(y_1))^{n_B - 1} \rangle = \frac{1}{n_B},$$

where $F(y)$ is the CDF of distribution $P_1(y)$ and we used the property $\langle F(y)^\alpha \rangle = 1/(1+\alpha)$ we proved before. Besides, for each index j (here $1 < j \leq n_B$),

$$\begin{aligned}
&\int_{-\infty}^{\infty} dy_1 P_1(y_1) \Big(\prod_{i=2, i\neq j}^{n_B} \int_{-\infty}^{y_1} dy_i P_1(y_i) \Big) \int_{-\infty}^{y_1} dy_j P_1(y_j) s(y_j) \epsilon_j \\
&= \int_{-\infty}^{\infty} dy_1 P_1(y_1) (F(y_1))^{n_B - 2} \int_{-\infty}^{y_1} dy_j P_1(y_j) s(y_j) \epsilon_j \\
&= \int_{-\infty}^{\infty} dy_j P_1(y_j) s(y_j) \epsilon_j \int_{y_j}^{\infty} dy_1 P_1(y_1) (F(y_1))^{n_B - 2} \\
&= \int_{-\infty}^{\infty} dy_j P_1(y_j) s(y_j) \epsilon_j \frac{1}{n_B - 1} (1 - F(y_j)^{n_B - 1}) \\
&= -\frac{1}{n_B - 1} \langle s(y_j) F(y_j)^{n_B - 1} \rangle \epsilon_j,
\end{aligned}$$

where we used the equality

$$\int_{y_j}^{\infty} dy_1 P_1(y_1)(F(y_1))^{n_B-2} = F(y_1)^{n_B-1}\Big|_{y_j}^{\infty} - (n_B-2)\int_{y_j}^{\infty} dy_1 P_1(y_1)(F(y_1))^{n_B-2}$$

to get

$$\int_{y_j}^{\infty} dy_1 P_1(y_1)(F(y_1))^{n_B-2} = \frac{1}{n_B-1}(1-F(y_j)^{n_B-1}).$$

In the last step, we used $\langle s(y_j)\rangle = 0$. All the averages are taking over $P_1(y)$. Hence, Eq. 8.15 now becomes

$$\xi_Y \approx \frac{1}{n_B} + \frac{1}{n_B-1}\langle s(y)F(y)^{n_B-1}\rangle \sum_{j=2}^{n_B}\epsilon_j, \tag{8.17}$$

which depends on the covariance between the score function and CDF to the power of n_B-1. According to the triangle inequality,

$$\langle s(y)F(y)^{n_B-1}\rangle^2 \leq \mathrm{var}(s(y))\cdot \mathrm{var}(F(y)^{n_B-1}) = \mathcal{I}_Y \cdot \big(\frac{1}{2n_B-1} - \frac{1}{n_B^2}\big), \tag{8.18}$$

where we used $\mathrm{var}(F(y)^{n_B-1}) = \langle F(y)^{2n_B-2}\rangle - \langle F(y)^{n_B-1}\rangle^2$. Finally we arrive at a simple upper bound for the discrimination fidelity between many B cells.

$$\xi_Y \leq \frac{1}{n_B} + \frac{1}{n_B\sqrt{2n_B-1}}\sqrt{\mathcal{I}_Y}\sum_{j=2}^{n_B}\epsilon_j + \sum_{j=2}^{n_B} o(\epsilon_j^2). \tag{8.19}$$

For exactly same B cells, the fidelity is $1/n_B$, as expected because the chance to choose E_1 is $1/n_B$ under random selection.

If the readout distribution is discrete, it seems there is no general and simple relation between ξ_Y and Fisher information like Eq. 8.19. However, in some special cases, we can get similar results. For example, consider the selection of one advantageously mutated B cell from many identical wide-type B cells, then we have $E_1 > E_2 = E_3 = ... = E_{n_B}$. One can replace the the integral in Eq. 8.15 with sum and Taylor expand $P_1(y)$ at $P_2(y)$ (readout distribution of wild-type B cells). After calculation, we get

$$\xi_Y \approx \langle F(y)^{n_B-1}\rangle + \langle s(y)F(y)^{n_B-1}\rangle\epsilon,$$

where $\epsilon = E1 - E_2$. Using the covariance inequality, we arrive at

$$\xi_Y \leq \langle F(y)^{n_B-1} \rangle + \sqrt{\mathcal{I}_Y} \sqrt{\mathrm{var}(F(y)^{n_B-1})} \epsilon + o(\epsilon^2), \tag{8.20}$$

which relies on the moments of its CDF, like the case of a continuous distribution. When the number of states is large, Eq. 8.20 is expected to converge to Eq. 8.19.

REFERENCES

[1] D. Eberly, R. Gardner, B. Morse, S. Pizer, and C. Scharlach. Ridges for image analysis. *Journal of Mathematical Imaging and Vision*, 4(4):353–373, 1994.

[2] Elizabeth Natkanski, Wing-Yiu Lee, Bhakti Mistry, Antonio Casal, Justin E. Molloy, and Pavel Tolar. B cells use mechanical energy to discriminate antigen affinities. *Science*, 340(6140):1587, 06 2013.

[3] Gabriel D. Victora and Michel C. Nussenzweig. Germinal centers. *Annual Review of Immunology*, 30(1):429–457, 2020/08/27 2012.

[4] Herman N. Eisen and Gregory W. Siskind. Variations in affinities of antibodies during the immune response. *Biochemistry*, 3(7):996–1008, 1964.

[5] Pavel Tolar. Cytoskeletal control of b cell responses to antigens. *Nature Reviews Immunology*, 17:621 EP –, 07 2017.

[6] Kihyuck Kwak, Nicolas Quizon, Haewon Sohn, Avva Saniee, Javier Manzella-Lapeira, Prasida Holla, Joseph Brzostowski, Jinghua Lu, HengYi Xie, Chenguang Xu, Katelyn M. Spillane, Pavel Tolar, and Susan K. Pierce. Intrinsic properties of human germinal center b cells set antigen affinity thresholds. *Science Immunology*, 3(29):eaau6598, 11 2018.

[7] Nilushi S. De Silva and Ulf Klein. Dynamics of b cells in germinal centres. *Nature Reviews Immunology*, 15:137 EP –, 02 2015.

[8] Frauke Muecksch, Yiska Weisblum, Christopher O. Barnes, Fabian Schmidt, Dennis Schaefer-Babajew, Zijun Wang, Julio C. C. Lorenzi, Andrew I. Flyak, Andrew T. DeLaitsch, Kathryn E. Huey-Tubman, Shurong Hou, Celia A. Schiffer, Christian Gaebler, Justin Da Silva, Daniel Poston, Shlomo Finkin, Alice Cho, Melissa Cipolla, Thiago Y. Oliveira, Katrina G. Millard, Victor Ramos, Anna Gazumyan, Magdalena Rutkowska, Marina Caskey, Michel C. Nussenzweig, Pamela J. Bjorkman, Theodora Hatziioannou, and Paul D. Bieniasz. Affinity maturation of sars-cov-2 neutralizing antibodies confers potency, breadth, and resilience to viral escape mutations. *Immunity*, 54(8):1853–1868.e7, 2021.

[9] Facundo D Batista and Michael S Neuberger. Affinity dependence of the b cell response to antigen: A threshold, a ceiling, and the importance of off-rate. *Immunity*, 8(6):751–759, 1998.

[10] Eric T. Boder, Katarina S. Midelfort, and K. Dane Wittrup. Directed evolution of antibody fragments with monovalent femtomolar antigen-binding affinity. *Proceedings of the National Academy of Sciences*, 97(20):10701, 2000.

[11] Hua-Xin Liao and Lynch et al. Co-evolution of a broadly neutralizing hiv-1 antibody and founder virus. *Nature*, 496(7446):469–476, 2013.

[12] Joseph C. Forbi, David S. Campo, Michael A. Purdy, Zoya E. Dimitrova, Pavel Skums, Guo-liang Xia, Lili T. Punkova, Lilia M. Ganova-Raeva, Gilberto Vaughan, Yousr Ben-Ayed, William M. Switzer, and Yury E. Khudyakov. Intra-host diversity and evolution of hepatitis c virus endemic to côte d'ivoire. *Journal of Medical Virology*, 86(5):765–771, 2022/05/20 2014.

[13] Leigh Van Valen. *A New Evolutionary Law*, volume 1. 01 1973.

[14] Shenshen Wang, Jordi Mata-Fink, Barry Kriegsman, Melissa Hanson, Darrell J. Irvine, Herman N. Eisen, Dennis R. Burton, K. Dane Wittrup, Mehran Kardar, and Arup K. Chakraborty. Manipulating the selection forces during affinity maturation to generate cross-reactive hiv antibodies. *Cell*, 160(4):785–797, 2015.

[15] GI Bell. Models for the specific adhesion of cells to cells. *Science*, 200(4342):618, 05 1978.

[16] E Evans and K Ritchie. Dynamic strength of molecular adhesion bonds. *Biophysical journal*, 72(4):1541–1555, 04 1997.

[17] Olga K. Dudko, Gerhard Hummer, and Attila Szabo. Intrinsic rates and activation free energies from single-molecule pulling experiments. *Physical Review Letters*, 96(10):108101–, 03 2006.

[18] Amar K. Garg, Rajat Desikan, and Narendra M. Dixit. Preferential presentation of high-affinity immune complexes in germinal centers can explain how passive immunization improves the humoral response. *Cell Reports*, 29(12):3946–3957.e5, 2019.

[19] Kayla G. Sprenger, Joy E. Louveau, Pranav M. Murugan, and Arup K. Chakraborty. Optimizing immunization protocols to elicit broadly neutralizing antibodies. *Proceedings of the National Academy of Sciences*, 117(33):20077, 08 2020.

[20] Jiming Sheng and Shenshen Wang. Coevolutionary transitions emerging from flexible molecular recognition and eco-evolutionary feedback. *iScience*, 24(8):102861, 2021.

[21] Robert G. Endres and Ned S. Wingreen. Maximum likelihood and the single receptor. *Physical Review Letters*, 103(15):158101–, 10 2009.

[22] Thierry Mora. Physical limit to concentration sensing amid spurious ligands. *Physical Review Letters*, 115(3):038102–, 07 2015.

[23] Junyi Wang, Feng Lin, Zhengpeng Wan, Xiaolin Sun, Yun Lu, Jianyong Huang, Fei Wang, Yingyue Zeng, Ying-Hua Chen, Yan Shi, Wenjie Zheng, Zhanguo Li, Chunyang Xiong, and Wanli Liu. Profiling the origin, dynamics, and function of traction force in b cell activation. *Science Signaling*, 11(542):eaai9192, 08 2018.

[24] Anita Kumari, Judith Pineau, Pablo J. Sáez, Mathieu Maurin, Danielle Lankar, Mabel San Roman, Katharina Hennig, Vanessa F. Boura, Raphael Voituriez, Mikael C. I. Karlsson, Martial Balland, Ana-Maria Lennon Dumenil, and Paolo Pierobon. Actomyosin-driven force patterning controls endocytosis at the immune synapse. *Nature Communications*, 10(1):2870, 2019.

[25] Christopher D. C. Allen, Takaharu Okada, and Jason G. Cyster. Germinal-center organization and cellular dynamics. *Immunity*, 27(2):190–202, 2007.

[26] Luka Mesin, Jonatan Ersching, and Gabriel D. Victora. Germinal center b cell dynamics. *Immunity*, 45(3):471–482, 2016.

[27] Jason G. Cyster and Christopher D. C. Allen. B cell responses: Cell interaction dynamics and decisions. *Cell*, 177(3):524–540, 2019.

[28] Mark J. Shlomchik, Wei Luo, and Florian Weisel. Linking signaling and selection in the germinal center. *Immunological Reviews*, 288(1):49–63, 02/21/2021 2019.

[29] F D Batista and M S Neuberger. B cells extract and present immobilized antigen: implications for affinity discrimination. *The EMBO journal*, 19(4):513–520, 02 2000.

[30] Facundo D. Batista, Dagmar Iber, and Michael S. Neuberger. B cells acquire antigen from target cells after synapse formation. *Nature*, 411(6836):489–494, 2001.

[31] S. J. Fleire, J. P. Goldman, Y. R. Carrasco, M. Weber, D. Bray, and F. D. Batista. B cell ligand discrimination through a spreading and contraction response. *Science*, 312(5774):738, 05 2006.

[32] Carla R Nowosad, Katelyn M Spillane, and Pavel Tolar. Germinal center b cells recognize antigen through a specialized immune synapse architecture. *Nature Immunology*, 17:870 EP –, 05 2016.

[33] Katelyn M. Spillane and Pavel Tolar. B cell antigen extraction is regulated by physical properties of antigen-presenting cells. *The Journal of Cell Biology*, 216(1):217, 01 2017.

[34] Christopher D. C. Allen, Takaharu Okada, H. Lucy Tang, and Jason G. Cyster. Imaging of germinal center selection events during affinity maturation. *Science*, 315(5811):528, 01 2007.

[35] Alexander D. Gitlin, Ziv Shulman, and Michel C. Nussenzweig. Clonal selection in the germinal centre by regulated proliferation and hypermutation. *Nature*, 509(7502):637–640, 2014.

[36] Ziv Shulman, Alexander D. Gitlin, Jason S. Weinstein, Begoña Lainez, Enric Esplugues, Richard A. Flavell, Joseph E. Craft, and Michel C. Nussenzweig. Dynamic signaling by t follicular helper cells during germinal center b cell selection. *Science*, 345(6200):1058, 08 2014.

[37] Katelyn M. Spillane and Pavel Tolar. Mechanics of antigen extraction in the b cell synapse. *Molecular Immunology*, 101:319–328, 2018.

[38] Peter Hänggi, Peter Talkner, and Michal Borkovec. Reaction-rate theory: fifty years after kramers. *Reviews of Modern Physics*, 62(2):251–341, 04 1990.

[39] H. A. Kramers. Brownian motion in a field of force and the diffusion model of chemical reactions. *Physica*, 7(4):284–304, 1940.

[40] S Izrailev, S Stepaniants, M Balsera, Y Oono, and K Schulten. Molecular dynamics study of unbinding of the avidin-biotin complex. *Biophysical journal*, 72(4):1568–1581, 1997.

[41] Keir C Neuman and Attila Nagy. Single-molecule force spectroscopy: optical tweezers, magnetic tweezers and atomic force microscopy. *Nature Methods*, 5(6):491–505, 2008.

[42] Florin Ernst-Ludwig, Moy Vincent T., and Gaub Hermann E. Adhesion forces between individual ligand-receptor pairs. *Science*, 264(5157):415–417, 2022/01/23 1994.

[43] Kuo Scot C. and Sheetz Michael P. Force of single kinesin molecules measured with optical tweezers. *Science*, 260(5105):232–234, 2022/01/23 1993.

[44] Rico Felix, Gonzalez Laura, Casuso Ignacio, Puig-Vidal Manel, and Scheuring Simon. High-speed force spectroscopy unfolds titin at the velocity of molecular dynamics simulations. *Science*, 342(6159):741–743, 2022/01/23 2013.

[45] R. Merkel, P. Nassoy, A. Leung, K. Ritchie, and E. Evans. Energy landscapes of receptor–ligand bonds explored with dynamic force spectroscopy. *Nature*, 397(6714):50–53, 1999.

[46] Torsten Strunz, Krisztina Oroszlan, Rolf Schäfer, and Hans-Joachim Güntherodt. Dynamic force spectroscopy of single dna molecules. *Proceedings of the National Academy of Sciences*, 96(20):11277, 09 1999.

[47] Gerhard Hummer and Attila Szabo. Kinetics from nonequilibrium single-molecule pulling experiments. *Biophysical Journal*, 85(1):5–15, 2021/11/14 2003.

[48] Gerhard Hummer and Attila Szabo. Free energy reconstruction from nonequilibrium single-molecule pulling experiments. *Proceedings of the National Academy of Sciences*, 98(7):3658, 03 2001.

[49] O. K. Dudko, A. E. Filippov, J. Klafter, and M. Urbakh. Beyond the conventional description of dynamic force spectroscopy of adhesion bonds. *Proceedings of the National Academy of Sciences*, 100(20):11378, 09 2003.

[50] Olga K. Dudko, Jérôme Mathé, Attila Szabo, Amit Meller, and Gerhard Hummer. Extracting kinetics from single-molecule force spectroscopy: Nanopore unzipping of dna hairpins. *Biophysical Journal*, 92(12):4188–4195, 2007.

[51] Jason G Cyster. B cell follicles and antigen encounters of the third kind. *Nature Immunology*, 11:989 EP –, 10 2010.

[52] Kazuhiro Suzuki, Irina Grigorova, Tri Giang Phan, Lisa M. Kelly, and Jason G. Cyster. Visualizing b cell capture of cognate antigen from follicular dendritic cells. *Journal of Experimental Medicine*, 206(7):1485–1493, 4/28/2020 2009.

[53] Baljon Arlette R. C. and Robbins Mark O. Energy dissipation during rupture of adhesive bonds. *Science*, 271(5248):482–484, 2022/02/15 1996.

[54] Benedikt Sabass and Ulrich S Schwarz. Modeling cytoskeletal flow over adhesion sites: competition between stochastic bond dynamics and intracellular relaxation. *Journal of Physics: Condensed Matter*, 22(19):194112, apr 2010.

[55] Xing Du, Yi Li, Yuan-Ling Xia, Shi-Meng Ai, Jing Liang, Peng Sang, Xing-Lai Ji, and Shu-Qun Liu. Insights into protein–ligand interactions: Mechanisms, models, and methods. *International Journal of Molecular Sciences*, 17(2), 2016.

[56] Nicolaas Godfried Van Kampen. *Stochastic processes in physics and chemistry*, volume 1. Elsevier, 1992.

[57] M. San Miguel and S. Chaturvedi. Limit cycles and detailed balance in fokker-planck equations. *Zeitschrift für Physik B Condensed Matter*, 40(1):167–174, 1980.

[58] P. Talkner. Mean first passage time and the lifetime of a metastable state. *Zeitschrift für Physik B Condensed Matter*, 68(2):201–207, 1987.

[59] J. S. Langer. Statistical theory of the decay of metastable states. *Annals of Physics*, 54(2):258–275, 1969.

[60] C. W. Parker, T. J. Yoo, M. C. Johnson, and S. M. Godt. Fluorescent probes for the study of the antibody-hapten reaction. i. binding of the 5-dimethylaminonaphthalene-1-sulfonamido group by homologous rabbit antibody*. *Biochemistry*, 6(11):3408–3416, 11 1967.

[61] ALBERTO J. L. MACARIO and EVERLY CONWAY DE MACARIO. Low and high affinity antibodies can alternate during the immune response. *Nature*, 245(5423):263–264, 1973.

[62] MARTIN G. WEIGERT, ITALO M. CESARI, SHIRLEE J. YONKOVICH, and MELVIN COHN. Variability in the lambda light chain sequences of mouse antibody. *Nature*, 228(5276):1045–1047, 1970.

[63] M B Lascombe, P M Alzari, G Boulot, P Saludjian, P Tougard, C Berek, S Haba, E M Rosen, A Nisonoff, and R J Poljak. Three-dimensional structure of fab r19.9, a monoclonal murine antibody specific for the p-azobenzenearsonate group. *Proceedings of the National Academy of Sciences*, 86(2):607, 01 1989.

[64] Tanja A. Schwickert, Randall L. Lindquist, Guy Shakhar, Geulah Livshits, Dimitris Skokos, Marie H. Kosco-Vilbois, Michael L. Dustin, and Michel C. Nussenzweig. In vivo imaging of germinal centres reveals a dynamic open structure. *Nature*, 446:83 EP –, 01 2007.

[65] Gabriel D. Victora, Tanja A. Schwickert, David R. Fooksman, Alice O. Kamphorst, Michael Meyer-Hermann, Michael L. Dustin, and Michel C. Nussenzweig. Germinal center dynamics revealed by multiphoton microscopy with a photoactivatable fluorescent reporter. *Cell*, 143(4):592–605, 2010.

[66] Thomas B Kepler and Alan S Perelson. Cyclic re-entry of germinal center b cells and the efficiency of affinity maturation. *Immunology Today*, 14(8):412–415, 1993.

[67] Michael Meyer-Hermann, Elodie Mohr, Nadége Pelletier, Yang Zhang, Gabriel D. Victora, and Kai-Michael Toellner. A theory of germinal center b cell selection, division, and exit. *Cell Reports*, 2(1):162–174, 2012.

[68] Shishi Luo and Alan S. Perelson. Competitive exclusion by autologous antibodies can prevent broad hiv-1 antibodies from arising. *Proceedings of the National Academy of Sciences*, 112(37):11654, 09 2015.

[69] J. Scott Shaffer, Penny L. Moore, Mehran Kardar, and Arup K. Chakraborty. Optimal immunization cocktails can promote induction of broadly neutralizing abs against highly mutable pathogens. *Proceedings of the National Academy of Sciences*, 113(45):E7039, 11 2016.

[70] Shenshen Wang. Optimal sequential immunization can focus antibody responses against diversity loss and distraction. *PLOS Computational Biology*, 13(1):e1005336–, 01 2017.

[71] Raman S. Ganti and Arup K. Chakraborty. Mechanisms underlying vaccination protocols that may optimally elicit broadly neutralizing antibodies against highly mutable pathogens. *Physical Review E*, 103(5):052408–, 05 2021.

[72] Marco Molari, Klaus Eyer, Jean Baudry, Simona Cocco, Rémi Monasson, Armita Nourmohammad, Naama Barkai, Andreas Mayer, and William S DeWitt III. Quantitative modeling of the effect of antigen dosage on b-cell affinity distributions in maturating germinal centers. *eLife*, 9:e55678, 2020.

[73] Y Zhang, M Meyer-Hermann, LA George, MT Figge, M Khan, M Goodall, SP Young, A Reynolds, F Falciani, A Waisman, CA Notley, MR Ehrenstein, M Kosco-Vilbois, and KM Toellner. Germinal center b cells govern their own fate via antibody feedback. *The Journal of Experimental Medicine*, 210(3):457–464, 2013-03-11 00:00:00.0.

[74] Michael Meyer-Hermann. Injection of antibodies against immunodominant epitopes tunes germinal centers to generate broadly neutralizing antibodies. *Cell Reports*, 29(5):1066–1073.e5, 2019.

[75] Assaf Amitai, Arup K. Chakraborty, and Mehran Kardar. The low spike density of hiv may have evolved because of the effects of t helper cell depletion on affinity maturation. *PLOS Computational Biology*, 14(8):e1006408–, 08 2018.

[76] Assaf Amitai, Luka Mesin, Gabriel D Victora, Mehran Kardar, and Arup K Chakraborty. A population dynamics model for clonal diversity in a germinal center. *Frontiers in microbiology*, 8:1693–1693, 09 2017.

[77] Michael Meyer-Hermann, Sebastian C. Binder, Luka Mesin, and Gabriel D. Victora. Computer simulation of multi-color brainbow staining and clonal evolution of b cells in germinal centers. *Frontiers in Immunology*, 9, 2018.

[78] Aurélien Pélissier, Youcef Akrout, Katharina Jahn, Jack Kuipers, Ulf Klein, Niko Beerenwinkel, and María Rodríguez Martínez. Computational model reveals a stochastic mechanism behind germinal center clonal bursts. *Cells*, 9(6), 2020.

[79] Rinako Nakagawa, Amparo Toboso-Navasa, Marta Schips, George Young, Leena Bhaw-Rosun, Miriam Llorian-Sopena, Probir Chakravarty, Abdul Karim Sesay, George Kassiotis, Michael Meyer-Hermann, and Dinis Pedro Calado. Permissive selection followed by affinity-based proliferation of gc light zone b cells dictates cell fate and ensures clonal breadth. *Proceedings of the National Academy of Sciences*, 118(2):e2016425118, 01 2021.

[80] Jeroen M. J. Tas, Luka Mesin, Giulia Pasqual, Sasha Targ, Johanne T. Jacobsen, Yasuko M. Mano, Casie S. Chen, Jean-Claude Weill, Claude-Agnès Reynaud, Edward P. Browne, Michael Meyer-Hermann, and Gabriel D. Victora. Visualizing antibody affinity maturation in germinal centers. *Science*, 351(6277):1048–1054, 2016.

[81] Zhengpeng Wan, Shaosen Zhang, Yilin Fan, Kai Liu, Feng Du, Angel M. Davey, Huiyuan Zhang, Weidong Han, Chunyang Xiong, and Wanli Liu. B cell activation is regulated by the stiffness properties of the substrate presenting the antigens. *The Journal of Immunology*, 190(9):4661, 2013.

[82] Samina Shaheen, Zhengpeng Wan, Zongyu Li, Alicia Chau, Xinxin Li, Shaosen Zhang, Yang Liu, Junyang Yi, Yingyue Zeng, Jing Wang, Xiangjun Chen, Liling Xu, Wei Chen, Fei Wang, Yun Lu, Wenjie Zheng, Yan Shi, Xiaolin Sun, Zhanguo Li, Chunyang

Xiong, Wanli Liu, and Michael L Dustin. Substrate stiffness governs the initiation of b cell activation by the concerted signaling of pkc$\beta$and focal adhesion kinase. *eLife*, 6:e23060, 2017.

[83] Robbert Hoogeboom, Elizabeth M Natkanski, Carla R Nowosad, Dessislava Malinova, Rajesh P Menon, Antonio Casal, and Pavel Tolar. Myosin iia promotes antibody responses by regulating b cell activation, acquisition of antigen, and proliferation. *Cell Rep*, 23(8):2342–2353, May 2018.

[84] Jinmin Lee, Prabuddha Sengupta, Joseph Brzostowski, Jennifer Lippincott-Schwartz, and Susan K. Pierce. The nanoscale spatial organization of b-cell receptors on immunoglobulin m–and g–expressing human b-cells. *Molecular Biology of the Cell*, 28(4):511–523, 2022/10/30 2016.

[85] Gitlin Alexander D., Mayer Christian T., Oliveira Thiago Y., Shulman Ziv, Jones Mathew J. K., Koren Amnon, and Nussenzweig Michel C. T cell help controls the speed of the cell cycle in germinal center b cells. *Science*, 349(6248):643–646, 2022/01/05 2015.

[86] Mayer Christian T., Gazumyan Anna, Kara Ervin E., Gitlin Alexander D., Golijanin Jovana, Viant Charlotte, Pai Joy, Oliveira Thiago Y., Wang Qiao, Escolano Amelia, Medina-Ramirez Max, Sanders Rogier W., and Nussenzweig Michel C. The microanatomic segregation of selection by apoptosis in the germinal center. *Science*, 358(6360):eaao2602, 2021/09/24 2017.

[87] Facundo D. Batista and Naomi E. Harwood. The who, how and where of antigen presentation to b cells. *Nature Reviews Immunology*, 9(1):15–27, 2009.

[88] F. Hjelm, F. Carlsson, A. Getahun, and B. Heyman. Antibody-mediated regulation of the immune response. *Scandinavian Journal of Immunology*, 64(3):177–184, 2021/11/20 2006.

[89] Michael M. Desai and Daniel S. Fisher. Beneficial mutation–selection balance and the effect of linkage on positive selection. *Genetics*, 176(3):1759, 2007.

[90] GEORGE R. PRICE. Selection and covariance. *Nature*, 227(5257):520–521, 1970.

[91] Florian Klein, Ron Diskin, Johannes F. Scheid, Christian Gaebler, Hugo Mouquet, Ivelin S. Georgiev, Marie Pancera, Tongqing Zhou, Reha-Baris Incesu, Brooks Zhongzheng Fu, Priyanthi N. P. Gnanapragasam, Thiago Y. Oliveira, Michael S. Seaman, Peter D. Kwong, Pamela J. Bjorkman, and Michel C. Nussenzweig. Somatic mutations of the immunoglobulin framework are generally required for broad and potent hiv-1 neutralization. *Cell*, 153(1):126–138, 2021/11/17 2013.

[92] Victor Ovchinnikov, Joy E Louveau, John P Barton, Martin Karplus, Arup K Chakraborty, and Aleksandra M Walczak. Role of framework mutations and antibody flexibility in the evolution of broadly neutralizing antibodies. *eLife*, 7:e33038, 2018.

[93] Kenneth B. Hoehn, Anna Fowler, Gerton Lunter, and Oliver G. Pybus. The diversity and molecular evolution of b-cell receptors during infection. *Molecular Biology and Evolution*, 33(5):1147–1157, 11/18/2021 2016.

[94] Wei Luo, Florian Weisel, and Mark J. Shlomchik. B cell receptor and cd40 signaling are rewired for synergistic induction of the c-myc transcription factor in germinal center b cells. *Immunity*, 48(2):313–326.e5, 2018.

[95] Wei Luo, William Hawse, Laura Conter, Nikita Trivedi, Florian Weisel, Daniel Wikenheiser, Richard T. Cattley, and Mark J. Shlomchik. The akt kinase signaling network is rewired by pten to control proximal bcr signaling in germinal center b cells. *Nature Immunology*, 20(6):736–746, 2019.

[96] Julia Morfill, Kerstin Blank, Christian Zahnd, Beatrice Luginbühl, Ferdinand Kühner, Kay-E. Gottschalk, Andreas Plückthun, and Hermann E. Gaub. Affinity-matured recombinant antibody fragments analyzed by single-molecule force spectroscopy. *Biophysical Journal*, 93(10):3583–3590, 2007.

[97] Masayuki Kuraoka, Aaron G. Schmidt, Takuya Nojima, Feng Feng, Akiko Watanabe, Daisuke Kitamura, Stephen C. Harrison, Thomas B. Kepler, and Garnett Kelsoe. Complex antigens drive permissive clonal selection in germinal centers. *Immunity*, 44(3):542–552, 2016.

[98] Simon Mitchell, Koushik Roy, Thomas A. Zangle, and Alexander Hoffmann. Nongenetic origins of cell-to-cell variability in b lymphocyte proliferation. *Proceedings of the National Academy of Sciences*, 115(12):E2888, 03 2018.

[99] William T. Yewdell, Ryan M. Smolkin, Kalina T. Belcheva, Alejandra Mendoza, Anthony J. Michaels, Montserrat Cols, Davide Angeletti, Jonathan W. Yewdell, and Jayanta Chaudhuri. Temporal dynamics of persistent germinal centers and memory b cell differentiation following respiratory virus infection. *Cell Reports*, 37(6):109961, 2021.

[100] Carola García de Vinuesa, Matthew C. Cook, Jennifer Ball, Marion Drew, Yvonne Sunners, Marilia Cascalho, Matthias Wabl, Gerry G. B. Klaus, and Ian C. M. MacLennan. Germinal centers without t cells. *Journal of Experimental Medicine*, 191(3):485–494, 10/6/2022 2000.

[101] Nicole Wittenbrink, Tom S. Weber, Anke Klein, Armin A. Weiser, Werner Zuschratter, Michael Sibila, Johannes Schuchhardt, and Michal Or-Guil. Broad volume distributions indicate nonsynchronized growth and suggest sudden collapses of germinal center b cell populations. *The Journal of Immunology*, 184(3):1339, 02 2010.

[102] Mao Hanbin, Cremer Paul S., and Manson Michael D. A sensitive, versatile microfluidic assay for bacterial chemotaxis. *Proceedings of the National Academy of Sciences*, 100(9):5449–5454, 2022/04/22 2003.

[103] Darrell J. Irvine, Marco A. Purbhoo, Michelle Krogsgaard, and Mark M. Davis. Direct observation of ligand recognition by t cells. *Nature*, 419(6909):845–849, 2002.

[104] Jun Huang, Mario Brameshuber, Xun Zeng, Jianming Xie, Qi-jing Li, Yueh-hsiu Chien, Salvatore Valitutti, and Mark M. Davis. A single peptide-major histocompatibility complex ligand triggers digital cytokine secretion in cd4$^+$ t cells. *Immunity*, 39(5):846–857, 2022/05/09 2013.

[105] Paul François, Guillaume Voisinne, Eric D. Siggia, Grégoire Altan-Bonnet, and Massimo Vergassola. Phenotypic model for early t-cell activation displaying sensitivity, specificity, and antagonism. *Proceedings of the National Academy of Sciences*, 110(10):E888, 03 2013.

[106] H. C. Berg and E. M. Purcell. Physics of chemoreception. *Biophysical Journal*, 20(2):193–219, 1977.

[107] Endres Robert G. and Wingreen Ned S. Accuracy of direct gradient sensing by single cells. *Proceedings of the National Academy of Sciences*, 105(41):15749–15754, 2022/05/09 2008.

[108] Thierry Mora and Ned S. Wingreen. Limits of sensing temporal concentration changes by single cells. *Physical Review Letters*, 104(24):248101–, 06 2010.

[109] Christopher C. Govern and Pieter Rein ten Wolde. Energy dissipation and noise correlations in biochemical sensing. *Physical Review Letters*, 113(25):258102–, 12 2014.

[110] Andre C. Barato and Udo Seifert. Thermodynamic uncertainty relation for biomolecular processes. *Physical Review Letters*, 114(15):158101–, 04 2015.

[111] Paul François and Grégoire Altan-Bonnet. The case for absolute ligand discrimination: Modeling information processing and decision by immune t cells. *Journal of Statistical Physics*, 162(5):1130–1152, 2016.

[112] Mayer Andreas, Balasubramanian Vijay, Walczak Aleksandra M., and Mora Thierry. How a well-adapting immune system remembers. *Proceedings of the National Academy of Sciences*, 116(18):8815–8823, 2022/05/09 2019.

[113] Duncan Kirby, Jeremy Rothschild, Matthew Smart, and Anton Zilman. Pleiotropy enables specific and accurate signaling in the presence of ligand cross talk. *Physical Review E*, 103(4):042401–, 04 2021.

[114] Robert C. Rickert. New insights into pre-bcr and bcr signalling with relevance to b cell malignancies. *Nature Reviews Immunology*, 13(8):578–591, 2013.

[115] Wanli Liu, Pavel Tolar, Wenxia Song, and Tae Jin Kim. Editorial: Bcr signaling and b cell activation. *Frontiers in Immunology*, 11, 2020.

[116] Munir Akkaya, Javier Traba, Alexander S. Roesler, Pietro Miozzo, Billur Akkaya, Brandon P. Theall, Haewon Sohn, Mirna Pena, Margery Smelkinson, Juraj Kabat, Eric Dahlstrom, David W. Dorward, Jeff Skinner, Michael N. Sack, and Susan K. Pierce. Second signals rescue b cells from activation-induced mitochondrial dysfunction and death. *Nature Immunology*, 19(8):871–884, 2018.

[117] Ashraf M. Khalil, John C. Cambier, and Mark J. Shlomchik. B cell receptor signal transduction in the gc is short-circuited by high phosphatase activity. *Science*, 336(6085):1178, 06 2012.

[118] Jackson Steed Turner, Fang Ke, and Irina Leonidovna Grigorova. B cell receptor crosslinking augments germinal center b cell selection when t cell help is limiting. *Cell Reports*, 25(6):1395–1403.e4, 2018.

[119] Julie Zikherman. Gc b cells 'akt'to blunt bcr signaling. *Nature Immunology*, 20(6):671–674, 2019.

[120] N. G. VAN KAMPEN. *Chapter VI - ONE-STEP PROCESSES*, pages 134–165. Elsevier, Amsterdam, 2007.

[121] Dibyendu Kumar Das, Yinnian Feng, Robert J. Mallis, Xiaolong Li, Derin B. Keskin, Rebecca E. Hussey, Sonia K. Brady, Jia-Huai Wang, Gerhard Wagner, Ellis L. Reinherz, and Matthew J. Lang. Force-dependent transition in the t-cell receptor β-subunit allosterically regulates peptide discrimination and pmhc bond lifetime. *Proceedings of the National Academy of Sciences*, 112(5):1517, 02 2015.

[122] Peter Bretscher and Melvin Cohn. A theory of self-nonself discrimination. *Science*, 169(3950):1042, 09 1970.

[123] T W McKeithan. Kinetic proofreading in t-cell receptor signal transduction. *Proceedings of the National Academy of Sciences*, 92(11):5042, 1995.

[124] Raman S. Ganti, Wan-Lin Lo, Darren B. McAffee, Jay T. Groves, Arthur Weiss, and Arup K. Chakraborty. How the t cell signaling network processes information to discriminate between self and agonist ligands. *Proceedings of the National Academy of Sciences*, 117(42):26020, 10 2020.

[125] Alexander Ly, Maarten Marsman, Josine Verhagen, Raoul Grasman, and Eric-Jan Wagenmakers. A tutorial on fisher information, 2017.

[126] Harald Cramer. *Mathematical methods of statistics*. Princeton University Press, Princeton, 1999.

[127] Srividya Iyer-Biswas and Anton Zilman. First passage processes in cellular biology, 2015.

[128] Thorsten Erdmann and Ulrich S. Schwarz. Stochastic dynamics of adhesion clusters under shared constant force and with rebinding. *The Journal of Chemical Physics*, 121(18):8997–9017, 2019/12/26 2004.

[129] Jefferson Foote and Herman N. Eisen. Breaking the affinity ceiling for antibodies and t cell receptors. *Proceedings of the National Academy of Sciences*, 97(20):10679, 09 2000.

[130] T. Erdmann and U. S. Schwarz. Stability of adhesion clusters under constant force. *Physical Review Letters*, 92(10):108102–, 03 2004.

[131] Todd A. Sulchek, Raymond W. Friddle, Kevin Langry, Edmond Y. Lau, Huguette Albrecht, Timothy V. Ratto, Sally J. DeNardo, Michael E. Colvin, and Aleksandr Noy. Dynamic force spectroscopy of parallel individual mucin1–antibody bonds. *Proceedings of the National Academy of Sciences of the United States of America*, 102(46):16638, 11 2005.

[132] M. Stein, A. Mezghani, and J. A. Nossek. A lower bound for the fisher information measure. *IEEE Signal Processing Letters*, 21(7):796–799, 2014.

[133] Ranjith Nair and Mankei Tsang. Far-field superresolution of thermal electromagnetic sources at the quantum limit. *Phys. Rev. Lett.*, 117:190801, Nov 2016.

[134] Tomasz Jetka, Karol Nienałtowski, Sarah Filippi, Michael P H Stumpf, and Michał Komorowski. An information-theoretic framework for deciphering pleiotropic and noisy biochemical signaling. *Nature Communications*, 9(1):4591, 2018.

[135] Pieter Rein ten Wolde, Andrew Mugler, Ronald Hancock, and Kwang W. Jeon. *Chapter Twelve - Importance of Crowding in Signaling, Genetic, and Metabolic Networks*, volume 307, pages 419–442. Academic Press, 2014.

[136] James Mueller, Mehrdad Matloubian, and Julie Zikherman. Cutting edge: An in vivo reporter reveals active b cell receptor signaling in the germinal center. *The Journal of Immunology*, 194(7):2993, 04 2015.

[137] Ofer Feinerman, Ronald N. Germain, and Grégoire Altan-Bonnet. Quantitative challenges in understanding ligand discrimination by $\alpha\beta$ t cells. *Molecular Immunology*, 45(3):619–631, 2008.

[138] Irena Štefanová, Bernhard Hemmer, Marco Vergelli, Roland Martin, William E. Biddison, and Ronald N. Germain. Tcr ligand discrimination is enforced by competing erk positive and shp-1 negative feedback pathways. *Nature Immunology*, 4(3):248–254, 2003.

[139] Grégoire Altan-Bonnet and Ronald N Germain. Modeling t cell antigen discrimination based on feedback control of digital erk responses. *PLOS Biology*, 3(11):e356–, 10 2005.

[140] Grégoire Altan-Bonnet, Thierry Mora, and Aleksandra M. Walczak. Quantitative immunology for physicists. *Physics Reports*, 849:1–83, 2020.

[141] Morgan Huse. Mechanical forces in the immune system. *Nature Reviews Immunology*, 17(11):679–690, 2017.

[142] Naomi E Harwood and Facundo D Batista. The cytoskeleton coordinates the early events of b-cell activation. *Cold Spring Harbor Perspectives in Biology*, 3(2):a002360, 2011.

[143] Joshua M. Brockman and Khalid Salaita. Mechanical proofreading: A general mechanism to enhance the fidelity of information transfer between cells. *Frontiers in Physics*, 7:14, 2019.

[144] Roshni Basu and Morgan Huse. Mechanical communication at the immunological synapse. *Trends in Cell Biology*, 27(4):241–254, 2017.

[145] Daniel T. Gillespie. Exact stochastic simulation of coupled chemical reactions. *The Journal of Physical Chemistry*, 81(25):2340–2361, 12 1977.

[146] Wenping Cui and Pankaj Mehta. Identifying feasible operating regimes for early t-cell recognition: The speed, energy, accuracy trade-off in kinetic proofreading and adaptive sorting. *PLOS ONE*, 13(8):e0202331–, 08 2018.

[147] Vahe Galstyan, Kabir Husain, Fangzhou Xiao, Arvind Murugan, and Rob Phillips. Proofreading through spatial gradients. *bioRxiv*, page 2020.05.23.112664, 01 2020.

[148] John W. Schrader. Antagonism of b lymphocyte mitogenesis by anti-immunoglobulin antibody. *The Journal of Immunology*, 115(2):323, 08 1975.

[149] John F. Kearney, Max D. Cooper, and Alexander R. Lawton. B lymphocyte differentiation induced by lipopolysaccharide. *The Journal of Immunology*, 116(6):1664, 06 1976.

[150] Stephen C. Jameson and Michael J. Bevan. T cell receptor antagonists and partial agonists. *Immunity*, 2(1):1–11, 1995.

[151] J Ruppert, J Alexander, K Snoke, M Coggeshall, E Herbert, D McKenzie, H M Grey, and A Sette. Effect of t-cell receptor antagonism on interaction between t cells and antigen-presenting cells and on t-cell signaling events. *Proceedings of the National Academy of Sciences*, 90(7):2671, 04 1993.

[152] Bernard Vanhove, Nicolas Poirier, Fadi Fakhouri, Laetitia Laurent, Bert 't Hart, Pedro H. Papotto, Luiz V. Rizzo, Masaaki Zaitsu, Fadi Issa, Kathryn Wood, Jean-Paul Soulillou, and Gilles Blancho. Antagonist anti-cd28 therapeutics for the treatment of autoimmune disorders. *Antibodies*, 6(4), 2017.

[153] Rana A. K. Singh, John R. Rodgers, and Michael A. Barry. The role of t cell antagonism and original antigenic sin in genetic immunization. *The Journal of Immunology*, 169(12):6779, 12 2002.

[154] Huw Colin-York, Yousef Javanmardi, Mark Skamrahl, Sudha Kumari, Veronica T. Chang, Satya Khuon, Aaron Taylor, Teng-Leong Chew, Eric Betzig, Emad Moeendarbary, Vincenzo Cerundolo, Christian Eggeling, and Marco Fritzsche. Cytoskeletal control of antigen-dependent t cell activation. *Cell Reports*, 26(12):3369–3379.e5, 2019.

[155] Siobain Duffy, Laura A. Shackelton, and Edward C. Holmes. Rates of evolutionary change in viruses: patterns and determinants. *Nature Reviews Genetics*, 9:267, Mar 2008.

[156] Mel Greaves and Carlo C. Maley. Clonal evolution in cancer. *Nature*, 481:306, Jan 2012.

[157] Melvin Lax. Fluctuations from the nonequilibrium steady state. *Reviews of modern physics*, 32(1):25, 1960.

[158] Hong Qian. Open-system nonequilibrium steady state: statistical thermodynamics, fluctuations, and chemical oscillations, 2006.

[159] Armita Nourmohammad, Jakub Otwinowski, and Joshua B. Plotkin. Host-pathogen coevolution and the emergence of broadly neutralizing antibodies in chronic infections. *PLOS Genetics*, 12(7):1–23, 07 2016.

[160] Cobey Sarah, Wilson Patrick, and Matsen Frederick A. The evolution within us. *Philosophical Transactions of the Royal Society B: Biological Sciences*, 370(1676):20140235, 2019/06/19 2015.

[161] Fabio Zanini, Johanna Brodin, Lina Thebo, Christa Lanz, Göran Bratt, Jan Albert, Richard A Neher, and Arup K Chakraborty. Population genomics of intrapatient hiv-1 evolution. *eLife*, 4:e11282, 2015.

[162] Richard A. Neher, Trevor Bedford, Rodney S. Daniels, Colin A. Russell, and Boris I. Shraiman. Prediction, dynamics, and visualization of antigenic phenotypes of seasonal influenza viruses. *Proceedings of the National Academy of Sciences*, 113(12):E1701, 03 2016.

[163] Marta Łuksza and Michael Lässig. A predictive fitness model for influenza. *Nature*, 507:57 EP –, 02 2014.

[164] Marta Łuksza, Nadeem Riaz, Vladimir Makarov, Vinod P. Balachandran, Matthew D. Hellmann, Alexander Solovyov, Naiyer A. Rizvi, Taha Merghoub, Arnold J. Levine, Timothy A. Chan, Jedd D. Wolchok, and Benjamin D. Greenbaum. A neoantigen fitness model predicts tumour response to checkpoint blockade immunotherapy. *Nature*, 551:517 EP –, 11 2017.

[165] J. S. Weitz, H. Hartman, and S. A. Levin. Coevolutionary arms races between bacteria and bacteriophage. *Proceedings of the National Academy of Sciences of the United States of America*, 102(27):9535, 07 2005.

[166] Serena Bradde, Marija Vucelja, Tiberiu Teşileanu, and Vijay Balasubramanian. Dynamics of adaptive immunity against phage in bacterial populations. *PLOS Computational Biology*, 13(4):1–16, 04 2017.

[167] Ulf Dieckmann, Michael Doebeli, Johan A. J. Metz, and Diethard Tautz. *Adaptive Speciation*. Cambridge University Press, Cambridge, 2004.

[168] Gregor F. Fussmann, Stephen P. Ellner, Kyle W. Shertzer, and Nelson G. Hairston Jr. Crossing the hopf bifurcation in a live predator-prey system. *Science*, 290(5495):1358–1360, 2000.

[169] Takehito Yoshida, Stephen P Ellner, Laura E Jones, Brendan J. M Bohannan, Richard E Lenski, and Nelson G Hairston, Jr. Cryptic population dynamics: Rapid evolution masks trophic interactions. *PLOS Biology*, 5(9):1–12, 09 2007.

[170] Laura E. Jones and Stephen P. Ellner. Effects of rapid prey evolution on predator–prey cycles. *Journal of Mathematical Biology*, 55(4):541–573, Oct 2007.

[171] Hong-Yan Shih and Nigel Goldenfeld. Path-integral calculation for the emergence of rapid evolution from demographic stochasticity. *Phys. Rev. E*, 90:050702, Nov 2014.

[172] Kalin Vetsigian. Diverse modes of eco-evolutionary dynamics in communities of antibiotic-producing microorganisms. *Nature Ecology &Amp; Evolution*, 1:0189 EP –, 06 2017.

[173] Wienand Karl, Frey Erwin, and Mobilia Mauro. Eco-evolutionary dynamics of a population with randomly switching carrying capacity. *Journal of The Royal Society Interface*, 15(145):20180343, 2019/06/19 2018.

[174] J. Halatek and E. Frey. Rethinking pattern formation in reaction–diffusion systems. *Nature Physics*, 14(5):507–514, 2018.

[175] Seyfullah Enes Kotil and Kalin Vetsigian. Emergence of evolutionarily stable communities through eco-evolutionary tunnelling. *Nature Ecology & Evolution*, 2(10):1644–1653, 2018.

[176] Michael E. Birnbaum, Juan L. Mendoza, Dhruv K. Sethi, Shen Dong, Jacob Glanville, Jessica Dobbins, Engin Özkan, Mark M. Davis, Kai W. Wucherpfennig, and K. Christopher Garcia. Deconstructing the peptide-mhc specificity of t cell recognition. *Cell*, 157(5):1073 – 1087, 2014.

[177] Linda Wooldridge, Julia Ekeruche-Makinde, Hugo A. van den Berg, Anna Skowera, John J. Miles, Mai Ping Tan, Garry Dolton, Mathew Clement, Sian Llewellyn-Lacey, David A. Price, Mark Peakman, and Andrew K. Sewell. A single autoimmune t cell receptor recognizes more than a million different peptides. *Journal of Biological Chemistry*, 287(2):1168–1177, 2012.

[178] Turing Alan Mathison. The chemical basis of morphogenesis. *Philosophical Transactions of the Royal Society of London. Series B, Biological Sciences*, 237(641):37–72, 2019/06/19 1952.

[179] Michael Sela. *The Antigens*, volume 6. Academic Press, 2014.

[180] Suganya Selvarajah, Bridget Puffer, Ralph Pantophlet, Mansun Law, Robert W Doms, and Dennis R Burton. Comparing antigenicity and immunogenicity of engineered gp120. *Journal of virology*, 79(19):12148–12163, 2005.

[181] Suraj B Sable, Mamta Kalra, Indu Verma, and GK Khuller. Tuberculosis subunit vaccine design: the conflict of antigenicity and immunogenicity. *Clinical immunology*, 122(3):239–251, 2007.

[182] M.H.V. Van Regenmortel. Antigenicity and immunogenicity of synthetic peptides. *Biologicals*, 29(3):209 – 213, 2001.

[183] Marten Scheffer and Egbert H. van Nes. Self-organized similarity, the evolutionary emergence of groups of similar species. *Proceedings of the National Academy of Sciences*, 103(16):6230–6235, 2006.

[184] Simone Pigolotti, Cristóbal López, and Emilio Hernández-García. Species clustering in competitive lotka-volterra models. *Phys. Rev. Lett.*, 98:258101, Jun 2007.

[185] Michael Doebeli and Iaroslav Ispolatov. Complexity and diversity. *Science*, 328(5977):494–497, 2010.

[186] T. Rogers, A. J. McKane, and A. G. Rossberg. Demographic noise can lead to the spontaneous formation of species. *EPL (Europhysics Letters)*, 97(4):40008, feb 2012.

[187] Lauren Ancel Meyers and James J. Bull. Fighting change with change: adaptive variation in an uncertain world. *Trends in Ecology and Evolution*, 17(12):551 – 557, 2002.

[188] Edo Kussell and Stanislas Leibler. Phenotypic diversity, population growth, and information in fluctuating environments. *Science*, 309(5743):2075–2078, 2005.

[189] Ville Mustonen and Michael Lässig. Molecular evolution under fitness fluctuations. *Phys. Rev. Lett.*, 100:108101, Mar 2008.

[190] Ville Mustonen and Michael Lässig. From fitness landscapes to seascapes: non-equilibrium dynamics of selection and adaptation. *Trends in Genetics*, 25(3):111–119, 2009.

[191] Ivana Cvijović, Benjamin H. Good, Elizabeth R. Jerison, and Michael M. Desai. Fate of a mutation in a fluctuating environment. *Proceedings of the National Academy of Sciences*, 112(36):E5021–E5028, 2015.

[192] BingKan Xue and Stanislas Leibler. Evolutionary learning of adaptation to varying environments through a transgenerational feedback. *Proceedings of the National Academy of Sciences*, 113(40):11266–11271, 2016.

[193] BingKan Xue, Pablo Sartori, and Stanislas Leibler. Environment-to-phenotype mapping and adaptation strategies in varying environments. *Proceedings of the National Academy of Sciences*, page 201903232, 2019.

[194] F. John Odling-Smee, Kevin N. Laland, and Marcus W. Feldman. Niche construction. *The American Naturalist*, 147(4):641–648, 1996.

[195] Jesse D. Bloom, Sy T. Labthavikul, Christopher R. Otey, and Frances H. Arnold. Protein stability promotes evolvability. *Proceedings of the National Academy of Sciences*, 103(15):5869–5874, 2006.

[196] Lizhi Ian Gong, Marc A Suchard, Jesse D Bloom, and Mercedes Pascual. Stability-mediated epistasis constrains the evolution of an influenza protein. *eLife*, 2:e00631, 2013.

[197] Nicholas C. Wu, C. Anders Olson, Yushen Du, Shuai Le, Kevin Tran, Roland Remenyi, Danyang Gong, Laith Q. Al-Mawsawi, Hangfei Qi, Ting-Ting Wu, and Ren Sun. Functional constraint profiling of a viral protein reveals discordance of evolutionary conservation and functionality. *PLOS Genetics*, 11(7):1–27, 07 2015.

[198] Ron Diskin, Florian Klein, Joshua A. Horwitz, Ariel Halper-Stromberg, D. Noah Sather, Paola M. Marcovecchio, Terri Lee, Anthony P. West, Han Gao, Michael S. Seaman, Leonidas Stamatatos, Michel C. Nussenzweig, and Pamela J. Bjorkman. Restricting hiv-1 pathways for escape using rationally designed anti-hiv-1 antibodies. *Journal of Experimental Medicine*, 210(6):1235–1249, 2013.

[199] Sébastien Boyer, Dipanwita Biswas, Ananda Kumar Soshee, Natale Scaramozzino, Clément Nizak, and Olivier Rivoire. Hierarchy and extremes in selections from pools of randomized proteins. *Proceedings of the National Academy of Sciences*, 113(13):3482–3487, 2016.

[200] Rhys M Adams, Thierry Mora, Aleksandra M Walczak, Justin B Kinney, and Jesse D Bloom. Measuring the sequence-affinity landscape of antibodies with massively parallel titration curves. *eLife*, 5:e23156, 2016.

[201] Anthony P. West, Louise Scharf, Joshua Horwitz, Florian Klein, Michel C. Nussenzweig, and Pamela J. Bjorkman. Computational analysis of anti-hiv-1 antibody neutralization panel data to identify potential functional epitope residues. *Proceedings of the National Academy of Sciences*, 110(26):10598–10603, 2013.

[202] Feng Gao, Mattia Bonsignori, Hua-Xin Liao, Amit Kumar, Shi-Mao Xia, Xiaozhi Lu, Fangping Cai, Kwan-Ki Hwang, Hongshuo Song, Tongqing Zhou, Rebecca M. Lynch, S. Munir Alam, M. Anthony Moody, Guido Ferrari, Mark Berrong, Garnett Kelsoe, George M. Shaw, Beatrice H. Hahn, David C. Montefiori, Gift Kamanga, Myron S. Cohen, Peter Hraber, Peter D. Kwong, Bette T. Korber, John R. Mascola, Thomas B. Kepler, and Barton F. Haynes. Cooperation of b cell lineages in induction of hiv-1-broadly neutralizing antibodies. *Cell*, 158(3):481 – 491, 2014.

[203] Penny L. Moore, Carolyn Williamson, and Lynn Morris. Virological features associated with the development of broadly neutralizing antibodies to hiv-1. *Trends in Microbiology*, 23(4):204 – 211, 2015.

[204] Natalia T. Freund, Haoqing Wang, Louise Scharf, Lilian Nogueira, Joshua A. Horwitz, Yotam Bar-On, Jovana Golijanin, Stuart A. Sievers, Devin Sok, Hui Cai, Julio C. Cesar Lorenzi, Ariel Halper-Stromberg, Ildiko Toth, Alicja Piechocka-Trocha, Harry B. Gristick, Marit J. van Gils, Rogier W. Sanders, Lai-Xi Wang, Michael S. Seaman, Dennis R. Burton, Anna Gazumyan, Bruce D. Walker, Anthony P. West, Pamela J. Bjorkman, and Michel C. Nussenzweig. Coexistence of potent hiv-1 broadly neutralizing antibodies and antibody-sensitive viruses in a viremic controller. *Science Translational Medicine*, 9(373), 2017.

[205] Rob J. De Boer and Alan S. Perelson. T cell repertoires and competitive exclusion. *Journal of Theoretical Biology*, 169(4):375 – 390, 1994.

[206] ROB J. DE BOER, ANTÓNIO A. FREITAS, and ALAN S. PERELSON. Resource competition determines selection of b cell repertoires. *Journal of Theoretical Biology*, 212(3):333–343, 2001.

[207] Andreas Mayer, Vijay Balasubramanian, Thierry Mora, and Aleksandra M. Walczak. How a well-adapted immune system is organized. *Proceedings of the National Academy of Sciences*, 112(19):5950–5955, 2015.

[208] Alan S. Perelson and George F. Oster. Theoretical studies of clonal selection: Minimal antibody repertoire size and reliability of self-non-self discrimination. *Journal of Theoretical Biology*, 81(4):645 – 670, 1979.

[209] Alexander W. Tarr, Richard A. Urbanowicz, Mohamed R. Hamed, Anna Albecka, C. Patrick McClure, Richard J. P. Brown, William L. Irving, Jean Dubuisson, and Jonathan K. Ball. Hepatitis c patient-derived glycoproteins exhibit marked differences in susceptibility to serum neutralizing antibodies: Genetic subtype defines antigenic but not neutralization serotype. *Journal of Virology*, 85(9):4246–4257, 2011.

[210] D. Noah Sather, Sara Carbonetti, Delphine C. Malherbe, Franco Pissani, Andrew B. Stuart, Ann J. Hessell, Mathew D. Gray, Iliyana Mikell, Spyros A. Kalams, Nancy L. Haigwood, and Leonidas Stamatatos. Emergence of broadly neutralizing antibodies and viral coevolution in two subjects during the early stages of infection with human immunodeficiency virus type 1. *Journal of Virology*, 88(22):12968–12981, 2014.

[211] L. Yan, R. Neher, and B. I. Shraiman. Phylodynamics of rapidly adapting pathogens: extinction and speciation of a red queen. *arxiv*, page 1810.11918, 2019.

[212] Andy Fenton and Sarah E. Perkins. Applying predator-prey theory to modelling immune-mediated, within-host interspecific parasite interactions. 137(6):1027–1038, 2010.

[213] Kimberly J. Schlesinger, Sean P. Stromberg, and Jean M. Carlson. Coevolutionary immune system dynamics driving pathogen speciation. *PLOS ONE*, 9(7):1–9, 07 2014.

[214] David Karig, K. Michael Martini, Ting Lu, Nicholas A. DeLateur, Nigel Goldenfeld, and Ron Weiss. Stochastic turing patterns in a synthetic bacterial population. *Proceedings of the National Academy of Sciences*, 115(26):6572–6577, 2018.

[215] Lingfa Yang and Irving R. Epstein. Oscillatory turing patterns in reaction-diffusion systems with two coupled layers. *Phys. Rev. Lett.*, 90:178303, May 2003.

[216] Richard A. Miller. The aging immune system: Primer and prospectus. *Science*, 273(5271):70–74, 1996.

[217] Justin R. Bailey and et al. Broadly neutralizing antibodies with few somatic mutations and hepatitis c virus clearance. *JCI Insight*, 2(9), 05 2017.

[218] ALICE S. HUANG and DAVID BALTIMORE. Defective viral particles and viral disease processes. *Nature*, 226(5243):325–327, 1970.

[219] R D Schrier, J W Gnann, A J Langlois, K Shriver, J A Nelson, and M B Oldstone. B- and t-lymphocyte responses to an immunodominant epitope of human immunodeficiency virus. *Journal of Virology*, 62(8):2531–2536, 1988.

[220] Hayley Crawford, Julia G. Prado, Alasdair Leslie, Stéphane Hué, Isobella Honeyborne, Sharon Reddy, Mary van der Stok, Zenele Mncube, Christian Brander, Christine Rousseau, James I. Mullins, Richard Kaslow, Paul Goepfert, Susan Allen, Eric Hunter, Joseph Mulenga, Photini Kiepiela, Bruce D. Walker, and Philip J. R. Goulder. Compensatory mutation partially restores fitness and delays reversion of escape mutation within the immunodominant hla-b*5703-restricted gag epitope in chronic human immunodeficiency virus type 1 infection. *Journal of Virology*, 81(15):8346–8351, 2007.

[221] George I. Bell. Mathematical model of clonal selection and antibody production. *Journal of Theoretical Biology*, 29(2):191–232, 1970.

[222] Eric Jones, Jiming Sheng, Jean Carlson, and Shenshen Wang. Aging-induced fragility of the immune system. *Journal of Theoretical Biology*, 510:110473, 2021.

[223] Julia Merkenschlager, Shlomo Finkin, Victor Ramos, Julian Kraft, Melissa Cipolla, Carla R. Nowosad, Harald Hartweger, Wenzhu Zhang, Paul Dominic B. Olinares, Anna Gazumyan, Thiago Y. Oliveira, Brian T. Chait, and Michel C. Nussenzweig. Dynamic regulation of tfh selection during the germinal centre reaction. *Nature*, 591(7850):458–463, 2021.

[224] M Goulian, R Bruinsma, and P Pincus. Long-range forces in heterogeneous fluid membranes. 22(2):145–150, 1993.

[225] R Bruinsma, M Goulian, and P Pincus. Self-assembly of membrane junctions. *Biophysical journal*, 67(2):746–750, 08 1994.

[226] Timo Bihr, Udo Seifert, and Ana-Sunčana Smith. Nucleation of ligand-receptor domains in membrane adhesion. *Physical Review Letters*, 109(25):258101–, 12 2012.

[227] Miloš Knežević, Hongda Jiang, and Shenshen Wang. Active tuning of synaptic patterns enhances immune discrimination. *Physical Review Letters*, 121(23):238101–, 12 2018.